Semi-analytical prediction of wake-interaction noise in counter-rotating open rotors

Arnulfo Carazo Méndez

N° of Order: 2012-12 **YEAR 2012**

THESIS

presented to
ÉCOLE CENTRALE DE LYON

for the Degree of
DOCTOR OF PHILOSOPHY
in ACOUSTICS

by

Arnulfo CARAZO MÉNDEZ

Semi-Analytical Prediction of Wake-Interaction Noise in Counter-Rotating Open Rotors

Defended the 14th June 2012 in front of the examining committee

JURY

Dr.	Sébastien	GUERIN	
Prof.	Stéphane	MOREAU	(Reviewer)
Prof.	Frank	SIMON	
Dr.	Pierre	SPIEGEL	
Prof.	Michel	ROGER	(PhD Advisor)
Prof.	Xin	ZHANG	(Reviewer)

Laboratoire de Mécanique des Fluides et d'Acoustique, UMR CNRS 5509
École Centrale de Lyon

Acknowledgments

I wish to thank all the people who contributed to make this CIFRE PhD research a very rewarding experience. I am honored to have completed this investigation for two institutions internationally known for their excellency, as École Centrale de Lyon and Airbus Operations SAS.

I sincerely thank Pr. Michel ROGER for his guidance and advisement. His detailed knowledge in the fields encompassed by this research has been an essential support since the beginning of this investigation. Thank you Michel for your patience and your availability for answering my innumerable questions. I also thank Magdi OMAÏS, my technical supervisor at the Airbus acoustic department, who provided me valuable supervision for the application of the theoretical developments to the industrial framework. Also, I am indebted to Yann COLIN (Airbus numerical methods) for his explanations and for providing me the CFD reference to validate models and routines.

I spent two pleasing years at Laboratoire d Mécanique des Fluides et d'Acoustique, at École Centrale de Lyon. I have but good memories of this interesting part of my life. I want to thank all the research team at Centre Acoustique, which made me feel welcomed and enabled me to work in excellent conditions. Special thanks to my fellow PhD candidates for the good time spent together. I remember particularly the advanced Bridge lessons, the Johnny's burgers and the mojito evenings at my place. Thanks to Didier DRAGNA, Nicolas DE CACQUERAY and Arthur FINEZ for our weekly squash sessions (Didier's *punishment*), to Korcan KUCUKCOSKUN, Adrien CAHUZAC, Gaëlle POIGNAND, Edouard SALZE, Benoit ANDRÉ and Benoit LEMOINE for the Poker-Pizza nights.

My gratefulness to the acoustic department of Airbus EEA, particularly to my colleagues of EEA7 for the interest they have manifested towards this investigation. Finally, I wish to express my gratitude to the members of the JURY, specially to my reviewers, for examining my work in detail.

I honestly thank all of you.

ÉCOLE CENTRALE LYON **Direction de la recherche**

Liste des personnes Habilitées à Diriger des Recherches en poste à l'Ecole Centrale de Lyon

Nom-Prénom	*Corps grade*	Laboratoire ou à défaut département ECL	Etablissement
BEROUAL Abderrahmane	*professeur*	AMPERE	ECL
BURET François	*professeur*	AMPERE	ECL
JAFFREZIC-RENAULT Nicole	*directeur de recherche*	AMPERE	CNRS/ECL
KRÄHENBÜHL Laurent	*directeur de recherche*	AMPERE	CNRS/ECL
NICOLAS Alain	*professeur*	AMPERE	ECL
NICOLAS Laurent	*directeur de recherche*	AMPERE	CNRS/ECL
SCORLETTI Gérard	*professeur*	AMPERE	ECL
SIMONET Pascal	*directeur de recherche*	AMPERE	CNRS/ECL
VOLLAIRE Christian	*professeur*	AMPERE	ECL
		Nbre Ampère 9	
HELLOUIN Yves	*maître de conférences*	DER EEA	ECL
		Nbre DER EEA 1	
GUIRALDENQ Pierre	*professeur émérite*	DER STMS	ECL
VINCENT Léo	*professeur*	DER STMS	ECL
		Nbre DER STMS 2	
LOHEAC Jean-Pierre	*maître de conférences*	ICJ	ECL
MAITRE Jean-François	*professeur émérite*	ICJ	ECL
MARION Martine	*professeur*	ICJ	ECL
MIRONESCU Elisabeth	*professeur*	ICJ	ECL
MOUSSAOUI Mohand	*professeur*	ICJ	ECL
MUSY François	*maître de conférences*	ICJ	ECL
ZINE Abdel-Malek	*maître de conférences*	ICJ	ECL
		Nbre ICJ 7	
DAVID Bertrand	*professeur*	ICTT	ECL
		Nbre ICTT 1	
CALLARD Anne-Ségolène	*professeur*	INL	ECL
CLOAREC Jean-Pierre	*maître de conférences*	INL	ECL
GAFFIOT Frédéric	*professeur*	INL	ECL
GAGNAIRE Alain	*maître de conférences*	INL	ECL
GARRIGUES Michel	*directeur de recherche*	INL	CNRS/ECL
GENDRY Michel	*directeur de recherche*	INL	CNRS/ECL
GRENET Geneviève	*directeur de recherche*	INL	CNRS/ECL
HOLLINGER Guy	*directeur de recherche*	INL	CNRS/ECL
KRAWCZYK Stanislas	*directeur de recherche*	INL	CNRS/ECL
LETARTRE Xavier	*chargé de recherche*	INL	CNRS/ECL
O'CONNOR Ian	*professeur*	INL	ECL
PHANER-GOUTORBE Magali	*professeur*	INL	ECL

ROBACH Yves	*professeur*	INL	ECL
SAINT-GIRONS Guillaume	*chargé de recherche*	INL	CNRS/ECL
SEASSAL Christian	*directeur de recherche*	INL	CNRS/ECL
SOUTEYRAND Eliane	*directeur de recherche*	INL	CNRS/ECL
TARDY Jacques	*directeur de recherche*	INL	CNRS/ECL
VIKTOROVITCH Pierre	*directeur de recherche*	INL	CNRS/ECL

Nbre INL 18

CHEN Liming	*professeur*	LIRIS	ECL

Nbre LIRIS 1

BAILLY Christophe	*professeur*	LMFA	ECL
BERTOGLIO Jean-Pierre	*directeur de recherche*	LMFA	CNRS/ECL
BLANC-BENON Philippe	*directeur de recherche*	LMFA	CNRS/ECL
BOGEY Christophe	*chargé de recherche*	LMFA	CNRS/ECL
CAMBON Claude	*directeur de recherche*	LMFA	CNRS/ECL
CARRIERE Philippe	*directeur de recherche*	LMFA	CNRS/ECL
CHAMPOUSSIN J-Claude	*professeur émérite*	LMFA	ECL
COMTE-BELLOT geneviève	*professeur émérite*	LMFA	ECL
FERRAND Pascal	*directeur de recherche*	LMFA	CNRS/ECL
GALLAND Marie-Annick	*professeur*	LMFA	ECL
GODEFERD Fabien	*directeur de recherche*	LMFA	CNRS/ECL
GOROKHOVSKI Mikhail	*professeur*	LMFA	ECL
HENRY Daniel	*directeur de recherche*	LMFA	CNRS/ECL
JEANDEL Denis	*professeur*	LMFA	ECL
JUVE Daniel	*professeur*	LMFA	ECL
LE RIBAULT Catherine	*chargée de recherche*	LMFA	CNRS/ECL
LEBOEUF Francis	*professeur*	LMFA	ECL
PERKINS Richard	*professeur*	LMFA	ECL
ROGER Michel	*professeur*	LMFA	ECL
SCOTT Julian	*professeur*	LMFA	ECL
SHAO Liang	*directeur de recherche*	LMFA	CNRS/ECL
SIMOENS Serge	*chargé de recherche*	LMFA	CNRS/ECL
TREBINJAC Isabelle	*maître de conférences*	LMFA	ECL

Nbre LMFA 23

BENAYOUN Stéphane	*professeur*	LTDS	ECL
CAMBOU Bernard	*professeur*	LTDS	ECL
COQUILLET Bernard	*maître de conférences*	LTDS	ECL
DANESCU Alexandre	*maître de conférences*	LTDS	ECL
FOUVRY Siegfrid	*chargé de recherche*	LTDS	CNRS/ECL
GEORGES Jean-Marie	*professeur émérite*	LTDS	ECL
GUERRET Chrystelle	*chargé de recherche*	LTDS	CNRS/ECL
HERTZ Dominique	*past*	LTDS	ECL
ICHCHOU Mohamed	*professeur*	LTDS	ECL
JEZEQUEL Louis	*professeur*	LTDS	ECL
JUVE Denyse	*ingénieur de recherche*	LTDS	ECL
KAPSA Philippe	*directeur de recherche*	LTDS	CNRS/ECL
LE BOT Alain	*directeur de recherche*	LTDS	CNRS/ECL
LOUBET Jean-Luc	*directeur de recherche*	LTDS	CNRS/ECL
MARTIN Jean-Michel	*professeur*	LTDS	ECL
MATHIA Thomas	*directeur de recherche*	LTDS	CNRS/ECL
MAZUYER Denis	*professeur*	LTDS	ECL
PERRET-LIAUDET Joël	*maître de conférences*	LTDS	ECL
SALVIA Michelle	*maître de conférences*	LTDS	ECL

SIDOROFF François	*professeur*	LTDS	ECL
SINOU Jean-Jacques	*professeur*	LTDS	ECL
STREMSDOERFER Guy	*professeur*	LTDS	ECL
THOUVEREZ Fabrice	*professeur*	LTDS	ECL
TREHEUX Daniel	*professeur*	LTDS	ECL
VINCENS Eric	*maître de conférences*	LTDS	ECL
		Nbre LTDS 25	
	Total HdR ECL	91	

Contents

Nomenclature

Greek Letters

α	Propeller angle of attack
α_f	Front-rotor angle of attack
α_k	Angle between gust frontwaves and segment LE
α_r	Rear-rotor angle of attack
$\beta(r)$	Angle between front-rotor and rear-rotor airfoils
δ	Semi-wake width
ϵ	Convergence error
η	Coordinate aligned with the segment LE
γ	Lean angle
Γ	Stationnary dipole angle
γ_φ	Gust wavenumber in the circumferential direction
γ_y	Gust wavenumber in the tangential direction
κ	Parameter of Helmholtz equation, defined in Eq.(3.12)
Λ	Convergence parameter
λ_ξ	Gust chordwise wavenumber
μ	Compressibility parameter ($= M_x k_1^* / \beta_x^2$)
ω	Acoustic frequency
ω_{km}	Rotor-rotor interaction acoustic mode frequency
Ω_1	Front-rotor angular speed
Ω_2	Rear-rotor angular speed
ω_s	Source frequency
Ω_T	Relative angular speed between both rotors
Φ	Velocity potential in the Prandtl-Glauert plane

ϕ'	Potential field due to gust-airfoil interaction
$\phi(y_1, y_3)$	Potential field independent of y_2 coordinate
Φ, Φ'	Observer angular position in $\mathcal{B}_3$,$\mathcal{B}_1$
ρ_∞	Reference fluid density
σ	Solidity parameter
θ, θ'	Observer angle from flight direction, rotation axis
φ	Circumferential direction
$\bar{\varphi}$	Parallelogram sweep angle
$(\bar{\varphi}_1, \bar{\varphi}_2)$	Sweep angles of trapezoid LE and TE, respectively
ξ	Coordinate aligned with the segment chord
ζ_{km}	Acoustic mode circumferential index

Roman Letters

$\tilde{A}_{le}$	Leading-edge factor
b	Chord half length
$B(r)$	Distance between front segment mid-chord point and rear segment LE
B_1	Front-rotor blade count
B_2	Rear-rotor blade count
B_5	Constant for Reynolds wake model
B_6	Constant for Reynolds wake model
c	Chord length
c_{0t}	Sound speed trace in the segment spanwise direction
c_0	Sound speed
C_d	Drag Coefficient
c_f	Chord of front-rotor element
D_c	Doppler factor ($=1 - M_X \cos\theta_e$)
D_T	Tangential distance covered by rear-rotor element during the interaction
D_5	Constant for Reynolds wake model
D_6	Constant for Reynolds wake model
E	Fresnel Integral
F	Acoustic dipole force
g	Reduced lift function
I_{te}	Trailing-edge effect index

k	Gust circumferential index *AND* loading harmonic index
k_ξ	Gust wavenumber in the trapezoid chordwise direction
k_{rp}	Projection of gust radial wavenumber on the trapezoid surface
k_a	Acoustic wavenumber
k_r	Gust radial wavenumber
ℓ	Unsteady loading
L	Parallelogram span
$\mathcal{L}$	Aeroacoustic Transfer Function
l_{LE}	Length of trapezoid leading-edge
m	Doppler dispersion index
M_x^*	Adamczyk's parameter
M_r	Mach number in the observer's direction
M_X	Mach number opposite to flight direction
M_x, M_y	Convection Mach number components following (y_1, y_2)
n	Gust radial index
$\mathcal{P}'$	Transfomed pressure verifying Eq.(3.11)
p_∞	Reference static pressure
r	Radius
r_1	Lower radius of blade segment
r_2	Upper radius of blade segment
R_e	Acoustic phase radius
r_m	Radius at trapezoid mid-span
R_s	Acoustic amplitude radius
r_T	Blade tip radius
s	Distance in the wake axis
s_T	Distance in the wake axis between FR TE and RR LE
$\mathcal{S}$	Flat segment surface
s'	Corrected wake-axis distance
s_0	Constant for Reynolds wake model
s_1	Constant for Reynolds wake model
t'	Emission time
t	Time value
T_r	Radial Period
U	Wake deficit profile

U_0	Convection velocity
U_c	Central velocity defect
U_i	Incident Velocity
v_{s0}	Critic sweep velocity
v_s	Sweep Velocity Amplitude
V_s	Global sweep velocity
v_{sr}	Radial projection of v_s
w_{kn}	Gust modal amplitude
w_u	Upwash Amplitude
y	Tangential distance
$\breve{y}$	Coordinate perpendicular to wake-axis
y_c	Intersection point tangential coordinate
y_s	Blade-to-blade circumferential distance
(u, v, w)	Flow velocity components in $\mathcal{B}_1$
(v_r, v_T, u)	Flow velocity components in $\mathcal{B}_2$
$(\bar{X}, \bar{Y})$	Trapezoid chord coordinates
(X, Y, Z)	Global Cartesian coordinates, in $\mathcal{B}_1$
$(\bar{x}_1, \bar{y}_1)$	Trapezoid LE coordinates
$(\bar{x}_2, \bar{y}_2)$	Trapezoid TE coordinates
(x_{LE}, y_{LE})	Coordinates of leading-edge line, in $\mathcal{B}_2$

Symbols

$\tilde{()}$	Frequency domain variable
$\hat{()}$	CAD coordinates
$()^*$	Non-dimensional value
$()'$	Observer's coordinate defined in $\mathcal{B}_1$

Vectors

$\mathcal{B}_0 = (\mathbf{e_1}, \mathbf{e_2}, \mathbf{e_3})$	Basis for infinite-span segment problem
$\mathcal{B}_1 = (\mathbf{e_{x'}}, \mathbf{e_{y'}}, \mathbf{e_{z'}})$	Basis aligned with the rotation axis $\mathbf{e_{x'}}$
$\mathcal{B}_2 = (\mathbf{e_r}, \mathbf{e_t}, \mathbf{e_{x'}})$	Basis aligned with local source radial, tangential and axial components
$\mathcal{B}_3 = (\mathbf{e_x}, \mathbf{e_{y'}}, \mathbf{e_z})$	Basis aligned with the flight direction (rotation of $\mathcal{B}_1$ around $\mathbf{e_{y'}}$)

$(\mathbf{e_{x_1}}, \mathbf{e_{y_1}})$	Vectors perpendicular and parallel to the trapezoid LE (see Fig. 3.11)
$(\mathbf{e}_\xi, \mathbf{e}_\eta \equiv \mathbf{e_{y_1}})$	Vectors aligned with the trapezoid chord and LE (see Fig. 3.11)
$\mathbf{F}$	Acoustic dipole force
$\mathbf{k}$	Dimensional gust wavenumber
$\mathbf{R}$	Distance between observer and center of rotation disc
$\mathbf{R_0}$	Radius of rotating dipole
$\mathbf{U_0}$	Gust convection velocity
$\mathbf{x}$	Observer Coordinates
$\mathbf{y}$	Source Coordinates

Subscripts

num	Numerical data
min	Minimum
max	Maximum
e	Acoustic emission coordinate

List of Acronyms

ACARE	Advisory Council for Aerospace Research in Europe
ADS	ADvance Surface
BCF	Brake Cooling Fan
BOS	Background Oriented Schlieren
BPF	Blade Passing Frequency
CAA	Computational AeroAcoustics
CAD	Computer-Aided Design
CFD	Computational Fluid Dynamics
CROR	Counter-Rotating Open Rotor
CRP	Counter-Rotation Propeller
DFT	Discrete Fourier Transform
DNW	(German-Dutch Wind Tunnels)
DTS	Dual Time Stepping
FA	Face Alignment
FFN	Far-Field Noise

FFT	Fast Fourier-Transform
FW-H	Ffowcs Williams and Hawkings
FR	Front Rotor
FTD	Flight-Test Demonstrator
GE	General Electric
HF	High Frequency
HTP	Horizontal Tail Plane
IGV	Inlet Guide Vane
LE	Leading-Edge
LF	Low Frequency
LLF	Large Low-Speed Facility
LMS	Least Mean-Square
MCA	Mid-Chord Alignment
MCS	Mean-Camber Surface
NACA	National Advisory Committee for Aeronautics (USA)
NASA	National Aeronautics and Space Administration (USA)
OASPL	Over-All Sound Pressure Level
OGV	Outlet Guide Vane
ORION	Open Rotor InteractiOn Noise
PBR	Propeller Blade Release
PCA	Pitch-Change Axis
PIV	Particle Image Velocimetry
PW	Pratt & Whitney
RDT	Rapid Distortion Theory
RPM	Revolutions Per Minute
RR	Rear Rotor
SPL	Sound Pressure Level
SRPT	Static-Rho-Pressure-Temperature normalization
SRP	Single-Rotation Propeller
TE	Trailing Edge
TF	Transfer Function
UDF	UnDucted Fan
URANS	Unsteady Reynolds-Averaged Navier Stockes
VTOL	Vertical Take-Off and Landing

VTP Vertical Tail Plane

WTT Wind-Tunnel Test

Introduction

A **C**ounter-**R**otating **O**pen **R**otor (CROR) engine is composed of two coaxial rotors spinning in opposite directions and separated by a short axial distance. The main objective of this complex aerodynamic system is to convert the swirling flow behind the upstream propeller into an additional source of thrust, thereby increasing its fuel-efficiency [1] [2] [3]. The introduction of CRORs to civil airliners was extensively investigated in the 80's, when several analytical, numerical and experimental studies were conducted to improve the system overall performances. These efforts led to successful flight tests using full-scale CRORs, for which fuel-efficiency expectations were confirmed [4]. Despite these achievements, the oil-crisis end and the advent of high-bypass ratio turbofan engines, at the end of the 80's, refrained CROR developments and prevented the design from entering into production. Nowadays, the concept is under study anew: engine and aircraft manufacturers are challenged to solve CROR drawbacks with modern aeronautical techniques. Amongst other issues, the unsteady phenomena governing noise emissions need to be understood and reduced. Even if Computational Fluid Dynamics (CFD) is the most accurate method for the task at hand, the time required by this technique is still incompatible with industrial constraints. This is the principal motivation for developing fast analytical methods, capable of providing general trends to help the design process.

In this context, a PhD research partnership between Airbus Operations SAS and École Centrale de Lyon started in 2009 with the objective of developing an enhanced fast-tool for predicting rotor-rotor interaction tonal noise and aerodynamic installation effects on noise, for low-speed operational conditions. Broadband noise is ignored in the present study. The research is focused on modelling the blade aeroacoustic response to oncoming aerodynamic perturbations, believed to be responsible for interaction noise sources. An effort has been made to include a realistic blade geometry representation in the analytical models accounting for blade response and noise radiation. The present PhD report exposes in detail these models, along with elements

for their numerical implementation.

Thesis Structure

Prior to the present investigation, a general research context is presented in Chapter 1. The CROR concept history, motivations and main technical features are exposed. Also, the proposed strategy for CROR tonal noise predictions is outlined.

The aerodynamic perturbations shed from the upstream rotor are studied in Chapter 2. An analytical model to include radial wake evolutions is derived in detail. As a second branch of the strategy, the post-processing of CFD flows impinging on the downstream rotor is presented. For both options, an expansion in sinusoidal gusts is necessary for defining the inputs required by the blade-response model.

As explained in Chapter 3, noise sources are calculated with an extension of Amiet's theory for high-frequency gust-airfoil interactions, derived in detail in Sec. 3.2. The extended theory includes gust obliqueness and non-parallel segment edges. Blade segments are approximated at best by flat trapezoids in unwrapped coordinates. The segment motion is assumed to be rectilinear in the tangential direction, for which uniform flow properties are assumed for each strip. The methodology convergence and robustness to blade segmentation are evaluated. The obtained sources are subsequently projected on the blade Mean-Camber Surface (MCS) for noise radiation.

A far-field noise theory is derived in detail in Chapter 4. Before the study of rotating blade elements, an assessment of segment shape effects is presented, for segments fixed with respect to the observer. Analytical radiation integrals are deduced for segments featuring swept parallelograms. The study of CROR noise radiation is addressed subsequently. Noise in the far-field is formulated for each rotating point dipole composing the source, its radial component being included. Forward flight and propeller incidence are accounted for in the theory.

Finally, the overall prediction scheme is assessed in Chapter 5 by comparing analytical results with CFD computations and Wind-Tunnel Test (WTT) measurements. For completeness, further research directions are presented in Chapter 6.

Chapter 1

Context of the Research

The investigation exposed in this thesis deals exclusively with CROR noise emissions. Nevertheless, it seemed important to provide an extended context to the present research, in order to understand the history, motivations and technical issues related to the CROR concept. The objective is to yield a general framework to apprehend the relative importance of CROR noise emissions to other technical issues and, ultimately, the importance of the present investigation. This chapter is divided in four parts. First, a historical review of CROR developments is exposed in Sec. 1.1. Secondly, a non-exhaustive outlook of CROR technical characteristics is exposed in Sec. 1.2. CROR noise emissions are considered in more detail in Sec. 1.3. Finally, a presentation of the present investigation is provided in Sec. 1.4.

1.1 CRORs Through History

Successful gliding devices, made at the end of the XIX century, were seen as a promise of human capability of mastering flight. Qualified scientists sought how to adapt marine screw propellers to provide the power needed by the future flight vehicles. Airscrew theories by Froude [5], Rankine [6] and Drzewiecki [7], along with a large amount of empirical research, ultimately led Willbur and Orville Wright to perform the first human powered-flight on December 17, 1903 [8]. Thrust was provided by twin two-bladed propellers of 2.6m diameter. This propulsion technology was born with aviation and has been under continuous development for more than a century.

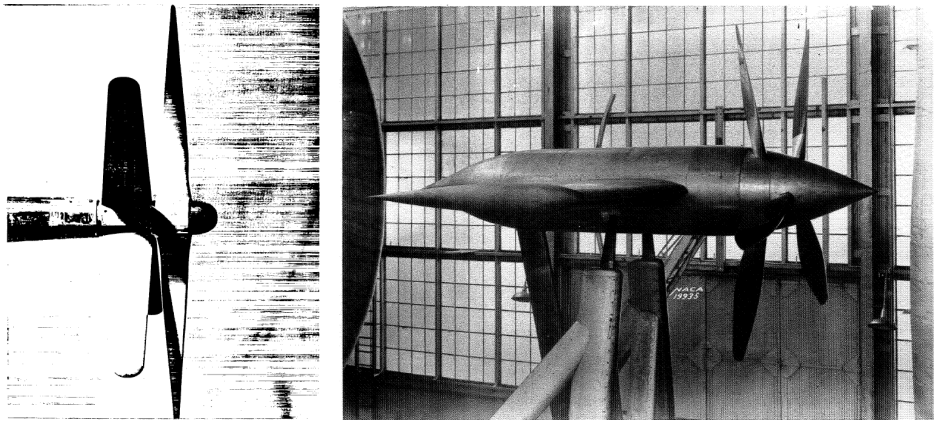

(a) Contra-vanes (1933) (b) CROR WTT (1940)

Figure 1.1: *Studies in the 40's aiming at reducing propeller swirl for increase efficiency. (a) Aircraft propeller (right) with fixed "contra-vanes" (left). From [9]. (b) WTT on CROR in the NACA 20-foot propeller-research wind tunnel. From [10].*

Amongst other sources of aerodynamic loss, tangential air velocity downstream a propeller, also known as *swirling flow* or *swirl*, has been recognized as an inherent loss in its efficiency. First attempts to recover, at least in part, energy losses linked to swirl resulted in the development of counter-propellers or contra-vanes. These devices consist in a row of fixed blades downstream the propeller, as shown in Fig. 1.1(a), to redirect swirl thereby inducing additional thrust. Experimental studies on such systems were made by De Caria [11] in 1931 and Lesley in 1933 [9]. Efficiency enhancements from 0% to 2%, attributable to the contra-vanes, were reported by the authors. Some theoretical studies, as the one by Weinig [12] in 1937, considered the idea of using not fixed contra-vanes but a second row of blades, rotating in the opposite direction of the primary propeller. The term "Counter-Rotating Propeller" (CRP) was coined.

CROR Beginnings (1940's): Military Aircraft

After the eruption of Wold War II, research on propeller efficiency received special attention from military strategists. CROR development was directly favored by these circumstances. In this context, the first WTT on CROR efficiency, carried out at NACA 20-foot propeller-research tunnel, was reported in 1940 by Biermann *et al.* [10]. Counter-rotation two- and three-bladed

(a) Boeing XF-8B (1944)

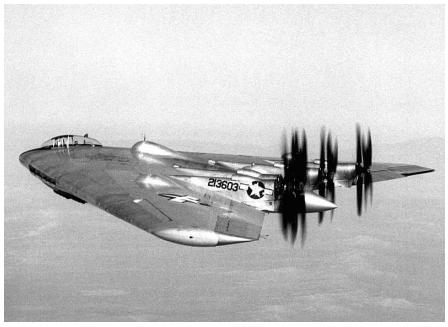

(b) Northrop XB-35 (1946)

(c) Hughes XF-11 (1946)

(d) US Lockheed XFV (1954)

Figure 1.2: *First implementation of CRORs in military Aircraft.*

propellers were embedded in flows ranging from 0 to 50m/s. The addition of the second row was shown to provide efficiency gains from 0% to 6%. Furthermore, aircraft wing, for wing-mounted CRORs, was shown to provide up to 3% of additional gains.

Under the war impetus, few years were necessary to see CRORs implemented in military aircrafts. One of the first examples of CROR-powered aircraft is the Boeing XF-8B, shown in Fig. 1.2(a). The aircraft, produced in 1944, was powered with two three-bladed CRORs driven by a Pratt & Whitney engine (XR-4360-10). Other examples of early CROR implementation in the US are Northrop flying-wing bomber XB-35, in Fig. 1.2(b), the Hughes XF-11 reconnaissance airplane, in Fig. 1.2(c), or the Vertical Take-Off and Landing (VTOL) airplane Lockheed XFV-1, shown in Fig. 1.2(d). All these airplanes were retired from the US Air Force at the end of the 40's, basically because of changes in postwar strategies and the advent of jet engine aircrafts.

However, several CROR-powered military aircraft entered in service in the 50's, mainly from British and Russian productions. One of the most emblematic CROR aircraft is the British

(a) Fairey Gannet (b) Shakleton Bomber

Figure 1.3: *Example of British military aircrafts powered with CRORs. (a) Fairey Gannet Aircraft. (b) Avro Shackleton Bomber.*

Fairey Gannet, in Fig. 1.3(a), produced by Fairey Aviation Company. This mid-wing monoplane used two four-bladed CRORs powered with Armstrong Siddeley double-mamba engines. This aircraft is remembered also by its three-folding wings, designed for easing airplane storage. Fairey Gannet was introduced in 1953 to be in service until 1978. Measurements on this aircraft were extensively used for validation of CROR analytical models in the 80's, as the noise theories of Hanson [13] and Parry [14], or the vibratory study of Turnberg & Brown [15]. Another British CROR aircraft receiving mention in this review is the maritime patrol aircraft Avro Shakleton. Four wing-mounted three-bladed CRORs provided the aircraft thrust, as shown in Fig. 1.3(b). They were powered with Rolls-Royce Griffon Engines. This aircraft was in service from 1951 to 1990 and was widely used by UK and South-African Air Forces.

The Russian designer Andrei Tupolev led the production of the most successful CROR aircraft: the bomber Tupolev Tu-95, known as "the bear". Its design was agreed in 1951 as a variant of Tu-85. The objective was to provide an airplane with a range of more then 8000 km without refuel. The aircraft is powered by four Kuznetsov NK-12 engines driving four-bladed CRORs. It entered in service in the Soviet Air Force in 1956 and is still in use today in the Russian Air Force, under its variant Tu-95MS, shown in Fig. 1.4(b). An interesting use of the same NK-12 engine is seen in the Antonov An-90, known as "the eaglet", in use from 1973 to 1993. The original architecture of this aircraft, shown in Fig. 1.4(c), is due to the requirement of being an amphibious assault unit, powered with a CROR engine. For take-off, CRORs were assisted by two turbofan engines located on the aircraft nose. At cruise, the whole power was provided by the CRORs. So far, the only civil passenger aircraft powered with CRORs and

(a) Tupolev Tu-114

(b) Tupolev Tu-95MS

(c) Antonov A-90

Figure 1.4: *Example of Soviet Aircrafts powered with CRORs. (a) Tupolev Tu-114. (b) Tupolev Tu-95MS. (c) Antonov An-90.*

having accomplished effective missions is the Russian Tupolev Tu-114, in Fig. 1.4(a). The airliner was in service from 1961 to 1991. The safety record during its service life is excellent, with only one fatal operational (non-airborne) accident.

CROR Second Wave (1980's): Development of Commercial Powerplants

The peak in US oil consumption in the mid 70's prompted American designers to develop fuel-efficient propulsion technologies, in order to adapt passenger airliners to the increasing fuel scarcity. Under this context, NASA Lewis initiated a research program in 1975 addressing high-speed propeller technology, in which CRORs were seen as primary candidates for subsonic aircraft propulsion. New numerical techniques and composite materials were seen as novel means to overcome CROR drawbacks unsolvable during the 40's. Advanced propellers in single- and

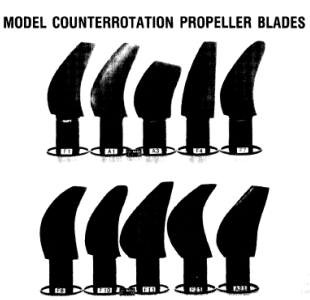

(a) Blades for parametric WTT

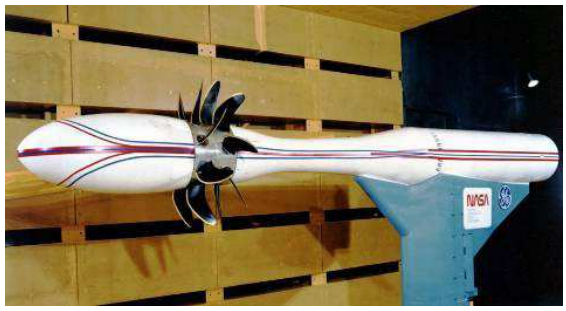

(b) UDF WTT rig

(c) FTD for GE36-UDF

(d) FTD for PW Allison-578DX

Figure 1.5: *Illustration of US research in the 80's under NASA funding. (a) Blade planforms used at NASA Lewis for researches on CRORs at cruise (from [16]) (b) Model of GE-UDF for WTT. (c) GE36-UDF engine full-scale FTD. (d) PW-Allison-578DX engine full-scale FTD.*

counter-rotation configurations were considered analytically, numerically and experimentally. The non-confidential reports written in the 80's under NASA funding represent an important legacy on the CROR research history.

Numerical means at the time were limited to 3D Steady Euler codes, but some 2D URANS codes were in the way to provide somewhat more accurate predictions. For this reason, studies at NASA Lewis had a great component of WTT. At the late 80's several developments in multidisciplinary analytical and numerical methods were made using these WTT results as reference. Further, close collaboration with engine manufacturers led to the development of commercial CROR powerplants, as the UnDucted Fan (UDF) engine of General Electric (GE). Tests on scale models led to full-scale ground tests in 1985. The integration of a full-scale

GE36-UDF "proof-of-the-concept" engine in a Boeing 727-100 was later achieved, as shown in Fig. 1.5(c), for successful flight tests in 1986 [4]. The constructor claimed 20% of gains in Specific Fuel Consumption (SFC) with respect to turbofan engines of that time, for an equivalent aircraft mission. Another engine manufacturer reaching sufficient technology-readiness to build a CROR Flight Test Demonstrator (FTD) was Pratt & Whitney (PW) with the engine PW-Allison-578DX, shown in Fig. 1.5(d).

CROR New Wave (2000's): Towards CROR-powered airliners

The CROR project was abandoned in the late 80's mainly because of the oil-crisis end and the advent of high-bypass ratio turbofan engines. However, a renewed interest on the concept was registered in the last decade, for two principal reasons. First, the potential risk of a new oil crash is motivating engine and aircraft manufacturers to invest some of their resources in the development of novel fuel-efficient propulsion programs, since conventional strategies to increasing engine bypass-ratio are reaching their limits. Secondly, the Advisory Council for Aerospace Research in Europe (ACARE), created in 2001, challenged civil aviation to reduce drastically environmental impacts in terms of air pollution (-50% of CO_2 and -80% of NO_x emissions) and noise around the airports (-10 dB with respect to 2000's levels) for 2020 [17]. Besides, the commitment of reducing greenhouse gases acquired in the Kyoto Protocol started in 2005 [18]. CRORs are good candidates for reducing air pollution. However, reductions in noise emissions represent a challenge.

Nowadays, researches are aimed at developing CRORs satisfying contemporary requirements of low pollution emissions and community noise impact. Modern CFD techniques are now used to study in detail fluid phenomena not reachable in the 80's (see for example the work of Stuermer [19] [20] [21] or Colin [22]). Modern non-invasive measurement techniques, as the Particle Image Velocimetry (PIV), Background Oriented Schlieren (BOS) and Beam-forming source localization are now available to understand the highly complex flow in-between CRORs [23]. Also, some recent theoretical developments provided more accurate pre-design tools integrable in multidisciplinary optimization routines, as the one presented by Marinus for propellers [24] or by Bechet for CRORs [25]. It is in this last category that the present investigation can be sorted. The present research is intended to provide a fast-tool for rotor-rotor interaction noise prediction, for blade pre-design optimization and engine integration.

1.2 CROR Technical Characteristics

An assessment of CROR benefits was made by Strack *et al.* in 1981 [26], in order to evaluate the viability of the project. Due to their larger by-pass ratio and swirl energy recovery, CRORs were shown to provide dramatic enhancements in aerodynamic efficiency with respect to both turbofan engines and Single Rotation Propellers (SRPs). However, an aircraft powerplant is a very complex device with multiple variables to be considered. In opposition to CROR advantages, a series of issues as new vibratory concerns, increased noise levels, added weight and costs in maintenance procedures have to be accounted for.

CROR Main Advantages

In Fig.1.6(a) is shown the initial forecast of CROR flight-efficiency, expected with technology of 1980. At that time, SRPs were estimated to provide gains of 15% in fuel-consumption efficiency with respect to turbofans, and CRORs were estimated to provide additional gains of 8%, including weight penalties for complex gearbox and increased cabin noise [27]. Besides, CRORs were predicted to have better propulsive efficiency at higher Mach number and more thrust per diameter than any other propulsion technology. These expectations hold today. The efficiency gains directly related to fuel savings, for equivalent aircraft missions, were shown to be at least of 15%, as shown in Fig.1.6(b). A recent review of these predictions by Guynn *et al.* [3] suggest that higher fuel efficiency should be expected from CRORs using current technologies. This arises from a combination of advanced airframe technology, core engine developments and general new open-rotor architectures. However, an update of fuel savings should be made using as a basis the fuel consumption of current turbofan engines.

CROR Main Issues

CROR gearbox is the main source of weight penalties and additional maintenance costs [1]. Besides, new noise sources, mainly due to rotor-rotor interaction or installation effects are an important drawback to be solved. This point will be exposed in more detail, further in this PhD thesis. New vibratory concerns are foreseen for CRORs with respect to SRPs. CRORs would be more sensitive to 1P excitations (oscillating forces perpendicular to the shaft due to angular inflows), according to flight stress measurements by Turnberg & Brown [15]. Further, Ferraris *et al.* have shown that CRORs with different RPM are exposed to four critical angular

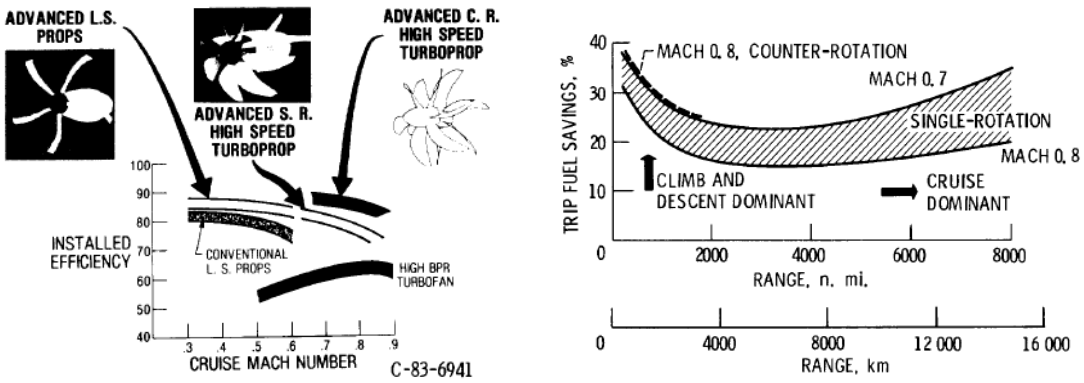

(a) Installed Efficiency Forecast (b) Fuel Savings in comparison to turbofan engines

Figure 1.6: *CROR benefits forecast in 1984. From [27]*

speeds for whirl response to mass imbalance [28]. Another issue with CRORs is the potential risk of Propeller Blade Release (PBR) to which few public investigations have been dedicated. Nevertheless private research has been active in this topic in the last decade.

CROR-Aircraft Integration

A fundamental question about CRORs is the strategy for their integration to the aircraft body. Two configurations are currently under study, namely the wing-mounted *puller*- (or tractor) CROR and the *pusher*-CROR, generally mounted at the aft end of the fuselage. The former configuration was the initial strategy adopted in 1940-50, an example of which is the Tupolev airliner Tu-114 in Fig. 1.4(a). Examples of the latter configuration are shown in Figs. 1.5(c) and 1.5(d). One of the advantages with pusher-CRORs is the reduced cabin noise levels. As the maximum of fuselage excitation is expected near the propeller plane, positioning the engine at the rear of the fuselage sensibly reduces noise levels inside the cabin. Also, pusher-CRORs are less sensitive to aircraft incidence since the fuselage has a tendency to redirect the flow into the CROR axis. In counterpart, handling qualities are deteriorated for engines at the rear of the fuselage. Furthermore, risks linked to PBR are exacerbated by the proximity of Horizontal Tail Plane (HTP) and Vertical Tail Plane (VTP). Another important feature of the pusher configuration is the interaction of CROR with the aerodynamic perturbations shed from pylon and hub. The effects are particularly important on CROR noise emissions, although the pylon boundary layer blowing technique can effectively reduce pylon induced noise [29] [30]. The viscous boundary layer originated at the hub is likely responsible for stall for blade sections

in the hub proximity. The related vortical flow impinges on the rear rotor, inducing additional noise sources.

1.3 Noise Radiation from CRORs

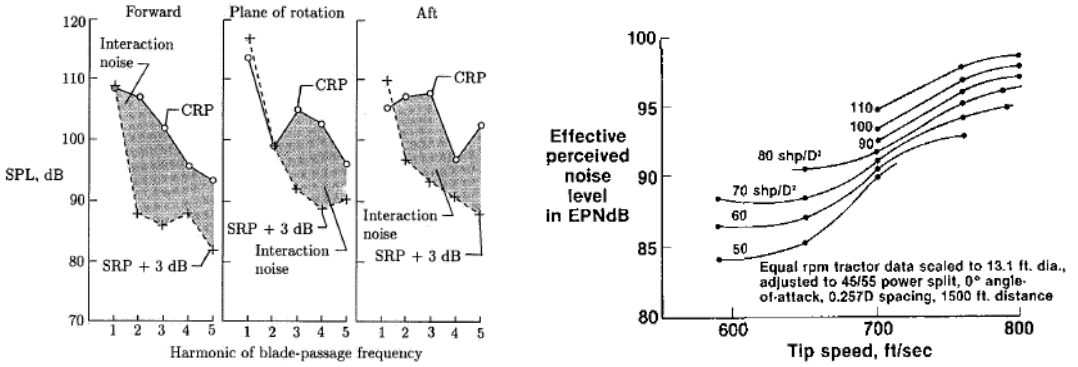

(a) (b)

Figure 1.7: *CROR noise characteristics. (a) Comparison between SRP and CROR noise, from Magliozzi [31]. (b) Effect of RPM and disc loading on CROR noise, from Metzger & Brown [32]*

An important technical issue of CRORs is the relative high level of noise radiation in comparison to SRPs or modern turbofan engines. Noise emissions must be reduced to provide CROR engines satisfying current thresholds of community noise certification and cabin comfort. The present study is focused on CROR tonal noise radiation. The reader is referred to the work of Blandeau [33], Blandeau *et al.* [34] or Parry [35] for an analysis of CROR broadband noise emissions, not addressed here.

Whereas a SRP will produce tonal noise only at multiples of its Blade Passing Frequency (BPF), CROR tonal noise is produced at combinations of both propellers BPFs. A qualitative comparison between CROR and SRP noise is given in Fig. 1.7(a), from experimental results by Magliozzi [31]. In this test, CROR consists in two rotors of same geometry, absorbed power and tip speed than the SRP, so that noise is produced at the same modal frequencies in both cases. Noise from SRP is raised by 3 dB, for comparison. Differences between both noise levels are explained by additional CROR sources, probably due to rotor-rotor interaction. It is noticed that CROR is significantly louder than SRP.

The physical mechanisms responsible for CROR tonal noise are listed in the following sections. First, isolated CROR engines are considered. Subsequently, additional noise sources due to the engine installation are exposed.

1.3.1 Noise Radiation From Isolated CRORs

Noise produced by a rotating blade can be formulated as the contribution of acoustic monopole, dipole and quadrupole sources, according to the Ffowcs Williams and Hawkings (FW-H) formulation [36]. The source circular motion produces a fluctuating Doppler shift in the observer's direction, for which the source energy at a given frequency is spread in a discrete set of noise frequencies in the observer's frame. This is the reason why steady phenomena in the blade frame are also responsible for noise radiation. For instance, steady monopoles in the blade frame, accounting for the blade volume displacement, produce *thickness noise* whereas mean forces on the blade result in *steady loading noise*. When the force is unsteady in the blade frame, the produced noise is referred to as *unsteady loading noise*. Quadrupole sources account for viscous and propagation effects in the flow surrounding the blades. Now, Hanson and Fink have shown that the contribution of quadrupoles to total noise can be neglected for fully subsonic or fully supersonic flows, their importance being restrained only to the sonic radius vicinity [37]. For this reason, CROR noise radiation at low flight speed is expected to be successfully modeled only with monopole and dipole sources.

While thickness and steady loading noise can be fairly predicted with tools initially developed for SRPs, unsteady loading noise prediction represents a further challenge. Unsteady loadings are produced by oncoming velocity disturbances requiring accurate description. Besides, the non-compact blade response to such incident excitations needs also to be modeled. The main aerodynamic mechanisms inducing unsteady loading noise on isolated CRORs at low flight-speed are known to be: ***a)*** The impingement of viscous wakes originated on the upstream (front) rotor onto the downstream (rear) rotor. This mechanism is believed to be a major contributor to rotor-rotor interaction noise. Although numerous researches have been conducted on the characterization of rotor wakes, very few dealt with the specific case of front-rotor viscous wakes in a CROR configuration. Only recently, such wakes have been studied in detail using modern CFD (see for example Boisard [38], Stuermer [20] or Colin [22]). The current noise theory for modeling this interaction mechanism has been provided by Hanson [13]. ***b)*** The interaction of rear-rotor blades with front-rotor tip-vortices. The aerodynamic excitation has

been modeled empirically by Majjigi & Gliebe [39] and semi-analytically by Kingan & Self [40], the blade response being obtained with the classic Amiet 2D theory [41] by strips. More recently, Roger & Schram have presented a full 2D analytical tip-vortex model associated with a blade-response model including sweep and tip-end effects [42]. This interaction mechanism has been shown as highly localized in the rear-rotor tip area, for which it is avoidable by reducing rear-rotor diameter (strategy known as cropping or clipping). ***c)*** Rotor-Rotor potential interaction. This mechanism is dependent on blade loading and rotor-rotor spacing. Modeled mainly by Parry [43], it is not believed to be dominant, at least for modern CROR architectures.

Parametric studies were made at NASA Lewis for reducing interaction noise on isolated CRORs. Dittmar studied the effect of rotor-rotor spacing in CRORs at cruise conditions [44]. It was shown that noise diminished as rotor spacing increased until a critical distance at which front-rotor power coefficient started to increase. Dittmar explained that front-rotor experienced higher blade loadings resulting in more intense wakes, ultimately increasing interaction noise levels. Similar effects were reported by Metzger & Brown [32] and by Magliozzi [31] for CRORs at take-off conditions. These observations suggest the existence of an optimum rotor spacing for reduced noise radiation.

Concerning tip-vortex interaction, experiments by Dittmar [45] have shown that reducing rear-rotor diameter provided up to 15 dB of interaction noise reductions at localized polar angles. Rear-rotor blades were larger in chord to provide the same thrust at the same rotational speed. Rear-rotor alone tones were also reduced as the relative tip Mach number was decreased.

1.3.2 Noise Radiation from Installed CRORs

Non-homogeneous flows, produced by the fuselage or by structure components used for engine-aircraft integration, result in additional CROR noise sources. Besides these *aerodynamic installation effects*, the acoustic field is also altered by the presence of these solid bodies. The produced modifications are referred to as *acoustic installation effects*. The nature of installation effects is dependent on the CROR-aircraft integration configuration. A wing-mounted puller-CROR will be impacted by the wing upwash and potential flows whereas a pusher-CROR will be sensitive to pylon wake, hub vortex and fuselage distortion of propeller inflow.

WTT on pusher-CRORs carried out at NASA Lewis by Woodward & Hughes (1989) [46] and by Shivashankara (1990) [29], and at DNW (German-Dutch Wind Tunnel) by Ricouard

et. al (2010) [30] shed the same conclusions on the effect of pylon on CROR noise radiations: pylon effects are large on front-rotor BPFs, less pronounced for rear-rotor BPFs and exhibit no noticeable tendency for rotor-rotor interaction tones. No experimental study dedicated to the analysis of hub vortex on CROR noise has been found. However, analytical modeling of this phenomenon has been provided by Majjigi and Gliebe [39].

Recent analytical modeling of acoustic installation effects have been reported by McAlpine & Kingan [47], Kingan *et al.* [48] and Kingan & Self [49] to simulate noise diffraction by aircraft fuselage and wings.

1.4 Outlook of the Present Investigation

A PhD sponsorship has been proposed by Airbus Operations SAS to École Centrale de Lyon, with the main objective of developing an analytical fast-tool to model rotor-rotor interaction and aerodynamic installation effects on CROR tonal noise at low speed. Two main axes of research have been proposed. First, the extension of current blade response and acoustic radiation functions is prescribed in order to enhance blade geometry representation. Secondly, the definition of a scheme strategy for importing aerodynamic inputs either from extended analytical models or from relatively fast CFD computations has been required.

This PhD report exposes in detail both the theory extensions behind the models and their implementation in a fast-tool.

1.4.1 Strategy Outlook

The interaction noise generation can be modeled by two transfer functions (TF), the first accounting for blade response to aerodynamic excitations and the second for the corresponding noise measured in the far-field, as shown in Fig. 1.8. In this approach, rear-rotor noise radiation is focused on but extensions to account for front-rotor radiation are possible.

The scheme of noise prediction could be divided in three main tasks. The first one is the determination of the oncoming velocity perturbations and their decomposition as a sum of sinusoidal gusts. An analytical modeling, or CFD importation, of front-rotor wakes, tip vortices and hub vortices is prescribed as a part of the strategy. In Chapter 2 are presented the main

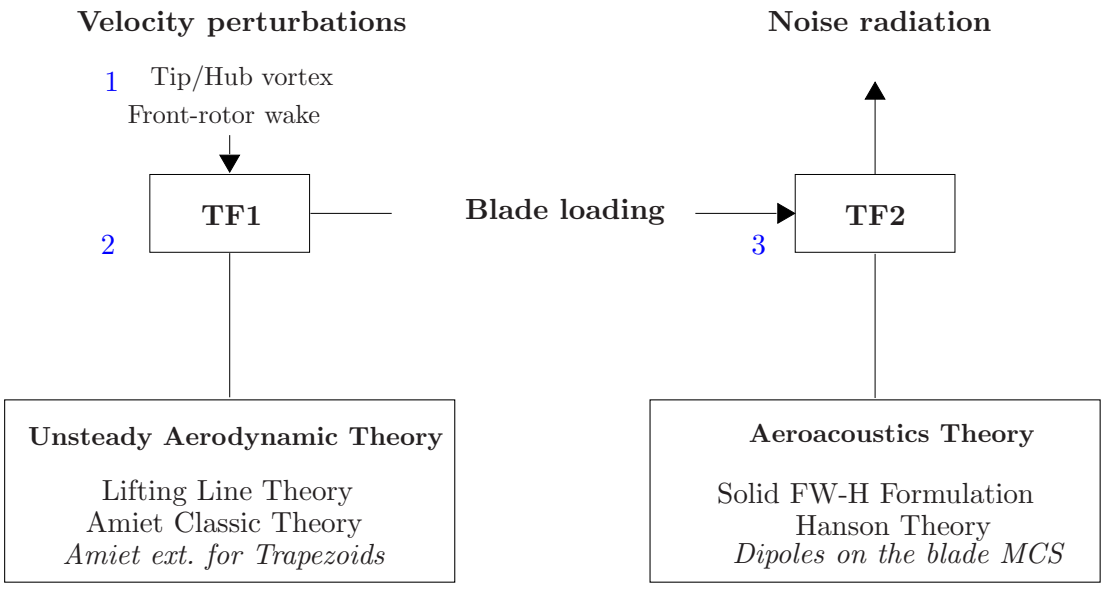

Figure 1.8: *Interaction noise generation as a chain of TFs. Italic text denotes the proposed PhD innovations.*

features of both strategies for the input determination. The main innovation in this step is an analytical handling of existing 2D empirical wake models to provide sinusoidal gusts accounting for radial wake evolutions. Also, a strategy to extract equivalent 2D sinusoidal gusts from CFD data is exposed in detail.

The second task is the definition of a TF between velocity perturbations and blade unsteady loadings. The blade response is predicted using the linearized thin-airfoil theory. This approach states the decoupling of mean and unsteady flow fields for thin blades, lightly loaded and of slight camber. Whereas blade mean loading is determined by mean incidence and blade actual geometry, loading fluctuations are determined on an equivalent thin plate interacting with sinusoidal gusts at zero angle of attack. The total field is found from linear addition of its mean and unsteady parts. The loadings are computed in the local coordinates of each blade segment, assumed to have a translating motion tangent to the real blade motion. The main PhD innovation concerning this task is the definition of a compressible blade response model accounting for blade sweep and chord variations with the span, as continuous parameters. The proposed blade response model, referred to as *Amiet ext. for Trapezoids* in Fig. 1.8, is derived in detail in Chapter 3.

Finally, the far-field noise calculation is achieved in the third task of the scheme. The required transfer function consists of an adaptation of FW-H formulation for the case of a single rotating point dipole with arbitrary force orientation. The main advantage of this approach, in comparison to current Hanson's CRP theory [13], is the possibility of locating the source on the blade mean-camber surface (MCS) and including a radial force component. A higher accuracy in blade geometry representation can be thereby achieved.

The proposed methodology for the tonal rotor-rotor noise prediction can be summarized as follows:

1. Rear-rotor blades are cut into annular segments, subsequently unwrapped and interpolated by flat trapezoids, accounting for blade sweep and chord spanwise variation.

2. Oncoming disturbances are expanded in a Fourier series in order to obtain 2D sinusoidal gusts. Wavenumbers, defined in radial and tangential directions, are projected on the principal directions of each blade segment, for unsteady loading computation.

3. Unsteady loadings are found in the frequency domain for each trapezoidal blade segment. Source phase distribution on the blade surface is defined from the time delay of the excitation at the leading-edge of each blade segment.

4. The loading distribution found in step 3 is projected onto the blade MCS. A set of acoustic dipoles is then defined, from unsteady loading and lattice orientation, for far-field noise computation.

Chapter 2

Front-Rotor Wake Representation

The aerodynamic perturbations originated in the front-rotor blades are a major contributor to CROR interaction noise. In this chapter, this excitation field is studied at the rear-rotor leading-edge. The emphasis is on tonal noise sources. For this reason, only the periodic part of the excitation will be retained. Two different options for acquiring the information are proposed. First, an analytical model based on the rotor geometry and flight conditions can be used to approximate the 3D excitation seen by the rear-rotor. Secondly, wakes computed with CFD techniques can be imported and adapted to be used as input for the blade-response routine.

The analytical methodology treats only the velocity defect originated on the front-rotor blades, but can be extended to include other aerodynamic excitation sources. It resorts to existing empirical two-dimensional wake models, based on the initial approach of Silverstein *et al.* for wing wakes [50]. A historical review of the development of such models is presented in Sec. 2.1. The most important models are listed in Sec. 2.2. Wake characteristics are deduced at each radius as a function of the distance in the wake axis, assumed to be aligned with the front-rotor chordwise direction. The excitation seen by the rear rotor is subsequently projected in the direction normal to its leading-edge and decomposed analytically in sinusoidal gusts.

Rotor wakes have a highly three-dimensional behavior, typically due to imbalance of centrifugal and pressure forces. Radial mixing affects the wake turbulence thereby modifying wake decay and intensity [51]. Furthermore, the presence of a second blade row will probably affect the incident upwash by mechanisms not yet entirely understood. The expected complexity of front-rotor wakes prompted the development of a second branch of the methodology, in which

CFD wakes are post-processed, as detailed in Sec. 2.4. These inputs are assumed to include wake features difficult to model analytically.

2.1 Precedent Researches

The wake behind airfoils has been one of the most important aeronautical research topics in the 20th century. The main reason is the direct link between the vortical region behind the wing and energy losses caused by air viscosity on the lifting surface, which determines in part the flight vehicle efficiency. This relationship was first formulated by Betz in 1925 [52], who defined the wake as a localized region of total pressure loss directly related to the net airfoil drag. This pioneering analysis was the basis for the first empirical model of the wake characteristics, namely the dynamic pressure loss at the wake center and the wake width at mid-height, casted in 1938 by Silverstein, Katzoff and Bullivant, from measurements on symmetric NACA airfoils [50]. The wake profiles were reasonably well predicted by both a squared cosine function and a Gaussian function.

Propeller wake measurements were also performed at that time, by placing stationary yaw probes at different axial and radial positions, in order to provide swirl and axial velocities as a function of space [53] [54]. Since the objective was the design of propellers with minimum induced loss, there was no need for a fine representation of the wake but only an estimation of the energy dissipation at each measurement location. Later on, with the advent of turbomachines, the interaction between rotor wakes and Outlet Guide Vanes (OGV), as well as the interactions in compressor stages, required a finer representation of the wake profile for aeroacoustic and aeroelastic analyses. Different rotor wake models were then developed, taking as a basis the approach by Silverstein *et al.* [50].

Kemp & Sears [55] developed such a model in 1955, for predicting the unsteady lift on a rotor blade due to the interaction with the wakes shed from stationary Inlet Guide Vanes (IGV). It was shown that Silverstein's model can be directly converted from dynamic pressure to flow velocity, for velocity deficits small in comparison to the free-stream values. The Gaussian shape was retained for a simplified mathematical analysis. The periodized incident wake was decomposed in spatial Fourier components by means of a Poisson summation formula. This analytical methodology is used in Sec. 2.3.2, for the sake of CROR interaction noise prediction. In the same decade one could mention the analytical work cast by Schlichting [56] for modeling

the wake of isolated plates and cylinders, in which the turbulent mixing length is assumed to be proportional to wake width. In the decade that follows, several attempts were undertaken to provide an enhanced empirical model of the flow behind a rotor. Some researchers used static cascades, for which rotating effects and angular acceleration were naturally not represented [57] [58]. Some others used rotating cascades with stationary measurement devices. Mean characteristics of the flow were then collected at some radial positions, all angular information being lost [59].

The first attempt to provide a complete mapping of the flow behind a rotor was performed by Whitfield *et al.* in 1972 [60]. The 3D velocity field was measured with a single stationary hot-wire probe. The probe was positioned at three orthonormal positions at each point. Assuming ideal directional characteristics, the three non-linear equations obtained for each probe position were inverted analytically, leading directly to the components of the 3D mean velocity field. Radial velocity and swirl angles were found to be dependent on radius, the 3D features being concentrated in the hub and tip regions. A more two-dimensional behavior was found at mid-span. Rotor-wake three-dimensionality was also studied by Raj & Lakshminarayana [51] in 1976 using a stationary tri-axial hot-wire probe. It was besides proved, as pointed out analytically in a previous work of the same authors [61], that the wake behaves differently near the trailing-edge than far from it, from which the near-wake and far-wake regions were defined. In the former region the deficit is of same order of magnitude as the free-stream velocity, whereas it is of one order less in the latter region. Using the far-wake approximation, the authors proposed an analytical solution of the non-linear flow equations, the comparison of which with experiments was rather satisfactory. The authors explained the existence of the two wake regions with the hypothesis that the high velocity gradients in the trailing-edge vicinity produce an intense turbulent mixing, inducing a rapid energy transfer from the mean velocity to the turbulent field. At some point, the mean velocity gradients become smaller than the turbulent gradients so that some energy is fed back to the mean velocity for reaching equilibrium, thus reducing the decay rate of the wake in the far-wake region [51]. This suggests that the computation of the mean velocity field in a rotor wake should be sensitive to the turbulence model.

By far, the most complete rotor-wake study found by the present author is exposed in the technical report by Reynolds & Lakshminarayana in 1979 [62] and its review by Reynolds *et al.* [63]. Similarities were found for wake measurements of a lightly-loaded rotor using, for the first time, rotating hot-wire tri-axial probes fixed in the rotor frame. A stationary probe downstream of the rotor was also used for comparison. The detail of measurement devices

and data post-processing is exhaustive. In total, 95 rotor wakes were correlated for blade incidences of 0°, 5° and 10°. The obtained 3D turbulent and mean wake velocities were reduced to similarity profiles. In the same report are presented similarities for isolated airfoils and cascade wake measurements published by Preston (1945), Mendelsohn (1947), Lieblein (1956) and Pollard (1967). The report exposes the state-of-the-art at the time, gathering the most relevant known data. Correlations are provided for isolated bodies, compressor cascades and lightly loaded rotors for both near-wake and far-wake regions. As a conclusion, it was stated that rotor wake had a weaker dependency on the drag coefficient C_d than an isolated body, as data correlates better with $C_d^{1/4}$ than with $C_d^{1/2}$, and that increasing rotor loading leads to more intense wake velocity deficits, lasting further in the far-wake region. The decay of rotor wakes was found to be faster than that of cascade or isolated body wakes in the near-wake region, but slower in the far-wake region. This point is shown in some detail further in this report. Later on, in 1984, Majjigi and Gliebe [39] proposed a rational wake model for lightly loaded rotors, using the argument that rational functions are perfectly suited to monotonically varying functions. A single law for near-wake and far-wake regions was thus proposed. The data arised from five different experiments, including Reynolds' results. Using linear-rational curve fitting, they found the best data correlation for $C_d^{1/8}$, which suggests a weaker dependence on drag coefficient than previously proposed by Reynolds. The last model presented in this chapter is the one developed in 1993 by Philbrick and Topol [64] using the same technique as Majjigi and Gliebe, this time to correlate data from highly-loaded rotors at high-speed.

Empirical rotor wake models are very few since 1993. In 2005 Cooper & Peake [65] proposed an analytical rotor-wake model in which the swirl is implicitly included in the inviscid equations after a Fourier decomposition of the flow in quasi-convected harmonic waves. The needed swirling flow is provided as a combination of rigid-body and free-vortex models, defined with arbitrary coefficients. This swirling flow could also be deduced, using Theodorsen's theory, from the bound-circulation on the rotor blades, which evolves with radius following the Kutta-Joukowsky lift theorem [66]. A representation of the swirl is necessary for an accurate representation of the wake inclination relative to the rear-rotor leading-edge which, as shown later on in this report, is of primary importance for the interaction tonal noise prediction.

In 2010 Neal reported a very complete experimental investigation of rotor wakes, using a new measurement technique that utilizes four-sensor probes in a double X-array (2X-probe) configuration [67]. A rotating blade geometry was designed using a single cross-section airfoil (cambered), which remained constant throughout the blade radial span. Measurements on this

isolated airfoil in stationary conditions were also conducted. Flow conditions at the rotating blade mid-span (relative velocity, airfoil cross-section and Reynolds number) were equivalent to the ones chosen for the stationary tests. It is the first study in which the wake of a cambered airfoil is compared in equivalent stationary and rotating environments. The conclusions of Neal's work are in agreement with Lakshminarayana's results: rotor wakes are more energetic and also wider in comparison to the wake of an equivalent isolated airfoil in similar conditions. Coriolis forces were put into evidence as a mechanism of radial momentum transport. Also in 2010, Roosemboom & Schröder presented modern non-invasive measurements of a propeller wake. Using Particle Image Velocimetry (PIV) and Background Oriented Schlieren (BOS) techniques, the 3D behavior of the wake was observed closely for two rotational speeds and propeller incidences [68]. It is shown how the incidence modifies the azimuthal distribution of disturbances and increases the vorticity on rotor wakes and tip vortices.

For the specific case of CROR no publication of hot-wire measurements has been found. Nevertheless, some recent activity has been reported at NASA for PIV measurements of the front-rotor wake on a CROR mock-up [23]. The increasing interest for CROR in the last decade motivated, on the other hand, the development of numerical simulation techniques. However, the maturity of the provided schemes is not sufficient to be used as an industrial tool for blade aeroacoustic design, despite the very encouraging results recently found. This is the reason for the alternative development of an analytical wake model for a mid-term strategy.

2.2 Survey of Empirical Wake Models

The main semi-empirical wake models mentioned in Sec. 2.1 are now detailed. The wake characteristics, namely the semi-wake width δ and center velocity deficit U_c, are presented in literature as functions of the distance to the trailing-edge in the direction of the wake axis s (assumed to be rectilinear for sake of simplicity), the airfoil drag coefficient C_d and the incident velocity U_i.

The wake profile U is given by

$$\frac{U}{U_c} = \exp\left[-0.69314\left(\frac{\breve{y}}{\delta/2}\right)^2\right], \tag{2.1}$$

where $\breve{y}$ is a coordinate perpendicular to s. An insight of the differences between isolated

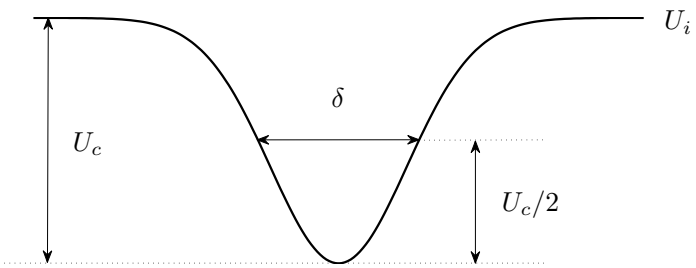

Figure 2.1: *Wake characteristics: Semi-wake width δ and center velocity deficit U_c.*

airfoil and rotor wake models was presented by Raj and Lakshminarayana [61]. Assuming flow incompressibility and self-similarity in the wake mean velocity profiles, the wake behavior is found to be dependent on the pressure gradient in the region where velocity recovery is expected, especially in the near-wake region. In the compressor case the wake centerline velocity is shown to recover more slowly than in the case of isolated non-lifting bodies. Conversely, the velocity defect was shown to recover faster for a propeller than in the two aforementioned cases. Following these arguments, an isolated airfoil wake model is expected to over predict the rotor wake in terms of centerline velocity defect and to under predict the value of its semi-wake width. The correlations presented by Reynolds [62], in Fig. 2.2, for isolated airfoil, cascade and rotor viscous wakes are in agreement with the conclusions of Raj exposed above. As Reynolds' model, presented in Sec. 2.2.3, presents two different correlations for the near-wake and the far-wake regions the plots in Fig. 2.2 are discontinuous. In practice an interpolation should be made in-between both wake regions.

2.2.1 Schlichting's Model (1951)

Schlichting correlated wakes behind isolated circular cylinders and flat plates with the square root of the measured drag coefficient $C_d^{1/2}$ [56]. Similarity profiles lead to the model

$$\frac{U_c}{U_i} = a_s \sqrt{\frac{C_d c}{s}}, \qquad \frac{\delta}{c} = \sqrt{0.2462 \times C_d \times s/c}, \tag{2.2}$$

where $a_s = 0.94664814$ and c denotes the airfoil chord value. The wake origin is located at the airfoil trailing-edge, $s = 0$, where velocity deficit diverges to infinity.

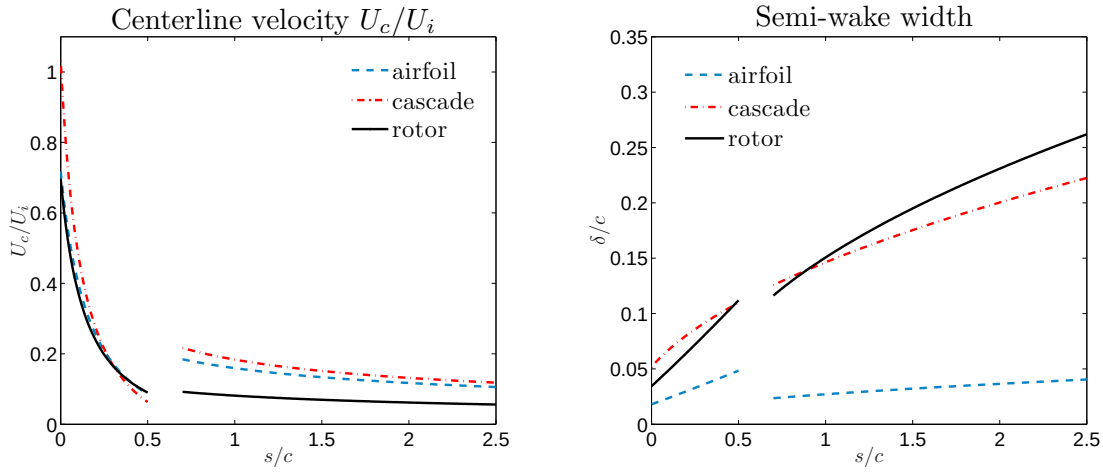

(a) (b)

Figure 2.2: *Reynolds' correlations for measured rotor, static cascade and isolated airfoil viscous wakes [62]. (a) Central velocity deficit. (b) Normalized Wake width. Parameters:* $y_s/c = 0.68$, $C_d = 0.015$ *and* $c = 0.152m$, *where* y_s *represents the blade-to-blade circumferential distance and* c *the rotor chord length.*

2.2.2 Model of Kemp & Sears (1955)

The original wake model cast by Silverstein is converted from dynamic pressure to velocity field. The model used for predicting the unsteady lift on rotor blades due to stator-rotor interaction reads

$$\frac{U_c}{U_i} = \frac{1.21 C_d^{1/2}}{s/c + 0.3}, \qquad \frac{\delta}{c} = (0.235) 0.68 \sqrt{C_d \, (s/c + 0.15)}. \tag{2.3}$$

In Kemp & Sears model, the wake origin is located $0.15c$ upstream of the airfoil trailing-edge. This "virtual origin" was chosen for avoiding the divergence encountered in Schlichting's model on this point. This choice is justified physically as the wake will have a finite width and velocity deficit at the airfoil trailing-edge.

2.2.3 Model of Reynolds & Lakshminarayana (1976)

This model arises from wake measurements on a twelve-bladed uncambered rotor. Each rotor blade section was a British C1 profile, the rotor being designed as a free-vortex type. The chord value, $c = 15.2$cm, was constant over the span. Stager angle at mid-span was 45°. Hub and tip radius were $r_H = 12.05$cm and $r_T = 27.8$cm, respectively.

As stated above, the wake parameters were found to be less dependent on C_d than for an isolated 2D body. The rotor-wake model reads:

$$\frac{U_c}{U_i} = C_d^{1/4}\left[B_5\left(\frac{s}{c}-\frac{s_0}{c}\right)^{-1/2} + B_6\left(\frac{s}{c}-\frac{s_0}{c}\right)^{-1}\right],$$

$$\frac{\delta}{y_s} = C_d^{1/4}\left[D_5\left(\frac{s}{c}-\frac{s_1}{c}\right)^{1/2} + D_6\left(\frac{s}{c}-\frac{s_1}{c}\right)\right], \tag{2.4}$$

where y_s, s_0, s_1 are the blade-to-blade circumferential distance and wake virtual origins, respectively. The virtual origins for near-wake and far-wake regions are given in Table 2.1

	B_5	B_6	D_5	D_6	s_0/c	s_1/c
Near-wake	-0.361	0.463	-0.306	0.845	-0.160	-0.4
Far-wake	0.271	0.0	0.735	0.0	-0.360	0.258

Table 2.1: *Constants for Reynolds' rotor wake model in Eqs. 2.4*

2.2.4 Model of Majjigi & Gliebe (1985)

A rational correlation for both the wake centerline velocity and semi-wake width was given by Majjigi, using the measurements presented by Reynolds [62] and Ravinadranath [69]. The linear curve fitting provided the following results

$$\frac{U_c}{U_i} = C_d^{1/4}\frac{0.3675(s/c)+1.95}{7.65(s/c)+1.0},$$

$$\frac{\delta}{y_s} = \frac{0.31875(s/c)C_d^{1/8} + 0.048}{0.268125(s/c)C_d^{1/8} + 1.0}. \tag{2.5}$$

It must be noticed that most of the empirical rotor-wake models were found from measurements on high solidity rotors. y_s is a characteristic dimension for such wakes, as the pressure gradient produced by adjacent blades is believed to modify the wake width. However, for low-solidity rotors, the assumption of wake width proportional to blade spacing becomes doubtful. An additional correlation of data with the airfoil chord was presented by Majjigi, probably more appropriate for propellers due to their low solidity, as

$$\frac{\delta}{c} = \frac{0.2375(s/c)C_d^{1/8} + 0.034125}{0.357(s/c)C_d^{1/8} + 1.0}. \tag{2.6}$$

2.2.5 Model of Philbrick & Topol (1993)

Philbrick cast the correlations for two highly-loaded transonic Propfan rotors of high solidity using the methodology exposed by Majjigi. The model reads

$$\frac{U_c}{U_i} = C_d^{1/4}\frac{1.175(s/c) + 1.286}{10.80(s/c) + 1.0},$$

$$\frac{\delta}{y_s} = \frac{1.636(s/c)C_d^{1/8} - 0.0194}{5.576(s/c)C_d^{1/8} + 1.0}. \tag{2.7}$$

The empirical models listed above are compared in Fig. 2.3 using the parameters of a typical front-rotor geometry at mid-span. Similar predictions of the normalized central velocity defect U_c/U_i are observed, especially in the far-wake region. Conversely, the predictions of wake width present a great scattering in both near-wake and far-wake regions, in terms of amplitude and trend. Notice that even the correlations of Majjigi, obtained from the same experimental data, provide very different predictions. This is so because the front-rotor low-solidity parameters are out of the definition range of these models, developed for turbofan high-solidity rotors. To elucidate this point, the value of δ provided by both Majjigi's models is plotted for different values of the parameter $\sigma = c/y_s$, which evolves proportionally to the rotor solidity. Keeping the chord value as constant, the value of δ is computed for different values of y_s (plain black lines).

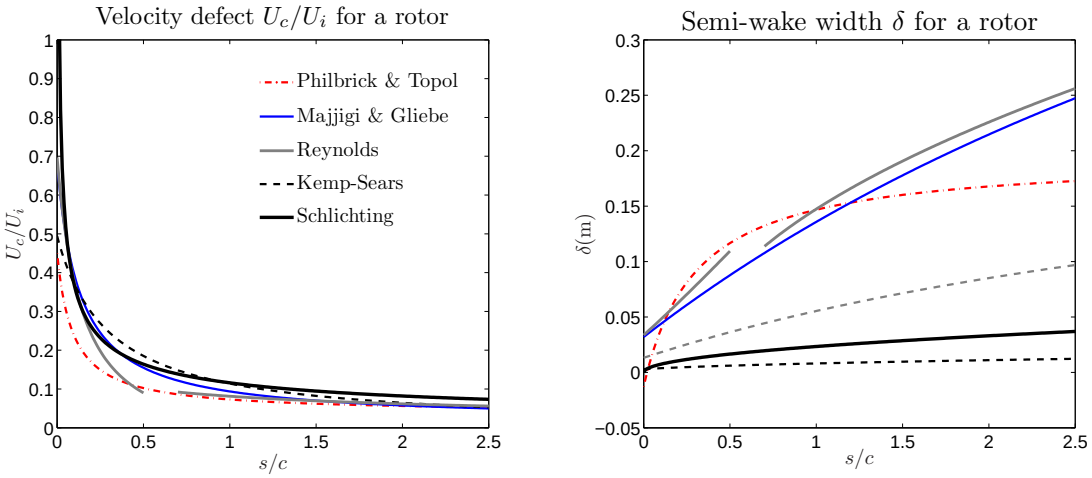

(a) (b)

Figure 2.3: *Comparison of rotor wake models for a typical CROR geometry at mid-span. (a) velocity defects. (b) semi-wake width for a typical front rotor blade at mid-span. Values used* $c = 0.38m$, $y_s = 0.665m$, $C_d = 0.015$. *The dashed gray line represents the Majjigi correlation with c for low-solidity rotors*

The dashed red line stands for the computation using the chord correlation. Two reference values of σ are to be examined. First, the typical CROR front-rotor value $\sigma = 0.52$. Secondly, the value at mid-span of the rotor used by Reynolds in Ref. [62], $\sigma = 1.47$. As shown in Fig. 2.4(a), both models fairly agree for the high-solidity rotor (dashed red line), whereas the predictions diverge for the CROR parameters (black squares vs. dashed red line). Now, the comparison of the models for the high-solidity parameters is presented in Fig. 2.4(b) for $\sigma = 1.47$. An agreement of the models for lightly-loaded rotors is noticed, whereas the isolated body models predict a much thinner wake width. It is also observed that the highly-loaded rotor model predicts a slower wake width evolution along s, which is in agreement with the observations by Reynolds [63]. Empirical models of rotor viscous wake provide physically consistent results only for high solidity rotors. CRORs are out of the definition range of these models.

2.3 Analytical Model of Front-Rotor Wake

In this section is presented a front-rotor wake model based on the analytical derivation of Kemp & Sears [55]. The goal is to provide a model of the 3D upwash seen at the rear-rotor leading-edge,

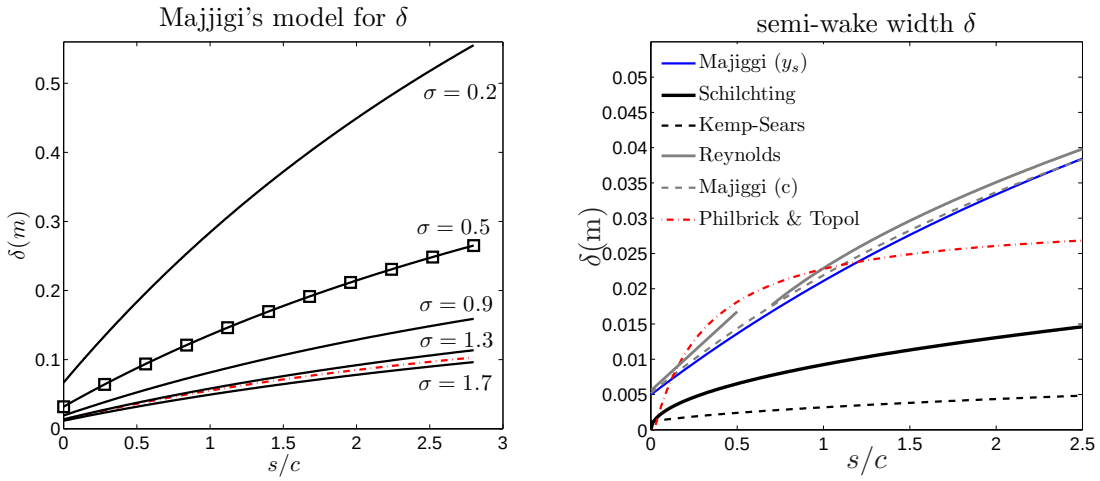

Figure 2.4: *Majjigi's models comparison. (a) Majjigi's semi-wake width model for correlation with c (red line) and y_s (black lines). The value $c = 0.348$ is kept constant for all the curves. (b) Comparison of semi-wake width models for the 12 bladed rotor studied by Reynolds. The values used are $c = 0.152m$, $\sigma = 1.47$, $C_d = 0.015$. The models are represented by the same colors as in Fig. 2.3*

allowing an enhanced interaction representation. The wake characteristics are dependent on s, which is here a function of the radius r. The value can be found from geometrical considerations if the wake axis direction is known. In what follows, front-rotor wake is assumed to follow the chordwise direction at each radius, which seems to be in agreement with measurements and 2D observations of CFD results at mid-span. A different hypothesis is probably needed in the hub and tip proximities due to secondary flows and tip vortex circulation, among other phenomena. The model must be further refined for a more accurate definition of the wake direction, taking into account Coriolis forces, swirl and rotor induced velocities as wake deviation parameters.

The model is developed within the scope of a strip-theory approach. The interaction is defined for 3D radial segments in unwrapped coordinates. The front-rotor segment is defined for arbitrary sweep, lean and twist, whereas the rear-rotor segment is represented by a flat panel featuring only arbitrary sweep and lean. The reasons for such modeling of the rear-rotor segment will be understood in Chapter 3, when dealing with the blade aerodynamic response. Our model is the superposition of an infinity of sheets along the radius, each one containing a 2D Gaussian model defined for the local aerodynamic values. Radial velocity is thus not taken into account.

First, the interaction due to the passage of a single blade is modeled. Subsequently, the upwash seen by the rear-rotor segment is periodized in space and decomposed in a Fourier series, in order to define equivalent sinusoidal gusts. Following the scope of linear this-airfoil theory, which is the basis of the blade response model in Chapter 3, only the velocity component perpendicular to the leading-edge of the rear-rotor segment will be retained for the upwash definition.

2.3.1 Upwash definition at the Rear-Rotor Leading-Edge

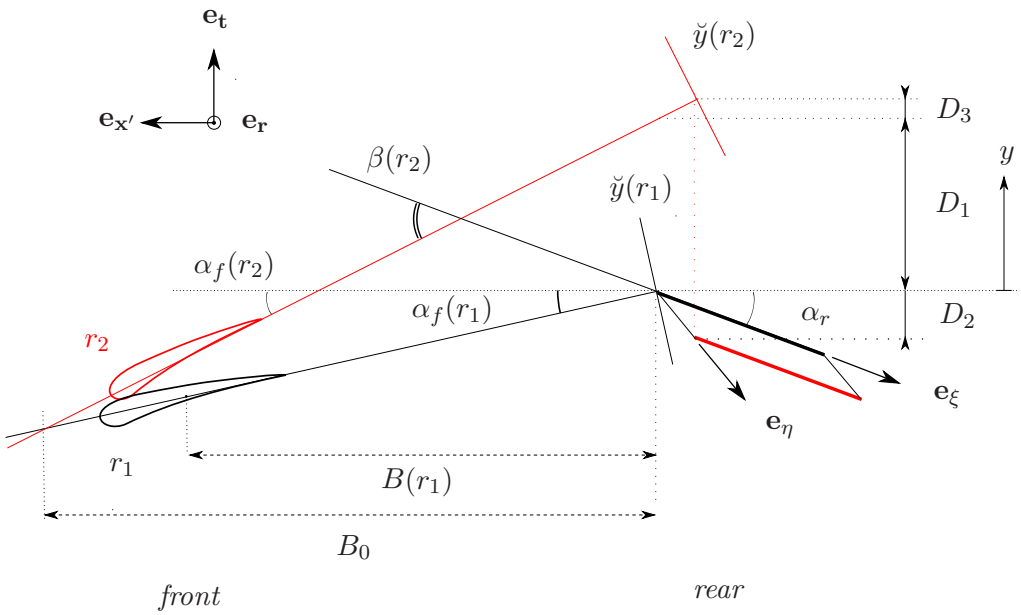

Figure 2.5: *Projection of the geometry in a strip in the* (x, y) *plane.*

Consider a front-rotor blade segment defined for $r_1 < r < r_2$, as shown in Fig. 2.5. Since the radii of wake origin and impact on the rear-rotor are assumed to be equal, the segments pertaining to each rotor are defined on the same radial region. If these segments are sufficiently short, and in analogy with a 2D cascade representation, the relative motion between them can be assumed to be rectilinear in the tangential direction y. The equivalent tangential velocity is approached by the mean value at the segment radial limits

$$\mathbf{v}_\varphi = \frac{(r_1 + r_2)}{2}\Omega_T \mathbf{e_t}, \tag{2.8}$$

where Ω_T is the angular speed of the rear segment relative to the front segment. The rear-rotor

segment is represented by a flat panel whose chordwise and spanwise directions are aligned with the vectors $\mathbf{e}_\xi$ and $\mathbf{e}_\eta$, respectively. The origin of the coordinate y is defined at the point where the rear-rotor element starts getting into the 3D viscous wake, as shown in Fig. 2.5. The distance s_T, in the wake-axis direction, between front-rotor trailing edge and rear-rotor leading edge depends on r. From inspection of Fig. 2.5 is found that

$$s_T(r) = \frac{B(r)}{\cos\alpha_f(r)} - \frac{c_f(r)}{2}, \tag{2.9}$$

where $c_f(r)$ is the front segment chord, $B(r)$ is the axial distance between the front segment mid-chord point and the rear segment leading-edge and $\alpha_f(r)$ is the stagger angle of the front-rotor segment. For the segments in Fig. 2.5, s increases with r which implies that, in this case, the wake is less intense and more diffused for the higher radial values.

The locus featured by the chord lines of the front-rotor sections presents an oblique surface to the leading-edge of the rear-rotor element. As a consequence, the excitation "sweeps" the rear segment leading-edge with a velocity $v_s\mathbf{e}_\eta$, while the element gets trough the 3D wake as it moves in the tangential direction. At each radial value corresponds a 2D Gaussian wake profile, the center of which is defined by the intersection of wake center-sheet and rear segment leading-edge. The intersection point is defined by its tangential coordinate y_c, related to the radius by

$$r = r_1 + v_{sr}t = r_1 + v_{sr}\frac{y_c}{v_\varphi}, \tag{2.10}$$

where t represents the time taken by the element to reach the position y_c traveling at $v_\varphi = \|\mathbf{v}_\varphi\|$ and v_{sr} represents the radial projection of v_s. The expression of v_{sr} is needed here to state this relationship. Noting Δt the time needed by the segment to go through the wake, simultaneity imposes

$$\Delta t = \frac{r_2 - r_1}{v_{sr}} = \frac{D_T}{v_\varphi}, \tag{2.11}$$

where $D_T = D_1 + D_2 + D_3$ represents the tangential distance covered by the segment during the interaction. By inspecting Fig. 2.5, one finds that

$$\begin{aligned} D_1 &= B_0(\tan\alpha_f(r_2) - \tan\alpha_f(r_1)) \\ D_2 &= y_{LE}(r_1) - y_{LE}(r_2) \\ D_3 &= (x_{LE}(r_2) - x_{LE}(r_1))\tan\alpha_f(r_2) \end{aligned} \quad , \tag{2.11}$$

where $(x_{lE}(r), y_{LE}(r))$ denote the coordinates of the leading-edge line as a function of radius. The introduction of Eq.(2.11) into Eq.(2.10) provides the intersection point coordinate

$$y_c(r) = \frac{r - r_1}{r_2 - r_1} D_T. \tag{2.12}$$

Now, the wake profile is defined by a coordinate perpendicular to the wake axis, given by $\breve{y}(y, r) = (y - y_c(r))\cos\alpha_f(r)$. An example of this coordinate is shown in Fig. 2.5, for r_1 and r_2. Note, however, that the rear segment cuts the wake obliquely in such way that the parameters of the excitation must also be dependent on y. By defining a corrected wake-axis distance $\breve{s}_T(y, r) = s_T(r) + (y - y_c)\tan\alpha_f(r)$, the wake profiles seen by the rear segment feature an asymmetric bell shape at each radius. Now, for the flight conditions to be simulated in this study (low-speed and highly-loaded rotors) the wake is sufficiently narrow in the region of interest to apply the approximation $\breve{s}_T \approx s_T$. This assumption is necessary for the application of the analytical Fourier decomposition in Sec. 2.3.2. For cases in which the wake asymmetry, which is strong for highly loaded blades, must be taken into account in the Fourier transform, one could apply the methodology proposed by Roger [70] for asymmetrical Gaussian functions, by defining an equivalent wake width for the pressure and the suction wake sides, or perform a numerical Fourier transform as explained in Sec. 2.4.2.

Taking into account these considerations, the wake profile in Eq.(2.1) is given by

$$U(y, r) = U_c(y, r)\exp\left\{-0.693\left(\frac{(y - y_c(r))\cos\alpha_f(r)}{\delta(r)/2}\right)^2\right\}, \tag{2.13}$$

from which the upwash, defined as the velocity perturbation perpendicular to the rear segment, reads

$$w_u(y, r) = U(y, r)\sin\beta(r), \tag{2.14}$$

with $\beta(r) = \alpha_f(r) + \alpha_r(r)$, as depicted in Fig. 2.5.

2.3.2 Analytical Fourier Components

The tangential distance between two front-rotor elements is defined by $y_s = \pi(r_1 + r_2)/B_1$, with B_1 being the front-rotor blade count, so that the wake shed by the *n-th* front-rotor blade is simply defined by replacing y by $y - ny_s$ in Eq.(2.13). The periodized velocity defect U_T seen by the rear element is the summation of all the wakes shed by the front-rotor, which is written

$$\frac{U_T}{U_c}(y,r) = \sum_{n=-\infty}^{\infty} \exp\left\{-0.693\left(\frac{(y - ny_s - y_c(r))\cos\alpha_f(r)}{\delta(r)/2}\right)^2\right\}. \tag{2.15}$$

A double Fourier transform must be performed on Eq.(2.15) to find the required sinusoidal upwash components. The transformation in the y direction is achieved by means of the Poisson summation formula

$$\sum_{n=-\infty}^{\infty} f(n) = \sum_{k=-\infty}^{\infty} \int_{-\infty}^{\infty} f(z)e^{i2\pi kz}dz, \tag{2.16}$$

with $i = (-1)^{1/2}$. Following the derivation of Kemp & Sears [55], let us define the variable $\zeta = K((y - y_c)/y_s - z)$, with $K(r) = 2\sqrt{0.693}\cos\alpha_f(r)y_s/\delta(r)$, so that the introduction of Eq.(2.15) into Eq.(2.16) yields to

$$\begin{aligned}
\frac{U_T}{U_c}(y,r) &= \frac{1}{K(r)}\sum_{k=-\infty}^{\infty}\int_{-\infty}^{\infty}\exp\left[-\zeta^2 - i2\pi k\left(\frac{\zeta}{K(r)} + \frac{(y_c(r) - y)}{y_s}\right)\right]d\zeta \\
&= \frac{1}{K(r)}\sum_{k=-\infty}^{\infty}\left(\int_{-\infty}^{\infty}\exp\left[-\left(\zeta + \frac{ik\pi}{K(r)}\right)^2\right]d\zeta\right)\exp\left[\frac{-i2\pi k(y_c(r) - y)}{y_s} - \frac{\pi^2k^2}{K^2(r)}\right] \\
&= \frac{\sqrt{\pi}}{K(r)}\sum_{k=-\infty}^{\infty}\exp\left[\frac{-i2\pi k(y_c(r) - y)}{y_s} - \frac{\pi^2k^2}{K^2(r)}\right].
\end{aligned} \tag{2.17}$$

The exponential function in Eq.(2.17) can be split into two functions, each being dependent just in one variable. As the dependence in y is an oscillatory function, an equivalent wavenumber in this direction, $\gamma_y = 2\pi/y_s$, is introduced, leading to

$$\frac{U_T}{U_c}(y,r) = \frac{\sqrt{\pi}}{K(r)} \sum_{k=-\infty}^{\infty} \exp\left[-\frac{\pi^2 k^2}{K^2(r)} - \frac{i2\pi k y_c(r)}{y_s}\right] e^{ik\gamma_y y}. \tag{2.18}$$

In order to expand the result in a Fourier series on r, an artificial radial period must be defined. This value must be greater than the rear-blade radial extent to avoid overlapping. Let the radial period be T_r and, thus, the radial wavenumber be $k_r = 2\pi/T_r$. The upwash is finally expressed by means of the following Fourier series in two-dimensions

$$w_u(y,r) = \sum_{k=-\infty}^{\infty} \sum_{n=-\infty}^{\infty} \tilde{w}_{kn} e^{ik\gamma_y y} e^{ink_r r}, \tag{2.19}$$

where the modal amplitude $\tilde{w}_{kn}$ is

$$\tilde{w}_{kn}(y,r) = \frac{\sqrt{\pi}}{T_r} \int_{r1}^{r_2} \frac{U_c(r)\sin\beta(r)}{K(r)} \exp\left[-\frac{\pi^2 k^2}{K(r)^2} - \frac{i2\pi k y_c(r)}{y_s} - \frac{i2\pi n r}{T_r}\right] dr. \tag{2.20}$$

Eq.(2.20) could be evaluated analytically, if further geometrical assumptions are made. Here we evaluate this integral numerically using the Matlab function *trapz.m* (Runge-Kutta approximation). The evaluation of the present theory is presented in Fig. 2.6. The wake profile seen by an unwrapped rear-rotor segment with radial span has been computed using Kemp's wake model. For this test the rear element is not swept, for which the wake inclination is solely due to the front element twist. The periodized deficit in the tangential direction is depicted in Figs. 2.6(a) and 2.6(b). As expected, the wake is less concentrated and more diffused for the higher radial values. The synthesized wake, found using Eq.(2.19) for harmonics (k,n) going from -5 to 5, is shown in Fig. 2.6(c). Now, let us introduce the convergence parameter Λ, such that $w_u^\Lambda = \sum_{k=-\Lambda}^{+\Lambda} \sum_{n=-\Lambda}^{+\Lambda} \tilde{w}_{kn} e^{ik\gamma_y y} e^{ink_r r}$. By definition, the Fourier synthesis is not perfect unless the value of Λ equals infinity. The value of Λ ensuring an acceptable convergence is found by evaluating the relative error of the synthesis with respect to the original wake, defined as

$$\epsilon(\Lambda)^2 = \frac{\sum_i \sum_j [w_u(i,j) - w_u^\Lambda(i,j)]^2}{\sum_i \sum_j w_u(i,j)^2}, \tag{2.21}$$

where (i,j) denote the radial and tangential indices. The evolution of ϵ with Λ is presented in Fig. 2.6(d), where a relative error of 10% is found for $\Lambda = 5$. This rough estimation is useful to allow the CPU resources required for a satisfactory wake representation.

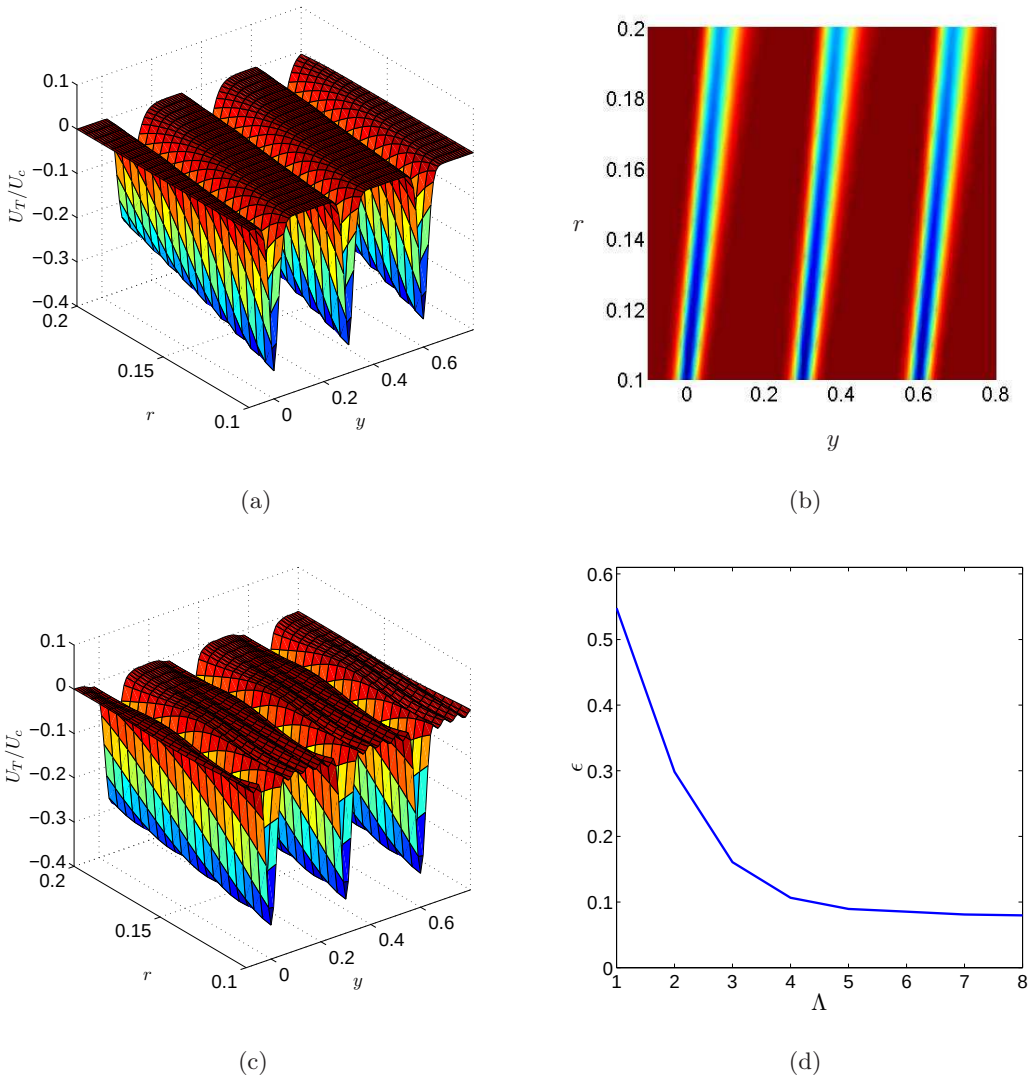

Figure 2.6: *Evaluation of the analytical methodology of Sec. 2.3.2 for radial segments in unwrapped coordinates (x, y, r). (a) 3D view of the original upwash calculated with Kemp's model. (b) Original upwash view in the (y, r) plane. (c) Upwash synthesis for $\Lambda = 5$. (d) Convergence relative error.*

2.3.3 Application to the rear-rotor

The upwash seen by the rear-rotor due to viscous wake interaction is now predicted using the present analytical model. A comparison of the wake characteristics predicted by the different

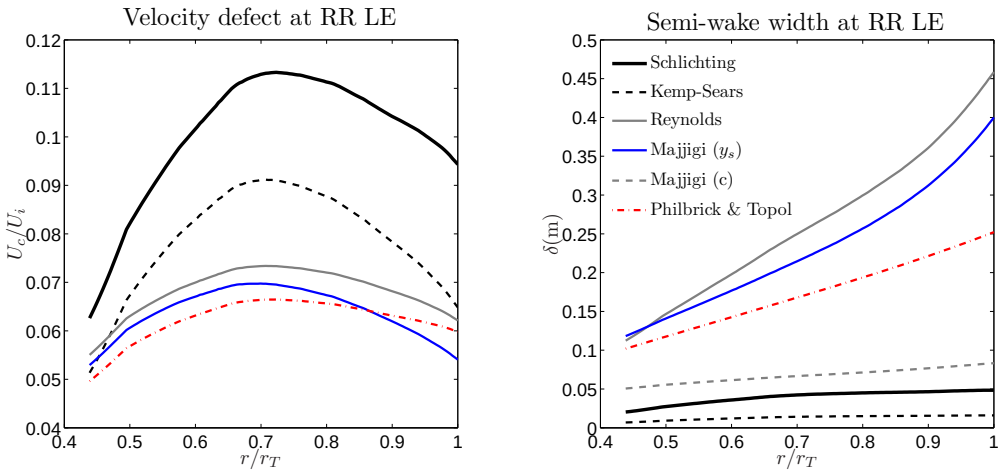

(a) (b)

Figure 2.7: *Front-rotor wake prediction at the rear-rotor leading edge location. The color code is the same as in Fig. 2.3. (a) velocity defects. (b) semi-wake width.*

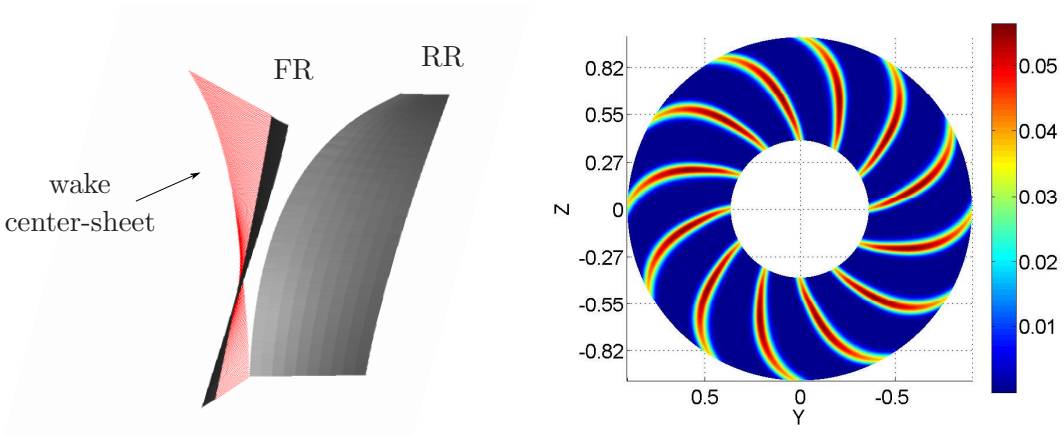

(a) (b)

Figure 2.8: *(a) Interaction scheme featuring one front-rotor blade and its wake and one rear-rotor blade. (b) Velocity defect at the leading-edge of the rear rotor, ratio to incident velocity (front view). Coordinates normalized by rear-rotor tip radius.*

models listed above is presented for a generic CROR geometry. Front-rotor steady drag coefficients are provided by the lifting-line in-house code LPC2 (see App. A6.1) . The results are presented in Fig. 2.7 as a function of normalized radius r/r_T, where r_T is the rear-rotor tip radius. For this front-rotor geometry, the value of σ decreases continuously with the radius within the range [0.36,0.83], which is typical of low-solidity rotors. As shown in Fig. 2.4, rotor wake models do not apply for these values of σ. For this reason, there is great divergence between the rotor models and the isolated-body models, believed to be more reliable at this step. According to these results, front-rotor wake will be more intense at mid-span, its width increasing continuously with radius.

The present analytical model allows a fine representation of the rotor-rotor viscous wake interaction, as shown in Fig. 2.8. However, the result is dependent on the applicability of the correlations used for determining the wake characteristics. The upwash can be plotted as a continuous function on the axisymmetric surface made by the rear-rotor leading-edge as it rotates. An example of such mapping is presented in Fig. 2.8(b) using Majjigi's model, for rotor-chord correlation.

2.4 CFD Wakes as Input Data

The analytical model developed in Sec. 2.3 is based on semi-empirical correlations which generally do not apply to the CROR case. Furthermore, some physical phenomena intrinsic to the CROR configuration are not taken into account by any empirical model, which increases the risk of their application for predicting front-rotor wakes. To the highly 3D behavior of the front-rotor wake must be added the rear-rotor perturbations which, by any means, could be considered as negligible. To illustrate the wake three-dimensionality, the radial velocity in the near-wake region typical of CRORs is depicted in Fig. 2.9. The observed velocity gradient will induce a different radial mixing for this CROR at take-off than for the case of a lightly loaded rotor, on which the available correlations are based. Wake characteristics could be greatly affected by this mixing. The main phenomena ignored in the available models can be listed as follows:

1. It is assumed that the perturbations issued from the front rotor at a given radius will impinge the rear rotor at the same radial value, whereas the *vena contracta* of both rotors deviates the flux.

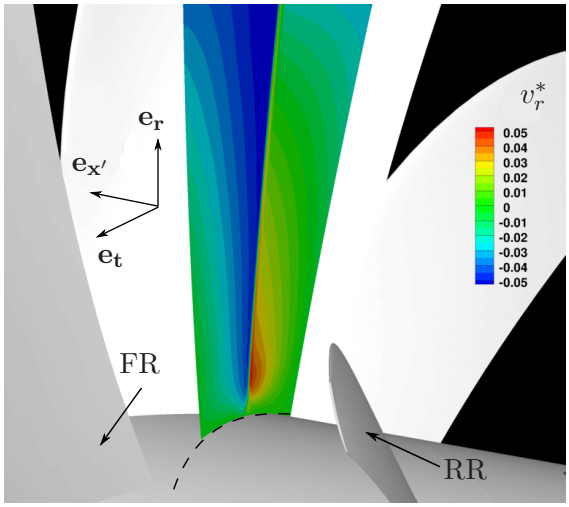

Figure 2.9: *Radial velocity extracted from a URANS computation in the near-wake region of the front-rotor. Non dimensional radial velocity* $v_r^* = v_r\sqrt{\rho_\infty/p_\infty}$. *The velocity is extracted on a plane of single axial value, covering one blade channel. Take-off condition* ($M_X = 0.23$).

2. The effect of Coriolis forces due to swirl is expected to be very dependent on blade twist and other design parameters.

3. Additional acceleration is expected from the rear-rotor thrust.

4. The influence of rear-rotor tip-vortex circulation may be not negligible.

An alternative strategy to determine the upwash at the rear-rotor leading-edge is presented in this section. It consists in the extraction of the front-rotor wake from CFD data, assumed to account for the aforementioned phenomena. The excitation is extracted from URANS computations for validation of the methodology. Sinusoidal gusts are subsequently extracted using a standard Discrete Fourier-Transform (DFT).

2.4.1 CFD Upwash Extraction

The velocity field can be interpolated in a reference surface close to rear-blade leading-edge, to provide the perturbation impinging on the rear rotor. The perturbation components, given in the global Cartesian frame, (u, v, w), are subsequently projected in radial, tangential and axial

components (v_r, v_T, u) for projection on the direction normal to the rear-rotor leading-edge. In Fig. 2.10 is shown an example of such decomposition. The tangential velocity of the particles flowing through the interpolation surface, depicted in Fig. 2.10(a), is represented in Fig. 2.10(b) for a given time step. The trace of the rear-rotor potential field (featured by the red arcs) are much more intense than the front-rotor perturbations, merely visible as light blue arcs curved oppositely. In what follows, the objective is to isolate the front-rotor wakes from the rear-rotor bounded flow, in order to extract the upwash needed as input by the analytical blade response model.

The velocity field on the interpolation surface can be expressed in a reference frame attached to the front-rotor, in which front-rotor wakes appear fixed in space while the rear-rotor locked flows spin at the relative angular velocity. A time integration in this frame provides the sum of front-rotor locked perturbations and rear-rotor mean flows blurred in the circumferential direction, for each radial value. After integration, the traces of the rear-rotor potential field are no longer noticeable and, in counterpart, front-rotor perturbations are highlighted, as seen in Fig. 2.10 (b). Applying the same strategy for each velocity component and then projecting these values on the direction normal to the rear-rotor leading-edge, the total aerodynamic excitation acting on the rear-rotor is provided. The associated upwash, as shown in Fig. 2.10(d), is subsequently found by subtracting the mean value at each radius to exclude the rear-rotor mean flow and the mean value of the front-rotor flow.

2.4.2 Numerical Fourier Components

The sinusoidal gusts required as input by the blade-response routine developed in Chapter 3 can be found from the upwash DFT in two dimensions, defined as

$$\tilde{w}_{num}(s,t) = \sum_{l=1}^{L} \sum_{m=1}^{M} W_{num}(l,m) e^{-i2\pi(l-1)(s-1)/L} e^{-i2\pi(m-1)(t-1)/M} \tag{2.22}$$

where (l,m), (s,t) are the indices of the original and transformed matrices, respectively, and L,M the number of points in the tangential and radial directions, for both matrices. The subscript num stands for numerical results. By definition, the original information is retrieved with the associated inverse transform

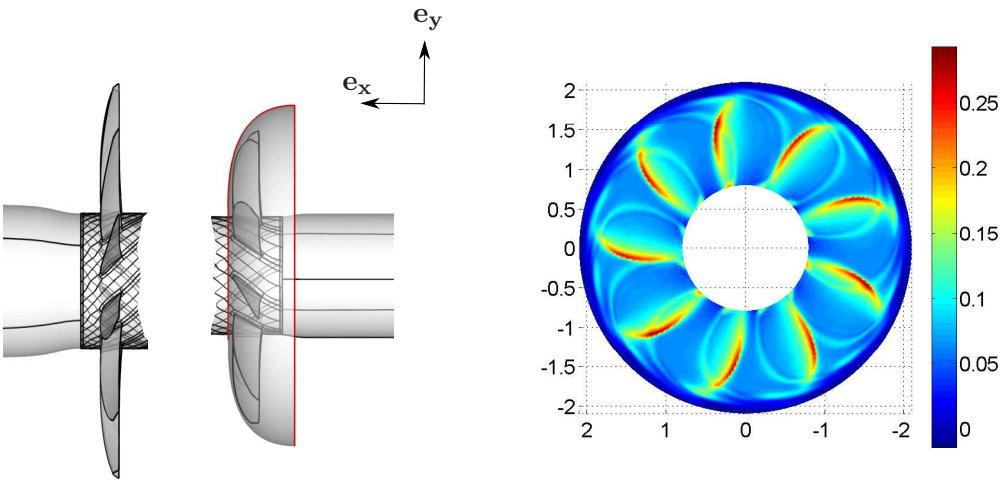

(a) (b)

Figure 2.10: *Extraction of CFD data. (a) Surface of velocity field interpolation. (b) Front view of interpolated tangential velocity. SRPT convention* ($v_T^* = v_T\sqrt{\rho_\infty/p_\infty}$).

$$W_{num}(l,m) = \frac{1}{LM}\sum_{s=1}^{L}\sum_{t=1}^{M}\tilde{w}_{num}(s,t)e^{i2\pi(l-1)(s-1)/L}e^{i2\pi(m-1)(t-1)/M}. \tag{2.23}$$

Eq.(2.23) can be expressed as a discrete sum of sinusoidal gusts, defined for space variables. For instance, the circumferential variable φ can be defined as

$$\varphi = (l-1)\Delta\varphi = (l-1)\frac{\varphi_{max}-\varphi_{min}}{L-1}, \tag{2.24}$$

where φ_{max} and φ_{min} are the angular domain limits and $\Delta\varphi$ represents the grid spacing, assumed to be regular. Any pattern in the angular direction will be expanded in sinusoidal components whose wavelength must be multiple of the domain length. This consideration leads to the equivalent angular wavenumber

$$\kappa_\varphi = \frac{2\pi}{\lambda_\varphi} = \frac{2\pi(s-1)(L-1)}{(\varphi_{max}-\varphi_{min})L} = (s-1)\gamma_\theta. \tag{2.25}$$

The same reasoning in the radial direction leads to the equivalent radial wavenumber

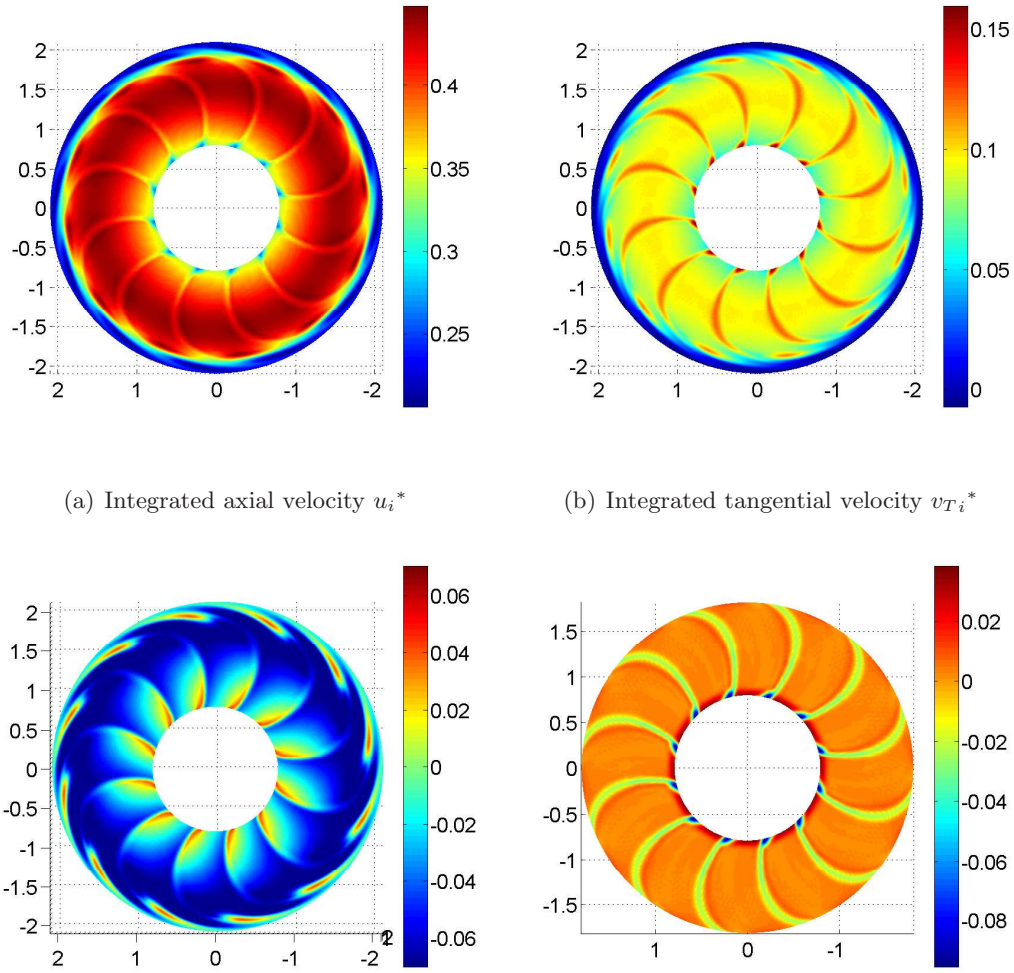

(a) Integrated axial velocity $u_i{}^*$

(b) Integrated tangential velocity $v_{Ti}{}^*$

(c) Integrated radial velocity $v_{ri}{}^*$

(d) Upwash $w_u{}^*$

Figure 2.11: *Time integration of the non-dimensional perturbation velocity components, performed in the front-rotor reference frame. Velocity components : (a) Axial (b) Tangential (c) Radial. (d) Upwash seen by the rear-rotor. SRPT convention* ($u_i^* = u_i\sqrt{\rho_\infty/p_\infty}$)

$$\kappa_r = \frac{2\pi(t-1)(M-1)}{(r_{max}-r_{min})M} = (t-1)k_r, \tag{2.26}$$

which allows writing Eq.(2.23) as :

$$W_{num}(\varphi, r) = \sum_{k=-\frac{L}{2}-1}^{\frac{L}{2}-1} \sum_{n=-\frac{M}{2}-1}^{\frac{M}{2}-1} \tilde{w}_{kn} e^{ik\gamma_\varphi \varphi} e^{ink_r r} \tag{2.27}$$

where $k = s - 1$, $n = t - 1$ and $\tilde{w}_{kn} = \tilde{w}_{num}(k, n)/LM$. For a sufficiently high number of grid points, this equation is identified with Eq.(2.19), with $y = \varphi r$ and $\gamma_\varphi = \gamma_y r$.

The equivalent sinusoidal gusts are expressed as functions of tangential and radial wavenumbers. A last step consists in their projection in the principal directions of the corresponding blade segment. This step is detailed further in Sec. 3.3.2.

A comparison between CFD and analytical wakes is presented in Chapter 5, in terms of tangential profiles and 3D inclination with respect to the rear-rotor leading-edge. The impact of the wake input on blade loading and radiated noise is also studied.

2.5 Conclusion

In this chapter is presented a methodology to obtain the aerodynamic excitations required by the blade-response model presented in Chapter 3. Two different strategies to obtain the required sinusoidal gusts are presented. The first is suited for the analytical model presented in Sec. 2.3. The second is based on the definition of the DFT, and is naturally suited for upwash obtained from CFD computations.

A historical review of previous studies on rotor wakes is presented and the most prominent models are listed. It is shown, from empirical correlations, that wakes behind isolated-bodies decay slower than those behind rotors. For this reason, isolated-body wake models are expected to over predict rotor wakes is terms of central velocity deficit, but to under predict the corresponding semi-wake width. Also, the wake width is shown to be larger for rotors than for static cascades or isolated bodies.

An important conclusion of this chapter is that available empirical models for wakes behind rotors are not applicable to the CROR case, due the assumed high solidity in the models. For this reason, isolated-body wake correlations are probably more reliable to provide the required information.

Chapter 3

Analytical Model of Blade Aerodynamic Response

This chapter describes the methodology to approximate the aerodynamic response of a rotor blade to an oncoming velocity perturbation. The noise source produced by the interaction is predicted by means of an analytical model, based on a proposed extension of Amiet's theory for gust-airfoil interaction. The present fast-tool approach contrasts with other hybrid prediction schemes in which the blade response is computed numerically for an analytical oncoming disturbance (see for example [71] for a ducted fan response or [72] for fan-wake-OGV interaction). The known benefits of the leading-edge sweep for reducing rotor-stator interaction noise [73] [74] [75] motivated the enhancement of the rear-rotor blade geometry representation. Sweep and chord variation with span are represented as continuous parameters by assimilating the blade geometry as a set of swept trapezoids in unwrapped coordinates. An interaction problem in Cartesian coordinates is subsequently formulated for each segment assuming uniform aerodynamic values between two radial cuts. The main difficulty is then to provide the source distribution over the entire blade surface accounting for the three-dimensional features of the interaction.

The proposed methodology is based on the thin-airfoil theory approximation. The blades are assumed to be thin, slightly cambered and lightly loaded, so that the unsteady part of the flow field can be decoupled from the inviscid aerodynamic equations and the blade geometry can be approximated by a set of flat segments. Rotor low-solidity is assumed; each blade is considered

independently by using isolated airfoil response functions. Besides, the incident perturbation is assumed to be unchanged over the blade chord length, which is consistent with the assumed front-rotor far-wake region. Thus, the model uses Taylor's hypothesis, also known as the "frozen gust approximation".

In Sec. 3.1 is detailed the iterative method by Amiet [41] for predicting the unsteady lift on an infinite-span segment due to its interaction with a high-frequency skewed gust. The goal is to provide the basis for the proposed theory extension, derived in Sec. 3.2 for two-dimensional segments with non-parallel edges. Subsequently, this extended response function is used to provide the approximated blade response in Sec. 3.3. For completeness, a study of the methodology sensitivity to the blade meshing and radial segmentation is shown in Sec. 3.3.3.

3.1 Unsteady Lift due to Gust-Segment Interaction

The aerodynamic response of flat segments has been under active research for more than 70 years. The theory has been continuously refined since 1938, when von Kármán and Sears provided the first one-dimensional model for a flat segment interacting with an incompressible gust [76]. In the original model, the airfoil response was in phase over the chord length due to the incompressibility assumption, for which the theory was confined to a narrow low frequency range. To overcome this limitation, compressibility analyses were carried out by Possio [77] and Amiet [78]. The latter researcher proposed a compressibility correction to the initial theory. Paterson & Amiet validated experimentally the progress achieved with this extension for symmetric unloaded airfoils embedded in turbulent flows, convected at velocities at which airfoil compactness can no longer be assumed [79]. However, this corrected model was still limited to low-frequency interactions. Meanwhile, Filotas proposed another extension to the original model [80] to take into account the gust obliqueness with respect to the segment leading-edge assuming incompressible aerodynamics, thereby providing the first two-dimensional approach to the problem. The interaction with compressible skewed gusts became the general problem to be solved, although no closed form for the segment loading has ever been reached for this case. In 1970 Graham [81] proposed to classify the existing theories into two groups, based on similarity arguments, in order to find an approximated solution to the general case by combining the tractable results a the time. Later on, alternative solutions based on iterative methods were proposed by Adamcyk [82] and Amiet [41], using the Wiener-Hopf and Schwarzshild's tech-

niques, respectively. These solutions are appropriate for the high-frequency interactions, for which only two iterations provide an acceptable loading approximation. However, recent comparison with experiments suggest that some low-frequency interaction can also be conveniently predicted with these approaches [83].

The iterative Amiet's method for high-frequency interactions is presented in detail in Secs. 3.1.1 and 3.1.2 since it has been chosen as the theoretical background for further developments. Using the similarity between potential field equations in fluid mechanics and electromagnetism, Schwarzschild's theory for light diffraction [84] has been adapted to find the trace on the segment surface of the potential field scattered at its edges. The incident perturbation is expanded into a sum of sinusoidal Fourier gusts, so that the induced loading is found by linear addition of the contribution of each component. The effect on the loading distribution of wavefront inclination is studied in Sec. 3.1.3. It is shown that there is a critical value at which the mathematical nature of the governing equation changes from hyperbolic to elliptic, which corresponds to a stronger concentration of the loadings in the segment leading-edge region.

3.1.1 Problem Formulation for the Perturbation Velocity Potential

Let us define an orthonormal basis $\mathcal{B}_0 = (\mathbf{e_1}, \mathbf{e_2}, \mathbf{e_3})$ associated with the local source coordinates (y_1, y_2, y_3). Consider a flat strip located at $y_3 = 0$, with infinite span in the $\mathbf{e_2}$ direction and defined for $-b < y_1 < b$, where b is the half chord value $c/2$. A velocity perturbation perpendicular to the segment $\mathbf{v_w} = w\mathbf{e_3}$ is convected towards its leading-edge at the velocity $\mathbf{U}_0 = U_x\mathbf{e_1} + U_y\mathbf{e_2}$. The perturbation is expanded into a sum of Fourier components, each of which is characterized by an aerodynamic wavenumber vector $\mathbf{k} = k_1\mathbf{e_1} + k_2\mathbf{e_2}$ and a modal amplitude $\tilde{w}(k_1, k_2)$. The wavenumber components verify $k_1 = \underline{k}\cos\alpha_k$ and $k_2 = \underline{k}\sin\alpha_k$, introducing the skewness aerodynamic angle α_k, with $\underline{k} = \|\mathbf{k}\|$. In Fig. 3.1 is depicted the interaction of such skewed sinusoidal gust with an infinite-span flat strip.

The interaction between this incident perturbation and the strip generates a potential field ϕ', which is related to the corresponding velocity and pressure fields by

$$\mathbf{u}' = \nabla\phi' \tag{3.1}$$

and

$$p'_\phi = -\rho_0\frac{D\phi'}{Dt} = -\rho_0\left(\frac{\partial\phi'}{\partial t} + U_x\frac{\partial\phi'}{\partial y_1} + U_y\frac{\partial\phi'}{\partial y_2}\right). \tag{3.2}$$

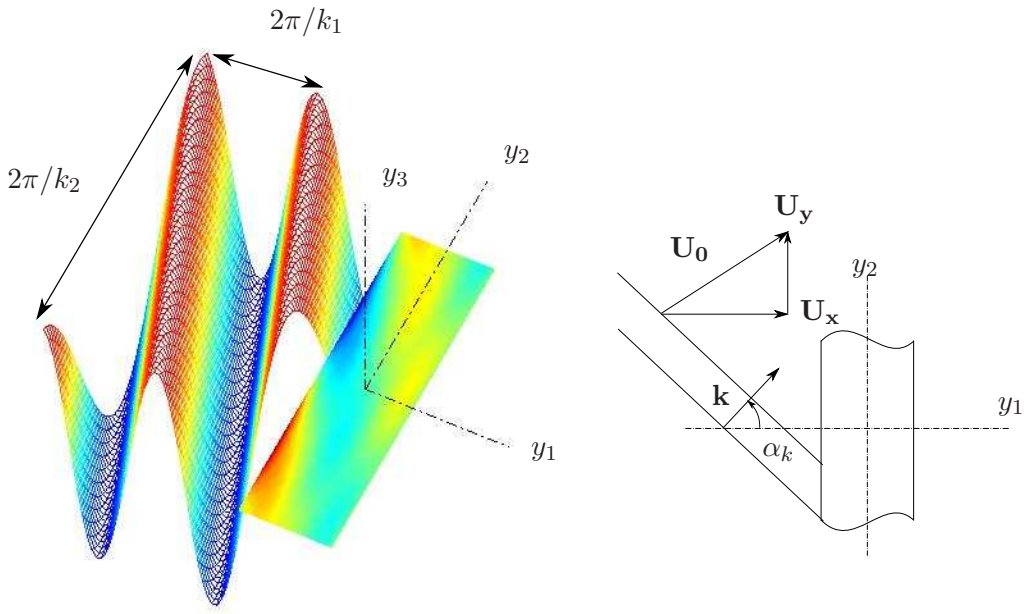

Figure 3.1: *Skewed gust interacting with an infinite-span segment. The velocity convection is aligned with the segment chord. The variable on the segment is the unsteady loading computed from Eqs.(3.19) and (3.24). Arbitrary color units.*

The incident fluctuations of density ρ'_w and pressure p'_w, around the mean values ρ_0 and p_0, can be set to zero at the first order [85], so that the total perturbation field $(\mathbf{v}', p', \rho')$ is given by

$$\mathbf{v}' = \mathbf{v_w} + \mathbf{u}',\ p' = p'_\phi \text{ and } \rho' = \rho'_\phi,$$

and is governed by the linearized equations for an isentropic and perfect gas, given by [86]

$$\frac{\partial \rho'}{\partial t} + \rho_0 \frac{\partial v'_i}{\partial y_i} + U_x \frac{\partial \rho'}{\partial y_1} + U_y \frac{\partial \rho'}{\partial y_2} = 0$$

$$\rho_0 \left(\frac{\partial v'_i}{\partial t} + U_x \frac{\partial v'_i}{\partial y_1} + U_y \frac{\partial v'_i}{\partial y_2} \right) = -\frac{\partial p'}{\partial y_i}, \tag{3.3}$$

$$p' = c_0^2 \rho'$$

where the subscript $i \in (1,2)$. The convected wave equation for the velocity potential is derived by introducing Eqs.(3.1) and (3.2) into the equation system (3.3). The result reads

$$\beta_x^2 \frac{\partial^2 \phi'}{\partial y_1^2} + \beta_y^2 \frac{\partial^2 \phi'}{\partial y_2^2} + \frac{\partial^2 \phi'}{\partial y_3^2} - 2\left(\frac{M_x}{c_0} \frac{\partial^2 \phi'}{\partial t \partial y_1} + \frac{M_y}{c_0} \frac{\partial^2 \phi'}{\partial t \partial y_2} + M_x M_y \frac{\partial^2 \phi'}{\partial y_1 \partial y_2} \right) - \frac{1}{c_0^2} \frac{\partial^2 \phi'}{\partial t^2} = 0, \quad (3.4)$$

where $M_j = U_j/c_0$ and $\beta_j^2 = 1 - M_j^2$, for $j \in (x, y)$.

The solution of Eq.(3.4) depends on the form of the incident perturbation and on the problem boundary conditions. Since linearity is assumed, the analysis can be continued for a single perturbation Fourier component defined by $\mathbf{W_u} = \tilde{w} \exp\{i(k_1 y_1 + k_2 y_2 - \omega t)\}\mathbf{e_3}$. The dispersion equation associated with Eq.(3.4) is found by introducing this gust expression in the second equation of the system (3.3), which provides

$$\omega = U_x k_1 + U_y k_2 = \mathbf{U_0} \cdot \mathbf{k}. \quad (3.5)$$

Now, the problem boundary conditions are defined for three regions of the plane $P(y_1, y_2, y_3 = 0)$, namely the upstream region ($y_1 < -b$), the strip region ($-b \leq y_1 \leq b$) and downstream region ($y_1 > b$). The upstream boundary condition states the cancellation of the velocity potential upstream of the leading edge, which is written

$$\phi'|_{y_3=0} = 0 \qquad \text{for} \qquad y_1 < -b. \quad (3.6)$$

Additionally, the strip surface is assumed to be perfectly rigid and impermeable, which implies the cancellation of the normal velocity over the strip region, so that

$$\frac{\partial \phi'}{\partial y_3}|_{y_3=0} = -\tilde{w} \exp\{i(k_1 y_1 + k_2 y_2)\} \qquad \text{for} \qquad -b \leq y_1 \leq b. \quad (3.7)$$

Finally, according to a full Kutta-Joukowsky condition, the pressure jump is equal to zero from the trailing-edge to the downstream wake, which is written

$$\Delta p'|_{y_3=0} = \Delta \left(\frac{\partial \phi'}{\partial t} + U_x \frac{\partial \phi'}{\partial y_1} + U_y \frac{\partial \phi'}{\partial y_2} \right) |_{y_3=0} = 0 \qquad \text{for} \qquad y_1 > b. \quad (3.8)$$

Since no condition is referring to the coordinate y_2, the velocity potential induced by a single gust can be put in the form $\phi' = \phi(y_1, y_3)\exp\{i(y_2 k_2 - \omega t)\}$, which application in Eq.(3.4) yields

$$\beta_x^2 \frac{\partial^2 \phi}{\partial y_1^2} + \frac{\partial^2 \phi}{\partial y_3^2} + 2i\left(k_a M_x - M_x M_y k_2\right)\frac{\partial \phi}{\partial y_1} + \left(k_a^2 - k_2^2\beta_y^2 - 2M_y k_a k_2\right)\phi = 0, \tag{3.9}$$

where $k_a = \omega/c_0$ is the acoustic wavenumber. Eq.(3.9) is the equation governing the gust-strip interaction. Along with the boundary conditions in Eqs.(3.6), (3.7) and (3.8), this equation provides the potential field, whose trace on the strip is responsible for noise radiation. The mathematical nature of Eq.(3.9) is put into evidence by applying the Reissner transformation. The transformed velocity potential is defined as

$$\Phi = \phi(y_1^*, y_3^*)e^{i\frac{M_x^2}{\beta_x^2}k_1^* y_1^*}, \tag{3.10}$$

where $y_1^* = y_1/b$, $y_2^* = y_2/b$ and $y_3^* = \beta_x y_3/b$ are the non-dimensional source coordinates and $k_1^* = k_1 b$ and $k_2^* = k_2 b$ are the non-dimensional gust wavenumber components. The introduction of these expressions in Eq.(3.9) provides the canonical Helmholtz's Equation in the reduced variable domain, also known as the Prandtl-Glauert plane

$$\frac{\partial^2 \Phi}{\partial y_1^{*2}} + \frac{\partial^2 \Phi}{\partial y_3^{*2}} + \kappa^2 \Phi = 0, \tag{3.11}$$

where

$$\kappa^2 = \frac{k_2^{*2}}{\beta_x^4}\left(\frac{M_x^2}{\sin^2\alpha_k} - 1\right). \tag{3.12}$$

In particular, if $\alpha_k = 0$ ($k_2^* = 0$),

$$\kappa^2 = \frac{M_x^2}{\beta_x^4}k^{*2}. \tag{3.13}$$

3.1.2 Amiet's Technique for Predicting Unsteady Lift Distribution

The German physicist and mathematician Karl Schwarzschild proposed a solution to the homogeneous wave equation expressed in real (x, y) coordinates

$$\frac{\partial^2\phi}{\partial x^2}+\frac{\partial^2\phi}{\partial y^2}+\kappa^2\phi=0,$$

and verifying the following set of boundary conditions

$$\begin{aligned}\phi(x,0)&=f(x) \qquad \text{for} \qquad x>0\\ \frac{\partial\phi}{\partial y}|_{y=0}&=0 \qquad \text{for} \qquad x<0\end{aligned}.$$

This solution is written [84]

$$\phi(x,y)=\frac{1}{\pi}\int_0^\infty G(x,\chi,y)f(\chi)d\chi, \tag{3.14}$$

where

$$G(x,\chi,y)=(-x/\chi)^{1/2}[1/(\chi-x)]e^{i\kappa(\chi-x)} \qquad \text{for} \qquad x<0.$$

This theorem, originally derived for the study of light diffraction, is used here to find a solution of Eq.(3.11). However, notice that Schwarzschild's theorem can satisfy only two of the three boundary conditions of our problem. To overcome this shortcoming, Amiet proposed to use this theorem in an iterative method, in which a solution is produced at each iteration to correct the unsatisfied boundary condition of the preceding one. Each iteration will verify the strip impermeability and the boundary condition associated with one edge. A dimensional analysis, achieved by Amiet [41], shows that for high-frequency interactions such that $\kappa > 0.4$, the unsteady loading can be satisfactorily described with the two first iterations, corresponding to the first-order leading-edge and trailing-edge contributions, respectively. Furthermore, for values $\kappa > \pi/4$ the same author shows that the strip loading can be approximated within 10% of accuracy with only the leading-edge first-order contribution.

Initial Potential

An initial velocity potential $\phi^{(0)}$ is necessary to start the iterative process. To satisfy the field cancellation as y_3 reaches infinity, the following initial potential is proposed

$$\phi^{(0)}=Ae^{ik_1y_1}e^{-a_0y_3}.$$

Introducing it in Eq.(3.9) provides $a_0^2 = k_1^2 + k_2^2 \equiv \underline{k}$. The strip rigidity and impermeability imply

$$\frac{\partial \phi^{(0)}}{\partial y_3}|_{y_3=0} = -a_0 A e^{ik_1 y_1} = -\tilde{w} e^{ik_1 y_1},$$

which yields to the amplitude value $A = \tilde{w}/a_0$. The use of this result leads to the initial potential in reduced variables

$$\Phi^{(0)} = \frac{b\tilde{w}}{\sqrt{k_1^{*2} + k_2^{*2}}} e^{ik_1^* y_1^*/\beta_x^2} e^{-\sqrt{k_1^{*2}+k_2^{*2}} y_3^*/\beta_x}. \tag{3.15}$$

Leading-Edge Term

The potential in Eq.(3.15) must be corrected to satisfy the boundary conditions at the strip edges. For the sake of simplicity, the strip is now defined in the leading-edge chordwise coordinate $y_L^* = y_1^* + 1$. The leading-edge contribution $\Phi^{(1)}$ resulting from this first iteration must satisfy the cancellation of the potential for $y_L^* < 0$ and the strip impermeability, which is written

$$\Phi^{(1)}|_{y_3^*=0} = -\Phi^{(0)} \qquad \text{for} \qquad y_L^* < 0$$

$$\frac{\partial \Phi^{(1)}}{\partial y_3^*}|_{y_3^*=0} = 0 \qquad \text{for} \qquad y_L^* > 0$$

.

$\Phi^{(1)}$ is deduced from Schwarzschild's theorem, for $x = -y_L^*$:

$$\Phi^{(1)}(y_L^*, \chi, 0) = \frac{-b\tilde{w}}{\pi\sqrt{k_1^{*2} + k_2^{*2}}} \int_0^\infty \sqrt{\frac{y_L^*}{\chi}} \frac{e^{i\kappa(\chi + y_L^*)} e^{-ik_1^* \chi/\beta_x^2}}{\chi + y_L^*} d\chi, \tag{3.16}$$

which, as detailed in App. A3.1, yields to the velocity potential integrating leading-edge effects as

$$\Phi_1(y_L^*,0) = \Phi^{(0)} + \Phi^{(1)} = \frac{b\tilde{w}}{\sqrt{k_1^{*2}+k_2^{*2}}} U^0\left[\left\{iy_L^*\left(k_1^*/\beta_x^2 - \kappa\right)\right\}^{1/2}\right] e^{iy_L^* k_1^*/\beta_x^2}, \tag{3.17}$$

where $U^0(Z)$ is the generalized error function for complex arguments.

The associated unsteady loading $\tilde{\ell}_1$ is found by introducing the velocity potential of the leading-edge contribution $\phi_1'(y_L^*, y_2^*) = \Phi_1 e^{ik_2^* y_2^*} e^{-i\omega t}$ into Eq.(3.2):

$$\tilde{\ell}_1 = 2p'_{\Phi_1} = -2\frac{\rho_0 U_x}{b}\left[\frac{\partial \Phi_1}{\partial y_L^*} - i\frac{k_1^*}{\beta_x^2}\Phi_1\right] e^{-i\mu M_x y_L^*} e^{ik_2^* y_2^*}, \tag{3.18}$$

with $\mu = \dfrac{M_x k_1^*}{\beta_x^2}$. The leading-edge contribution to the unsteady loading is found after evaluation of the partial derivative in Eq.(3.18). The result, expressed in the initial coordinate system, with reference at mid-chord, reads

$$\tilde{\ell}_1 = -\frac{2\rho_0 U_x \tilde{w} e^{i\pi/4}}{\sqrt{\pi(k_1^* + \beta_x^2\kappa)(y_1^*+1)}} e^{-i(\mu M_x - \kappa)(y_1^*+1)} e^{ik_2^* y_2^*} e^{-i\omega t}. \tag{3.19}$$

Trailing-Edge Term (Kutta Correction)

The trailing edge correction can be directly found from Eq.(3.19), since the Kutta condition is defined for the pressure and not for the velocity potential. For applying Schwarzschild's theorem, the leading-edge term is transformed to be a solution of Eq.(3.11). The result is expressed back in the physical domain afterwards. The pressure associated with the leading-edge contribution, and satisfying Eq.(3.11), is given by

$$\mathcal{P}'_{\Phi_1}(y_1^*, 0) = p'_{\Phi_1} e^{i\mu M_x (y_1^*+1)} = -\frac{\rho_0 U_x \tilde{w} e^{i\pi/4}}{\sqrt{\pi(k_1^* + \beta_x^2\kappa)(y_1^*+1)}} e^{i\kappa(y_1^*+1)}. \tag{3.20}$$

Let us define the trailing-edge chordwise coordinate $y_T^* = y_1^* - 1$. The trailing-edge contribution verifies the boundary conditions

$$\begin{aligned} \mathcal{P}'_{\Phi_2}(y_T^*,0)|_{y_3=0} &= -\mathcal{P}'_{\Phi_1}(y_T^*,0) \qquad \text{for} \qquad y_T^*>0 \\ \frac{\partial \mathcal{P}'_{\Phi_2}}{\partial y_3^*}|_{y_3=0} &= 0 \qquad \text{for} \qquad y_T^*<0 \end{aligned} \quad . \tag{3.21}$$

Schwarzschild's theorem is now applied for $x = y_T^*$, leading to

$$\mathcal{P}'_{\Phi_2} = \frac{\rho_0 U_x \tilde{w} e^{i\pi/4}}{\pi\sqrt{\pi(k_1^* + \beta_x^2\kappa)}} \sqrt{-y_T^*} e^{-i\kappa y_T^*} e^{2i\kappa} \int_0^\infty \frac{\chi^{-1/2} e^{2i\kappa\chi}}{(\chi - y_T^*)\sqrt{\chi+2}} d\chi. \tag{3.22}$$

Since the largest contribution to this integral is given by small values of χ, the radical in the integral can be fairly approximated to $\sqrt{\chi+2} \approx \sqrt{2}$. The result in App. A3.1 is used again to find the converted pressure associated with the trailing-edge Kutta correction

$$\mathcal{P}'_{\Phi_2} \approx \frac{\rho_0 U_x \tilde{w} e^{i\pi/4}}{\sqrt{2\pi(k_1^* + \beta_x^2\kappa)}} \left(1 - U^0[(2i\kappa y_T^*)^{1/2}]\right) e^{i\kappa y_T^*}. \tag{3.23}$$

The corresponding contribution to the unsteady loading is given in the initial coordinate system by

$$\tilde{\ell}_2 = \frac{2\rho_0 U_x \tilde{w} e^{i\pi/4}}{\sqrt{2\pi(k_1^* + \beta_x^2\kappa)}} \left(1 - (1+i)E^*[2\kappa(y_1^* - 1)]\right) e^{-i(\mu M_x - \kappa)(y_1^*+1)} e^{ik_2^* y_2^*} e^{-i\omega t}, \tag{3.24}$$

where $E[x] = \displaystyle\int_0^x \frac{e^{it}}{\sqrt{2\pi t}} dt$ is the Fresnel integral, the asterisk denoting the complex conjugate.

The results in Eqs.(3.19) and (3.24), found with the Amiet-Schwarzschild technique, are equivalent to the original formulation deduced by Adamczyk using the Wiener-Hopf technique [82]. The total unsteady lift on the strip is $\tilde{\ell} = \tilde{\ell}_1 + \tilde{\ell}_2$, from which we define the reduced lift function g such that

$$\tilde{\ell} = 2\pi\rho_0 U_x \tilde{w} e^{i\pi/4} g(y_1^*, k_1^*, k_2^*) e^{ik_2^* y_2^*} e^{-i\omega t}. \tag{3.25}$$

The theory allows modeling swept segments, since convection velocity and gust wavefronts are defined with an arbitrary inclination with respect to the strip edges. The technique will

be extended in Sec. 3.2, in order to take into account the influence of non parallel leading and trailing edges on the unsteady loading distribution.

3.1.3 Subcritical and Supercritical Gusts

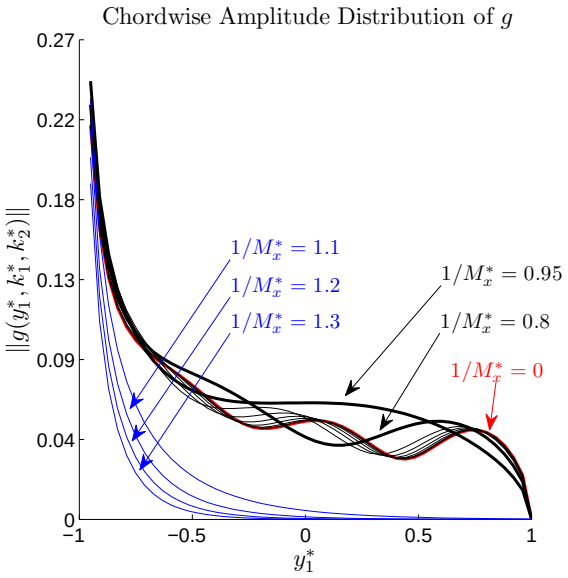

Figure 3.2: *Amplitude of the reduced lift function for different skewed gusts. The red curve corresponds to the parallel gust (Sears' problem). Black curves: supercritical gusts. The non-labeled black curves correspond to* $0.1 < 1/M_x^* < 0.7$. *Blue curves: subcritical gusts. Simulation parameters:* $k_1^* = 3\pi$, $M_x = 0.44$, $U_y = 0$.

The nature of Eq.(3.11), governing the gust-airfoil interaction, depends on the relationship between the gust inclination and the chordwise component of the convection velocity. Graham analyzed this dependency by introducing a similarity parameter to define the interaction as supercritical or subcritical for values of κ being real or imaginary, respectively [81]. Graham's parameter is defined as $\Theta = \mu\beta_x/k_2^*$ so that

$$\kappa^2 = \left(\frac{k_1^* M_x}{\beta_x^2}\right)^2 \left(1 - 1/\Theta^2\right). \tag{3.26}$$

For $\Theta \leq 1$, the interaction, governed by an elliptic equation, is said *subcritical*. Conversely, for $\Theta > 1$ the interaction is said *supercritical* and is governed by a hyperbolic equation. As

explained later on, in Sec. 4.1.2, a subcritical interaction is unable to produce propagative waves for an infinite-span strip, due to its subsonic spanwise trace velocity of the aerodynamic excitation. For segments having a finite span, subcritical gusts provide a finite acoustic contribution but significantly smaller than the supercritical interactions [87]. Adamczyk proposed another parameter to classify the interactions. Noting $\kappa^2 = (M_x^{*2} - 1)k_2^{*2}/\beta_x^4$, with $M_x^* = M_x/\sin\alpha_k$, an interaction is supercritical only if $M_x > \sin\alpha_k$. This implies that for a given M_x, the value $\alpha_k = \arcsin(M_x)$ defines a critical gust inclination from which the infinite-span strip cannot radiate noise.

The sensitivity of unsteady loading to gust obliqueness is shown in Fig. 3.2, for different values of $1/M_x^*$. The reduced lift chordwise distribution is plotted for gusts going from the parallel gust, corresponding to the compressible Sears' problem [88], to some subcritical gusts. The amplitude induced on the strip by the interaction seems to be larger for the supercritical cases. Also, the loadings are more distributed over the chord length for these cases. Conversely, subcritical gusts produce a weaker interaction, very rapidly decreasing from the leading-edge singularity. These differences, solely due to the gust inclination, demonstrate that the response of a swept segment to a given gust cannot be replaced by that of a set of unswept phased segments covering the same span region. If in the first case we have a subcritical interaction, the second case will provide a succession of acoustically efficient Sears' problems.

The effects of gust inclination and convection velocity are now analyzed for the loading terms associated with each edge. The convection velocity is assumed to be parallel to the strip chord, for simplicity. For this analysis, the leading-edge term amplitude is expressed as

$$\|\tilde{\ell}_1\| = \frac{2\rho\|\tilde{w}\|\tilde{A}_{le}}{\sqrt{y_1^* + 1}} \qquad \text{where} \qquad \tilde{A}_{le} = \left\| \frac{U_x}{\sqrt{\pi(k_1^* + \beta_x^2\kappa)}} \right\|. \tag{3.27}$$

The value of $\tilde{A}_{le}$, referred to as the leading-edge factor, defines the strength of the leading-edge term amplitude, whereas its chordwise distribution is determined solely by the square root $\sqrt{y_1^* + 1}$ in Eq.(3.27), for supercritical interactions. The subcritical cases are also affected by an exponential decrease from the leading-edge. In Fig. 3.3 are depicted the isovalue lines of $\tilde{A}_{le}$ as a function of M_x and $\sin\alpha_k$, for three values of k_1^*, for chordwise non-compactness effect analysis. As expected, a change of regime is observed on the critical diagonal where $M_x^* = 1$. However, recall that for values of $\|\kappa\| < 0.4$ Amiet's technique presented in Sec. 3.1 does not apply in principle. Indeed, to provide an acceptable solution of Eq.(3.11), higher order terms

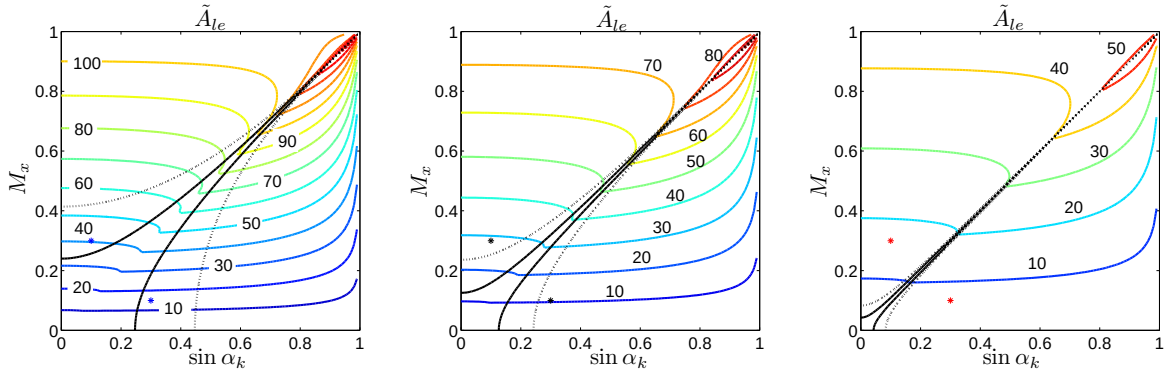

(a) $k_1^* = \pi/2$ (b) $k_1^* = \pi$ (c) $k_1^* = 3\pi$

Figure 3.3: *Isovalue lines of $\tilde{A}_{le}$ as a function of M_x and $\sin\alpha_k$. Plain black lines: $\|\kappa\| = 0.4$. Dashed black lines: $\|\kappa\| = \pi/4$.*

should be needed for which analytical evaluation is no longer possible. The plain black lines in the figures delimit the region in which the present high-frequency theory is not valid whereas the dashed lines define the limit $\|\kappa\| = \pi/4$, from which the trailing-edge correction could be neglected, according to Amiet's analysis.

As shown in Figs. 3.3(a), (b) and (c), for a given convection velocity the leading-edge contribution will increase with gust inclination, as the real value of κ decreases. After reaching zero on the critical diagonal, κ becomes purely imaginary inducing a rapid reduction of the leading-edge factor in the subcritical region. Now, for a given gust inclination the leading-edge factor increases with M_x with a higher sensitivity in the subcritical region. Also, the comparison of the $\tilde{A}_{le}$ levels in these three figures shows that the efficiency of the interaction decreases as the gust non-dimensional chordwise increases.

The assessment of the trailing-edge correction effect is now analyzed for the interaction cases of Fig. 3.3. The evaluated parameter is referred to as the trailing-edge effect index I_{te}, defined as quadratic error between the amplitudes of the total airfoil response $\tilde{\ell}$, which includes interferences with the trailing-edge correction, and the leading-edge term $\tilde{\ell}_1$

$$I_{te} = \left[\frac{\sum_{y_1^*} (\|\tilde{\ell}(y_1^*)\| - \|\tilde{\ell}_1(y_1^*)\|)^2}{\sum_{y_1^*} \|\tilde{\ell}_1(y_1^*)\|^2} \right]^{1/2} . \tag{3.28}$$

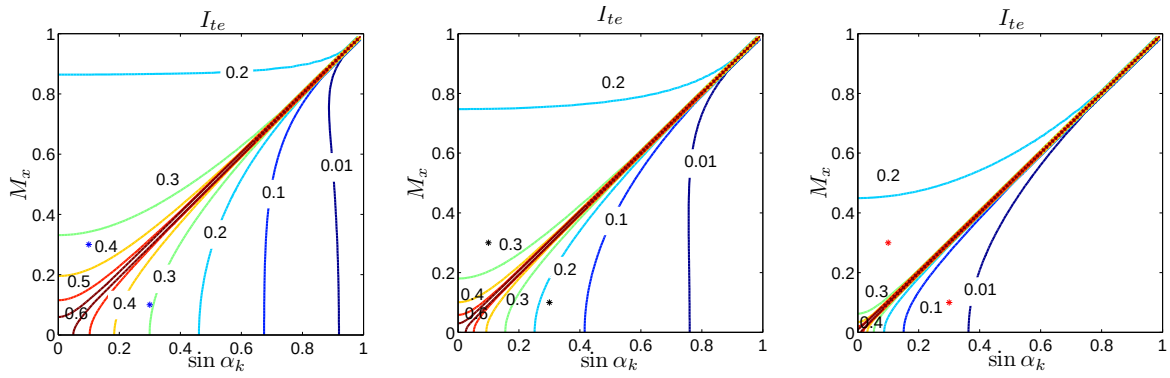

(a) $k_1^* = \pi/2$ (b) $k_1^* = \pi$ (c) $k_1^* = 3\pi$

Figure 3.4: *Trailing-edge effect index I_{te} as a function of M_x and* $\sin\alpha_k$.

The isovalue lines of I_{te} are depicted in Fig. 3.4. The results agree with Adamczyk conclusions for supercritical interactions [82]: as the value of κ increases, the leading-edge contribution increases whereas the effect of the trailing-edge correction decreases. Also, we find that the supercritical interactions are more affected by the trailing-edge correction than subcritical interactions and that trailing-edge correction affects the total response out of the region defined by Amiet. To ascertain the application range of the Kutta-correction, the chordwise reduced lift function g is plotted in Fig. 3.5 for the interactions defined in Table 3.1. The studied cases are identified with the colored asterisks in Figs. 3.3 and 3.4. As expected, the leading-edge contribution is reduced as k_1^* is increased for both subcritical and supercritical interactions. The values of I_{te} seem to be consistent with the trailing-edge effects found for these particular cases.

Color	k_1^*	M_x	$\sin\alpha_k$	κ	$\tilde{A}_{le}$	I_{te}
blue	$\pi/2$	0.3	0.1	0.49	40.57	0.33
		0.1	0.3	$0.47i$	14.98	0.30
black	π	0.3	0.1	0.98	28.68	0.27
		0.1	0.3	$0.94i$	11.64	0.18
red	3π	0.3	0.1	2.94	17.30	0.23
		0.1	0.3	2.82	3.70	0.04

Table 3.1: *Parameters for the interactions in Fig. 3.5*

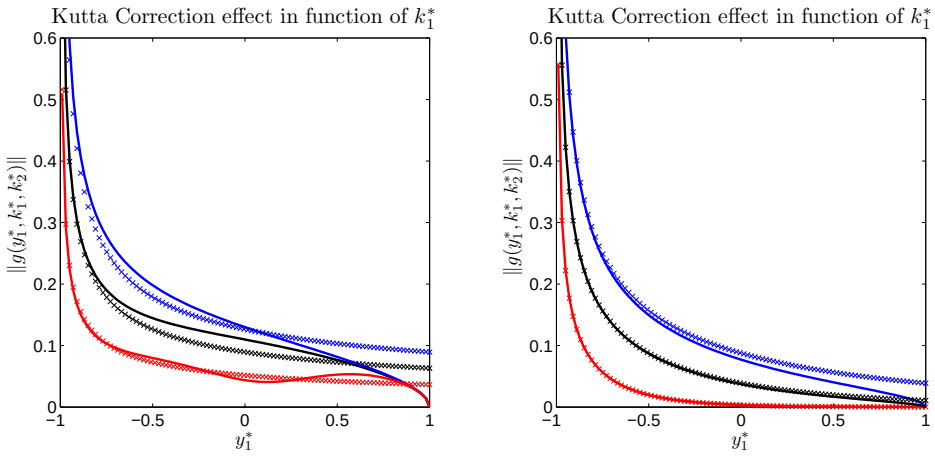

(a) $M_x = 0.3$, $\sin\alpha_k = 0.1$.

(b) $M_x = 0.1$, $\sin\alpha_k = 0.3$.

Figure 3.5: *Reduced lift function amplitude for the interactions in Table 3.1. Blue curves: $k_1^* = \pi/2$. Black curves: $k_1^* = \pi$. Red Curves: $k_1^* = 3\pi$. Plain lines: Total strip response $\tilde{\ell}$. Crosses: Leading-edge term $\tilde{\ell}_1$. (a) Supercritical Interactions. (b) Subcritical Interactions.*

From the comparisons shown in this section, one concludes that the trailing-edge correction should be included for $I_{te} > 0.2$, which increases considerably the application range originally defined by Amiet. This observation is in agreement with the conclusions of Moreau & Roger [83] who, comparing Amiet's theory with experimental results, pointed out that the present high-frequency approximation provided adequate predictions even for low frequencies, out of the initial definition range of the theory. It is expected that the theory extension in Sec. 3.2, which can be seen as the definition of an oblique Kutta condition, would apply at most in the same range as the trailing-edge correction evaluated in this section.

3.2 Theory Extension: Formulation for Swept Trapezoids

For most advanced-rotor designs, a rear-blade segment features a flat trapezoid in unwrapped coordinates, with non parallel leading and trailing edges and spanwise end-cuts parallel to the relative flow direction. The Amiet's theory extension developed in this section allows the assessment of the segment shape effects on the unsteady loading distribution due to the segment interaction with a skewed gust convected at a velocity U_0 aligned with the segment chord, as

defined parallel to the cuts.

The trapezoid geometry is defined with three coordinate systems $(\bar{X}, \bar{Y})$, $(\bar{x}_1, \bar{y}_1)$ and $(\bar{x}_2, \bar{y}_2)$, respectively aligned with the segment chord, leading edge and trailing edge, as shown in Fig. 3.6. The coordinates are made non-dimensional by the trapezoid half-chord at mid-span, b. The coordinate system associated with the leading edge is defined so as to locate the trapezoid leading edge at $\bar{x}_1 = -2$. The relation between leading-edge and trailing-edge coordinates is given by

$$\begin{cases} \bar{x}_1 = \cos\bar{\varphi}_T \bar{x}_2 - \sin\bar{\varphi}_T \bar{y}_2 + 2(\cos\bar{\varphi}_1 - 1) \\ \bar{y}_1 = \sin\bar{\varphi}_T \bar{x}_2 + \cos\bar{\varphi}_T \bar{y}_2 + 2\sin\bar{\varphi}_1 \end{cases}, \tag{3.29}$$

where $\bar{\varphi}_1$ and $\bar{\varphi}_2$ are the sweep angles of leading edge and trailing edge, and $\bar{\varphi}_T = \bar{\varphi}_1 + \bar{\varphi}_2$.

3.2.1 Leading-Edge Term

The leading-edge response to the oncoming sinusoidal gust $W_u = \tilde{w}\exp\{i(\bar{k}_{x1}\bar{x}_1 + \bar{k}_{y1}\bar{y}_1 - \omega t)\}$ is found by adapting Eq.(3.19) to the present trapezoid notations:

$$\tilde{\ell}_1(\bar{x}_1, \bar{y}_1) = \frac{-2\rho_0 U_{x1}\tilde{w}e^{i\pi/4}}{\sqrt{\pi(\bar{k}_{x1} + \beta_{x1}{}^2\kappa)(\bar{x}_1 + 2)}} e^{-i(\mu M_{x_1} - \kappa)(\bar{x}_1 + 2)} e^{i\bar{k}_{y1}\bar{y}_1} e^{-i\omega t}, \tag{3.30}$$

where $(\bar{k}_{x1}, \bar{k}_{y1})$ are non-dimensional aerodynamic wavenumbers along $\bar{x}_1$ and $\bar{y}_1$, respectively, U_{x1} is the convection velocity component perpendicular to the leading edge, $M_{x1} = U_{x1}/c_0$, $\beta_{x1}^2 = 1 - M_{x1}^2$,

$$\kappa = \frac{1}{\beta_{x1}}\left[\frac{(b\omega/c_0 - \bar{k}_{y1}M_{y1})^2}{\beta_{x1}^2} - \bar{k}_{y1}^2\right]^{1/2} \qquad \text{and} \qquad \mu = \frac{\bar{k}_{x1}M_{x1}}{\beta_{x1}^2}. \tag{3.31}$$

The back-scattering Kutta correction will be found again from Schwarzschild's theorem, which requires the segment trailing-edge definition with a constant coordinate value. This requirement is fulfilled by expressing Eq.(3.30) in the trailing-edge coordinates ($\bar{x}_2$,$\bar{y}_2$). Amiet's technique cannot be directly applied because the change of variables induces a coupling between $\bar{x}_2$ and $\bar{y}_2$ in the square root of Eq.(3.30). The problem is solved by making the reasonable assumption of small aspect-ratio $\sin(\bar{\varphi}_T)\bar{y}_2/2 \ll 1$, which provides the following approximation for Eq.(3.30), valuable around mid-span

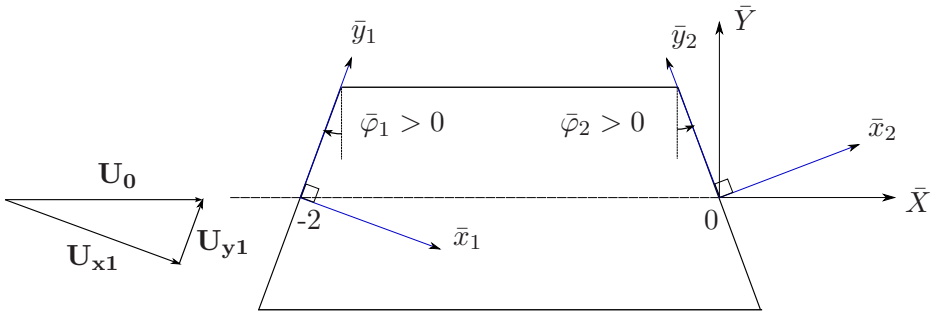

Figure 3.6: *Trapezoid geometry for Amiet's technique extension.*

$$\tilde{\ell}_1(\bar{x}_2,\bar{y}_2) \approx \frac{-2\rho_0 U_{x1}\tilde{w}e^{i(a_1\bar{x}_2+a_{20}\bar{y}_2+a_3+\pi/4)}}{\sqrt{\pi(\bar{k}_{x1}+{\beta_{x1}}^2\kappa)(\cos\bar{\varphi}_T\bar{x}_2+2\cos\bar{\varphi}_1)}} \times \left[1+\frac{e^{+i\sin\bar{\varphi}_T\bar{y}_2/2}-e^{-i\sin\bar{\varphi}_T\bar{y}_2/2}}{2i(\cos\bar{\varphi}_T\bar{x}_2+2\cos\bar{\varphi}_1)}\right], \tag{3.32}$$

with

$$a_1=(\bar{k}_{y1}\sin\bar{\varphi}_T-B\cos\bar{\varphi}_T),\ a_{20}=(\bar{k}_{y1}\cos\bar{\varphi}_T+B\sin\bar{\varphi}_T) \text{ and } a_3=2(\bar{k}_{y1}\sin\bar{\varphi}_1-B\cos\bar{\varphi}_1),$$

for $B=(\mu M_{x1}-\kappa)$. In Eq.(3.32), the transposed leading-edge contribution is split into three terms $\tilde{\ell}_1=\tilde{\ell}_{10}+\tilde{\ell}_{1+}+\tilde{\ell}_{1-}$, each of which is characterized by a different wavenumber in the direction of $\bar{y}_2$, namely a_{20}, $a_{2+}=a_{20}+(\sin\bar{\varphi}_T)/2$ and $a_{2-}=a_{20}-(\sin\bar{\varphi}_T)/2$.

3.2.2 Trailing-Edge Corrections

Schwarzschild's theorem is now applied independently to each of the three leading-edge contributions. For $\tilde{\ell}_{10}$ the transformed pressure is defined in the Prandtl-Glauert plane by

$$\mathcal{P}'_{10}=\frac{\tilde{\ell}_{10}}{2}e^{i\frac{M_{x2}^2\bar{k}_{x2}}{\beta_{x2}^2}\bar{x}_2}, \tag{3.33}$$

so that the corresponding trailing-edge correction $\mathcal{P}'_{20}$ will verify the governing equation

$$\frac{\partial^2\mathcal{P}'_{20}}{\partial\bar{x}_2^2}+\frac{\partial^2\mathcal{P}'_{20}}{\partial\bar{z}^2}+\hat{\kappa}_0^2\mathcal{P}'_{20}=0 \tag{3.34}$$

and satisfy the boundary conditions

$$\begin{aligned} \mathcal{P}'_{20}(\bar{x}_2,0)|_{\bar{z}=0} &= -\mathcal{P}'_{10}(\bar{x}_2,0) \qquad \text{for} \qquad \bar{x}_2 > 0 \\ \frac{\partial \mathcal{P}'_{20}}{\partial \bar{z}}|_{\bar{z}=0} &= 0 \qquad \text{for} \qquad \bar{x}_2 < 0 \end{aligned}, \tag{3.35}$$

where $\bar{z}$ is the non-dimensional coordinate in the direction perpendicular to the segment and

$$\hat{\kappa}_0 = \frac{1}{\beta_{x2}} \left[\frac{(b\omega/c_0 + a_{20}M_{y2})^2}{\beta_{x2}^2} - a_{20}^2 \right]^{1/2}.$$

M_{x2} represents the convection Mach number in the x_2 direction, $\beta_{x2}^2 = 1 - M_{x2}^2$ and M_{y2} represents the transverse Mach number component, defined positive in the negative direction of y_2. Schwarzschild's theorem provides the solution of Eqs.(3.33) and (3.35), which leads to the first trailing-edge term as

$$\tilde{\ell}_{20}(\bar{x}_2,\bar{y}_2) = \frac{2\rho_0 U_{x1}\tilde{w}e^{i(a_1\bar{x}_2 + a_{20}\bar{y}_2 + a_3 + \pi/4)}}{\sqrt{\pi(\bar{k}_{x1} + {\beta_{x1}}^2\kappa)(2\cos\bar{\varphi}_1)}} \times \{1 - (i+1)E^*[\bar{x}_2(\hat{\kappa}_0 + A_0)]\}, \tag{3.36}$$

where

$$A_0 = a_1 + \frac{M_{x2}}{\beta_{x2}^2}(b\omega/c_0 + a_{20}M_{y2}).$$

The formulae for the other two correcting terms are found by replacing a_{20} with a_{2+} or a_{2-}, and by multiplying the result by the amplitude factor $C_\pm = \pm 1/(4i\cos\bar{\varphi}_1)$. The total unsteady lift on the trapezoid surface is given by $\tilde{\ell} = \tilde{\ell}_1 + \tilde{\ell}_2$, where $\tilde{\ell}_2$ is the sum of the three trailing-edge terms. An example of unsteady lift distribution obtained for a trapezoidal segment interacting with a skewed sinusoidal gust is depicted in Fig. 3.7. The comparison between the leading edge contribution (white sheet) and the total unsteady lift (colored sheet), shows how the Kutta-condition corrective terms cancel the loading at the trailing-edge location and induce interferences upstream along the chord.

3.2.3 Assessment of Segment Shape on Unsteady Lift Distribution

The sensitivity of loading distribution to segment leading-edge sweep and non-parallel trailing edge is now evaluated. To achieve an independent analysis of these parameters, the studied

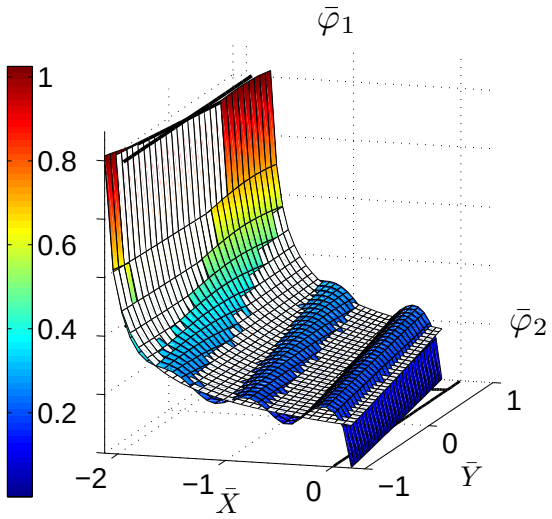

Figure 3.7: *Sample result for a sinusoidal gust interacting with a trapezoidal segment. Unsteady lift module normalized by its maximum value, at* $\bar{x}_1 = -1.99$*. White sheet: leading-edge term. Colored sheet: total unsteady lift corrected by the trailing-edge terms.* $\bar{\varphi}_1 = 10°$*,* $\bar{\varphi}_2 = 10°$*, aspect ratio (mid-span)* $L/c = 1$*,* $k_a c = 7.5$*, convection velocity* $U_0 = 150m/s$*, parallel to the segment chord. Gust wavefronts perpendicular to the convection velocity.*

segments will naturally feature swept parallelograms and swept trapezoids. The response of the canonical rectangular segment is also considered as reference, for completeness. Two gust inclinations are chosen for this study, the other parameters of the interaction being constant.

First, the gust wavefronts are chosen parallel to the rectangle leading-edge. The resulting interactions are depicted in Fig. 3.8(a). The interaction with the rectangular segment corresponds to the compressible one-dimensional theory, which is the current capability of most analytical schemes for the noise prediction of rotating machines. The comparison with the swept segment responses shows the strong influence of leading-edge sweep on the loading distribution and therefore the importance of including skewed gusts in the noise source prediction. The relevance of including subcritical interactions, which are exclusively produced by skewed gusts, has already been stressed in literature. For instance, Moreau *et. al* showed that for a NACA0012 airfoil embedded in a turbulent flow, subcritical interactions dominate noise radiation away from the normal direction to the airfoil, particularly at low frequencies [89]. As explained later on in Sec. 4.1.2, the potential induced by subcritical gusts on a rectangular segment is solely due to

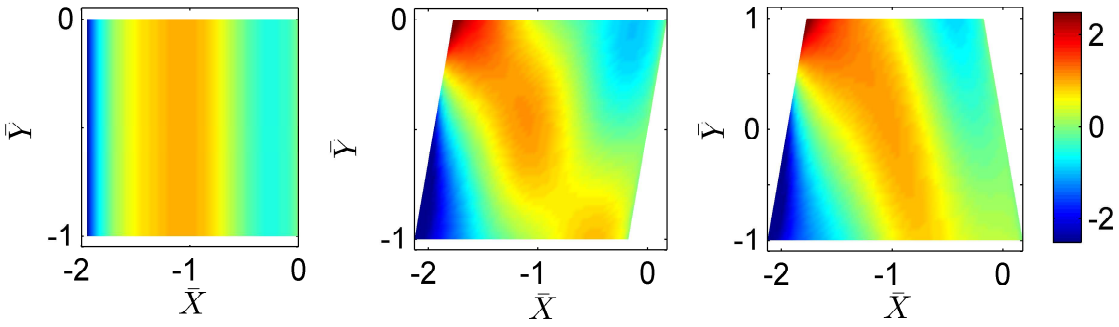

(a) Gust wavefronts parallel to the rectangular segment.

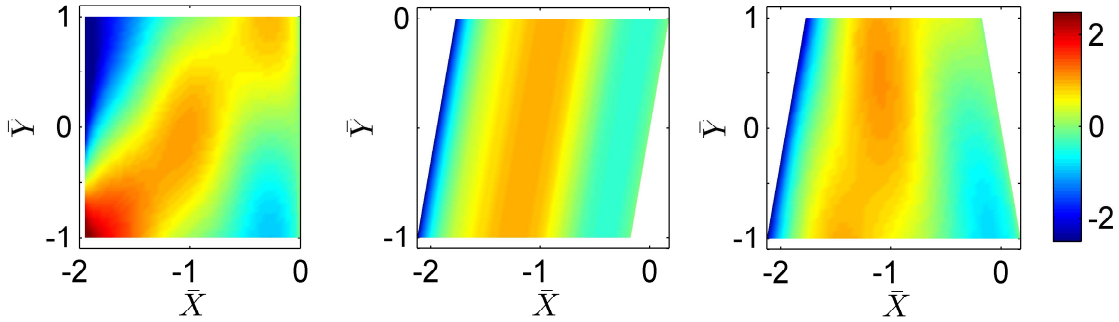

(b) Gust wavefronts parallel to the swept segments.

Figure 3.8: *Unsteady loading distribution due to interaction with a Fourier gust. The convection velocity is aligned with the direction of $\bar{X}$. The sources on (a) will produce the acoustic lobes in Figs. 4.7(a) and 4.7(c), whereas the sources on (b) the lobes in Figs. 4.7(b) and 4.7(d). Parameters of the simulation: $\bar{\varphi}_1 = 10°$, $\bar{\varphi}_2 = \pm 10°$, aspect ratio (mid-span) $L/c = 1$, $k_a c = 7.5$, $M_x = 0.44$.*

the finiteness of the segment span-ratio. Later on, Roger showed that, for the case of a circular ring interacting with a turbulent flow, subcritical gusts dominate the noise radiation at low frequencies both close and away to the normal to the local airfoil [90].

Now, notice the difference between the parallelogram and the trapezoid responses, which is solely due to the different trailing-edge obliqueness. The effect, noticeable for more than a half of the segment surface, illustrates the improvement in the blade geometry representation

expected from the theory extension proposed herein. The noise source difference on the three segments studied for this interaction will produce noticeable differences in the radiated noise, as depicted in Figs. 4.7(a) and 4.7(c), analyzed later on in Chapter 4.

A second test is carried out for gust wavefronts parallel to the leading-edge of the swept segments, in Fig. 3.8(b). In this case, the rectangular segment presents an oblique loading distribution, whereas on the parallelogram the loadings feature isovalue lines parallel to the segment edges. The response of the trapezoid differs once again from that of the parallelogram. The oblique Kutta condition spoils the loading symmetry imposed by the leading-edge singularity and induces a shifted lift amplitude towards the negative $\bar{Y}$. As a result, the acoustic lobes will present a different inclination for each segment, as will be depicted in Fig. 4.7(d).

3.3 Application to Rear-Rotor Blades

The unsteady loading on the rotor blades is now approximated by using a procedure based on the theory of Sec. 3.2. The blade geometry is decomposed in radial segments subsequently assimilated to flat trapezoids in unwrapped coordinates, in order to define an equivalent gust-segment interaction problem for each radial strip. The loading thereby obtained must be correctly phased from one segment to the others, for the sake of reproducing a continuous and expectedly accurate lift distribution over the blade surface. Now, since an approximate problem is formulated for each segment, specifically by assuming uniform aerodynamic variables between two radial cuts, the wall-pressure found with this method will be discontinuous at the segment boundaries. An interpolation is proposed to eliminate the discontinuities. Finally, the loadings are back-projected on the blade mean-camber surface for acoustic radiation concerns.

The purpose of this section is to detail the aforementioned steps. First, the technique used to represent a numerical blade geometry with a set of flat trapezoids in which the extended Amiet's technique applies, is exposed in detail. Afterwards, the use of the obtained loadings to approximate the blade response is outlined. Finally, the methodology convergence to the blade radial segmentation and meshing is presented.

3.3.1 Geometry Approximation

An industrial blade geometry is usually stored in a Computer-Aided Design (CAD) file, with an irregular surface meshing. The adaptation of such set of scattered points, identified with the CAD coordinates $(\hat{x}, \hat{y}, \hat{z})$, to the analytical approach for loading computation presented in this chapter requires a computational strategy, summarized as follows

1. Interpolate the blade pressure and suction sides into regular radial cuts.
2. Unwrap the radial blade profiles and find for each of them the mean-camber line so as to define, profile by profile, the blade Mean-Camber Surface (MCS).
3. Decompose the blade MCS into extended radial segments and find the best interpolation plane fitting the leading-edge region.
4. Project each segment upon its corresponding approximation plane and determine the flat trapezoid to be used in extended Amiet's approach.

Cylindrical Interpolation of the Blade CAD Geometry

The interpolation radial domain is limited by the minimum and maximum radial values at which the blade can be cut from edge to edge, the cutting line laying always on the blade surface. This corresponds typically to the radial extent of the blade leading-edge. Once the number of radial cuts is defined, the radial values at which the interpolated blade coordinates will pile become a known parameter of the problem.

The blade surface is then limited, at each radius, by two circumferential angles $(\varphi_{LE}, \varphi_{TE})$, corresponding to the leading-edge and trailing-edge positions, respectively. The determination of these angles requires the blade edges interpolation on the desired radial values. The researched coordinates, say for the leading-edge, (y'_{LE}, z'_{LE}) must verify the circle equation at the interpolation radius R_0 and the linear interpolation from the closest two points in the leading-edge line, $(\hat{y}_A, \hat{z}_A)$ and $(\hat{y}_B, \hat{z}_B)$. These considerations lead to the equation system

$$\begin{cases} R_0^2 = {y'_{LE}}^2 + {z'_{LE}}^2 \\ z'_{LE} = c_1 + c_2 y'_{LE} \end{cases}, \tag{3.37}$$

with $c_1 = (\hat{z}_A\hat{y}_B - \hat{z}_B\hat{y}_A)/(\hat{y}_B - \hat{y}_A)$ and $c_2 = (\hat{z}_B - \hat{z}_A)/(\hat{y}_B - \hat{y}_A)$. The physical solution of this system provides the interpolated leading-edge coordinates. The same procedure is then applied to find the trailing-edge interpolated coordinates.

Blade pressure and suction sides are then discretized in the angular domain, from which one obtains the interpolated blade coordinates (y', z'). Now, the axial coordinate x' is determined for each blade side, independently. The hypothesis to determine x' is that the interpolated point lays on the plane defined by the three closest points of the corresponding CAD blade side. To do so, the planar distance, involving the known coordinates (y', z'), between the interpolation point and each of the CAD points is computed. The three closest points are labeled as $(\hat{x}_1, \hat{y}_1, \hat{z}_1)$, $(\hat{x}_2, \hat{y}_2, \hat{z}_2)$ and $(\hat{x}_3, \hat{y}_3, \hat{z}_3)$, so that the vector perpendicular to the plane defined by these points is given by

$$\mathbf{n} = \mathbf{V_{12}} \wedge \mathbf{V_{23}} = \begin{vmatrix} (\hat{y}_2 - \hat{y}_1)(\hat{z}_3 - \hat{z}_2) - (\hat{y}_3 - \hat{y}_2)(\hat{z}_2 - \hat{z}_1) \\ (\hat{x}_3 - \hat{x}_2)(\hat{z}_2 - \hat{z}_1) - (\hat{x}_2 - \hat{x}_1)(\hat{z}_3 - \hat{z}_2) \\ (\hat{x}_2 - \hat{x}_1)(\hat{y}_3 - \hat{y}_2) - (\hat{x}_3 - \hat{x}_2)(\hat{y}_2 - \hat{y}_1) \end{vmatrix} = \begin{vmatrix} n_x \\ n_y \\ n_z \end{vmatrix}, \tag{3.38}$$

whereas the vector defined by the interpolation point with one of the points on the plane, for instance the first point, is given by

$$\mathbf{V_{01}} \begin{vmatrix} (\hat{x}_1 - x') \\ (\hat{y}_1 - y') \\ (\hat{z}_1 - z') \end{vmatrix}.$$

The interpolation point lays in the aforementioned plane only if $\mathbf{n} \cdot \mathbf{V_{01}} = 0$, from which is found the interpolated axial value

$$x' = \hat{x}_1 + \frac{n_y}{n_x}(\hat{y}_1 - y') + \frac{n_z}{n_x}(\hat{z}_1 - z'). \tag{3.39}$$

This "cylindrical interpolation" procedure is used to find the blade cross-section airfoil as the intersection of the blade surface with the cylinder of radius R_0.

Blade MCS definition

Each airfoil, after being unwrapped, is expressed in a reference frame in which the abscissa is aligned with its chord line. In this frame, the airfoil mean-camber line is defined as the line containing the mean value of the pressure and suction side ordinates. The locus of mean-camber lines, expressed in the original coordinate system, produces the blade MCS.

Approximation of the Blade MCS with a set of flat trapezoids

The blade MCS is now decomposed in extended radial strips. For each strip, an approximation plane is found using a standard Least-Mean Square (LMS) interpolation procedure. Since the aerodynamic interaction is very sensitive to the segment sweep, and since the obtained loadings are concentrated in the leading-edge region (especially at high frequencies), we chose to interpolate only the leading-edge vicinity of each MCS strip (15% of the chord value for each radial segment). The MCS radial segments are subsequently projected on their corresponding approximation planes.

Each plane is characterized by a centroid point and a normal vector, from which an orthonormal basis and a local coordinate system are defined. The corresponding MCS strip is subsequently expressed in these plane local coordinates. The surface projection is achieved by equaling the strip coordinate in the direction normal to the plane to zero, so that all the projected points lay on the plane surface. The obtained projection is approximated by a flat trapezoid by fitting its edges with straight lines. Using the inverse passage matrix, the trapezoids are expressed in the global coordinates for the interaction simulation.

The methodology steps are depicted in Fig. 3.9. An industrial CAD blade geometry is compared with the blade MCS in Fig. 3.9(a). Note that the original CAD profiles do not pile in radial lines, which justifies the application of the cylindrical interpolation procedure. In Fig. 3.9(b) is depicted the same MCS, on which an extended radial segment is defined between two radial cuts. The segment is compared in Fig. 3.9(c) with its projection on the leading-edge interpolation plane, in unwrapped coordinates. The upper view shows the segment projection fitted with an equivalent trapezoid, whereas the lower view emphasizes the fact that the plane is interpolated from the leading-edge region and provides a poor trailing-edge fitting. Finally, in Fig. 3.9(d) is shown the blade MCS and its approximation in flat trapezoids on which the unsteady loadings can be computed.

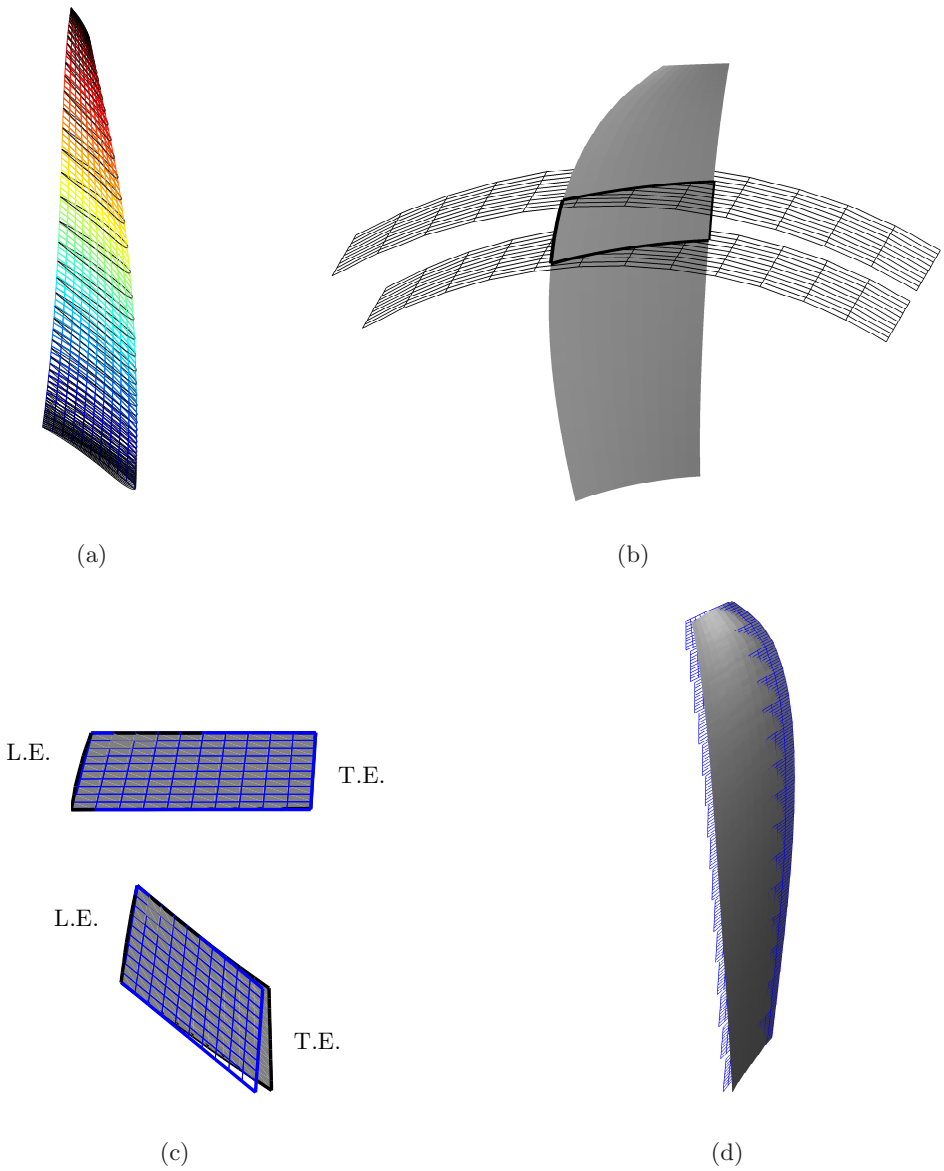

Figure 3.9: *Blade Geometry approximation procedure. (a) CAD geometry of an industrial geometry (black profiles) compared with the blade MCS (colored surface). (b) Definition of an extended radial segment from the blade MCS. (c) Radial segment in unwrapped coordinates and its projection on the interpolation plane on two different views. (d) Blade MCS and its final approximation with flat trapezoids, for loading computation.*

3.3.2 Blade Loading Approximation

This section details the procedure to approximate the induced unsteady loading over the rear-rotor blade MCS. The source approximation on the blade surface is divided in three steps. First, the gust wavenumbers, defined with angular and radial components, need to be projected on the principal directions of the corresponding trapezoid. Secondly, the loading singularity at the segment leading-edge is approximated by a finite value, using an exact analytical integration on leading-edge lattices featuring swept parallelograms. Finally, the loading obtained for each segment is phased from each strip to the others, in order to provide the final source distribution.

Gust Wavenumber Projection

The Fourier description of the upwash, given in Secs. 2.3.2 or 2.4.2, is adapted here to the gust-segment problem defined in Sec. 3.2. Gust wavenumbers, defined with angular and radial components, are now projected on the principal directions of the trapezoid leading-edge ($\mathbf{e_{x_1}}, \mathbf{e_{y_1}} \equiv \mathbf{e}_\eta$) associated respectively with the coordinates $(\bar{x}_1, \bar{y}_1)$. The upwash amplitude, which accounts already for projection on the leading-edge normal direction, is unchanged in this process. Let us define two new vectors ($\mathbf{e}_\xi, \mathbf{e_{rp}}$) aligned with the trapezoid chordwise direction and with the projection of the radial direction on the segment surface, respectively.

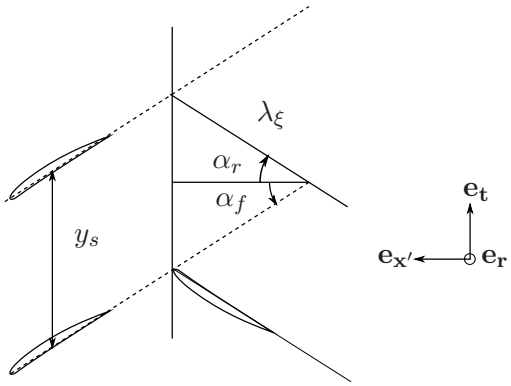

Figure 3.10: *Definition of the wavelength in the trapezoid chord direction λ_ξ. The angles are positive as depicted.*

The wake-interaction with a radial blade segment will be characterized by the aerodynamic values at its mid-span. The gust chordwise wavelength λ_ξ is found from the projection tangential component of the wavelength on the direction defined by $\mathbf{e}_\xi$. This value depends on the

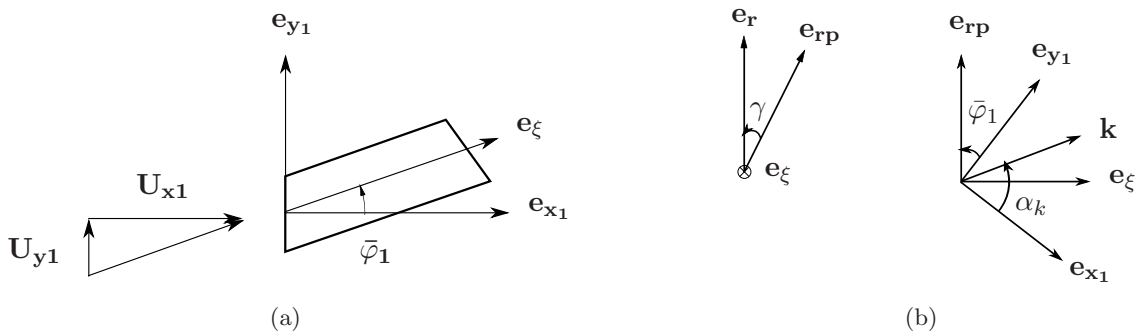

Figure 3.11: *Rear rotor segment principal directions.*

inclination of the wake centerline, assumed to follow the front-rotor airfoil chord at an angle α_f from the rotation axis $\mathbf{e_{x'}}$, and on the rear-rotor segment inclination to the same axis, defined by α_r. From an inspection of Fig. 3.10 one finds that

$$y_s = \lambda_\xi(\sin\alpha_r + \cos\alpha_r \tan\alpha_f),$$

from which

$$\lambda_\xi = \frac{y_s \cos\alpha_f}{\sin(\alpha_f + \alpha_r)}. \tag{3.40}$$

The rear-blade trapezoidal segments present an inclination with respect to the radial direction, defined by the lean angle γ. From Fig. 3.11(b) one finds that the projection of the radial wavelength on the trapezoid plane is given by $\lambda_{rp} = \lambda_r / \cos\gamma$. The projection of $(\mathbf{e_\xi}, \mathbf{e_{rp}})$ on $(\mathbf{e_{x_1}}, \mathbf{e_{y_1}})$ leads to the aerodynamic wavenumber components on the leading-edge principal directions

$$\begin{cases} \bar{k}_{x1} = k_\xi \cos\bar{\varphi}_1 - k_{rp} \sin\bar{\varphi}_1 \\ \bar{k}_{y1} = k_\xi \sin\bar{\varphi}_1 + k_{rp} \cos\bar{\varphi}_1 \end{cases}, \tag{3.41}$$

where $k_\xi = 2\pi/\lambda_\xi$ and $k_{rp} = k_r \cos\gamma$.

The time needed by the rear-rotor segment to cover the distance y_s equals the time needed by the wake projection, on the $\mathbf{e_\xi}$ direction, to cover the distance λ_ξ. It follows that

$$U_0 = (\Omega_1 + \Omega_2) r_m \frac{\lambda_\xi}{y_s}, \tag{3.42}$$

where $U_0 = \|\mathbf{U_0}\|$, is the equivalent velocity convection. The interaction with a gust defined by the wavenumbers $(k\gamma_y, nk_r)$, is characterized by the interaction frequency ω_s, found from Eq.(3.5)

$$\omega_s = k k_\xi U_0 = k B_1 (\Omega_1 + \Omega_2), \tag{3.43}$$

which depends only on the tangential order k. This value corresponds to the frequency in the frame attached to the segment which differs from the radiated frequency for the case of rotating segments, as detailed later in Sec. 4.2.1.

Loading Analytical Integration for the Leading-Edge Lattice

The loading singularity at the segment leading-edge must be reduced to a finite value for the final noise source definition. The strength of the leading-edge dipoles can be found by integrating Eq.(3.30) on parallelogram-shaped lattices of elementary surface $\Delta S = \epsilon \Delta g$, where ϵ and Δg are the lattice span and chord. The integration on a lattice located at $(\bar{x}_1 = -2, \bar{y}_1 = g)$ can be put in the form

$$F_{\Delta S} = \frac{1}{\tau} \int_{-2\tau}^{(\epsilon-2)\tau} \int_{g-\Delta g/2}^{g+\Delta g/2} \tilde{\ell}(\xi^*, \eta^*) d\xi^* d\eta^*, \tag{3.44}$$

where $\tau = 1/\cos\bar{\varphi}_1$ and (ξ^*, η^*) are the non-dimensional principal directions of the parallelogram, given by $\xi^* = (\bar{x}_1 + 1)\tau$ and $\eta^* = \bar{y}_1 - (\bar{x}_1 + 2)\tan\bar{\varphi}_1$. Using these variables, the source strength on the leading-edge lattice is given by

$$F_{\Delta S} = \frac{1}{\tau} \frac{-2\rho_0 U_{x1} \tilde{w} e^{i\pi/4}}{\sqrt{\pi(\bar{k}_{x1} + {\beta_{x1}}^2 \kappa)}} \int_{-\tau}^{(\epsilon-1)\tau} \frac{e^{iD(\xi^*/\tau+1)}}{(\xi^*/\tau + 1)} d\xi^* \int_{g-\Delta g/2}^{g+\Delta g/2} e^{i\bar{k}_{y1}\eta^*} d\eta^*, \tag{3.45}$$

with $D = \bar{k}_{y1}\tan\bar{\varphi}_1 - B$. The change of variable $\chi = D(\xi^*/\tau + 1)$ is now made to put into evidence the Fresnel integral over ξ^*, which leads to the result

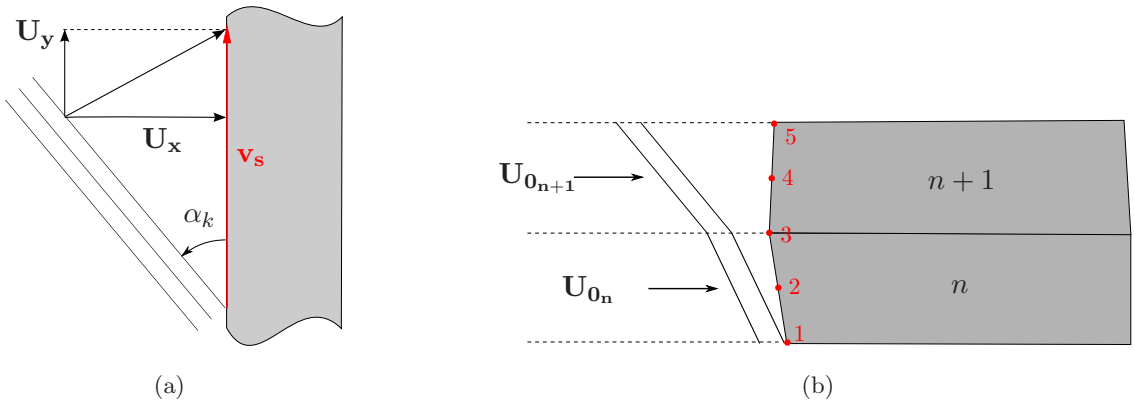

Figure 3.12: *Sweep velocity definition. (a) General case of a skewed gust convected at an oblique velocity with respect to an infinite-span airfoil. (b) Phasing of the responses of two successive blade segments.*

$$F_{\Delta S} = \frac{-2\sqrt{2}\rho_0 U_{x1}\tilde{w}e^{i\pi/4}\Delta g}{\sqrt{(k_{x1}+\beta_{x1}^2\kappa)}}\frac{E[\epsilon D]}{\sqrt{D}}\left\{\mathrm{sinc}(\bar{k}_{y1}\Delta g/2)e^{i\bar{k}_{y1}(g+\Delta g/2)}\right\}, \tag{3.46}$$

where $\mathrm{sinc}(x)$ denotes the sine cardinal function $\sin x/x$. The source on the remaining surface of the segment is found from numerical integration using standard quadrature.

Strip Phasing Strategy

Since the loading is computed independently for each blade segment, a phasing of the obtained responses is needed to provide the source distribution. The phase lag $\Delta\vartheta$ to be imposed to the response of two segments is proportional to the time Δt needed by the excitation to travel from one segment to the other. This value is naturally linked to the velocity v_s at which the excitation "sweeps" the blade leading-edge, referred to as the *sweep velocity* in Sec. 2.3.1. For the case of a sinusoidal gust the sweep velocity value depends on the velocity convection components and on the angle α_k of the wavefronts relative to the segment leading-edge, as depicted in Fig. 3.12(a). Using the notations of Sec. 3.1, the gust sweep velocity is expressed as

$$v_s = \frac{U_x}{\tan\alpha_k} + U_y = \frac{\omega}{k_2}. \tag{3.47}$$

The loading phasing over the blade surface can be determined by using Eq.(3.47). In

Fig. 4.5(b) are depicted two blade segments for which a different interaction problem is formulated. The phase lag at each segment extremities, represented here by $\Delta\vartheta_{13}$ and $\Delta\vartheta_{35}$, is determined by the loading spanwise variation for each interaction case. For the segment n we have, *in trapezoid notations* ($k_2 \equiv \bar{k}_{y1}$), that $\Delta\vartheta_{13} = \bar{k}_{y1_n} l_{LE_n}$, where l_{LE_n} is the segment leading-edge length. Introducing Eq.(3.47) into this result provides $\Delta\vartheta_{13} = \omega\Delta t_n$, where $\Delta t_n = l_{LE_n}/v_{sn}$. This shows that the spanwise phase variation can be determined from an equivalent time delay and, therefore, that the present strategy of source phasing is consistent with the theory.

Now, notice that for the interaction problem in Sec. 3.2, the loading phase equals $\pi/4$ at the leading-edge at mid span *independently of the wavenumber components*. For this reason, this point becomes the reference for the application of the phase lag to relate the segment responses. For two successive segments, as depicted in Fig. 3.12(b), the source time delay to be applied is given by

$$\Delta t_{24} = 0.5 \left(\frac{l_{LEn}}{V_{sn}} + \frac{l_{LEn+1}}{V_{sn+1}} \right). \tag{3.48}$$

The value given in Eq.(3.48) will not be applied to each loading component but to the total response of the segment. For this reason, the value V_{sn} in Eq.(3.48) denotes the sweep velocity of the total aerodynamic excitation, found from the inclination of the wake center-sheet (an example of which is shown in Fig. 2.8(a)), the relative angular velocity and the rear-rotor leading-edge sweep. This value is used as reference to phase all the loading components on the segment.

3.3.3 Methodology Convergence

The sensitivity of the blade response model to the blade meshing and radial segmentation is now evaluated. First, the integrated unsteady loading convergence is assessed as a function of the number of chordwise lattices. The goal is to observe the representation of the chordwise non-compactness and to assess the analytical integration on the leading-edge cell. In Fig. 3.13(a) is shown the chordwise distribution at mid-span of the first loading harmonic for a realistic CROR wake-interaction. The integration is carried out on 10, 60 and 100 lattices covering the chord length. The analytical leading-edge integration provides results that are consistent with the numerical result on the remaining cells. The rapid decay of the loading amplitude in

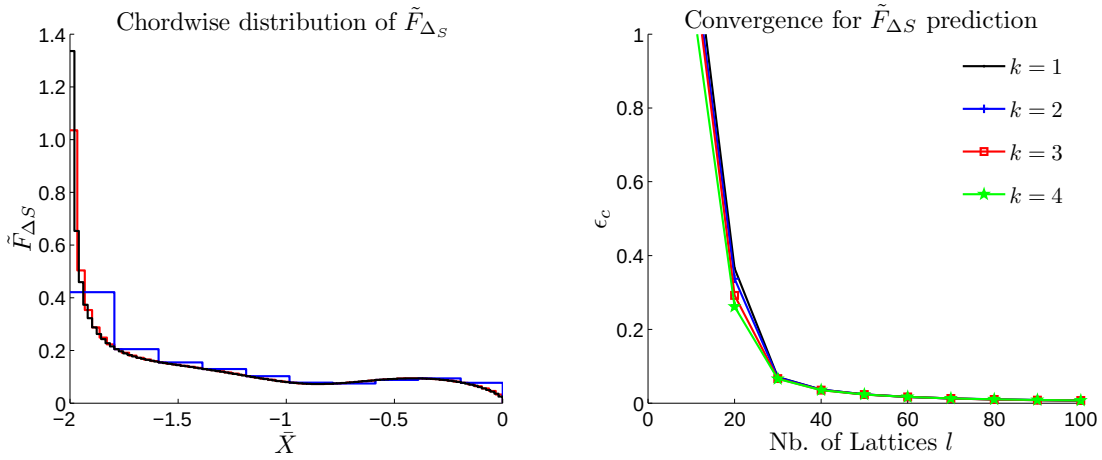

(a) (b)

Figure 3.13: *Convergence of the integrated unsteady loading. (a) Chordwise loading distribution for the first loading harmonic $k = 1$. The integration on the first lattice (from $\bar{X} = -2$) is performed analytically, using Eq.(3.46). The integration on the remaining chord distance is preformed numerically. Arbitrary units. Blue line: 10 lattices. Red line: 60 lattices. Black line: 100 lattices. (b) Convergence of the prediction for the first four harmonics.*

the leading-edge region is not captured with the coarser mesh of 10 cells, whereas the 60 and 100 cells meshes converge in the prediction of such behavior. The convergence of the loading prediction is depicted in Fig. 3.13(b) for the first four loading harmonics of the same interaction, as a function of chordwise discretization. The convergence error is computed on the blade MCS in order to assess the convergence of the total source distribution. The blade discretization in the chordwise goes from 1 to 100 lattices by steps of 10. Each meshing can be assimilated as a n-iteration whose result is compared with that of the precedent iteration using the convergence error

$$\epsilon_c = \left[\frac{1}{l} \frac{\sum_\nu (\tilde{F}_{(n)_\nu} - \tilde{F}_{(n-1)_\nu})^2}{\sum_\nu \tilde{F}^2_{(n)_\nu}} \right]^{1/2}, \tag{3.49}$$

where l is the number of chordwise lattices and ν is the lattice index, covering the entire blade surface. The results of the first four loading harmonics are found to converge for values of $\epsilon_c \approx 1\%$ for 60 cells in the chordwise direction. For this reason, this lattice quantity becomes

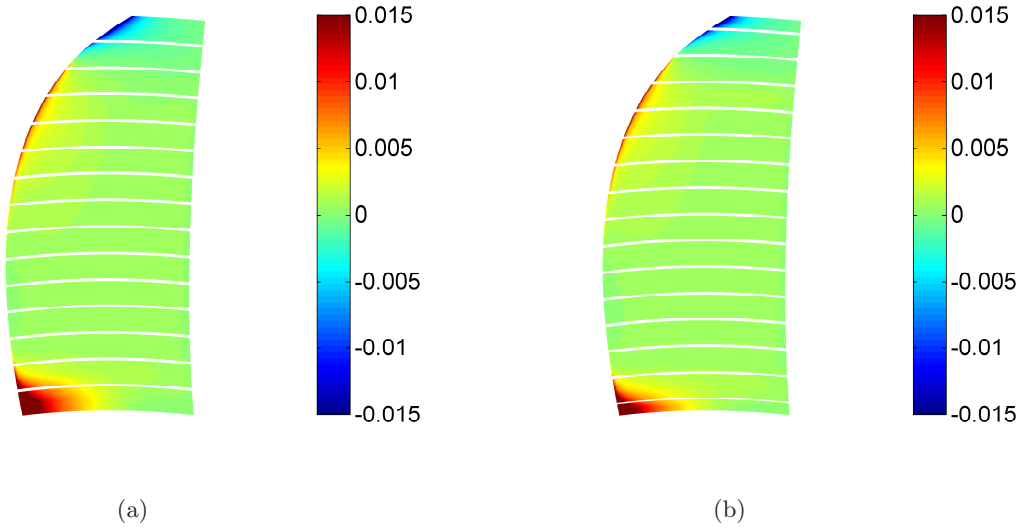

(a) (b)

Figure 3.14: *Sensitivity of the blade response model to the radial segmentation. Real part of the non-dimensional pressure jump $\tilde{\ell}/p_\infty$. Loading harmonic $k = 1$. CFD wake input. (a) Regular blade segmentation. (b) Shifted blade segmentation.*

the reference for future computations. The impact of the chordwise meshing on the noise prediction is evaluated further in Sec. 5.3, once the radiation scheme is defined and validated.

The effect of the radial blade segmentation is now assessed using as input the CFD upwash of Fig. 2.11, chosen for its concentrated hub excitation. The objective is to assess the model capability of predicting localized loadings and the sensitivity of this result to the definition of the blade radial segments, for the same spanwise meshing. To ascertain this effect, the blade radial segments are defined with two topologies. First, a regular cutting is tested, providing radial segments of same height. Secondly, a shifted cutting is defined, in which the first and the last segments radially extend over half a segment span of the first topology, whereas the remaining segments have the same extent. By doing so, the segments boundaries are located at half-span of the first topology, as shown in Fig. 3.14, but numbers of segments are the same. Here the first loading harmonic is depicted. The concentrated excitation in the hub region is reproduced in both cases. However, the shifted cutting predicts a more concentrated excitation, suggesting that a refined segment cutting could be needed near the hub, for reaching convergence. The loading distribution on the remaining surface is very similar for both cases, proving the robustness of the methodology.

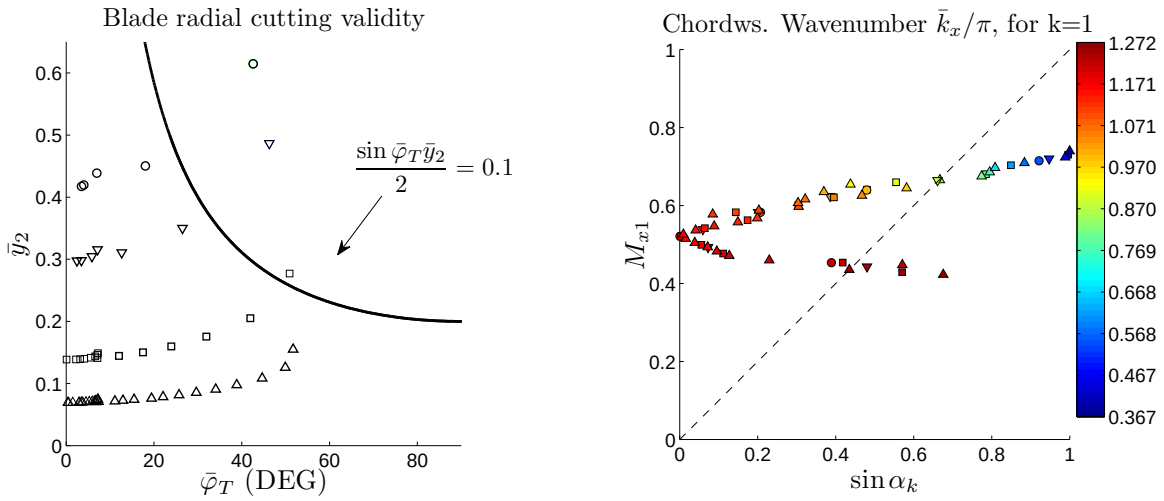

(a) (b)

Figure 3.15: *Blade segments characterization for different cuttings. ○: 5 segments, ▽: 7 segments, □: 15 segments, △: 30 segments. (a) Validity of the segment geometry. (b) Interaction characteristics for the first loading harmonic $k = 1$. Values of $\bar{k}_x/\pi$ as color scale.*

The source convergence to the number of radial cuts is now studied for a regular blade segmentation going from 5 to 30 segments. The resulting flat trapezoids must first satisfy a low aspect-ratio criterion for the application of the theory extension developed in Sec. 3.2. To assess this property, the trapezoids pertaining to each blade cutting are represented in the plane of the segment characteristics, in which the abscissa represents the value of $\sin\bar{\varphi}_T$ whereas the ordinate represents the maximum value of $\bar{y}_2$ of the trapezoid, as shown in Fig. 3.15(a). The theory is believed to apply for the segments laying under the black curve, using the theoretical threshold $\frac{\sin\bar{\varphi}_T\bar{y}_2}{2} < 0.1$. The high sweep in the tip region imposes a fine regular cutting. For an accurate tip region representation, it is necessary to have at least 17 radial segments. This value is taken as the reference for further computations. Now, the relevance of using the theory extension for trapezoids on the present case is assessed by identifying the value M_x^* for the interaction problem of each blade segment. As the flight conditions are known for the geometry under study, we are able to locate each interaction in the same plane as in Figs. 3.3 and 3.4. This is useful to assess the trailing-edge effect on the source distribution for a given wake harmonic, and thus the pertinence of taking into account the trailing-edge obliqueness. In Fig. 3.15(b) is shown such a plot for the first front-rotor wake component ($k = 1$). The gust non-dimensional

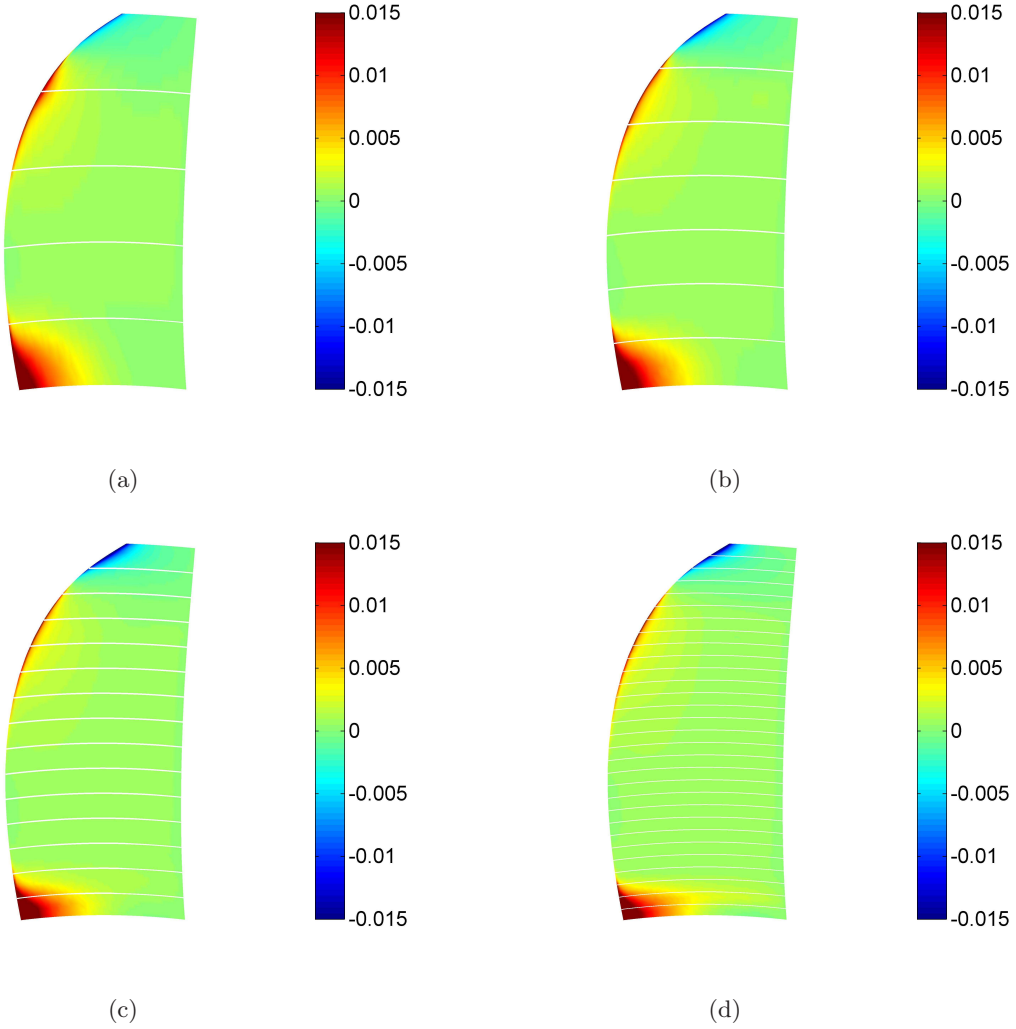

Figure 3.16: *Convergence of blade loading prediction for different radial blade segmentations, the white line denoting the segment boundaries. Real part of the non-dimensional pressure jump $\tilde{\ell}/p_\infty$. Chorochronic wake input, $k = 1$. (a) 5 radial cuts. (b) 7 radial cuts. (c) 15 radial cuts. (d) 30 radial cuts.*

wavenumber in the direction $\bar{y}_1$ varies from 1.3π to 0.4π, for relative Mach numbers from 0.4 to 0.7, respectively. The values I_{te} for these interactions suggest that trailing-edge obliqueness should be included in the loading prediction for $k = 1$.

The comparison of the source distributions evaluated in this test is shown in Fig. 3.16. One striking conclusion is the model capability to predict the loading patterns even for the coarser

blade segmentation, which shows the advantage of defining the sweep as a continuous parameter for each segment. Some differences are however found in the prediction of the hub excitation. As the cutting gets finer, the excitation is predicted in a more concentrated region. Based on these results, we could suggest the creation of an adaptive blade cutting procedure in order to concentrate the blade segments in regions where localized phenomena are to be captured.

3.4 Conclusion

A procedure for getting a reliable approximation of the aerodynamic response of a rotor blade to wake impingement has been exposed in detail. The motivation is to provide an enhanced fast-tool routine, for blade aeroacoustic pre-design. The methodology is based on an extension of the standard gust-airfoil interaction problem formulated by Amiet in the high-frequency domain. As a preliminary analysis, the effect of the trailing-edge term on the total response of an infinite-span airfoil has been evaluated. It is shown that at high-frequencies one could neglect the trailing-edge effect, although its range of influence is found to be considerably larger than initially defined by Amiet. It is expected that the proposed theory extension, which is seen as an oblique Kutta condition, would apply at most in the same range of influence of the non-oblique Kutta condition. The relevance of this extension for the case of CROR noise has been evaluated by using an industrial blade geometry, for which numerical results are available at low-speed flight conditions. The actual CAD geometry is approximated by a set of flat trapezoids for which an equivalent interaction problem is defined for each incident wake Fourier component. Each interaction is located in the $(\sin\varphi_k, M_x^*)$ plane, for trailing-edge influence assessment. The extension is shown to apply, at least for the first loading harmonic of the interaction case studied in this chapter.

The phasing of the independently computed segment responses is achieved by considering the time lag of the excitation at the blade spanwise values of the blade segment boundaries. This time lag is found from the value of the excitation sweep velocity on the blade leading-edge and from the value of the segment leading-edge length. Also, the noise source definition requiring a finite value at the segment leading-edge, an analytical integration has been proposed on parallelogram-shaped lattices composing the leading-edge region. The methodology has been evaluated in terms of blade meshing and radial segmentation, from which its robustness and capability of representing the blade non-compactness have been evaluated.

APPENDIX

A3.1 Solution of the Schwarzschild integral

Eq.(3.16) can be reformulated as:

$$\Phi^{(1)}(y_1^*,\chi,0) = \frac{-b\tilde{w}e^{-i\kappa y_1^*}}{\pi\sqrt{k_1^{*2}+k_2^{*2}}}\sqrt{y_1^*}\int_0^\infty \chi^{-1/2}\left[\chi+y_1^*\right]^{-1} e^{-i\left(\kappa+k_1^*/\beta_x^2\right)}d\chi \tag{A3.1}$$

The integral of Eq. A3.1 can be solved by using tables of integrals, as the one presented by Abramowitz & Stegun [91]. The result

$$\int_0^\infty x^{\nu-1}(x+\beta)^{(-\nu-\frac{1}{2})}e^{-\mu x}dx = 2^\nu\Gamma(\nu)\beta^{-\frac{1}{2}}e^{\beta\frac{\mu}{2}}D_{-2\nu}(\sqrt{2\beta\mu}) \tag{A3.2}$$

is presented in this reference, for $\nu \in \Re$. In our case $\nu = 1/2$, $\mu = i(\kappa + k_1^*/\beta_x^2)$, $\beta = y_1^*$, and $x = \chi$, so we have $\Gamma(1/2) = \sqrt{\pi}$ and

$$D_{-1}(Z) = e^{Z^2/4}\sqrt{\pi/2}\left[1-U^0(Z/\sqrt{2})\right] \qquad \text{with} \qquad U^0(Z) = \frac{1}{\sqrt{\pi}}\int_0^{Z^2}\frac{e^{-t}}{\sqrt{t}}dt.$$

The insertion of these values in Eq.(A3.1) yields to

$$\Phi^{(1)}(y_1^*,0) = \frac{-b\tilde{w}}{\sqrt{k_1^{*2}+k_2^{*2}}}e^{i(k_1^*/\beta_x^2)y_1^*}\left(1-U^0\left[\sqrt{iy_1^*\left(\kappa+k_1^*/\beta_x^2\right)}\right]\right). \tag{A3.3}$$

The addition of this result with Eq.(3.15) provides directly Eq.(3.17).

Chapter 4

Acoustic Formulation for a Far-Field Observer

This chapter deals with the tonal noise produced by a CROR engine due to rotor-rotor interaction. A far-field formulation is developed for a compact lattice of the rear-rotor acting as an acoustic point dipole. With the present formulation, the noise source can be located on any reference surface of the blades, which represents an improvement of to the current CROR noise theories assuming non-cambered blades [13].

Since the noise source is determined by a methodology allowing an enhanced blade geometry representation, the present analysis starts by assessing noise sensitivity to segment shape. Prior to the study of rotating segments, the analysis addresses segments fixed with respect to the observer and embedded in a uniform flow.

The integration, on the segment surface, of the far-field noise produced by each dipole composing the source will provide the total acoustic field produced by the segment, in a procedure following the analysis pioneered by Amiet for rectangular segments interacting with turbulent flows [92]. The methodology is extended in Sec. 4.1.1 for swept segments featuring a parallelogram with upper and lower cuts aligned with the convective flow. Such a formulation represents an enhancement of the current capabilities of blade geometry representation.

The noise emitted from rotating segments is subsequently studied in Sec. 4.2. For this case, the acoustic pressure in the far-field is directly formulated for each rotating dipole as a

function of its force frequency content. For the prediction of rotor noise, the source is integrated numerically over the blade surface.

4.1 Acoustic Radiation from Stationary Flat Segments

The noise resulting from gust-airfoil interaction has been formulated by Amiet for fixed segments embedded in a uniform flow and interacting with sinusoidal gusts with two wavenumber components in the frame aligned with the segment chord [92]. The acoustic response of the segment is characterized by the chordwise integration of the noise produced by the dipoles composing the source. The result, referred to as the *radiation integral*, has been extensively studied for the case of rectangular segments whose chord is aligned with the convection velocity direction. Analytical expressions for the radiation integral have been proposed by Amiet [41], for the case of a compressible two dimensional Fourier gust interacting with a rectangular segment. The acoustic results found with this technique are in agreement with the results shown by Atassi using a semi-analytical method [93], who besides pointed out the reduced acoustic efficiency of skewed gusts. Lockard and Morris reproduced, with a full CAA computation, Atassi's results for a gust parallel to the leading edge and verified the linearity of the theory for a wide range of gust amplitudes [94].

As exposed above, noise radiation for rectangular segments has been formulated and validated with measurements and CAA computations. However, there has been little research on the noise emitted by segments featuring other shapes than a rectangle. There is not availability of analytical radiation integrals for segments featuring swept parallelograms or trapezoids which, as shown in Chapter 3, provide the best geometrical representation of a rotating blade segment. For this case, the result can still be found numerically but such a technique becomes prohibitive for perturbations rich in Fourier components.

4.1.1 Radiation Integral for Flat Parallelograms

In this section is derived the radiation integral for a fixed flat parallelogram embedded in a uniform flow parallel to its end-cuts. The segment unsteady loading is found from the infinite span segment formulations, presented in Sec. 3.1.2. The parallelogram surface is defined on the infinite span segment by following the convection velocity direction, as depicted in Fig. 4.1.

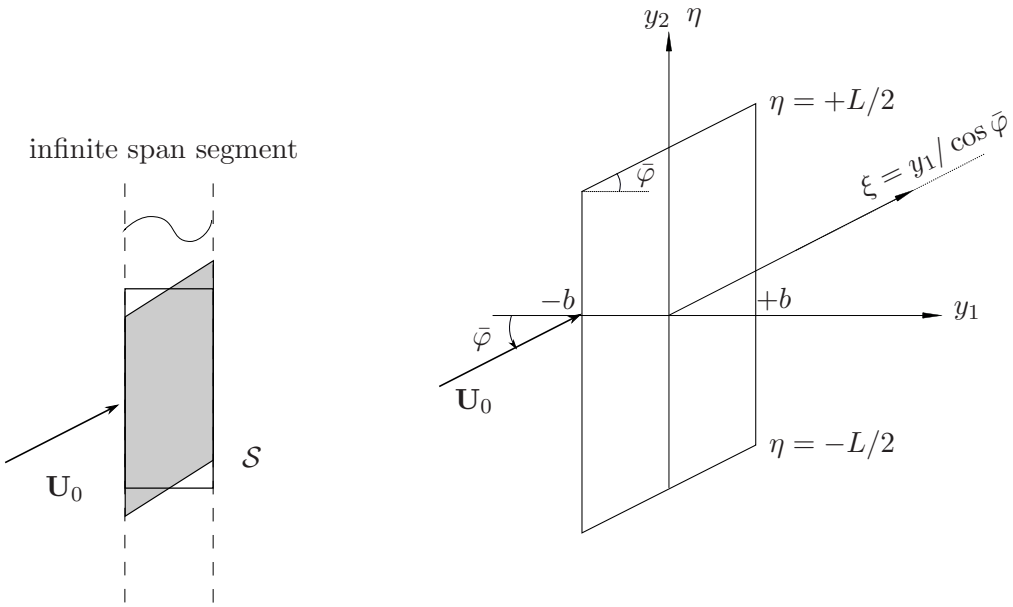

Figure 4.1: *Radiating parallelogram surface. Left : Comparison of baseline rectangular segment (white) with the proposed surface of integration (gray). The segments have the same surface $\mathcal{S}$. Right : Segment geometry.*

Observer and source coordinates, noted $\mathbf{x}$ and $\mathbf{y}$, are expressed in the reference frame associated to $\mathcal{B}_0 = (\mathbf{e_1}, \mathbf{e_2}, \mathbf{e_3})$, as defined in Sec. 3.1. The uniform flow, defined by $\mathbf{U}_0 = U_x\mathbf{e_1} + U_y\mathbf{e_2}$, presents an angle $\bar{\varphi}$ with respect to the segment leading-edge normal. The flat segment is located at $y_3 = 0$ and its normal vector is $\mathbf{e_3}$.

The sound field of the equivalent distributed dipoles on the segment verifies the non-homogeneous wave equation for linear acoustics

$$\left(\frac{1}{c_0^2}\frac{D^2}{Dt^2} - \Delta^2\right) dp(\mathbf{x}, t) = -\frac{\partial}{\partial y_i} dF_i(t'), \tag{4.1}$$

where dp is the acoustic contribution of a single point dipole of strength $d\mathbf{F}$, emitted at time t' and received at time t. By virtue of Green's theorem, and for the convected case studied here, the acoustic pressure is given by

$$dp(\mathbf{x}, t) = -\frac{1}{4\pi}\int_{t'} \frac{\partial}{\partial y_i}(dF_i)\frac{\delta(t - t' - R_e/c_0)}{R_s} dt', \tag{4.2}$$

where $R_s^2 = \beta_y^2 R_1^2 + \beta_x^2 R_2^2 + \beta_0^2 R_3^2$ and $R_e = \dfrac{1}{\beta_0^2}(R_s - M_x R_1 - M_y R_2)$, with $R_i = (x_i - y_i)$. The integration by parts of Eq.(4.2) leads directly to the pressure radiated by the dipole as a function of the spatial derivative [95]

$$dp(\mathbf{x},t) = \frac{1}{4\pi}\frac{\partial}{\partial x_i}\left[\frac{dF_i}{R_s}\right]_{t-R_e/c_0}, \tag{4.3}$$

where the squared bracket denotes evaluation in the source time. Using the permutation rules between spatial and time derivatives, given for example by Farassat [96], the far-field acoustic pressure radiated by the segment of surface $\mathcal{S}$ can be expressed as

$$p(\mathbf{x},t) = \int_{\mathcal{S}} \frac{R_3}{4\pi c_0 R_s^2}\left[\frac{\partial F}{\partial t'}\right]_{t-R_e/c_0} dS. \tag{4.4}$$

The dipole strength is related to the local unsteady loading by $d\mathbf{F} = \ell(\mathbf{y},t')dS\mathbf{e_3}$, with $dS = dy_1 dy_2$. Thus, the acoustic pressure in the frequency domain reads

$$\begin{aligned}\tilde{p}(\mathbf{x},\omega) &= \int_{\mathcal{S}} \frac{R_3}{4\pi c_0 R_s^2}\left(\frac{1}{2\pi}\int_{-\infty}^{\infty}\left[\frac{\partial \ell}{\partial t'}\right] e^{i\omega(t'+R_e/c_0)}dt'\right) dS \\ &= \int_{y_1}\int_{y_2} \frac{i\omega R_3}{4\pi c_0 R_s^2}\tilde{\ell}(\mathbf{y},\omega)e^{i\omega R_e/c_0}dy_1 dy_2. \end{aligned} \tag{4.5}$$

Noting $S_0^2 = \beta_y^2 x_1^2 + \beta_x^2 x_2^2 + \beta_0^2 x_3^2$, the following approximations are found for the geometrical far-field ($y_1 \ll x_1, y_2 \ll x_2$)

$$R_s^2 \approx S_0\left(1 - \frac{\beta_y^2 x_1 y_1 + \beta_x^2 x_2 y_2}{S_0^2}\right), \tag{4.6}$$

$$R_e \approx \frac{1}{\beta_0^2 S_0}\{[S_0 M_x - \beta_y^2 x_1]y_1 + [S_0 M_y - \beta_x^2 x_2]y_2\}, \tag{4.7}$$

$$R_3 \approx x_3 \qquad \text{and} \qquad \frac{1}{R_s^2} \approx \frac{1}{S_0^2}. \tag{4.8}$$

The surface integration in Eq.(4.5) is now expressed in the parallelogram principal directions (ξ,η). Noting $a = \tan\bar{\varphi}$ and $\tau = \sqrt{1+a^2}$, the change of variables $y_1 = \xi/\tau$ and $y_2 = \eta + a\xi/\tau$

yields the differential product $dy_1 dy_2 = d\xi d\eta/\tau$, so that the far-field pressure in Eq.(4.5) is given by

$$\begin{aligned}\tilde{p}(\mathbf{x},\omega) &= \frac{ik_a x_3 \rho_0 U_x \tilde{w}}{2S_0^2\tau} \times \int_{-b\tau}^{b\tau} g(k_1^*,k_2^*) e^{-\frac{i\xi}{\tau}\left\{\frac{k_a}{\beta_0^2 S_0}\left[\beta_y^2 x_1 - S_0 M_x + a(\beta_x^2 x_2 - S_0 M_y)\right] - ak_2\right\}} d\xi \\ &\times \int_{-L/2}^{L/2} e^{-i\eta\left(\frac{k_a}{\beta_0^2 S_0}(\beta_x^2 x_2 - S_0 M_y) - k_2\right)} d\eta. \end{aligned} \tag{4.9}$$

where $g(k_1^*, k_2^*)$ is the reduced lift function, defined in Eq.(3.25), L is the parallelogram span and $k_a = w/c_0$ is the acoustic wavenumber. The radiated pressure is expressed in Eq.(4.9) as the product of two decoupled integrals, evaluated over the principal directions of the parallelogram. Solving the integral over η, introducing the sine cardinal function in the result and defining the non-dimensional coordinate $\xi^* = \xi/b$, the radiated pressure is finally expressed as

$$\tilde{p}(\mathbf{x},\omega) = \frac{ik_a x_3 \rho_0 U_x \tilde{w} b L}{2S_0^2\tau} \times \mathcal{L}(\mathbf{x}, k_1^*, k_2^*) \times \mathrm{sinc}\left[\frac{L}{2}\left(k_2 - \frac{k_a}{\beta_0^2 S_0}(\beta_x^2 x_2 - S_0 M_y)\right)\right], \tag{4.10}$$

where

$$\mathcal{L}(\mathbf{x}, k_1^*, k_2^*) = \int_{-\tau}^{\tau} g(k_1^*, k_2^*) e^{-\frac{i\xi^* b}{\tau}\left\{\frac{k_a}{\beta_0^2 S_0}\left[\beta_y^2 x_1 - S_0 M_x + a(\beta_x^2 x_2 - S_0 M_y)\right] - ak_2\right\}} d\xi^*, \tag{4.11}$$

is the non-dimensional radiation integral of the segment also known as the *non-dimensional aeroacoustic transfer function* of the segment. The radiation integral is further decomposed into two terms, namely $\mathcal{L} = \mathcal{L}_1 + \mathcal{L}_2$, accounting respectively for the segment leading-edge and trailing-edge contributions. The corresponding expressions are derived subsequently, starting from the unsteady loading on an infinite span segment, given in Eqs.(3.19) and (3.24), respectively.

Leading Edge Term

The reduced lift function associated with the leading-edge singularity is found by comparing Eqs.(3.19) and (3.25). It is expressed here as a function of the reduced coordinate ξ^* by

$$g_1(k_1^*, k_2^*) = -\frac{1}{\pi} \frac{e^{-i(\mu M_x - \kappa)(\xi^*/\tau + 1)}}{\sqrt{\pi(k_1^* + \beta_x^2\kappa)(\xi^*/\tau + 1)}}. \tag{4.12}$$

The corresponding contribution to the radiation integral is found by introducing Eq.(4.12) into Eq.(4.11). Noting $\theta_1 = (\kappa - \mu M_x) - b\left\{\frac{k_a}{\beta_0^2 S_0}\left[\beta_y^2 x_1 - S_0 M_x + a(\beta_x^2 x_2 - S_0 M_y)\right] - ak_2\right\}$, the integral is given by

$$\mathcal{L}_1(\mathbf{x}, k_1^*, k_2^*) = -\frac{1}{\pi}\frac{e^{-i(\mu M_x - \kappa)}e^{i\pi/4}}{\sqrt{\pi(k_1^* + \beta_x^2\kappa)}}\int_{-\tau}^{\tau}\frac{e^{+i\xi^*/\tau\theta_1}}{\sqrt{\xi^*/\tau + 1}}d\xi^*. \tag{4.13}$$

The change of variable $t = \theta_1(\xi^*/\tau + 1)$ puts into evidence the Fresnel Integral in Eq.(4.13), so that the leading-edge term finally reads

$$\begin{aligned}\mathcal{L}_1(\mathbf{x}, k_1^*, k_2^*) &= -\frac{\tau}{\pi}\frac{e^{-i(\mu M_x - \kappa)}e^{i\pi/4}}{\sqrt{\pi(k_1^* + \beta_x^2\kappa)}}\sqrt{\frac{2\pi}{\theta_1}}e^{-i\theta_1}\int_0^{2\theta_1}\frac{e^{+it}}{\sqrt{2\pi t}}dt \\ &= -\frac{\tau e^{-i\theta_2}}{\pi}\sqrt{\frac{2}{\pi(k_1^* + \beta_x^2\kappa)\theta_1}}E[2\theta_1],\end{aligned} \tag{4.14}$$

with

$$\theta_2 = \theta_1 + (\mu M_x - \kappa) - \pi/4.$$

Trailing Edge Term

The reduced lift function associated with the trailing-edge Kutta correction is now expressed as a function of the reduced coordinate ξ^*

$$g_2(k_1^*, k_2^*) = \frac{1}{\pi}\frac{e^{-i(\mu M_x - \kappa)(\xi^*/\tau + 1)}}{\sqrt{2\pi(k_1^* + \beta_x^2\kappa)}}\left(1 - (1+i)E^*[2\kappa(\xi^*/\tau - 1)]\right). \tag{4.15}$$

The trailing-edge contribution to the radiation integral is found using the same technique as before. The derivation, detailed in App. A4.1, provides

$$\mathcal{L}_2(\mathbf{x}, k_1^*, k_2^*) = \frac{\tau e^{-i\theta_2}}{\pi\theta_1\sqrt{2\pi(k_1^* + \beta_x^2\kappa)}}\left[i(1 - e^{2i\theta_1}) - (1+i)\{E[4\kappa] - \sqrt{2\kappa/\theta_3}e^{2i\theta_1}E[2\theta_3]\}\right], \tag{4.16}$$

with

$$\theta_3 = 2\kappa - \theta_1.$$

The expressions Eqs.(4.14) and (4.16) are extensions of the existing models of noise radiation from flat segments. The present theory allows an enhanced geometry representation of swept blade segments, the cuts of which are chosen parallel to the relative flow velocity. The expressions for a rectangular segment, as presented by Roger [97], can be directly found assuming $\bar{\varphi} = 0$. Notice that the present results are equivalent to the complex conjugate of the original equations derived by Amiet due to the opposite Fourier transform convention.

The preliminary assessment of the shape effects on noise is conducted by comparing the radiation integral for a parallelogram and a rectangle with the same sweep, as the segments depicted in Fig. 4.1-left. The Fourier gust wavefronts are parallel to the leading-edge of both segments whereas the convection velocity is parallel to the end-cuts of the parallelogram. As shown in Fig. 4.2, the leading-edge contribution to the radiation integral $\mathcal{L}_1$ presents noticeable differences for both segments, especially for high sweep angles. The proposed formulation provides consistent behavior and trend in comparison to the baseline equations for both reduced frequencies $k_a c$.

Now, the radiated noise due to the interaction defined above is addressed. The acoustic pressure is represented by the directivity function

$$\mathrm{D}_f = \frac{k_a x_3 c}{S_0 \tau} \left\| \mathcal{L}(\mathbf{x}, k_1^*, k_2^*) \mathrm{sinc} \left[\frac{L}{2} \left(k_2 - \frac{k_a}{\beta_0^2 S_0} (\beta_x^2 x_2 - S_0 M_y) \right) \right] \right\|. \tag{4.17}$$

As shown in Figs. 4.3-a and -b, the segment shape has a noticeable impact on the radiated noise, even for two segments having the same sweep . For this case, the main lobe seems to be tilted in the sweep direction which is following $\mathbf{e}_2$ in the trailing-edge region. The secondary lobes seem to lean in the opposite direction, following the surface inclination in the leading-edge region. It must be noted that, in this case, the wavefronts being parallel to the segments leading-edge, the loading is constant in the y_2 direction. For this reason, the source is exactly the same in both cases, only the integration surface differs. The corresponding radiation lobes are plotted in Figs. 4.3(a) and (b). Now, consider a skewed gust interacting with these segments. The sources on the rectangle are not exactly the same as the ones on the parallelogram due to the different spanwise variations of the lift trace. As a consequence, larger deviations of the radiation lobes are noticeable, as shown in Figs. 4.3(c) and (d).

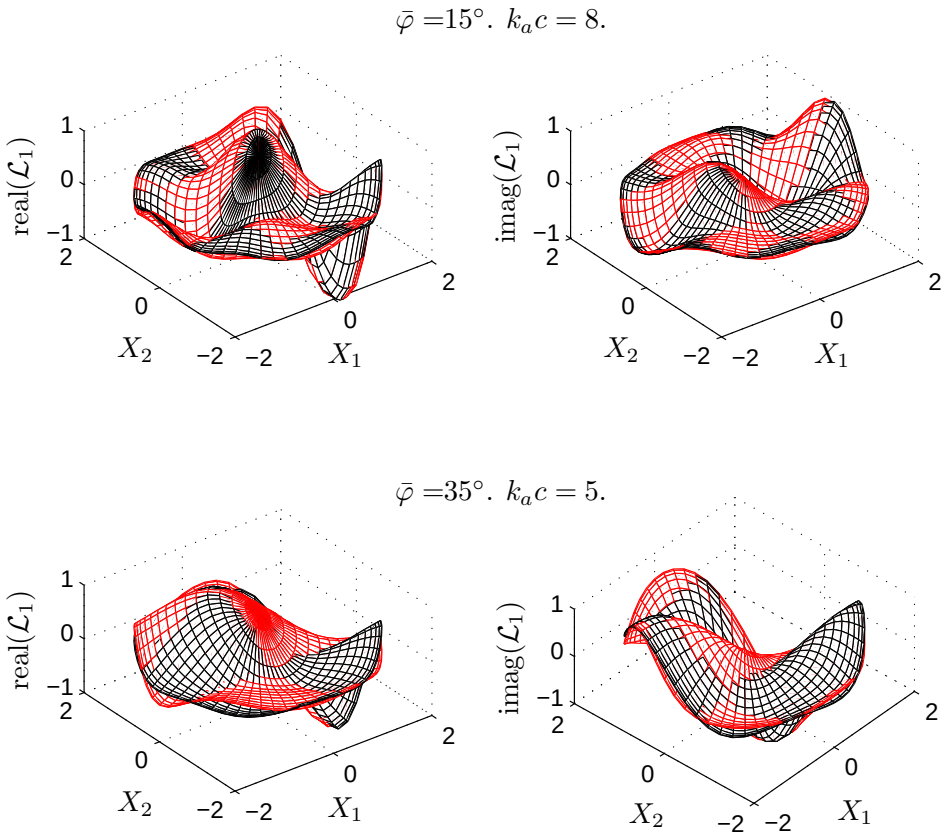

Figure 4.2: *Leading-edge radiation integrals for the rectangular segment (black) and the parallelogram-shaped segment (red) of Fig. 4.1, in the plane of coordinates* $(X_1, X_2) = (x_1, x_2)/R$ *(observer on a half-sphere of radius R, arbitrary units).* $L/c = 1.5$. $M_0 = 0.44$.

For segments with different sweep but interacting with the same gust, the differences in the radiated noise are larger. Taking the same segments as in Fig. 4.3(a), but sweeping the parallelogram in order to align its end-cuts with those of the rectangle, we obtain the geometries to be considered in Fig. 4.4. The convection velocity is now perpendicular to the rectangle leading-edge. For wavefronts perpendicular to the convection velocity, the rectangle radiation shows a symmetry with respect to the $\mathbf{e}_3$ direction due to the symmetry of the segment and the excitation. In contrast, the parallelogram radiates in an oblique direction. For wavefronts

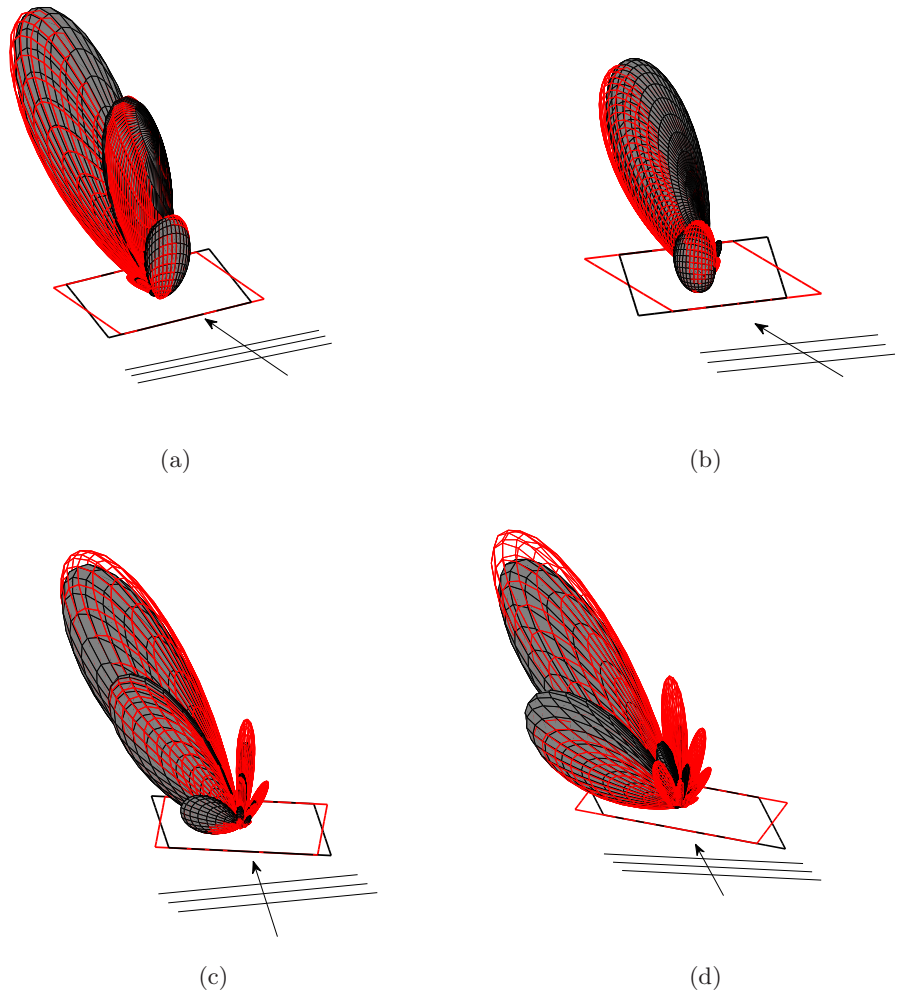

Figure 4.3: *Acoustic Radiation from flat segments. Top : Acoustic lobes corresponding to the radiation integrals in Fig. 4.2. Red: swept rectangle. Gray: Swept parallelogram. (a) lobes for* $\bar{\varphi} = 15°$ *and* $k_a c = 8$. *(b) lobes for* $\bar{\varphi} = 35°$ *and* $k_a c = 5$. *Bottom : Acoustic lobes for segments of same sweep interacting with a skewed gust. For all cases the gust wavefront present an angle of* $15°$ *with respect to the leading-edge.* $M_0 = 0.44$, $L/c = 1.5$ *(c)* $k_a c = 8$, $\bar{\varphi} = 15°$. *(d)* $k_a c = 5$, $\bar{\varphi} = 35°$.

parallel to the swept parallelogram, the parallelogram response tends to point normal to the surface but exhibits a slight asymmetry due to that of the segment surface, whereas the rectangle now radiates at an oblique direction. These results show the importance of a proper account of

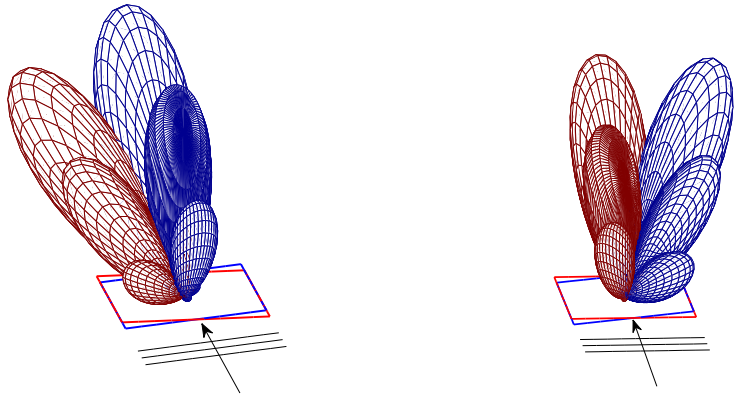

(a) (b)

Figure 4.4: *Acoustic radiation from a rectangular segment and a swept parallelogram for $\bar{\varphi} = 15°$, $k_a c = 8$, $L/c = 1.5$ and $M_0 = 0.44$. Blue: Rectangular segment. Red: Swept parallelogram. (a) wavefronts parallel to the rectangle leading-edge. (b) wavefronts parallel to the swept parallelogram leading-edge.*

the segment sweep. When the inclination of the wavefronts relative to the segment leading-edge is modified, a different spanwise trace of the excitation velocity is defined leading to a different inclination of the radiation lobes. As a result, the pressure measured in a fixed observer position is different from one case to the other.

4.1.2 Effect on Noise of Gust Skewness

The interaction of a skewed gust with an infinite span airfoil can be classified as *supercritical* or *subcritical* depending on its capability to induce or not an acoustic wave in the surrounding fluid, respectively. In this section, this notion is related to the trace velocity at which the aerodynamic excitation sweeps the segment in the spanwise direction, referred to as the sweep velocity v_s in Sec. 3.3.2.

The interaction is supercritical if the sweep velocity, conjugated with the convection velocity, produces a trace velocity in any direction at least equal to the sound speed *relatively to the convected flow*. Let us define c_{0t} as the spanwise velocity that conjugated with U_x will produce a trace velocity equal to the sound speed c_0 in the reference of the infinite-span airfoil, as depicted in Fig. 4.5. Therefore $c_0^2 = c_{0t}^2 + U_x^2$. Now, since a sonic trace velocity with respect

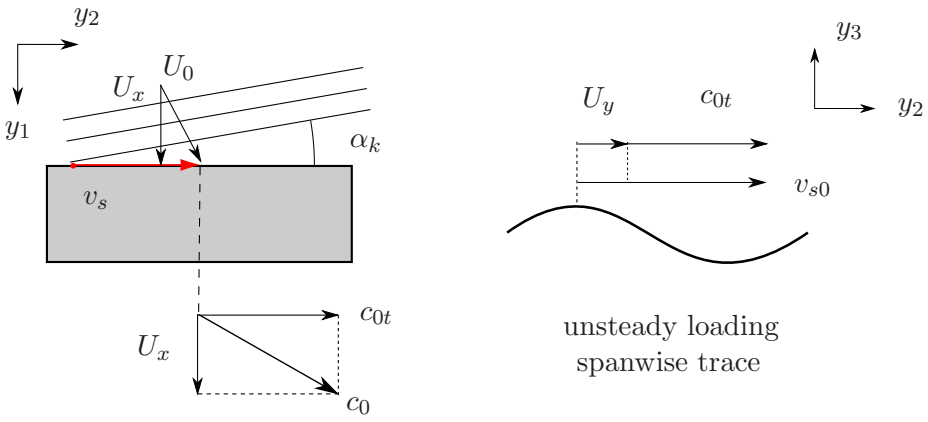

Figure 4.5: *Sweep velocity limit for noise radiation v_{s0}.*

to the moving fluid is required for noise radiation, the critical value of the sweep velocity v_{s0} verifies $v_{s0} = c_{0t} + U_y$. It comes that $c_0^2 = (v_{s0} - U_y)^2 + U_x^2$. This means the interaction will radiate noise only if $v_s > \sqrt{c_0^2 - U_x^2} + U_y$. Using the definition of v_s given in Eq.(3.47), this radiation condition can be put in the form

$$\frac{M_x^2 k^2}{k_2^2} > 1, \tag{4.18}$$

which is exactly the condition to get a positive value of κ^2, according to Eq.(3.12). This reasoning shows that an imaginary κ corresponds exactly to a subcritical interaction, unable to produce propagative waves and that the condition for noise radiation involves $v_s > U_y + c_{0t}$ and not $v_s > c_0$ (a supersonic sweep velocity) as it is often misunderstood.

To illustrate the effect of the angle α_k in the radiated noise, the directivity lobes for some skewed gusts are compared is Fig. 4.6. The lobes for supercritical interactions with skewed gusts at $\alpha_k = 0°, 15°$ and $25°$ are plotted in Fig. 4.6(a), whereas the lobes for subcritical interactions at $\alpha_k = 30°$ and $35°$ are plotted in Fig. 4.6(a) and compared with the supercritical case at $\alpha_k = 25°$, for scaling considerations. As one can notice, as the value of α_k is raised in the supercritical case, the acoustic lobes are tilted towards the direction aligned with the sweep velocity, in which the energy of the interaction is now directed at a finite velocity. The acoustic efficiency of the interaction is mildly reduced as the lobes are tilted. This effect is characterized by the reduction of the secondary radiation lobes. When the value of α_k is increased enough, here from $25°$ to $30°$, the interaction goes from supercritical to subcritical. The acoustic radiation is drastically

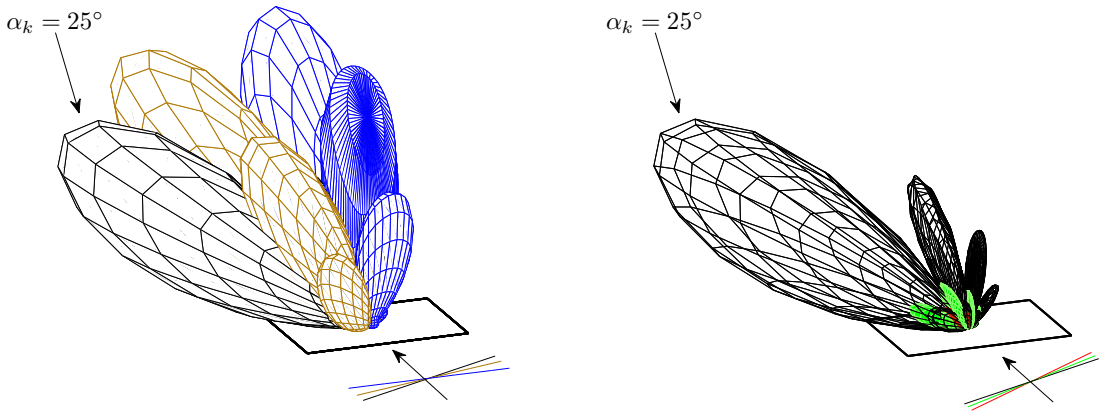

(a) (b)

Figure 4.6: *Noise radiated from skewed gusts. The colored lines represent the wavefronts of different gusts convected at the same velocity. For all the lobes* $k_a c = 8$, $M_0 = 0.44$, $\bar{\varphi} = 0°$ *and* $L/c = 1.5$. *(a) supercritical gusts. Blue:* $\alpha_k = 0°$, $\kappa = 4.96$. *Brown:* $\alpha_k = 15°$, $\kappa = 4.15$. *Black:* $\alpha_k = 25°$, $\kappa = 1.5231$. *(b) Subcritical Gusts compared with the case* $\alpha_k = 25°$. *Green:* $\alpha_k = 30°$, $\kappa = 3.09i$. *Red:* $\alpha_k = 35°$, $\kappa = 5.06i$.

reduced when κ becomes imaginary. The pressure suffers from an exponential attenuation from the segment surface and reduces almost to zero for a far-field observer. The inclination of the wavefronts relative to the segment leading edge acts therefore as a cut-off criterion, defining a radiating sub-set of skewed gusts for which $\kappa^2 > 0$. Note the segment sweep is able to make supercritical gusts which would be subcritical for zero sweep if the value of α_k is decreased. Increasing the segment sweep not always lead to noise reduction, excitation must be taken into account.

4.1.3 Assessment of Segment Shape Influence on Noise Radiation

Given the radiated noise sensitivity to the gust wavefront inclination with respect to the leading-edge of an airfoil, it seems justified to properly take this parameter into account in a noise prediction scheme. For a blade segment this stresses the effect of local sweep, the effect of

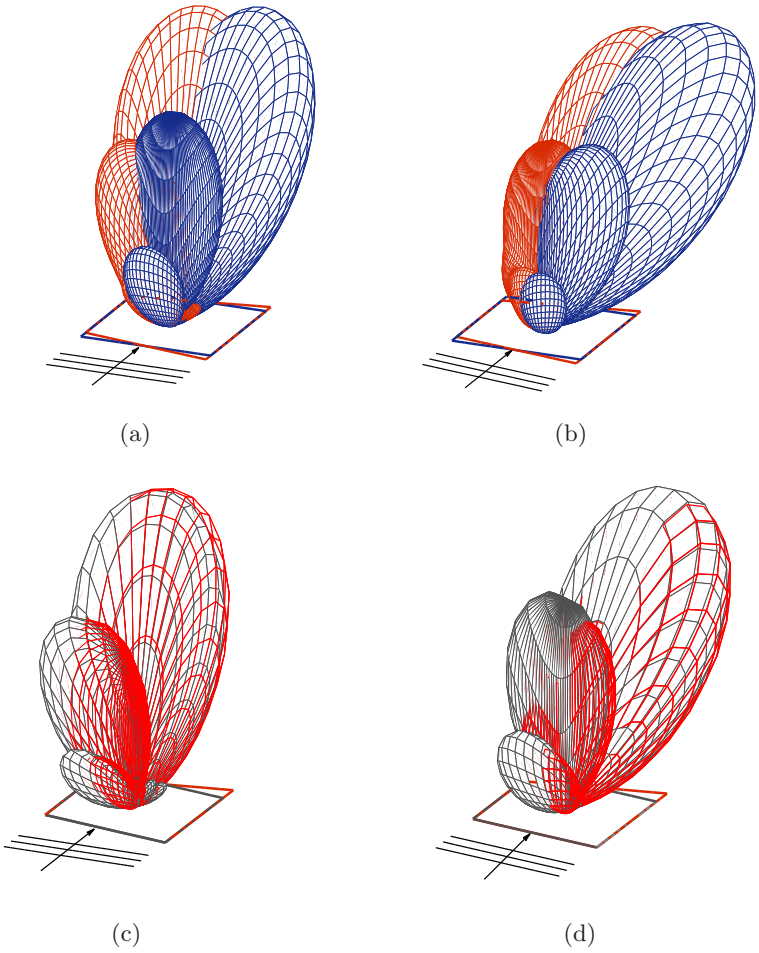

Figure 4.7: *Effects of segment shape on far-field radiation. Upper figures: directivity lobes for a canonical rectangular segment (blue) and a trapezoidal segment, accounting for swept leading and trailing edges (red). (a) Wavefronts parallel to the rectangle leading-edge. (b) Wavefronts parallel to the trapezoid leading-edge. - Lower figures: directivity lobes for a swept parallelogram (gray) and a trapezoidal segment (red). (c) Wavefronts perpendicular to the convection velocity, as in (a). (d) Wavefronts parallel to the swept leading-edge.* $\bar{\varphi}_1 = 10°$, $\bar{\varphi}_2 = 10°$, *aspect ratio (mid-span)* $L/c = 1$, $k_a c = 7.5$, $M_x = 0.44$.

which on rotor noise has been recognized as important [98] [75]. The segment unsteady lift due to the interaction with a skewed gust if formulated in Eqs.(3.19) and (3.24) and integrated over a parallelogram surface in Eq.(4.10), which allows an enhanced representation of rotating segments.

The effect of a non parallel trailing-edge is now investigated. The segment features a trapezoid with end-cuts parallel to the convection velocity. An extended segment response was proposed in Sec. 3.2 to take into account the trailing-edge obliqueness in the segment unsteady lift distribution. The effect on noise radiation is investigated here by means of a numerical integration, as the derivation of analytical expressions was extremely tedious for the general case (but still possible). However, for the particular case of a trapezoidal segment with leading-edge perpendicular to the convection velocity, an analytical expression of the radiation integral leading-edge term has been proposed in reference [99].

The segment shape effect is evaluated by comparing the radiation from the rectangular baseline segment and that from a swept trapezoid of same chord at mid-span, which includes leading-edge sweep and a non parallel trailing-edge. In Fig 4.7.-top is shown the sensitivity of the noise to these geometrical features. The lobes have different levels and inclinations, which alters significantly the perceived noise level at a fixed observer position. The lobes modifications due solely to the trailing edge obliqueness are assessed in the bottom of the figure. The radiation from a swept trapezoid is compared to that of a parallelogram of same sweep, so that only the trailing-edge obliqueness modifies the source distribution from one case to the other. As expected, trailing-edge sweep changes the radiation in a lesser extent than leading-edge sweep, although the effects are still noticeable.

The present analysis on fixed segments clearly justifies the need for an enhanced geometry representation for rotating blade segments. Particularly, the leading-edge sweep of the blade segments will have an important impact on rotor noise, following the present results. The extended unsteady loading formulation will be used to define the source corresponding to each wake Fourier component on the trapezoid defining each blade strip at best. However, the tonal noise from rotating segments will not make use of the radiation integrals developed in this section. The retained strategy is based on the rotating-dipole formula and on the distribution of the source on the blade Mean-Camber Surface (MCS). The total noise is then found from linear addition.

4.2 General CROR Noise Formulation

In this section is derived the noise formulation for an acoustically compact cell of the rear-rotor of a CROR system. At this stage, the noise sources are assumed to be known from CFD

computations or from the analytical model presented in Chapter 3. The formulation can be seen as a synthesis of various equations cast by D. B. Hanson, dealing with Single Rotation Propellers (SRP) and Counter-Rotation Propellers (CRP) unsteady loading noise in forward flight. Hanson's initial theory is based on a change of variables to represent the blade motion as a translation in a helicoidal reference frame [100]. Acoustic sources, with radial dipole component discarded, are located on the helicoidal ADvance Surface (ADS). An equation for CROR tonal noise has been further derived with the same assumptions [13]. Hanson & Parzych proposed another formulation for single propellers, in which acoustic sources, including radial dipole component, can be located on any surface of reference [101]. This formulation allows also the simulation of angular inflows in the propeller plane, encountered when the propeller axis is not aligned with the flight direction as in take-off and landing operations. Hanson & Parzych's equation cannot be directly extended to the CROR case because in the derivation methodology the radiated noise is assumed to be periodic with the Blade-Passing Frequency (BPF) as fundamental frequency. This property of SRP noise is not applicable to CROR. Another methodology is thus necessary to derive a formulation of CROR tonal noise retaining the level of generality of Hanson & Parzych's equation, including radial forces, angular inflow and allowing source integration on any surface of reference. The purpose of this section is to expose this methodology and the resulting CROR noise formula.

The radial component of the dipole source has often been discarded, its amplitude being assumed to be negligible in comparison to that of tangential and axial components. However, as shown later on, radial forces radiate with the same directivity as the volume displacement sources of a rotor. Interference between both sources is then expected. Furthermore, as pointed out by Hanson, the vortex flow in a blade-tip region produces a radial suction force, the dipole radiation of which could have an important influence on noise [102]. Also worthy of investigation, the influence of the reference surface where the equivalent acoustic dipoles are located can be studied with the formulation presented in this section. More accuracy is expected when studying blade shape influence on noise radiation.

The methodology used here is different from the one used by Hanson, although the result is consistent with the aforementioned formulations, which can be retrieved from the general formula derived in this section. In what follows, the noise radiation is first formulated assuming rotating dipoles in a quiescent medium. The effect of forward flight at angular incidence is introduced afterwards in Sec. 4.2.3.

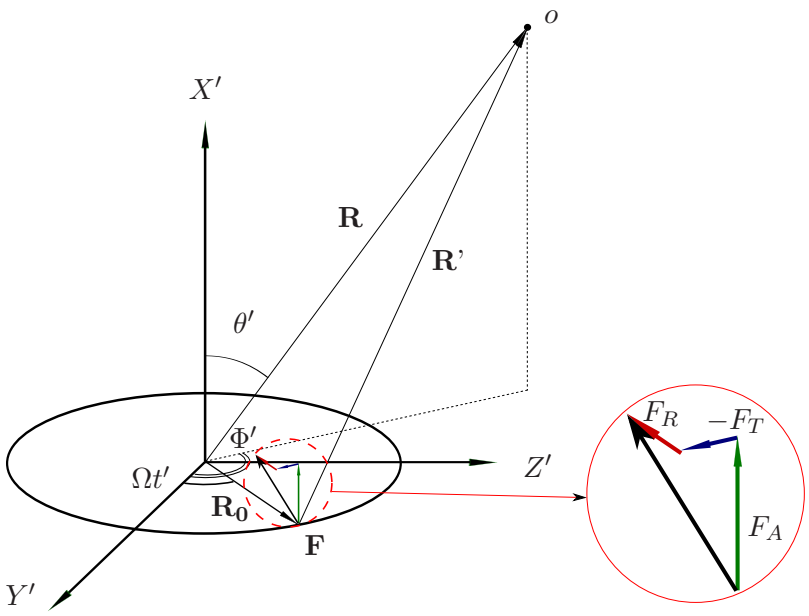

Figure 4.8: *Rotating dipole geometry.*

Consider a point dipole with arbitrary orientation rotating around the axis X', as shown in Fig. 4.8. Let us define two orthonormal bases, $\mathcal{B}_1 = (\mathbf{e}_{\mathbf{x}'}, \mathbf{e}_{\mathbf{y}'}, \mathbf{e}_{\mathbf{z}'})$ and $\mathcal{B}_2 = (\mathbf{e}_{\mathbf{r}}, \mathbf{e}_{\mathbf{t}}, \mathbf{e}_{\mathbf{x}'})$, associated to the source Cartesian and polar coordinates, respectively. The dipole path has a constant axial coordinate x'_d and a constant radius R_0. Notice that x'_d is equal to zero in Fig. 4.8, for simplicity. The dipole force is defined by $\mathbf{F} = F_R\mathbf{e}_{\mathbf{r}} + F_T\mathbf{e}_{\mathbf{t}} + F_A\mathbf{e}_{\mathbf{x}'}$, where F_R, F_T and F_A are the radial, tangential and axial components, depicted in Fig. 4.8 by the red, blue and green vectors, respectively.

The observer position, radial direction and dipole force are defined by the following vectors in the Cartesian basis $\mathcal{B}_1$:

$$\begin{array}{c|c} \mathbf{R} & \\ & R\cos\theta' \\ & R\sin\theta'\cos\Phi' \\ \mathcal{B}_1 & R\sin\theta'\sin\Phi' \end{array} \quad \begin{array}{c|c} \mathbf{R_0} & \\ & 0 \\ & R_0\cos\Omega t' \\ \mathcal{B}_1 & R_0\sin\Omega t' \end{array} \quad \begin{array}{c|c} \mathbf{F} & \\ & F_A \\ & -F_T\sin\Omega t' + F_R\cos\Omega t' \\ \mathcal{B}_1 & F_T\cos\Omega t' + F_R\sin\Omega t' \end{array} \tag{4.19}$$

where $R = \|\mathbf{R}\|$. Using these expressions, the source-observer distance is given by $\mathbf{R}' = \mathbf{R} - \mathbf{R}_0 - \mathbf{x}'_{\mathbf{d}}$, which leads to

$$\begin{array}{c|c} \mathbf{R}' & R\cos\theta' - x'_d \\ & R\sin\theta'\cos\Phi' - R_0\cos\Omega t' \\ \mathcal{B}_1 & R\sin\theta'\sin\Phi' - R_0\sin\Omega t' \end{array} \tag{4.20}$$

From vector representation in Eqs.(4.19) and (4.20) the following expressions are found, needed in subsequent steps of the derivation:

$$\mathbf{F}\cdot\mathbf{R}' = R[F_A\cos\theta' - F_T\sin\theta'\sin(\Omega t' - \Phi') + F_R\sin\theta'\cos(\Omega t' - \Phi')] - F_A x'_d - F_R R_0 \tag{4.21}$$

$$R' = \|\mathbf{R}'\| = R\left(1 + \frac{R_0^2}{R^2} - \frac{2R_0}{R}\sin\theta'\cos(\Omega t' - \Phi') - \frac{2x'_d\cos\theta'}{R} + \frac{{x'_d}^2}{R^2}\right)^{1/2} \tag{4.22}$$

4.2.1 Noise From a Rotating Dipole in a Medium at Rest

The acoustic pressure p emitted at time t' by a point dipole in subsonic motion and measured at time t at the observer Cartesian coordinates $\mathbf{x}' = (x'_1, x'_2, x'_3)_{\mathcal{B}_1}$ is given by

$$p(\mathbf{x}', t) = \frac{1}{4\pi}\frac{\partial}{\partial x'_i}\left[\frac{F_i(t')}{R'(1 - M_r)}\right] \tag{4.23}$$

where $M_r = \mathbf{M}\cdot\mathbf{R}'/\|\mathbf{R}'\|$ is the source Mach number in the observer direction, with $R' = \|\mathbf{R}'\|$, and where the squared brackets stand for retarded-time evaluation. This equation is reformulated here by using the common permutation rules between spatial and retarded time derivatives as

$$p(\mathbf{x}', t) = -\frac{1}{4\pi}\left(\frac{1}{c_0}\frac{\partial}{\partial t'}\left[\frac{F_i R_i'}{R'^2(1 - M_r)}\right] + \left[\frac{F_i R_i'}{R'^3(1 - M_r)}\right]\right). \tag{4.24}$$

Note that no assumption has been made to derive Eq.(4.24), which therefore holds for geometrical near-field and far-field. Radiated noise in the near-field is a valuable information for predicting interior noise and structural stresses. However, in this section, intended to provide an acoustic far-field formulation for $R \gg R_0$ and $R \gg x'_d$, only the first order approximation

of the equations will be retained. For Eq.(4.24), this approximation is given, in the frequency domain, by

$$\tilde{p}(\mathbf{x}',\omega) = \frac{1}{2\pi}\int_{-\infty}^{+\infty} -\frac{F_i}{1-M_r}\frac{\partial}{\partial\tau}\left(\frac{R_i\text{'}}{4\pi c_0 R\text{'}^2}e^{i\omega(\tau+R\text{'}(\tau)/c_0)}\right)d\tau. \tag{4.25}$$

where τ is here a dummy variable of integration. Developing the time derivative in Eq.(4.25), for the far-field approximations of Eqs.(4.21) and (4.22), and retaining only the first-order terms from the result leads to (see App. A4.2)

$$\tilde{p}(\mathbf{x}',\omega) = \frac{i\omega}{8\pi^2 c_0}\int_{-\infty}^{+\infty}\frac{\mathbf{F}\cdot\mathbf{R}\text{'}}{R^2}e^{i\omega(\tau+R\text{'}/c_0)}d\tau. \tag{4.26}$$

Next, by defining each force component as an inverse Fourier transform

$$F_i(\tau) = \int_{-\infty}^{+\infty}\tilde{F}_i(\bar{\omega})e^{-i\bar{\omega}\tau}d\bar{\omega},$$

and with convenient factorization, the radiated pressure can be expressed as

$$\begin{aligned}\tilde{p}(\mathbf{x}',\omega) =& \frac{i\omega e^{i\omega(R-x'_d cos\theta')/c_0}}{8\pi^2 R c_0\Omega}\int_{-\infty}^{+\infty}\left[\tilde{F}_A\cos\theta'\left(\int_{-\infty}^{+\infty}e^{i\vartheta}d\tau\right) - \tilde{F}_T\sin\theta'\right.\\ &\left.\times\left(\int_{-\infty}^{+\infty}\sin(\Omega\tau-\Phi')e^{i\vartheta}d\tau\right) + \tilde{F}_R\sin\theta'\left(\int_{-\infty}^{+\infty}\cos(\Omega\tau-\Phi')e^{i\vartheta}d\tau\right)\right]d\bar{\omega},\end{aligned} \tag{4.27}$$

where $\vartheta = (\omega-\bar{\omega})\tau - \dfrac{\omega R_0}{c_0}\sin\theta'\cos(\Omega\tau-\Phi')$.

The evaluation of the integrals in Eq.(4.27) is carried out by expanding the function $e^{i\vartheta}$ on a basis of Bessel functions of the first kind, as shown in App. A4.3. A Dirac delta function, namely $\delta[(\bar{\omega}-\omega)/\Omega - n]$, found as a factor of the result, is used to solve the integral over $\bar{\omega}$. Finally, the far-field pressure radiated by a rotating point dipole in a quiescent medium reads

$$\begin{aligned}\tilde{p}(\mathbf{x}',\omega) =& \frac{i\omega e^{i\omega(R-x'_d cos\theta')/c_0}}{4\pi R c_0}\sum_{n=-\infty}^{+\infty}e^{in(\Phi'-\pi/2)}\left[\left\{\tilde{F}_A(\omega-n\Omega)\cos\theta' + \tilde{F}_T(\omega-n\Omega)\frac{nc_0}{\omega R_0}\right\}\right.\\ &\left.\times J_n\left(\frac{\omega R_0\sin\theta'}{c_0}\right) + i\sin\theta'\tilde{F}_R(\omega-n\Omega)J'_n\left(\frac{\omega R_0\sin\theta'}{c_0}\right)\right].\end{aligned} \tag{4.28}$$

Eq.(4.28) is the basis for loading noise formulation of any open rotating machine in free field. It states that a signal of frequency ω, measured in a far-field point, is produced by a sum of force harmonics of frequency $(\omega - n\Omega)$. This frequency modulation is a signature of the Doppler effect caused by the source circular motion and it is independent of its frequency content. The noise radiation of a mode n will be dominated by the arguments of the Bessel function larger than its order, which means that a source will radiate efficiently only if it verifies

$$-1 \leq \frac{nc_0}{\omega R_0 |\sin\theta'|} \leq 1. \tag{4.29}$$

Therefore, the source frequency range responsible for the noise radiated at ω is approximately

$$\omega(1 - M_T|\sin\theta'|) \leq \omega_s \leq \omega(1 + M_T|\sin\theta'|), \tag{4.30}$$

where $M_T = \Omega R_0/c_0$ is the tangential Mach number and ω_s denotes the source frequency. Notice that for increasing values of M_T, the source frequency range gets wider, which implies an increased efficiency of energy transfer from the source to the radiated noise.

4.2.2 Source-Mode Representation

Eq.(4.28) states that the noise radiated by a rotating dipole can be interpreted as an infinite sum of modes. The mode of order n has n lobes in the circumferential direction and spins around the rotation axis at the velocity $v_\varphi = \omega/(2\pi/\lambda_\varphi) = \omega/n$, where ω is the frequency in the radiated field and λ_φ is the circumferential wavelength. Intuitively, each mode can be reproduced by a continuous circular distribution of stationary dipoles with exactly the same frequency, orientation and amplitude, but with a convenient phase lag to reproduce the mode spinning velocity and number of lobes. Two dipoles laying on this distributed source and separated by an angle Γ will experience a time delay $\Delta t' = \Gamma/v_\varphi = n\Gamma/\omega$. Hence, taking as reference the dipole located at $\Gamma = 0$, the force distribution over the circle can be defined as

$$F(\Gamma, t') = F\left(0, t' - \frac{n\Gamma}{\omega}\right) \tag{4.31}$$

The expression of F is given by $F(0,t') = \tilde{A}e^{-in\omega t'}$, where $\tilde{A}$ is the strength of the dipole distribution. The vector description of Eq.(4.19) can be used to predict the radiated noise, by

replacing $(\Omega t')$ by Γ. Introducing these notations into Eq.(4.24), the far-field pressure of the dipole located at Γ is found to be

$$\tilde{p}(\mathbf{x}', \omega)^{\Gamma} = \frac{i\omega e^{i\omega(R - x'_d cos\theta')/c_0}}{4\pi R c_0} e^{in\Gamma} \left\{ \tilde{A}_A \cos\theta' + \tilde{A}_T \sin\theta' \sin(\Phi' - \Gamma) + \tilde{A}_R \sin\theta' \cos(\Phi' - \Gamma) \right\}, \tag{4.32}$$

where $(\tilde{A}_R, \tilde{A}_T, \tilde{A}_A)$ are the radial, tangential and axial components of $\tilde{A}$. The integration of this formula over Γ provides exactly the form of a single mode in Eq.(4.28), from which one identifies $2\pi\tilde{A}_i = \tilde{F}_i$. By virtue of its properties, the continuous array of phased dipoles is henceforth referred to as a **source-mode**. This representation is used subsequently to introduce forward flight effects on the radiated noise.

4.2.3 Rotating Dipole Embedded in a Uniform Flow

The frequency domain approach developed so far can be extended to account for forward flight as long as the associated Doppler effect is ignored. Such condition is fulfilled by making the observer move at the same advancing speed than the rotating dipole, so that forward flight is represented by a uniform flow opposite to the flight direction. If the flow is not aligned with the axis of rotation, the propeller is said to have an non-zero incidence angle α. As a consequence, there is a flow component normal to the propeller shaft axis, referred to as *angular inflow*. Besides at landing and take-off flight phases, in which large incidence angles are usual, angular inflows can be encountered at cruise if an aircraft component deflects the otherwise axial flow. This situation occurs, for example, with the wing upwash on a puller wing-mounted propeller. The effect of angular inflow on noise radiation is twofold. First, noise sources are modified by the presence of a "one per revolution" aerodynamic excitation which increases the unsteady loadings on the blades. Secondly, the propagation of sound is modified by convective effects. As shown by the experiments conducted by Block [103], the combination of both effects has a noticeable influence on SRP and CRP noise: the directivity patterns are no longer axisymmetric and changes of noise level up to 1 dB per degree of angle of incidence are expected in the vicinity of the plane of rotation, for highly loaded propellers.

An analytical model of propeller noise with angular inflow has been cast by Mani [104] for small angles of attack, and extended by Kresja [105] to arbitrary angle values. The incidence effects are expressed in a modal basis, which leads to a propeller noise expression with an infinite

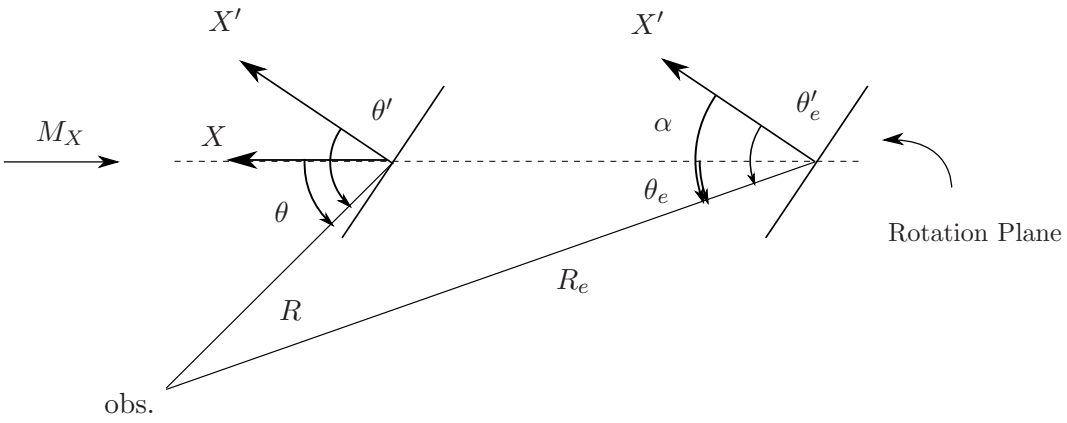

Figure 4.9: *Emission and visual coordinates, as defined by Hanson [106]. α is positive as depicted.*

summation accounting for tilt effects. An alternative formulation has been derived by Hanson, in which incidence effects on noise propagation are included in the Green's function, expressed in a reference frame with one direction aligned with the flight direction [106]. In what follows, the coordinate systems defined by Hanson will be used to extend Eq.(4.28) to account for the effects of forward flight at finite incidence on the noise radiated by a rotating point dipole.

Let us introduce the orthonormal basis $\mathcal{B}_3 = (\mathbf{e_x}, \mathbf{e_{y'}}, \mathbf{e_z})$ and the associated frame (X, Y', Z). $\mathbf{e_x}$ is aligned with the flight direction, so that the equivalent flow has a unique component in -$\mathbf{e_x}$ direction, as shown in Fig. 4.9. Observer's spherical coordinates, associated with the frame (X, Y', Z), are (R, Φ, θ). In what follows, the angle of incidence is denoted by α and has only a pitch component (defined by rotation around $\mathbf{e_{y'}}$). The extension to include roll and yaw components, not exposed here, is cumbersome but straightforward.

The passage formulae between the observer spherical coordinates in $\mathcal{B}_3$ (θ, Φ) and $\mathcal{B}_1$ (θ', Φ') are given by Hanson [106] as:

$$\begin{aligned} \cos\theta' &= \cos\theta\cos\alpha + \sin\theta\sin\Phi\sin\alpha \\ \sin\theta'\cos\Phi' &= \sin\theta\cos\Phi \\ \sin\theta'\sin\Phi' &= -\cos\theta\sin\alpha + \sin\theta\sin\Phi\cos\alpha \end{aligned} \tag{4.33}$$

The acoustic propagation in the moving medium is governed by the convected Green's function given by

$$G_c(\mathbf{x}, t/\mathbf{y}, t') = \frac{\delta(t' - t + R_e/c_0)}{4\pi R_s} \tag{4.34}$$

where

$$R_e = R - \frac{R_0 \sin\theta'_e \cos(\Omega t' - \Phi')}{1 - M_X \cos\theta_e} - \frac{x'_d \cos\theta'_e}{1 - M_X \cos\theta_e}$$

and

$$R_s = R_e(1 - M_X \cos\theta_e),$$

where M_X is the flight Mach number. The passage formulae between visual (θ, R) and emission (θ_e, R_e) coordinates are given by [101]

$$M_X + \frac{R\cos\theta}{R_s} = \frac{\beta_X^2 \cos\theta_e}{(1 - M_X \cos\theta_e)} \qquad \text{and} \qquad \frac{R\sin\theta}{R_s} = \frac{\sin\theta_e}{(1 - M_X \cos\theta_e)}. \tag{4.35}$$

where $\beta_X^2 = 1 - M_X^2$. The subscript e refers to equivalent emission coordinates as shown in Fig. 4.9 whereas $\mathbf{y}$ denotes the same position in the Cartesian coordinates associated with $\mathcal{B}_3$. Using the source-mode representation of Sec. 4.2.2, the noise emitted by the stationary dipole located at Γ can be formulated using Eq.(4.34) to include uniform flow. The derivation is made for coordinates projected in $\mathcal{B}_3$, in which dipole force and source-observer distance are given by

$$\begin{array}{c|c} \mathbf{F} & \tilde{A}_A \cos\alpha - (\tilde{A}_T \cos\Gamma + \tilde{A}_R \sin\Gamma)\sin\alpha \\ & -\tilde{A}_T \sin\Gamma + \tilde{A}_R \cos\Gamma \\ \mathcal{B}_3 & \tilde{A}_A \sin\alpha - (\tilde{A}_T \cos\Gamma + \tilde{A}_R \sin\Gamma)\cos\alpha \end{array} \tag{4.36}$$

and

$$\begin{array}{c|c} \mathbf{R}' & R\cos\theta - x'_d \cos\alpha + R_0 \sin\Gamma \sin\alpha \\ & R\sin\theta\cos\Phi - R_0 \cos\Gamma \\ \mathcal{B}_3 & R\sin\theta\sin\Phi - R_0 \sin\Gamma\cos\alpha - x'_d \sin\alpha \end{array} . \tag{4.37}$$

For the convected problem described above, the passage formula between time and space derivatives is given in the geometrical far-field as

$$\frac{\partial}{\partial x_i} = -\frac{1}{c_0 R_s} \begin{pmatrix} \frac{1}{\beta_X^2}\frac{R'_1}{R_s} - \frac{M_X}{\beta_X^2} \\ \frac{R'_2}{R_s} \\ \frac{R'_3}{R_s} \end{pmatrix}_{\mathcal{B}_3} \frac{\partial}{\partial t'}, \tag{4.38}$$

where the subscripts $(1,2,3)$ denote the Cartesian components defined in $\mathcal{B}_3$. Introducing Eqs.(4.36), (4.37) and (4.38) in Eq.(4.3), the far-field noise radiated by the stationary dipole located at Γ is given, in the frequency domain, by

$$\tilde{p}^{\Gamma}(\mathbf{x},\omega) = \frac{i\omega}{4\pi R_s^2 c_0} e^{i\omega R_e/c_0} e^{in\Gamma} \left\{ \frac{1}{\beta_X^2}(R'_1 + M_X R_s)\tilde{A}_1 + R'_2\tilde{A}_2 + R'_3\tilde{A}_3 \right\}. \tag{4.39}$$

Introducing in Eq.(4.39) the vector components detailed in Eqs.(4.36) and (4.37), and using the passage formulae Eqs.(4.33) and (4.35) leads to the radiated pressure by the dipole located at Γ

$$\tilde{p}^{\Gamma}(\mathbf{x},\omega) = \frac{i\omega}{4\pi R_s^2 c_0} e^{i\omega R_e/c_0} e^{in\Gamma} \left\{ \frac{\tilde{A}_A}{D_c}\cos\theta'_e + \frac{\tilde{A}_T}{D_c}\sin\theta'_e \sin(\Phi' - \Gamma) + \frac{\tilde{A}_R}{D_c}\sin\theta'_e \cos(\Phi' - \Gamma) \right\}, \tag{4.40}$$

where $D_c = 1 - M_X \cos\theta_e$. The noise radiated by a rotating point dipole embedded in a uniform flow is found by integrating Eq.(4.40) over Γ (see App. A4.4) and from the identification of the result with Eq.(4.28). The expression is given by

$$\begin{aligned} \tilde{p}(\mathbf{x},\omega) = & \frac{i\omega e^{i\omega(R - \frac{x'_d \cos\theta'_e}{D_c})/c_0}}{4\pi R_e D_c c_0} \sum_{n=-\infty}^{+\infty} e^{in(\Phi' - \pi/2)} \left[\left\{ \tilde{F}_A(\omega - n\Omega)\frac{\cos\theta'_e}{D_c} + \tilde{F}_T(\omega - n\Omega)\frac{nc_0}{\omega R_0} \right\} \right. \\ & \left. \times J_n\left(\frac{\omega R_0 \sin\theta'_e}{D_c c_0}\right) + i\frac{\sin\theta'_e}{D_c}\tilde{F}_R(\omega - n\Omega) J'_n\left(\frac{\omega R_0 \sin\theta'_e}{D_c c_0}\right) \right] \end{aligned} \tag{4.41}$$

Eq.(4.41) provides a general formulation without restrictive hypothesis on the source frequency content and allowing arbitrary values of the angle between the flow and the axis of

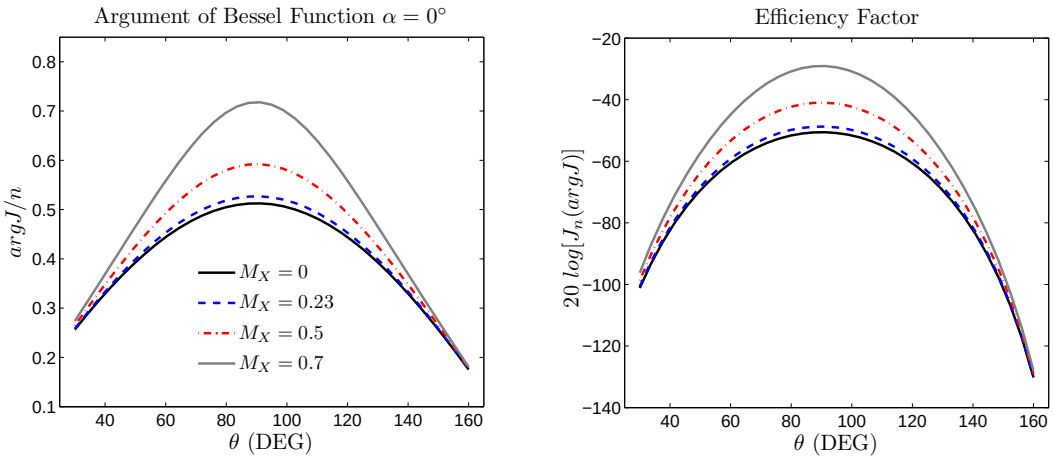

(a) (b)

Figure 4.10: *Effect of axial forward flight on the radiated noise level. (a) Argument of the Bessel function. (b) Effect on the efficiency factor. Parameters of the computation:* $\omega = 1046.2Hz$, $n = 9$, $R_0 = 1.5m$, $\alpha = 0°$.

rotation. This formula can be easily adapted to the case of tonal or broadband noise of any open rotating machine in free field, embedded or not in a uniform flow. For instance, the tonal noise formula given in [101] for a SRP at angle of attack is found for $n = mB - k$, $\omega = mB\Omega$ and assuming a harmonic source, the k harmonic of which is defined by $\omega_k = k\Omega$. The general result presented above will be used to derive the CROR tonal noise formula proposed in the next section.

An insight into the physics behind Eq.(4.41) is provided here for two parameters of the formulation, namely the flow velocity and its angle with respect to the axis of rotation. The effects of these parameters *on the noise propagation* are studied separately ignoring the source changes due to the corresponding aerodynamic modifications. Thus, the noise sensitivity to M_X and α is assessed only by the sensitivity of the Bessel function, referred to as *the efficiency factor*, irrespective of the amplitude of the force component involved in the noise generation. For simplicity, let us express this function as $J_n(argJ)$ with $argJ = \omega R_0 \sin\theta'_e / D_c c_0$.

The response of the efficiency factor to variations of $argJ$ is characterized by the value $argJ/n$. If this ratio remains less than 1 when $argJ$ is modified, the value of the Bessel function is located at the left of its first lobe maximum, for which an increase in $argJ$ will always lead to an increase of the radiated noise. For this case, the effect of M_X on the efficiency factor is shown

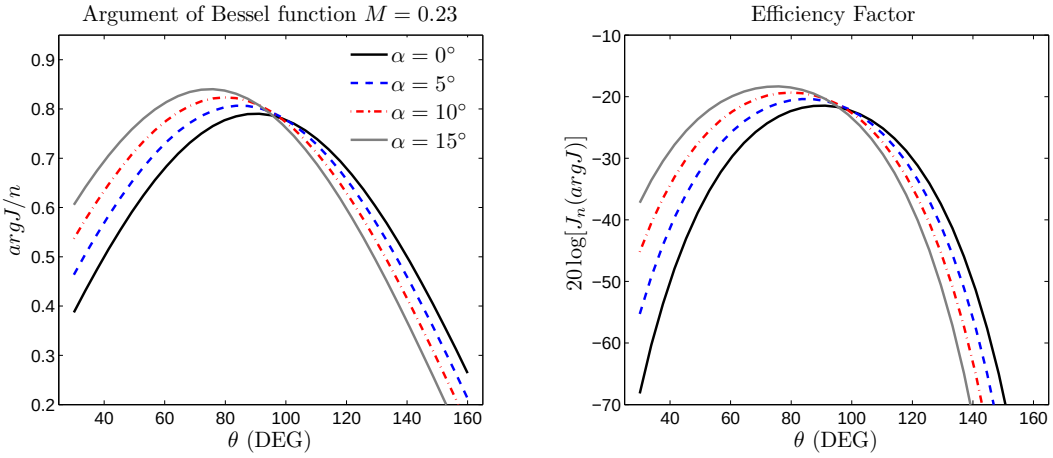

(a) (b)

Figure 4.11: *Effect of propeller incidence angle on radiated noise. (a) Argument of the Bessel function. (b) Effect on the efficiency factor. Parameters of the computation:* $\omega = 1569.2Hz$, $n = 9$, $R_0 = 1.5m$, $M_X = 0.23$.

in Fig. 4.10. The Bessel function argument is increased on the over the whole angular domain as the value of M_X is raised, without modification of its maximum angular position. This leads to a very efficient amplification of the radiated noise. The parameters used here are representative of SRP steady loading noise, for which the ratio $argJ/n$ is the same for all noise harmonics, since $n = mB$ and $\omega = mB\Omega$. As a consequence, as flight speed is increased, convective effects will provide an amplification of the noise radiated by the steady loading source, specially in the propeller plane ($\theta = 90°$) and its vicinity.

The effects of angular inflow on noise radiation are now studied for a fixed value of M_X. First, by retaining axial flow and tilting the dipole rotation axis, in order to model a propeller aircraft advancing horizontally with an angle of attack. Secondly, by changing gradually the angular inflow inclination on a dipole with a horizontal axis of rotation. The latter case is easily found by rotating observer's positions of the first case. For simplicity, and following Hanson's analysis in ref [106], let us locate the observer at $\Phi = 270°$, so that $\theta'_e = \theta_e + \alpha$.

For the first case, the range of $argJ$ is again broadened at both boundaries, its maximum value increasing with α. However, since the angles in $argJ$ numerator and denominator are different, its maximum is now shifted from $\theta = 90°$ by exactly α. Physically, the shift and amplification of the radiated noise are explained by the increased relative Mach number (of the

source with respect to the surrounding fluid) in observer's direction. As shown in Fig. 4.11, the amplification due to changes on the incidence angle is very efficient for $argJ/n < 1$. When this ratio exceeds unity, the effect of altering α on noise directivity depends on whether or not the altered values of $argJ$ are found in the set of values taken by $argJ$ for the initial value of α. If this condition is verified, a simple angular shift on the directivity will be produced. Conversely, if the altered value is out of the initial set of values, typically by being lager than its maximum, an effective modification on the radiated noise level can be expected. This behavior is clearly exposed in App. A4.5.

For a dipole rotating with respect to a horizontal axis and in the presence of an angular inflow, the maximum of noise radiation is expected for $\theta = 90°$ independently of the inflow inclination. The results shown in Fig. 4.12 are found by rotating the observer position of results presented in Figs. 4.11 and 4.17, for the low frequency case ($argJ/n < 1$) and high frequency case ($argJ/n > 1$), respectively. An efficiency factor amplification is found on the whole angular domain for the low frequency case, as shown in the bottom of Figs. 4.12(a) and (b). For the high-frequency case, the efficiency factor amplification is confined to the region neighboring the rotation plane, the effect being otherwise a pure angular shift towards the axis of rotation.

4.2.4 Formula for CROR Interaction Tonal Noise

CROR tonal noise specificities are now introduced in Eq.(4.41) to find the contribution of an acoustically compact lattice of the rear-rotor. The result is subsequently integrated over its blade surface, to predict the rotor total radiation. The perturbations shed from the front-rotor are assumed to be periodic in the angular direction, which implies that rear-rotor unsteady loadings are periodic in time, with fundamental frequency $\omega_s = B_1(\Omega_1 + \Omega_2)$, where B_1 is the front-rotor blade count and (Ω_1,Ω_2) are the front-rotor and rear-rotor angular velocities, respectively. In that case, the dipole force $F(t)$ can be expanded into the following Fourier series

$$F(t) = \sum_{k=-\infty}^{+\infty} F_k e^{-ik\omega_s t}, \text{ where } F_k = \frac{\omega_s}{2\pi} \int_0^{2\pi/\omega_s} F(t) e^{ik\omega_s t},$$

its Fourier transform being given by

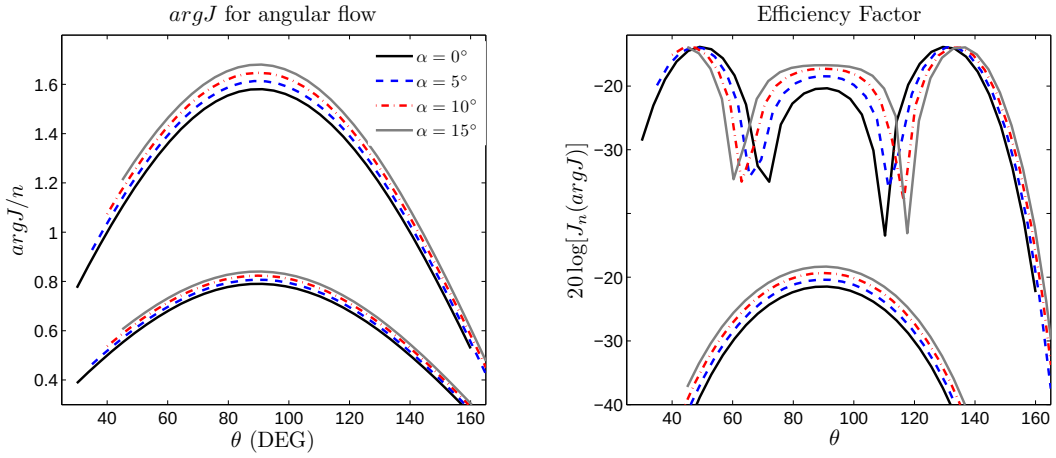

(a) (b)

Figure 4.12: *Influence of angular inflow inclination on noise radiated by a rotating dipole with fixed (horizontal) rotation axis. (a) Argument of the Bessel function. (b) Efficiency factor. Top : high frequency case* $\omega = 3138.4Hz$. *Bottom: low frequency case* $\omega = 1569.2Hz$. *Parameters of the computation:* $n = 9$, $R_0 = 1.5m$, $M_X = 0.23$.

$$\tilde{F}(\omega - n\Omega_2) = \sum_{k=-\infty}^{+\infty} F_k \delta(\omega - n\Omega_2 - k\omega_s). \tag{4.42}$$

From now on, let us assume that each rear-rotor blade will see the same incoming perturbation, only shifted in time and space, so that the interference effect of multiple blades can be modeled by defining a phase term for the dipoles constituting a single blade. In that manner, each rear-rotor blade will be represented by a phase lag with respect to the reference blade, accounting for emission location and time effects. For a symmetric rear-rotor of equally-spaced B_2 blades, numbered with an index b_2, Eq.(4.41) can be rewritten as [13]

$$\tilde{p} = \sum_{n=-\infty}^{+\infty} p_n \sum_{b_2=1}^{B_2} \exp\left[-i2\pi \frac{b_2}{B_2}(n + kB_1)\right] = B_2 \sum_{m=-\infty}^{+\infty} p_{mB_2 - kB_1}, \tag{4.43}$$

where p_n is the pressure contribution of the mode n. Introducing Eqs.(4.42) and (4.43) in Eq.(4.41) and then applying an inverse Fourier transform leads to the time history of the acoustic pressure radiated by a *point dipole* of the rear-rotor, including radial forces and forward flight

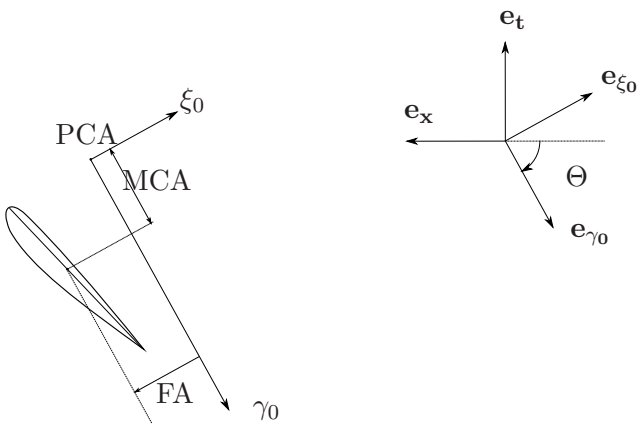

Figure 4.13: *Advancing surface coordinate system, as defined by Hanson [100]. The origin of the 2D reference frame is located at the Pitch-Change Axis (PCA). The blade airfoil is characterized by its Mid-Chord Alignment (MCA) in the direction γ_0, and by its Face-Alignment (FA) in the direction ξ_0.*

at angular incidence:

$$p(\mathbf{x},t) = \frac{iB_2}{4\pi c_0 R_e D_c} \sum_{m=-\infty}^{+\infty} \sum_{k=-\infty}^{+\infty} \omega_{km} \exp\left\{ i\left[\omega_{km}\left(\frac{R_e}{c_0} - \frac{\cos\theta'_e}{D_c c_0}(x'_d - x'_0) - t \right) + \zeta_{km}(\Phi' - \pi/2 - \phi'_0) \right] \right\} \times \left[\left\{ F_k^A \frac{\cos\theta'_e}{D_c} + F_k^T \frac{\zeta_{km} c_0}{\omega_{km} R_0} \right\} J_{\zeta_{km}}\left(\frac{\omega_{km} R_0 \sin\theta'_e}{D_c c_0} \right) + i \frac{\sin\theta'_e F_k^R}{D_c} J'_{\zeta_{km}}\left(\frac{\omega_{km} R_0 \sin\theta'_e}{D_c c_0} \right) \right] \tag{4.44}$$

where

$$\omega_{km} = kB_1\Omega_1 + mB_2\Omega_2 \quad \text{and} \quad \zeta_{km} = mB_2 - kB_1,$$

are the mode frequency and circumferential order, respectively. The coordinates (ϕ'_0, x'_0) stand for the dipole position at $t' = 0$. This equation is qualified as a frequency-domain formulation because the field is explicitly described as a sum of modes. The integration of Eq.(4.44) over a single rear blade surface provides the total rear-rotor acoustic radiation. For comparison with Hanson's equation for CRP noise [13], Eq.(4.44) can be expressed in the ADS coordinate system, though this integration can be performed numerically on any surface of reference. Notice that $\alpha = 0°$ in Hanson's formula, which allows us dropping the prime on all the space coordinates. Let us define the advancing orthonormal basis $\mathcal{B}_4 = (\mathbf{e_r}, \mathbf{e_{\gamma_0}}, \mathbf{e_{\xi_0}})$, as depicted in Fig. 4.13. The dipole component projection onto this surface leads to

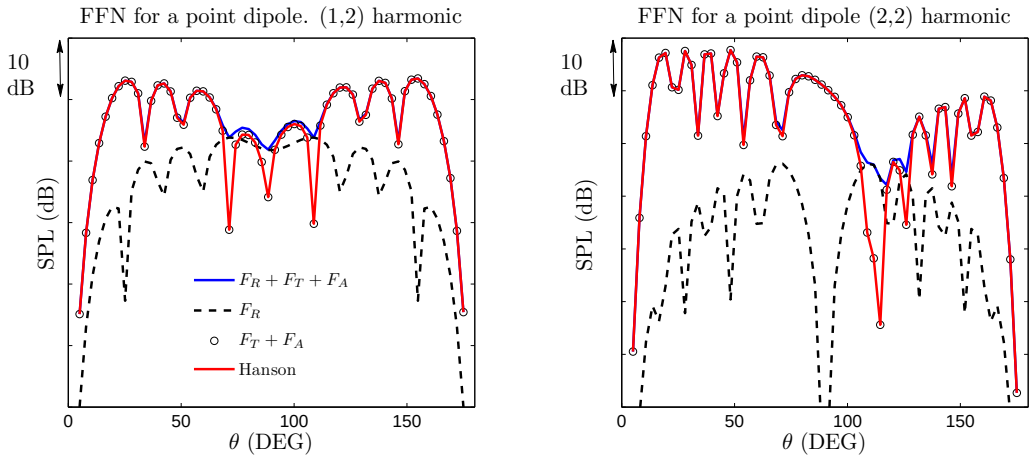

Figure 4.14: *Far-field radiation of a rear-rotor blade point dipole, according to the reference Hanson's solution and the present formulation.*

$$\begin{cases} F_A = F_L \sin\Theta - F_D \cos\Theta \\ F_T = -F_L \cos\Theta - F_D \sin\Theta \end{cases}, \tag{4.45}$$

where

$$\sin\Theta = \Omega_2 R_0 / V_{r2} \qquad \text{and} \qquad \cos\Theta = V_x / V_{r2}.$$

V_x and V_{r2} represent the flight velocity and the advancing velocity in the helical direction $-\gamma_0$, respectively. Also, in Eq.(4.45), F_L and F_D stand for the force components in the directions defined by $-\mathbf{e}_{\xi_0}$ and $\mathbf{e}_{\gamma_0}$. Hanson's equation is recovered with two more substitutions in Eq.(4.44), namely

$$x_d = -\gamma_0 \cos\Theta - \xi_0 \sin\Theta \qquad \text{and} \qquad \Phi = -\frac{\gamma_0 \sin\Theta}{R_0} + \frac{\xi_0 \cos\Theta}{R_0},$$

by expanding lift and drag coefficients into Fourier series and by performing analytical integration over the profile chord projection on γ_0. An assessment of the CROR tonal noise formulation presented in this section can be achieved by considering the rear-rotor unsteady loadings as known. As a preliminary test case, the far-field noise has been computed using Eq.(4.44)

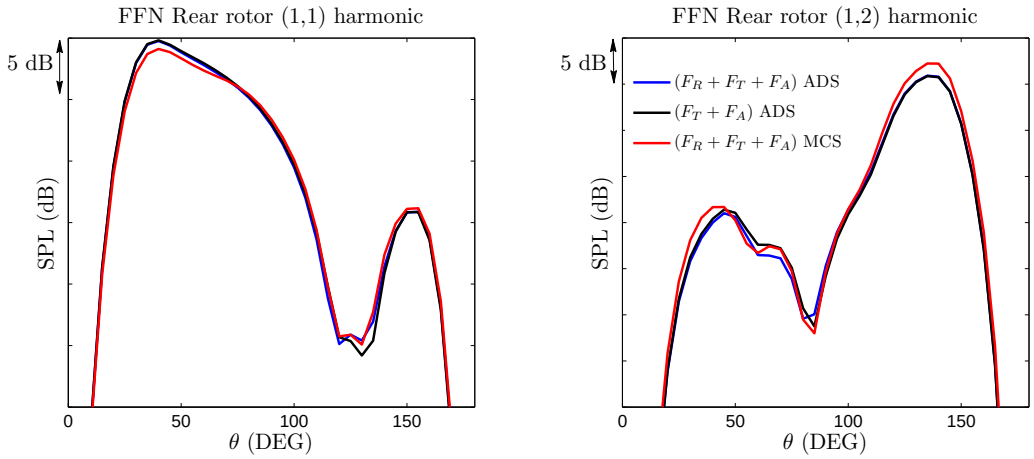

Figure 4.15: *Typical effect of surface of reference and radial force component on directivity patterns. Black line: tangential and axial dipole components integrated on the Advancing Surface (Hanson's equation). Blue line: all dipole components integrated on the Advancing Surface. Red line: all dipole components distributed on the blade MCS.*

and original Hanson's equation for an acoustically compact cell of the rear-blade tip region of a realistic CROR geometry. The force amplitude components normalized by the axial component are $F_A = 1$, $F_T = 0.8282$ and $F_R = 0.0940$. As shown in Fig. 4.14, if the radial component is ignored, Eq.(4.44) provides the same result as Hanson's equation. When the radial component is included, some differences are noticeable at localized angles, although the main trend and level are unchanged. Greater differences are expected if tip suction forces are included. The importance of radial forces also strongly depends on blade design. It is expected to increase with increasing sweep.

The effect of the reference surface used to represent the blade is now evaluated, for a given acoustic source. The baseline result is found by distributing the source, its radial component being ignored, over the rear-rotor blade ADS (Hanson's original approach). Next, radial components are included on this computation to assess their effect when the source is integrated over the entire blade surface. A new computation is performed, in which the source, all components included, is distributed over the blade MCS, thought to better represent the blade geometry. In Fig. 4.15 is shown a comparison between these results. Differences up to 2dB are noticeable when distributing the source over different reference surfaces.

4.3 Conclusion

The noise radiation from a CROR engine is studied in this chapter. The acoustic analysis starts from the assessment of the geometrical features taken into account in Chapter 3 on the unsteady lift distribution. Specifically, the noise sensitivity to leading-edge sweep and radial chord variations are analyzed for fixed segments as a preliminary study of rotating segments. It is shown that the noise is very sensitive to the segment sweep. The interaction is greatly altered when the wavefront inclination with respect to the leading-edge is modified. There is a critical inclination from which the interaction is unable to radiate noise. Therefore, sweep acts as a cut-on criterion defining a sub-set of gusts able to radiate noise, depending on the content of the excitation. This effect will be assessed for the case of the entire blade radiation in the next chapter, now that the prediction scheme has been entirely defined.

The strategy for noise prediction from rotating segments makes use of the radiation formula of a rotating point dipole, embedded in a uniform flow. Within the scope of linear acoustics, the total blade radiation is found by adding the contribution of each point dipole constituting the blade. An expression for a compact lattice of the rear-rotor is given in Eq.(4.44). This equation allows modelling angular inflows and locating the noise source on any surface of reference, as the blade MCS. An analysis of the sensitivity of this equation to the values of the advancing speed and the propeller angle of attack is provided in this chapter.

APPENDIX

A4.1 Derivation of the Radiation Integral

The trailing-edge contribution to the radiation integral is found by comparison of Eqs.(4.15) and (4.11)

$$\mathcal{L}_2(\mathbf{x}, k_1^*, k_2^*) = \alpha' \int_{-\tau}^{+\tau} e^{i\theta_1 \xi^*/\tau} \left(1 - (i+1)E^*[2\kappa(\xi^*/\tau - 1)]\right) d\xi^*. \tag{A4.1}$$

with $\alpha' = \dfrac{e^{-i(\mu M_x - \kappa)}}{\pi\sqrt{2\pi(k_1^* + \beta_x^2\kappa)}}$. This integral is decomposed in two parts, so its value is expressed as $\mathcal{L}_2 = \alpha'(I_1 + I_2)$, where

$$I_1 = \int_{-\tau}^{+\tau} e^{i\theta_1 \xi^*/\tau} d\xi^* = \frac{ie^{-i\theta_1}\tau}{\theta_1}(1 - e^{i2\theta_1}) \tag{A4.2}$$

and

$$I_2 = -(i+1) \int_{-\tau}^{\tau} e^{i\theta_1 \xi^*/\tau} E^*[Z], \tag{A4.3}$$

with $Z = 2\kappa(\xi^*/\tau - 1)$. Using the chain rule $\dfrac{\partial E^*}{\partial \xi^*} = \dfrac{\partial E^*}{\partial Z}\dfrac{\partial Z}{\partial \xi^*}$, the integral I_2 is integrated by parts leading to the result

$$I_2 = \frac{-(1+i)\tau}{\theta_1} \left\{ ie^{-i\theta_1} E^*[-4\kappa] - \sqrt{\frac{2\kappa}{\theta_3}} e^{i\theta_1} E[2\theta_3] \right\}, \tag{A4.4}$$

with $\theta_3 = 2\kappa - \theta_1$. Using the property $iE^*[-x] = E[x]$ and adding the expressions of I_1 and I_2, one finds the trailing-edge contribution to the radiation integral $\mathcal{L}_2$, given in Eq.(4.16).

A4.2 Far-Field Approximation for Rotating Dipole Geometry

The far-field approximation of Eqs. 4.21 and 4.22, is obtained by retaining only the first order terms for $R \gg R_0$ and $R \gg x_d$. This leads to:

$$\mathbf{F}\cdot\mathbf{R}\text{'} \approx R[F_A\cos\theta' - F_T\sin\theta'\sin(\Omega\tau-\Phi') + F_R\sin\theta'\cos(\Omega\tau-\Phi')], \tag{A4.5}$$

$$R\text{'} \approx R - R_0\sin\theta'\cos(\Omega\tau-\Phi') - x'_d\cos\theta', \tag{A4.6}$$

$$\frac{1}{R\text{'}} \approx \frac{1}{R}. \tag{A4.7}$$

Developing the retarded time derivative of Eq.(4.25), and including Eqs.(A4.5), (A4.6) and (A4.7) provides:

$$\begin{aligned}\tilde{p}(\mathbf{x}',\omega) =& \frac{1}{2\pi}\int_{-\infty}^{+\infty}\frac{F_iR_i}{4\pi c_0R^2}\left\{i\omega + \frac{2M_r}{(1-M_r)R}\right\}e^{i\omega(\tau+R'/c_0)}d\tau \\ &+ \frac{1}{2\pi}\int_{-\infty}^{+\infty}\frac{\Omega F_TR_0}{4\pi c_0(1-M_r)R^2}e^{i\omega(\tau+R'/c_0)}d\tau\end{aligned} \tag{A4.8}$$

The second integral in Eq.(A4.8) is a second-order term, and is then discarded in this analysis. Only the first term in the first bracket of the integral is retained. The result leads directly to Eq.(4.26).

A4.3 Derivation of Rotating Dipole Formula

By introducing the notations $a = \omega R_0\sin\theta'/c_0$, $b = (\bar{\omega}-\omega)/\Omega$ and $\zeta = \Omega\tau - \Phi'$, and with appropriate factorization, Eq.(4.26) can be expressed as

$$\tilde{p}(\mathbf{x}',\omega) = \frac{i\omega e^{i\omega(R-x'_d cos\theta')/c_0}}{8\pi^2Rc_0}\int_{-\infty}^{+\infty}\left[\tilde{F}_A\cos\theta'(I_1) - \tilde{F}_T\sin\theta'(I_2) + \tilde{F}_R\sin\theta'(I_3)\right]d\bar{\omega} \tag{A4.9}$$

where

$$I_1 = \int_{-\infty}^{+\infty} e^{-i[b(\Phi'+\zeta)+a\cos\zeta]}d\zeta$$

$$I_2 = \int_{-\infty}^{+\infty} \sin\zeta\, e^{-i[b(\Phi'+\zeta)+a\cos\zeta]}d\zeta$$

$$I_3 = \int_{-\infty}^{+\infty} \cos\zeta e^{-i[b(\Phi'+\zeta)+a\cos\zeta]} d\zeta.$$

The evaluation of the retarded time integrals in Eq.(A4.9) is carried out by using the following identity:

$$e^{-ia\cos\zeta} = \sum_{n=-\infty}^{\infty} (-i)^n J_n(a) e^{-in\zeta}. \tag{A4.10}$$

In that way, I_1 is developed as

$$\begin{aligned} I_1 =& e^{-ib\Phi'} \sum_{n=-\infty}^{+\infty} (-i)^n J(a) \int_{-\infty}^{+\infty} e^{-i\zeta(b-n)d\zeta} \\ &= 2\pi\delta(b-n) e^{-ib\Phi'} \sum_{n=-\infty}^{+\infty} (-i)^n J_n(a) \end{aligned} \tag{A4.11}$$

The same technique is applied to solve I_2 and I_3. Here, the derivatives of A4.10 with respect to ζ and then to a, lead to

$$I_2 = -2\pi\delta(b-n) e^{-ib\Phi'} \frac{n}{a} \sum_{n=-\infty}^{+\infty} (-i)^n J_n(a) \tag{A4.12}$$

$$I_3 = i2\pi\delta(b-n) e^{-ib\Phi'} \sum_{n=-\infty}^{+\infty} (-i)^n J'_n(a) \tag{A4.13}$$

where $J'_n(a)$ is the derivative of the Bessel function with respect to its argument. Eq.(4.28) is found by expressing these results in the main text notations and by using the properties of the Dirac delta function to solve the integral over $\bar{\omega}$.

A4.4 Integration of Source-Mode in Uniform Flow

The integration of Eq.(4.40) over Γ follows the technique explained in App. A4.3. The far-field approximations of R_e and R_s are given by

$$R_e \approx R - \frac{\cos\theta'_e x'_d}{D_c} - \frac{\sin\theta'_e R_0}{D_c}\cos(\Phi' - \Gamma) \tag{A4.14}$$

and

$$R_s \approx R_e(1 - M_X \cos\theta_e). \tag{A4.15}$$

Hence, the integration of Eq.(4.40) is given by

$$p(\mathbf{x},\omega) = \frac{i\omega}{4\pi R_e D_c c_0} e^{i\frac{\omega}{c_0}(R-\cos\theta'_e x'_d/D_c)} \left\{ \frac{\tilde{A}_A}{D_c}\cos\theta'_e I_4 + \frac{\tilde{A}_T}{D_c}\sin\theta'_e I_5 + \frac{\tilde{A}_R}{D_c}\sin\theta'_e I_6 \right\} \tag{A4.16}$$

where

$$I_4 = 2\pi(-i)^n J_n\left(\frac{\omega R_0 \sin\theta'_e}{D_c c_0}\right) e^{in\Phi'}, \tag{A4.17}$$

$$I_5 = 2\pi\frac{nD_c c_0(-i)^n}{\omega\sin\theta'_e R_0} J_n\left(\frac{\omega R_0 \sin\theta'_e}{D_c c_0}\right) e^{in\Phi'} \tag{A4.18}$$

and

$$I_6 = i2\pi(-i)^n J'_n\left(\frac{\omega R_0 \sin\theta'_e}{D_c c_0}\right) e^{in\Phi'}. \tag{A4.19}$$

A4.5 Sensitivity of Efficiency Factor to α

In this appendix, the value of $argJ/n$ is increased above unity by raising the value of ω at which the mode contributes. The other parameters are the same as in the case presented in Fig. 4.11, referred here as the Low Frequency (LF) case. As explained in the main text, when the value of α is changed, for example from 0° to 15°, the range of $argJ$ is also altered (in the present case broadened) as shown in Fig. 4.16. For altered values of $argJ$ (for $\alpha = 15°$) laying outside the intersection of altered and unaltered ranges, e.g. the zone between the dashed an plain lines in Fig. 4.16, an effective modification of the radiated noise will be produced. For the values

inside the intersection region, a directivity angular shift without level amplification is expected. These effects are noticeable in Fig. 4.17. Lateral lobes in Fig. 4.17(b) are shifted without level amplification whereas the central lobes are both shifted and amplified.

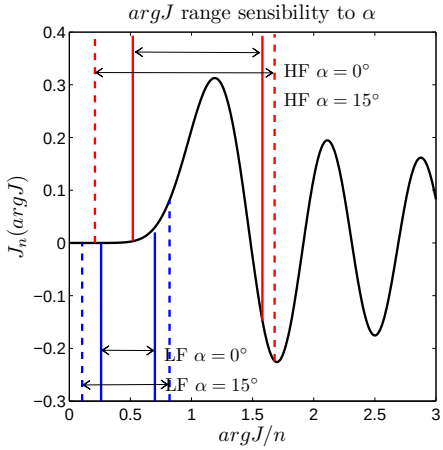

Figure 4.16: *Range broadening when increasing α. Blue : low frequency case as presented in Fig. 4.11. Red : high frequency case as presented in Fig. 4.17.*

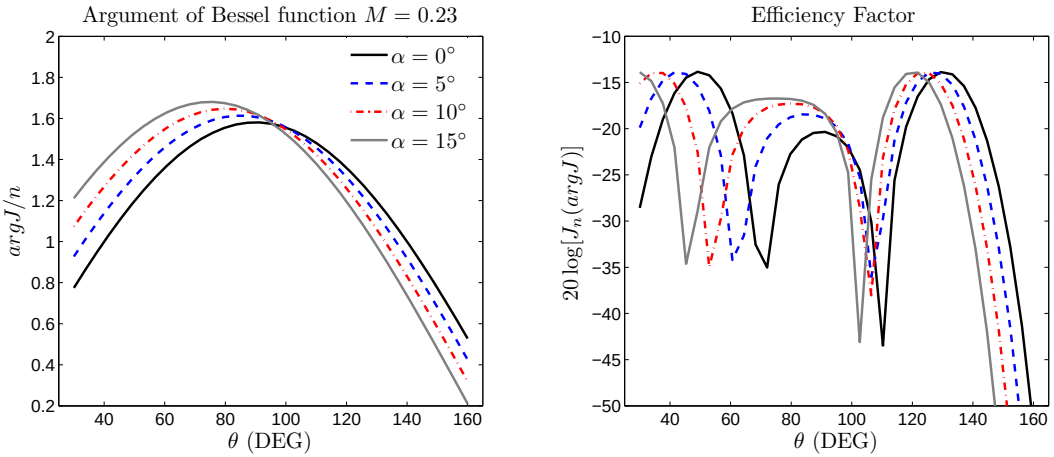

Figure 4.17: *Effect of propeller angle of attack on radiated noise. (a) Argument of the Bessel function. (b) Effect on the efficiency factor. Parameters of the computation: $\omega = 3138.4Hz$, $n = 9$, $R_0 = 1.5m$, $M_X = 0.23$.*

Chapter 5

Methodology Assessment

The methodology for CROR tonal noise prediction has led to the development of the Airbus in-house tool ORION (Open Rotor InteractiOn Noise). The code is structured as a chain of transfer functions, each of which accounts for a physical aspect from front-rotor wake generation to acoustic pressure radiation. This approach allows the assessment of each transfer function independently, by comparing the responses of both the tested routine and an appropriate reference method, to the same input. For the task at hand, there is availability of refined numerical computations and WTT measurements on the same isolated CROR engine. This chapter begins with a presentation of these reference techniques.

The present assessment will follow the inverse path of the physical mechanisms involved in noise production. First, the noise radiation routine is assessed with an in-house numerical tool for acoustic propagation. In that manner, the proposed routine can be used to compare subsequent assessment results in terms of noise. Secondly, the blade response model is assessed using CFD results. The analytical unsteady lift obtained for a numerical upwash is compared to the wall pressure obtained in the same CFD computation. The code capability of predicting the source distribution on the blade surface is assessed in terms of amplitude and phase. The noise predicted by the analytical source is computed with the radiation routine, validated at this stage. The result is compared to the noise produced by a full numerical computation and, for completeness, to WTT measurements. Finally, noise sensitivity to wake input is assessed. The impact of the wake model on unsteady loading and radiated noise is studied.

The whole scheme sensitivity to flight conditions is evaluated using CFD simulations and

WTT data for different engine rotation speeds.

5.1 Presentation of Reference Data

5.1.1 Numerical Techniques

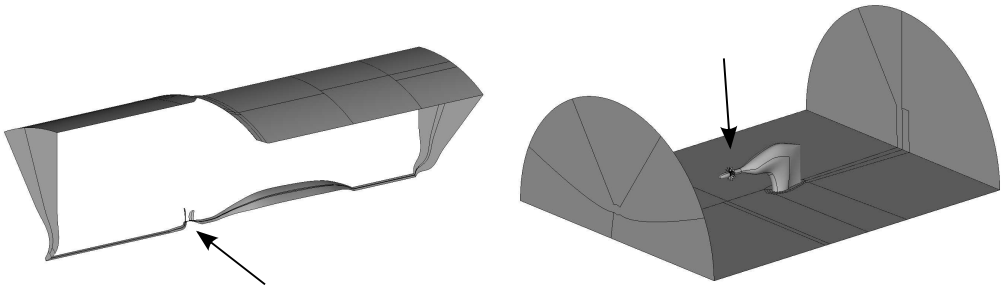

(a) (b)

Figure 5.1: *Illustration of the available numerical domains for code assessment. (a) Chorochronic technique single-channel domain. (b) Chimera technique full-annulus. Arrows indicate the location of the CROR (From [22] with permission).*

For assessing ORION results, CFD simulations carried out with the 3D URANS solver elsA are available from previous Airbus studies on CROR noise. In this section are outlined the two computational techniques providing the CFD references for the present assessment. First, a full-annulus computation is performed using the CHIMERA technique [107]. The computational domain is split into two regions, each one pertaining to one propeller. The meshing on each region is attached to the corresponding propeller. The computation is done in the stationary reference frame, for which both meshes appear to rotate in opposite directions. There is an overlap region between the rotating meshes in which the transfer of information is ensured by means of a sliding interpolation. The advantage of such a technique is that non-axisymmetric flow features, such as installation effects or propeller incidence, can be captured. However, the very refined mesh required to correctly transport the front-rotor velocity defects implies a high computational cost, exacerbated as the full-annulus geometry must be meshed. For the CHIMERA results presented in this assessment, the full annulus contains 120M nodes. Time integration is based on the Dual Time Stepping approach (DTS), with a time step corresponding to a relative motion of $1/3°$.

As an alternative, inputs from the chorochronic technique [108] can be post-processed. Taking advantage of the double time-space periodicity of the wake-interactions, the computation can be performed on a single channel and periodized in the angular domain afterwards. The advantage is the reduced computational cost in comparison to CHIMERA, which implies that finer meshes can be prescribed. The drawback is that the flow has to be axisymmetric, apart from the interaction features, so that only isolated configurations free of any installation effect can be computed. In the results presented hereafter, the blade channel is meshed with 28M nodes structured in a O-H topology. Time integration is based in the same DTS approach as the one used in CHIMERA computations.

The far-field noise is computed using the time-domain tool KIM [109]. In what follows the solid FW-H formulation is used, taking only the rear-rotor blade surfaces into account. A homogeneous moving atmosphere, modeling convection effects due to flight speed, is assumed between source and observer. For this reason, propagation effects such as acoustic refraction due to propeller inflow gradients are not taken into account. Such effects are included in the quadrupole term of the analogy, not computed here. A Fourier transform of KIM results is necessary for comparisons with ORION outputs.

Giving more details of these computational techniques is out of the scope of the present work. The reader is directed to the reference paper [22].

5.1.2 WTT experiments

Experiments on the same CROR geometry as used in the numerical simulations were performed in 2008 at the DNW LLF (Large Low-Speed Facility) open test-section wind-tunnel. The tested rig, a 1:6 mock-up powered electrically, is embedded in an axial uniform flow of Mach number $M_X = 0.23$. The main acoustic instrumentation used for this test is made of out-of-the-flow microphones. In total, nine lines of microphones have been operated to capture CROR noise polar and azimuthal directivities. The microphones are distributed so as to provide a grid step of 5° in emission angles. Data for small angles is not accessible due to the shadow zone produced by the refraction at the wind-tunnel jet shear layer.

For comparison with numerical results, a correction of the aforementioned refraction has been applied to WTT data. Amiet's refraction 2D model [110] has been used to this end. The correction does not take into account additional refraction due to the mean shear of the

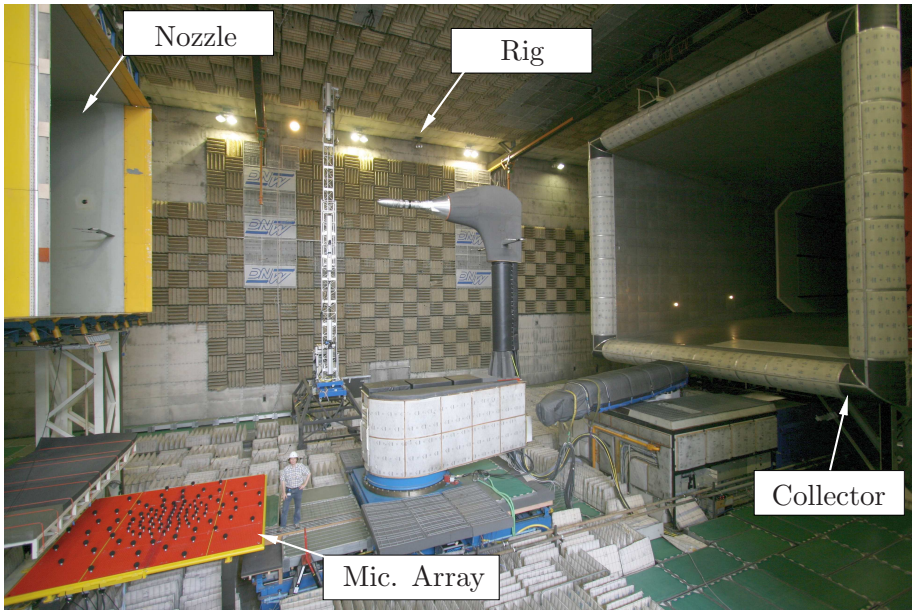

Figure 5.2: *Open test-section at DNW LLF.*

propeller inflow, for which results at downstream angles must be handled carefully. Besides, the model neglects noise attenuation due to haystacking through the shar-layer turbulence. Due to transmission through the shear-layer, the energy of sharp frequency peaks is distributed in the surrounding frequencies, resulting on a broader blunt peak of less amplitude at the peak frequency [111].

5.2 Radiation Routine Assessment

In Sec.4.2 is developed a theory for computing the acoustic far-field radiated by a rotating point dipole, the strength of which is defined with arbitrary radial, tangential and axial components. The source provided by the blade response model is the pressure jump on the blade MCS. Each equivalent dipole is aligned with the normal to the associated MCS lattice, assumed to be acoustically compact. Note that the present routine interprets every force fluctuation as a lift dipole radiating efficiently. However, CFD wall pressure could contain pressure fluctuations associated to non-radiating phenomena on the one hand, and tangential forces due to viscosity on the other hand. Since the noise source used in this assessment must be correctly interpreted by both radiation tools, it seems appropriate to use a source composed only by pressure jump

fluctuations because the analytical source model is inviscid. Viscous forces are ignored but they remain negligible in comparison to lift forces. For the test, the source is provided by the analytical blade response to the wakes generated in the CHIMERA simulation. KIM is used to compute the far-field noise. The inputs required by KIM are the position of the rear-rotor and the source distributed on its blades at each time step. An inverse Fourier transform is applied to the loading harmonics to find the time-domain source to be distributed on the blade MCS coordinates, varying at each time value. The propeller is assumed to be at zero incidence, so that an axial flow opposite to the flight direction is included in both computations. The results of this comparison are analyzed in the frequency domain, for compatibility with further results presented in this chapter. As shown in Fig. 5.3, an excellent agreement is found between both routines in terms of levels and trends at least for the modes (1,1), (1,2) and (2,2). For other modes, at observation angles far from 90°, significant sound levels are predicted by the numerical simulations whereas the analytical solution in the frequency domain drops to zero on the rotation axis. These discrepancies are likely due to numerical spurious noise induced by the procedure applied to feed KIM. However, they occur at levels lower than the SPL of interest.

These results validate the analytical routine for noise prediction, used in the following assessment steps to show the noise sensitivity to source variations.

5.3 Assessment of Blade-Response Model

The blade response model is evaluated using CFD results obtained with the chorochronic technique. The finer meshing allows a better modeling of rotor-rotor interaction, especially for high loading frequencies. The numerical upwash as seen by the rear-rotor blades is obtained using the procedure exposed in Sec. 2.4. This data is used as input for the analytical blade model, detailed in Chapter 3. For this computation the rear-blade MCS was split into 19 radial segments. Equivalent flat plates were computed from LMS interpolation for the 15% of the blade chord, from the leading-edge. Each equivalent trapezoid has 61 nodes in the chordwise direction and 7 nodes in the spanwise direction. The obtained sinusoidal gusts are projected in the principal directions of the equivalent trapezoids, using the relationships in Eq.(3.41). The pressure jump on each trapezoid is computed from Eqs.(3.32) and (3.36). Finally, the analytical blade response is obtained after source phasing, following the technique exposed in Sec. 3.3.2.

This analytical unsteady lift is compared with the numerical unsteady wall pressure directly

found from the same CFD computation of the upwash used above. It must be noticed that the analytical result also depends on the procedure of upwash computation and expansion in sinusoidal gusts. A comparison of the analytical loadings with the CFD wall pressure assesses both the blade response model and the routine defining the input. Further tests should be performed to assess these functionalities independently.

The source non-compactness prompted the assessment of its distribution on the blade surface. Also, 2D graphs are provided at constant radius for a finer source comparison. For completeness, the extended blade response is compared to Amiet's theory for high-frequency interactions with parallel gusts (k_2^*=0 in the notations of Sec. 3.1), in order to evaluate the enhancement provided by the theory extension developed in Sec. 3.2 with respect to current prediction schemes.

5.3.1 Compared CFD and Analytical Loading Distributions

The code capability to predict the unsteady lift from a numerical upwash is now assessed. Comparisons are carried out in the frequency domain, for which a Fourier transform of the original CFD field is necessary. The time domain data at each blade point is transformed to the frequency domain, so that the surface distribution of each loading harmonic can be plotted by selecting the value of the same frequency peak at each blade point. Such a plot is compared to ORION output in Fig. 5.4 for the first loading harmonic ($k = 1$). A good agreement is found in terms of amplitude distribution, except in the tip region. The rear-blade tip-vortex may be responsible for this difference. The concentrated hub loading (attributed to front-rotor stall due to hub boundary layer) is correctly predicted by the analytical blade response. However, CFD data presents a faster amplitude decrease in the chordwise direction. Phase predictions present more significant differences. Particularly, the source phase inversion in the trailing-edge region up to the mid-span is not predicted by the analytical tool. The differences could be due to a hub effect not modeled in analytical theory. However, even if phase distributions disagree in this region, the impact on noise radiation could be negligible given the concerned loading amplitudes. Higher harmonics were also compared to find if this phase disagreement persists as frequency increases. In Fig. 5.5 is shown the same comparison, now for the second loading harmonic ($k = 2$). The phase prediction is quite satisfactory at this source frequency, except in tip and hub regions. A pronounced variation concentrated near the blade leading-edge suggests the presence of a leading-edge vortex, later mixing with the rear-

rotor tip-vortex. The phase disagreement at mid-span in Figs. 5.4(b) and 5.4(d) is not observed at higher harmonics, therefore it is likely associated with a phenomenon occurring only at the fundamental interaction frequency. Globally, the blade model provides good predictions of the source surface distribution.

Two-dimensional comparisons are now used for a finer assessment of source amplitude and phase predictions. The comparisons are made at $r/r_T = 0.55$, which is lower than the leading-edge excitation probably due to a vortex reattachment. In Fig. 5.6 are shown the three first loading harmonics at this radial value. The CFD unsteady lift is compared to the present response function and to that obtained with Amiet's 2D theory. The circles represent the loading maximum at leading-edge, obtained with the analytical integration presented in Sec. 3.3.2. One surprising conclusion of this test is the capability of the 2D Amiet's theory to predict loading amplitudes and phases. Small differences are observed between both models, especially in terms of amplitude. However, the extended theory predicts a higher loading at the leading-edge, closer to the CFD results. The fact that a skewed supercritical gust produces higher interaction amplitudes has been pointed out in Sec. 3.1.3, from analysis of Figs. 3.2 and 3.3. The value of $\tilde{A}_{le}$ increases with gust inclination in the supercritical region. Nevertheless, the radiated noise tends to be reduced for a skewed gust due to source phasing in the spanwise direction.

In the present comparisons, the noise source seems to be correctly predicted by the methodology in terms of amplitude and phase, using both response models.

The model capability of predicting the source distribution at a given time step is also evaluated in this section. The required time snapshot is obtained by inverse Fourier transform of the first four analytical loading harmonics. For comparison, the unsteady CFD wall pressure is also computed by dropping the time-averaged value from the total field. Both outputs are compared in Fig. 5.7 at an equivalent time. The loading levels and surface distribution are in rather good overall agreement. As expected, major differences are observed in tip and leading-edge regions. The phase inversion near the hub observed in the first harmonic is probably responsible for the differences of time domain data in this region. Anyway, the present assessment shows that ORION is able to realistically predict the blade loadings induced by a numerical upwash. The subsequent step consists in the evaluation of the differences of the noise emitted by analytical and CFD loadings.

5.3.2 Noise Sensitivity to Source Convergence

Prior to the comparison of CFD and analytical loadings in terms of noise signature, it is necessary to assess the sensitivity of noise to source definition. In other words, source convergence, already studied in Sec. 3.3.3, is now evaluated in terms of radiated noise. Besides chordwise and spanwise meshing, which must ensure acoustic lattice compactness, the source is sensitive to the blade radial segmentation. When the problem is sliced in different radial regions, an equivalent wake inclination and blade geometry is defined for each radial slice, from which sweep velocity and relative segment phasing are defined. If the segment count is changed, the routine generates a new set of equivalent problems, providing an entirely new source phased with different sweep velocity values. The convergence of this process to blade segmentation is evaluated in Fig. 5.8 for some harmonics and for the rotor-rotor interaction OASPL, computed for combinations of $(k, m) \in [1, 4]$. The figures in Fig. 3.16, show the convergence to radial blade segmentation of the first loading harmonic ($k = 1$), responsible for the noise in Figs. 5.8(a) and 5.8(b). As observed, noise predictions vary within a range of 5 dB from the coarser to the most refined blade segmentations, keeping always the same directivity trend. From 19 segments the results converge into a range of 1 dB, for which this quantity of segments is retained as a reference for future computations. The OASPL sensitivity to chordwise and spanwise meshing is shown in Figs. 5.8(e) and 5.8(f). As expected, the convergence of noise for these parameters is faster. The radiation scheme seems to be robust with respect to the source definition.

5.3.3 Noise Prediction for a Numerical Wake

The noise obtained using chrochronic upwash and blade response model, for Amiet's theory with $k_2^* = 0$ and extended Amiet's theory, is now compared to the results obtained with the chain elsA-KIM and WTT measurements. It must be noted that noise measurements combine all interaction mechanisms and sources of noise, including radiation from the front-rotor and potential interactions. The comparison with experimental data is relevant only for noise harmonics whose main source is located on the rear-rotor. Using the solid FW-H formulation on both propellers, we are able to identify the noise harmonics fulfilling this requirement, and therefore eligible for the aforementioned comparisons. In Fig. 5.9 are presented the results for some noise harmonics dominated by the rear-rotor. Rotor-rotor interaction OASPL is also compared to provide a global assessment of noise predictions. It is observed that the measured lobe locations are in disagreement with both analytical and CFD predictions. The refraction correc-

tion applied to the measurements is believed to be one the causes of these differences. Indeed, the correction assumes an homogeneous and thin open-jet shear-layer, whereas its thickness increases from the nozzle to the collector. Besides, as already mentioned, noise refraction through the shear-layer caused by propeller inflow is no modeled in the correction. Nevertheless, since lobe levels are supposed to be less affected then their position, a qualitative assessment is always possible from this data. The agreement in terms of number and amplitude of lobes is quite good for both 2D and 3D theories, with respect to elsA-KIM predictions. Furthermore, experimental trends seem to be well predicted by the numerical and analytical schemes.

The extended blade response seems to provide closer predictions to elsA-KIM reference, since it provides generally higher noise levels than the Amiet's theory with $k_2^* = 0$. It is observed that analytical predictions overestimate the reference in the downstream region, whereas a better agreement is found for the upstream angles. It is possible that leading-edge and rear-blade tip vortex be responsible for these differences, but no research has been yet conducted to verify this hypothesis. The present evaluation shows that the scheme provides a reliable tool for assessing not only trends but also absolute values for blade aeroacoustic design.

The enhancement in acoustic predictions achieved with our theory extension could be higher for modern blade geometries, characterized by stronger 3D features than the blade selected in the present assessment [24].

5.4 Sensitivity to Wake Inputs

The noise prediction scheme has been assessed using numerical inputs, in terms of unsteady loading and radiated noise. The sensitivity of noise to the wake input is now studied. The wake models presented in Sec. 2.2 are used here as aerodynamic inputs for noise prediction. The evaluation is twofold. First, the effect of wake on blade loading is assessed using source distribution graphs and 2D plots. Secondly, the noise produced by the related sources is evaluated.

Wake tangential profiles have been compared in Sec. 5.4.1. Another important aspect of the 3D excitation is studied in the present section, namely the inclination of the central-wake sheet with respect to the blade leading-edge. All the analytical wakes are assumed to follow the front-rotor chordwise direction, whereas CFD wakes include swirl, Coriolis forces and propeller-induced velocities as deviation parameters. These methods provide different upwash inclinations

to the rear-rotor blade, as shown in Fig. 5.10. As a consequence, the sweep velocity of the excitation is changed for these inputs, from which a different source phasing is defined. To clarify this point, the source time delay at the blade leading-edge ΔT, with respect to its reference at hub, is presented in Fig. 5.11 for analytical and numerical wakes. Negative slopes of ΔT represent sweep velocities towards the hub. The numerical upwash sweeps the leading-edge towards the hub for $r/r_T < 0.6$, whereas the analytical upwash sweeps the leading-edge towards the blade-tip on the entire leading-edge. This means that sources produced by the analytical upwash are more phased over the blade surface. The effect on loading and noise of source phasing is evaluated subsequently.

5.4.1 Comparison of Wake Inputs

The upwash patterns obtained with analytical and numerical techniques are now compared, for an isolated CROR engine without incidence. In what follows, the chorochronic input is taken as reference for comparison with the analytical models defined in Sec. 2.3. The upwash is normalized by the incident velocity to the front-rotor $U_0(r)$, computed analytically from flight speed and front-rotor rotational velocity. In Fig. 5.12 are compared the tangential upwash profiles seen at rear-rotor mid-span. As expected, the isolated-body models are in better agreement with the numerical inputs, whereas rotor-wake models seem to overpredict the wake diffusion and deficit recovery. This agrees with observations by Parry [112]. The Fourier components of these profiles decay faster than the isolated body models. This is explained by the fact that wider Gaussian functions concentrate the energy at low frequencies. For a given wake central deficit, a diminution of the wake width will lead to an energy distribution towards the high frequencies for which the low harmonics will experience a decay in amplitude. This explains why the two numerical inputs of Fig. 5.12 provide almost the same result for the first two harmonics, whereas their tangential profiles greatly differ.

The 3D features of the normalized upwash are compared in Fig. 5.10. The analytical wakes disagree with the shape predicted by the CFD inputs, specially in hub and tip regions. Tip vortices of both rotors, hub vortex excitation, swirl and induced velocities are believed to be responsible for these differences. In terms of amplitude, the best model found for this configuration is the one proposed by Kemp and Sears. However, CFD wakes are thinner than predicted by any empirical model. It is possible that the turbulence gradients in the wake region prevent the wake mixing, thereby leading to a slower deficit decay.

5.4.2 Effect of Wake on Blade Loading

The blade response to a 3D Kemp-Sears wake is compared to its response to the chorochronic wake, in Fig 5.13. Extended 2D Amiet's theory is used in this test. The real part of the first loading harmonic is presented, in order to provide an information of amplitude and phase distribution in a single plot. The higher inclination of the analytical upwash results in a higher source phase lag in the spanwise direction, clearly seen in the blade leading-edge region. Besides the hub excitation, not modeled analytically, source phasing is the main difference between these loadings. Other empirical wake correlations would provide the same spanwise source phasing, defined solely by the wake center-sheet inclination. What will change from one wake model to the other is the amplitude of the interaction, dictated by the wake harmonic amplitude at each radius. The loadings obtained for each wake model are compared in Fig. 5.14, for the same radial value as in Fig. 5.6. A direct relationship between wake harmonic amplitude (depicted in Fig. 5.12(b)) and loading amplitude at the leading-edge can be noticed. Rotor-wake models largely overestimate the leading-edge amplitude of the first loading harmonic, but underestimate the level for higher harmonics. A much better agreement with CFD loading is found for the isolated body wake models, as expected according to the conclusions of Sec. 5.4.1. The response to the chorochronic upwash provides slightly better predictions in terms of 2D loading distribution. These interesting results show that isolated body wake models provide good agreement of both upwash tangential profile and 2D blade loading distribution. The differences in phase caused by the upwash inclination seem to be the parameter to be refined for using these analytical inputs.

5.4.3 Effect of Wake on Acoustic Field

The radiated noise obtained for each wake input is depicted in Fig. 5.15. CFD wake input provides by far a better agreement with elsA-KIM results than any analytical wake model. However, isolated-body models provide good trends and levels, still usable for blade aeroacoustic pre-design. Rotor-wake models provide good predictions of the noise produced by the first loading harmonic, that is at noise frequencies $\omega_{1m} = B_1\Omega_1 + mB_2\Omega_2$, as shown in Figs. 5.15(a) and 5.15(b). The noise produced by higher loading harmonics is dramatically underestimated. The good agreement in OASPL using rotor-wake models puts into evidence the importance of the first loading harmonic in the overall noise production.

Now, it must be noted that isolated-body wake models provide a good approximation of CFD wakes in terms of tangential upwash profile and induced 2D unsteady loading, but agree poorly in terms of wake center-sheet and therefore in terms of source spanwise correlation. To clarify the effect of wake inclination on radiated noise, the source phasing found for the chorochronic upwash is applied to the analytical wakes. This test is easily made by importing the values of V_s found for the numerical wake center-sheet. The resulting noise is plotted in Fig. 5.16 and compared with the noise obtained for the analytical values of V_s. The enhancement in the predictions is surprising. The number and amplitude of lobes are now in fair agreement with both the predictions using the CFD wake and the results of elsA-KIM. This test points out the key importance of an accurate representation of the wake inclination for rotor-rotor interaction noise prediction. Besides, the high sensitivity of noise to non-compact source interferences has been also put into evidence in this test.

Theoretically, a more pronounced front-rotor wake inclination has the same effect as a higher rear-blade sweep, since it is the relative inclination between both which determines the source phasing on the blades.

5.5 Scheme Assessment: RPM Effects

As exposed above, ORION main functionalities have been validated using CFD results as reference. The sensitivity of the whole scheme to the flight conditions is now evaluated, using previous in-house Airbus studies on the RPM effects on CROR noise radiation. For each case tested, WTT measurements are available along with chorochronic elsA-KIM computations. ORION uses chorochronic upwash as input for each computation.

Flight Mach number and rotor pitch are constant in the present test. Only the rotational speed of both propellers varies from one case to the other. The engine RPM is changed from the nominal value at approach to that corresponding to take-off. The test results are shown in Fig. 5.17 for noise harmonics (1,1), (1,2) and (2,2), for which the noise has been shown to be dominated by the rear-rotor. The notations Nx refer to the sum of the nominal RPM value at approach N plus xRPM. N300 corresponds to the rotational speed at take-off, which is 300RPM higher than the nominal value at approach. At a first glance, one concludes that reducing rotational speed leads to a decrease of noise emissions. This is explained by the fact that front-rotor mean loading decreases with rotational speed, which results in a reduction of

the interaction upwash amplitude. Furthermore, a reduction of the equivalent gust convection velocity is obtained when the RPM is reduced. From Eqs.(3.19) and (3.24) it is found that a reduction in both parameters leads to a reduction of the noise source. Besides, from Eq.(4.44) it comes that the pressure amplitude of an acoustic mode is proportional to its modal frequency ω_{km}, which is also reduced as rotational speed decreases.

The theory also predicts that directivity lobes near to the rotation axis are shifted towards the plane of rotation as RPM is reduced. Variations of the rotational speed lead to the same effects depicted in Fig. 4.12(b). Here, the value of $argJ/n \equiv (\omega_{km} R_0 \sin\theta_e)/(D_c c_0 \zeta_{km})$ is increased on the overall angular domain as ω_{km} is raised. As explained in App. A4.5, the set of $argJ/n$ values common to two test cases provides an angular shift of the directivity lobes, whereas the set of different values produces an effective change in the directivity patterns. This analysis, carried out for a single rotating dipole, seems to apply for the present 3D non-compact source, as shown in Fig. 5.17. The directivity shifts are also predicted by elsA-KIM but are less perceptible in the experimental data.

Finally, ORION seems to provide good predictions of the effects of changing the engine RPM on radiated noise.

5.6 Conclusion

The methodology for CROR noise prediction has been assessed in this chapter, using CFD results as reference. The routine for noise computation provides excellent agreement with the time-domain tool KIM, for a noise source composed by pressure forces.

An evaluation of the blade response model has been achieved by comparing the predicted noise sources to CFD unsteady pressure jumps, for the first two harmonics. Even though the leading-edge and blade-tip vortices are not modelled, a good agreement between CFD and analytical source distributions is found in terms of amplitude and phase. Furthermore, the noise predicted for the analytical source retains the principal characteristics of elsA-KIM results. Not only trends, but number and amplitude of directivity lobes is predicted. However, some differences are still noticeable, maybe due to leading-edge or tip vortices. Further research could be conducted for ascertain this point. An open question remains concerning the enhancement achieved with the theory extension developed in the present investigation. It seems odd that

so little progress in the blade response is made in comparison to the classic Amiet's theory ($k_2^* = 0$), especially when one considers the important effects found for fixed segments, as shown for example in Fig. 4.3.

Once the blade-response model is evaluated, the code has been used to assess in detail how different aerodynamic inputs affect blade loading and radiated noise. A relationship has been found between wake harmonic amplitude, loading amplitude and radiated noise. Rotor-wake models do not provide reliable inputs for CROR simulations. Generally, these models result in overestimation of levels for the first excitation harmonic and drastic underestimation for higher frequencies. However, these effects somehow compensate for OASPL predictions, which are in fair agreement with CFD computations and WTT.

The importance of the relative inclination between upwash and blade leading-edge is pointed out in the present assessment. A comparison of Figs. 5.15 and 5.16 reveals the expected sensitivity of changing blade sweep or front-rotor wake inclination.

Finally, the tool capability of predicting increments associated with variations in the simulation inputs is evaluated. Although these relative predictions seem to be overestimated when comparing to WTT results, the present code remains competitive with respect to the much more refined and expensive CFD computations.

The present assessment shows that the developed tool is a good candidate to provide noise predictions for blade aeroacoustic preliminary design.

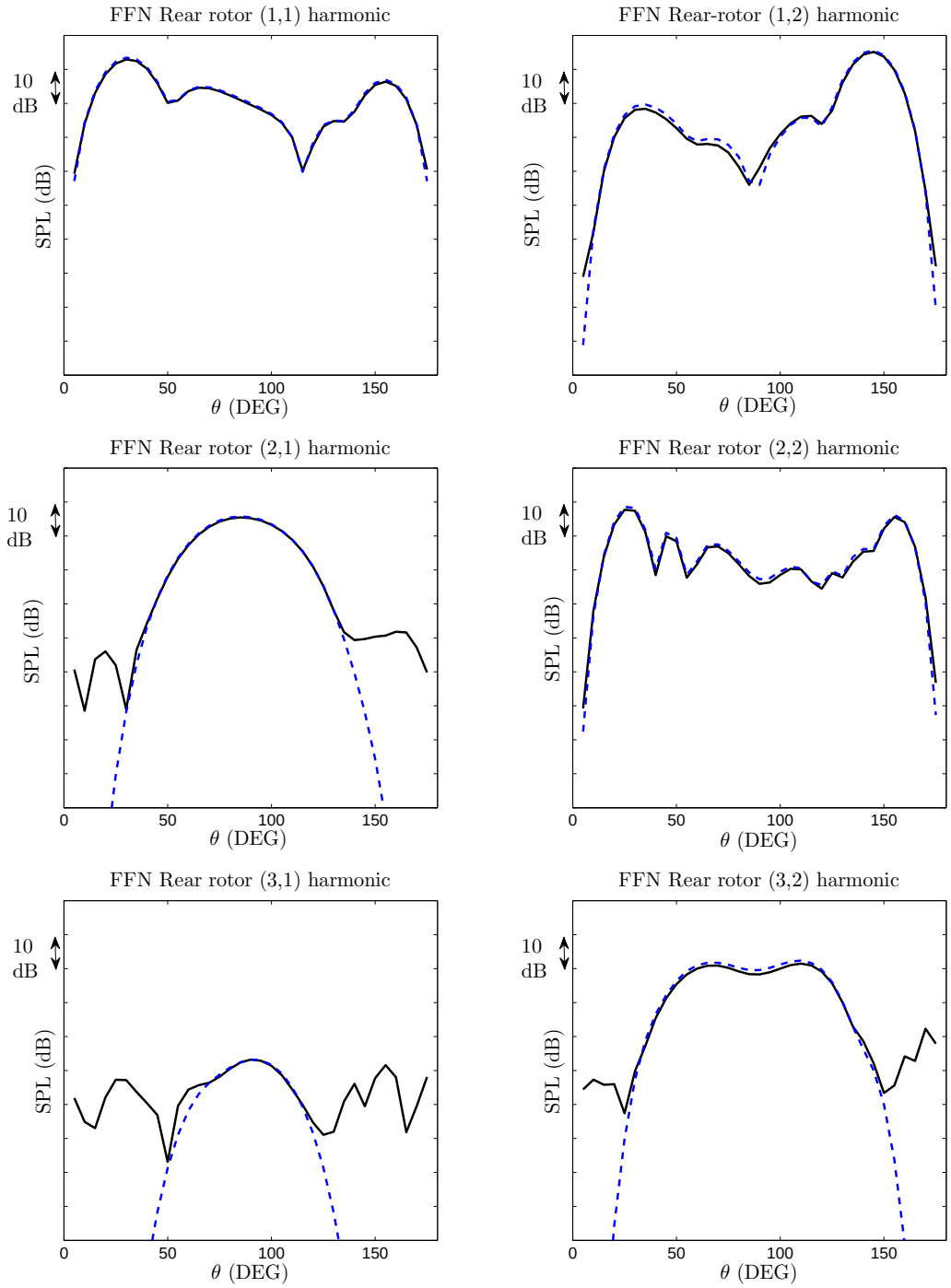

Figure 5.3: *Validation of the general CROR tonal noise formula in Eq.(4.44) by comparison with KIM results. Analytical loadings from CHIMERA Wake. Black line: KIM results for solid FW-H. Dashed blue line: results using Eq.(4.44).*

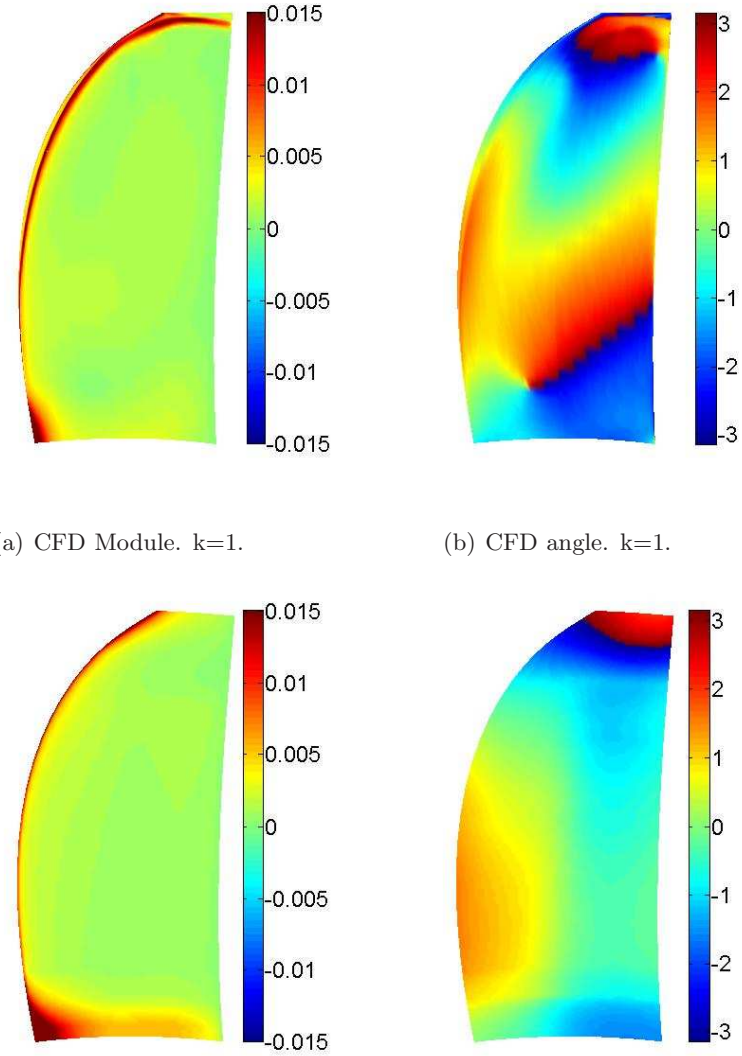

(a) CFD Module. k=1.

(b) CFD angle. k=1.

(c) Analytical Module. k=1.

(d) Analytical Angle. k=1.

Figure 5.4: *Assessment of the first loading harmonic (k=1) prediction. (a) and (b): CFD (chorochronic) unsteady wall pressure. (c) and (d): analytical blade response to chorochronic upwash.*

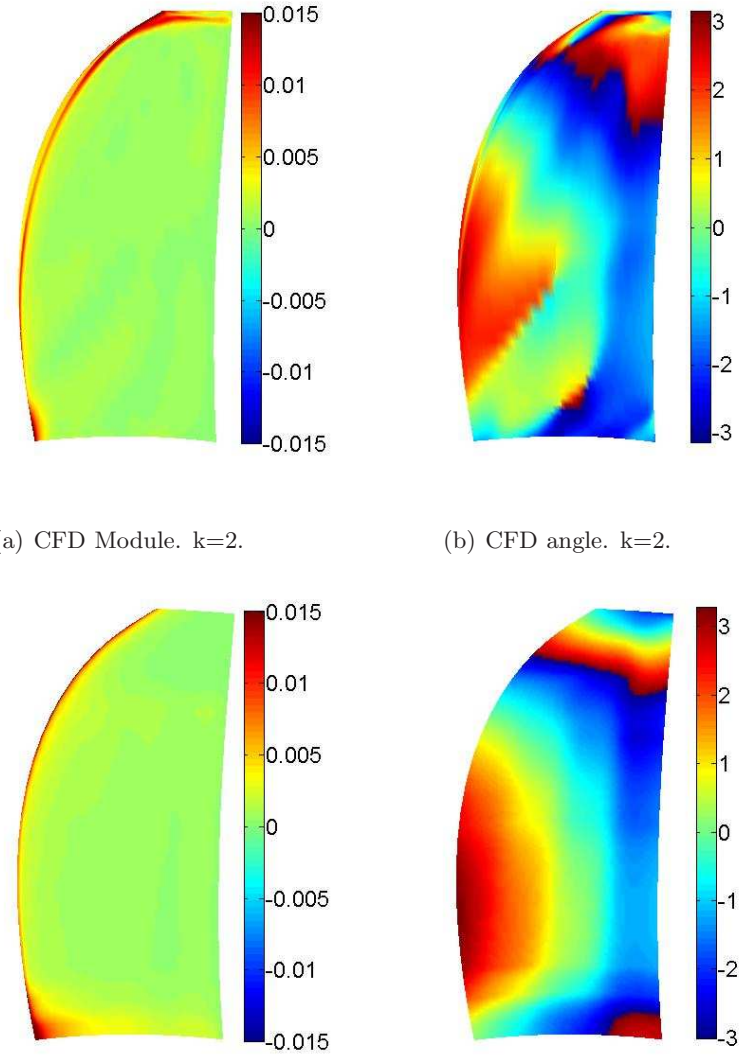

(a) CFD Module. k=2.

(b) CFD angle. k=2.

(c) Analytical Module. k=2.

(d) Analytical Angle. k=2.

Figure 5.5: *Assessment of the second loading harmonic (k=2) prediction. (a) and (b): CFD (chorochronic) unsteady wall pressure. (c) and (d): analytical blade response to chorochronic upwash.*

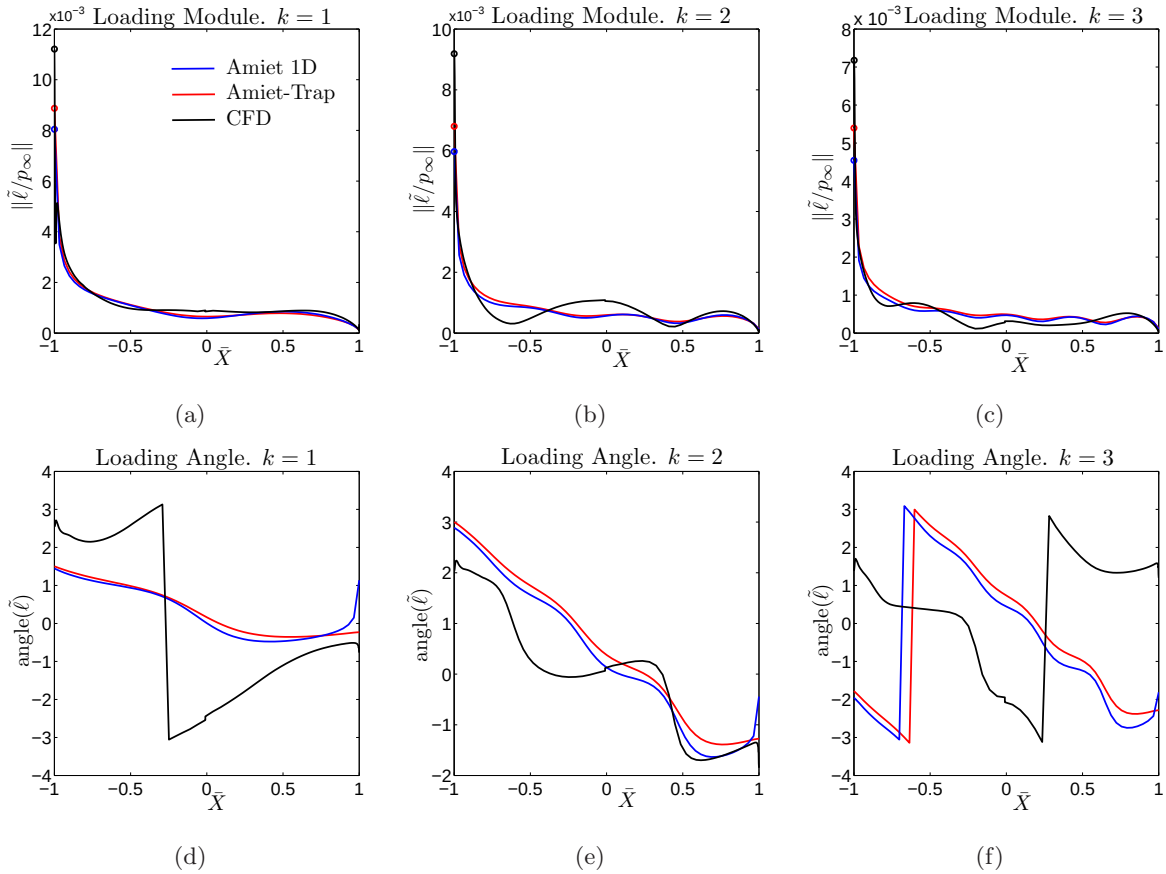

Figure 5.6: *Assessment of predicted unsteady loading at $r/r_T = 0.55$. (a), (b) and (c): Module computation for $k = 1$, $k = 2$ and $k = 3$, respectively. (d), (e) and (f): Angle computation for $k = 1$, $k = 2$ and $k = 3$, respectively. Black line: CFD Wall pressure. Red line: Extended Amiet response of Sec. 3.2. Blue line: Amiet for parallel gusts ($k_2^* = 0$).*

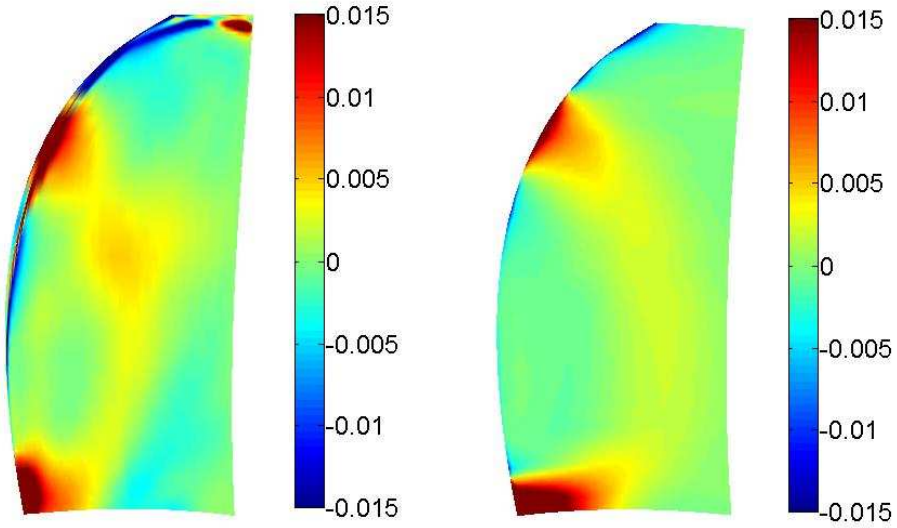

(a) CFD Field (b) Present Model

Figure 5.7: *Unsteady lift ($\tilde{\ell}/p_\infty$) snapshot at a given instant. (a) CFD (chorochronic) unsteady rear-rotor wall pressure. (b) Analytical rear-rotor wall pressure using a chorochronic wake as input. The first four analytical harmonics are used.*

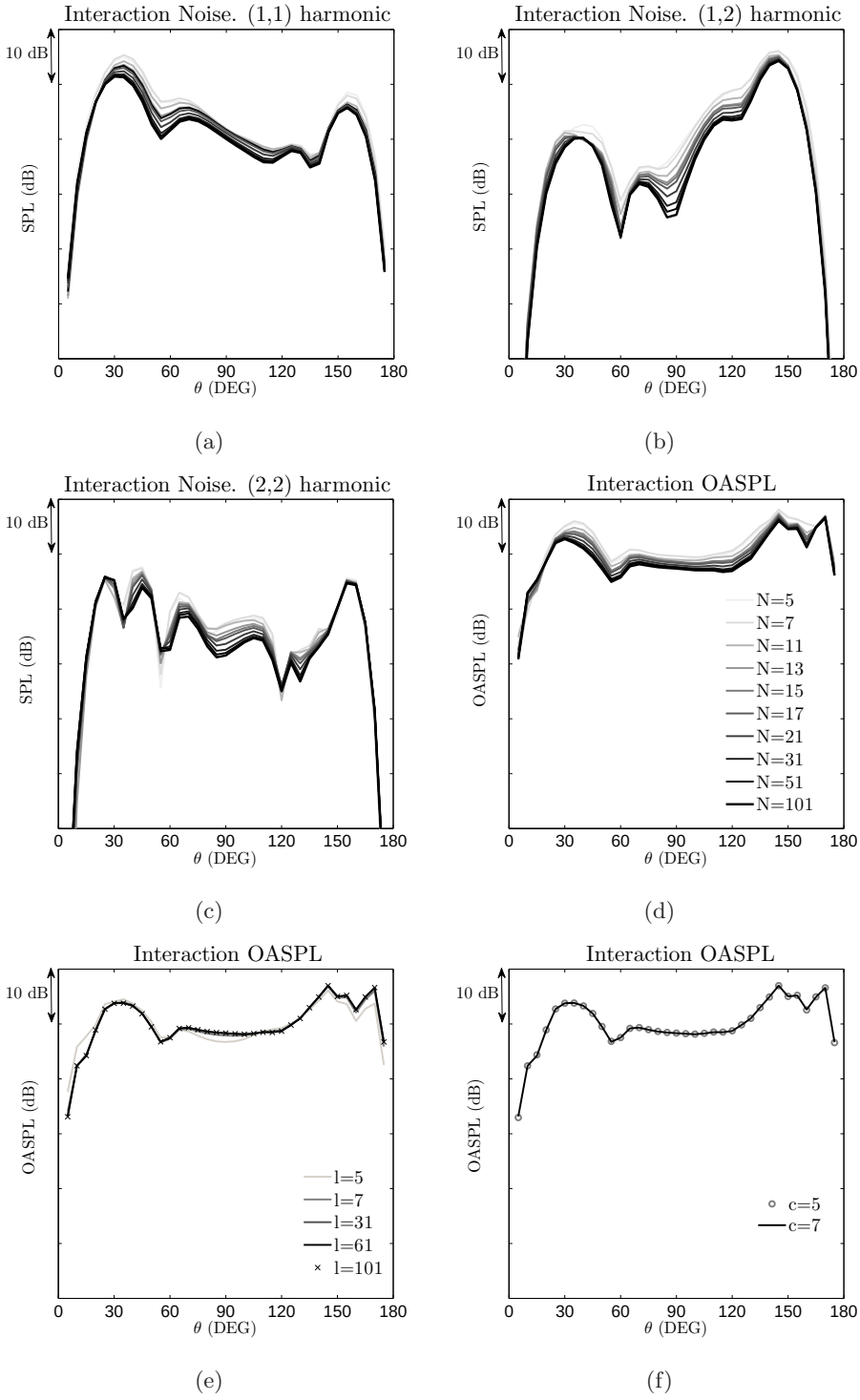

Figure 5.8: *Noise sensitivity to source definition. (a) to (d): Sensitivity to blade segmentation. (e) Sensitivity to chordwise lattices. N=19, c=7. (f) Sensitivity to spanwise lattices. N=19, l=61.*

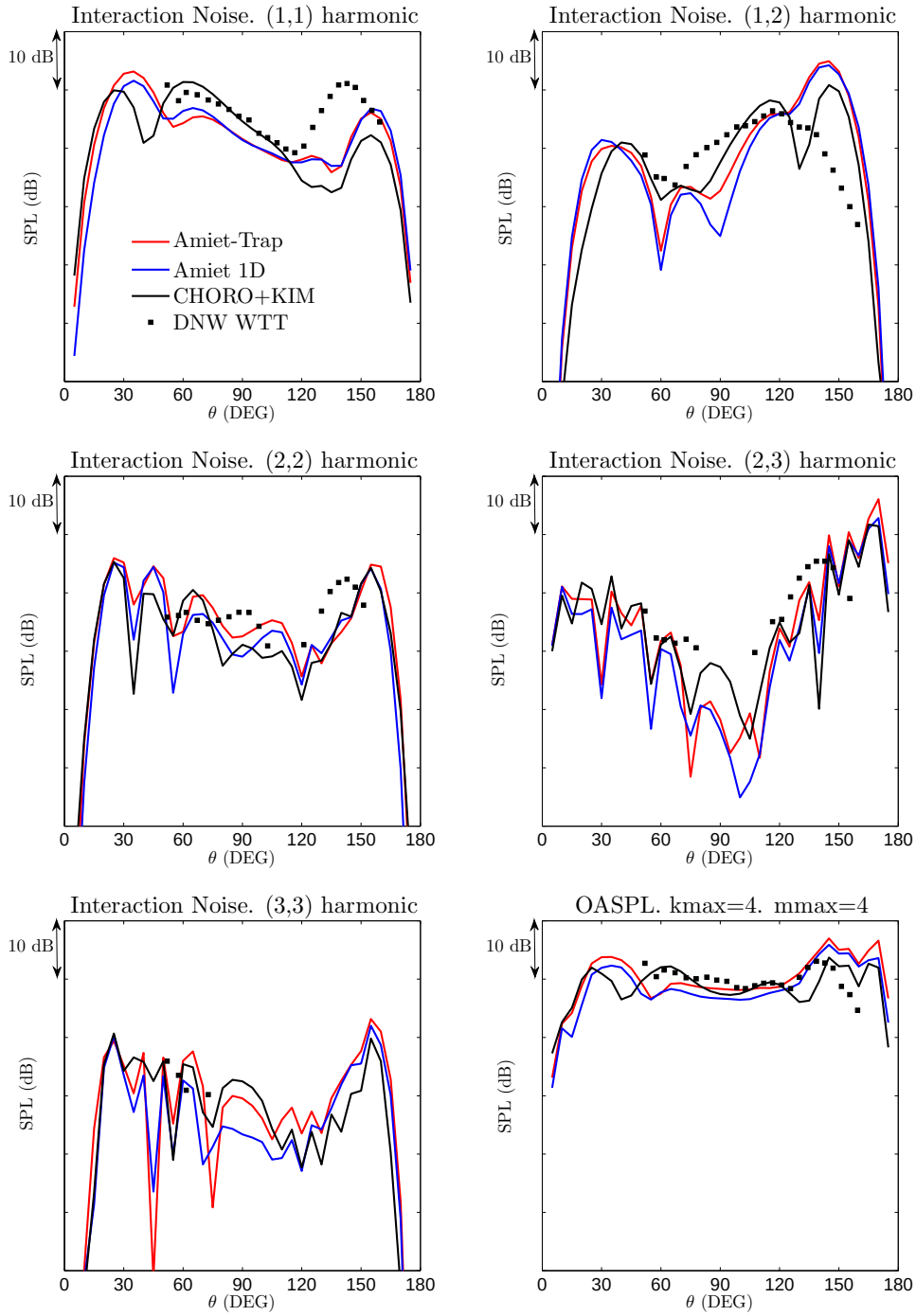

Figure 5.9: *Noise prediction using chorochronic wakes as input data. Blue: Amiet's theory for parallel gusts ($k_2^* = 0$). Red: Extended theory of Sec. 3.2. Black: CFD wall pressure. Dots: DNW WTT.*

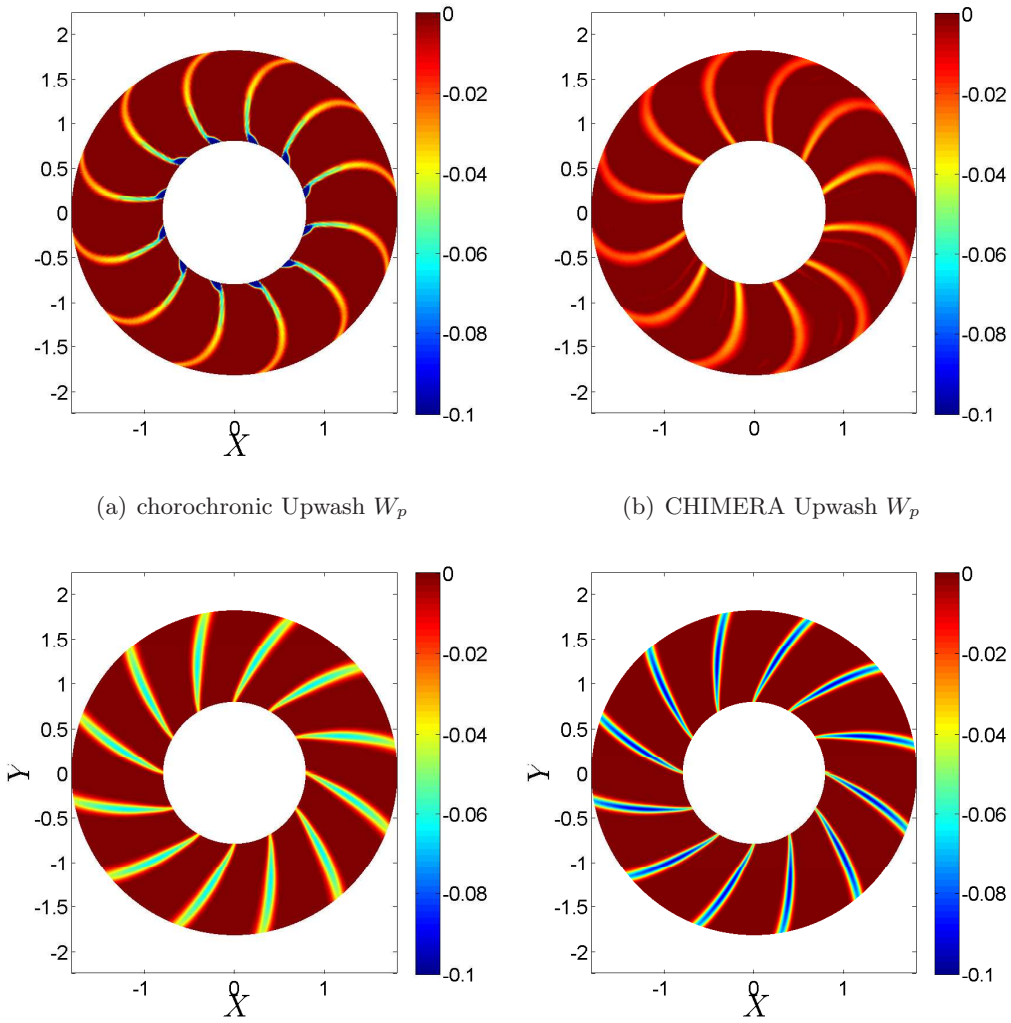

(a) chorochronic Upwash W_p

(b) CHIMERA Upwash W_p

(c) Kemp and Sears Upwash W_p

(d) Schlichting Upwash W_p

Figure 5.10: *Normalized Upwash, $W_p = w_u/U_0$, seen at the rear-rotor leading-edge, from different techniques. (a) and (b): Numerical techniques. (c) and (d): Analytical technique, using isolated-body wake models.*

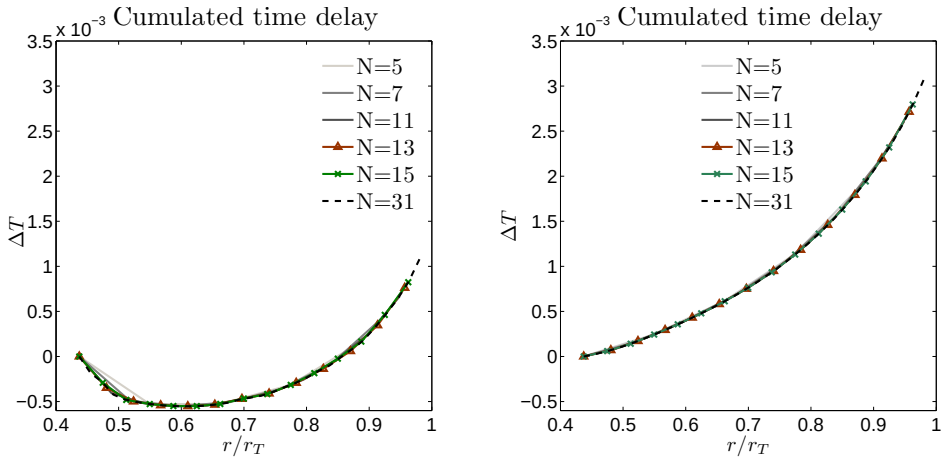

(a) (b)

Figure 5.11: *Convergence of source time delay with respect to its reference at hub. (a) ΔT extracted from Chonochronic input. (b) ΔT extracted from analytical wake center-sheet.*

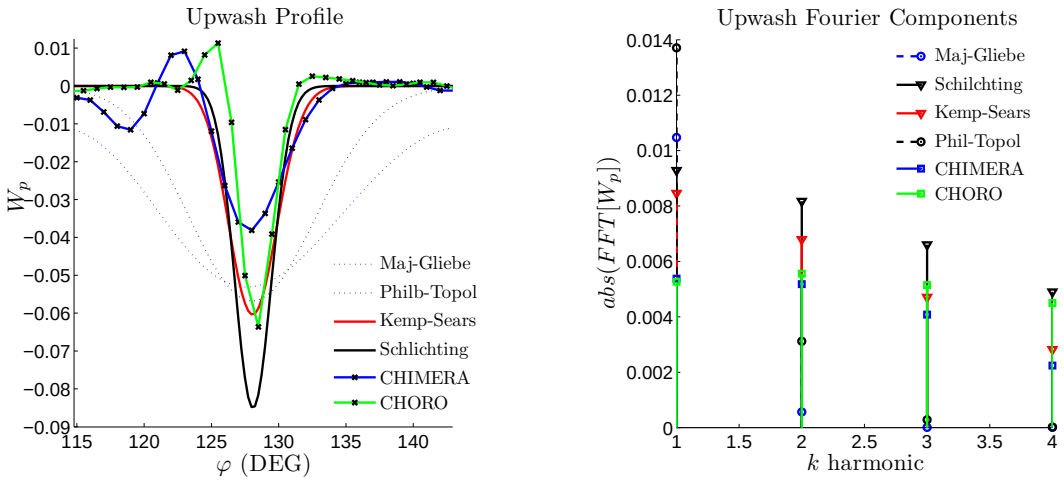

(a) (b)

Figure 5.12: *Normalized upwash $W_p = w_u/U_0$ at rear-rotor mid-span. Comparison for analytical and numerical techniques. (a) Upwash tangential profile. Dashed lines: rotor-wake models. Plain lines: isolated-body models. Crosses: Numerical inputs. (b) Fourier Transform Amplitude. Circles: rotor-wake models. Triangles: isolated-body models. Squares : Numerical inputs.*

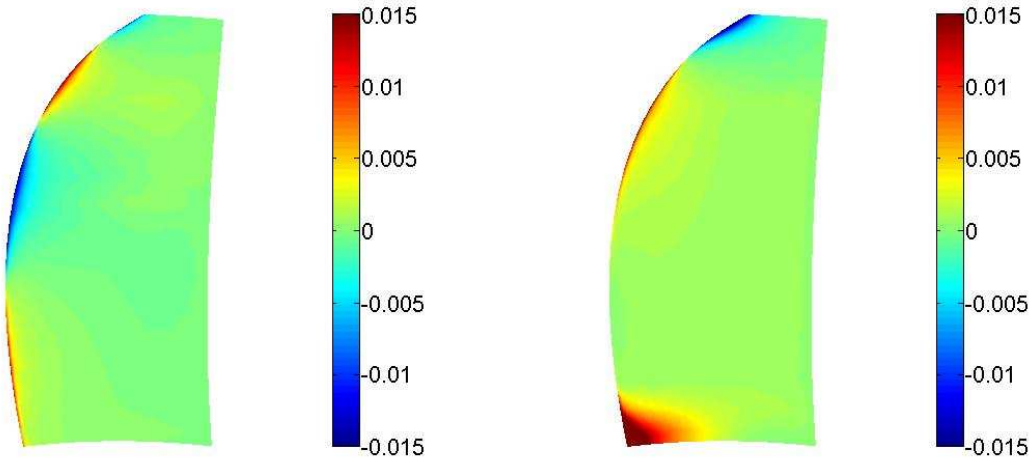

(a) (b)

Figure 5.13: *Real part of the unsteady loading ($\tilde{\ell}/p_\infty$) for the first loading harmonic (k=1). (a) Loadings for Kemp-Sears model. (b) Loadings using a chorochronic CFD wake.*

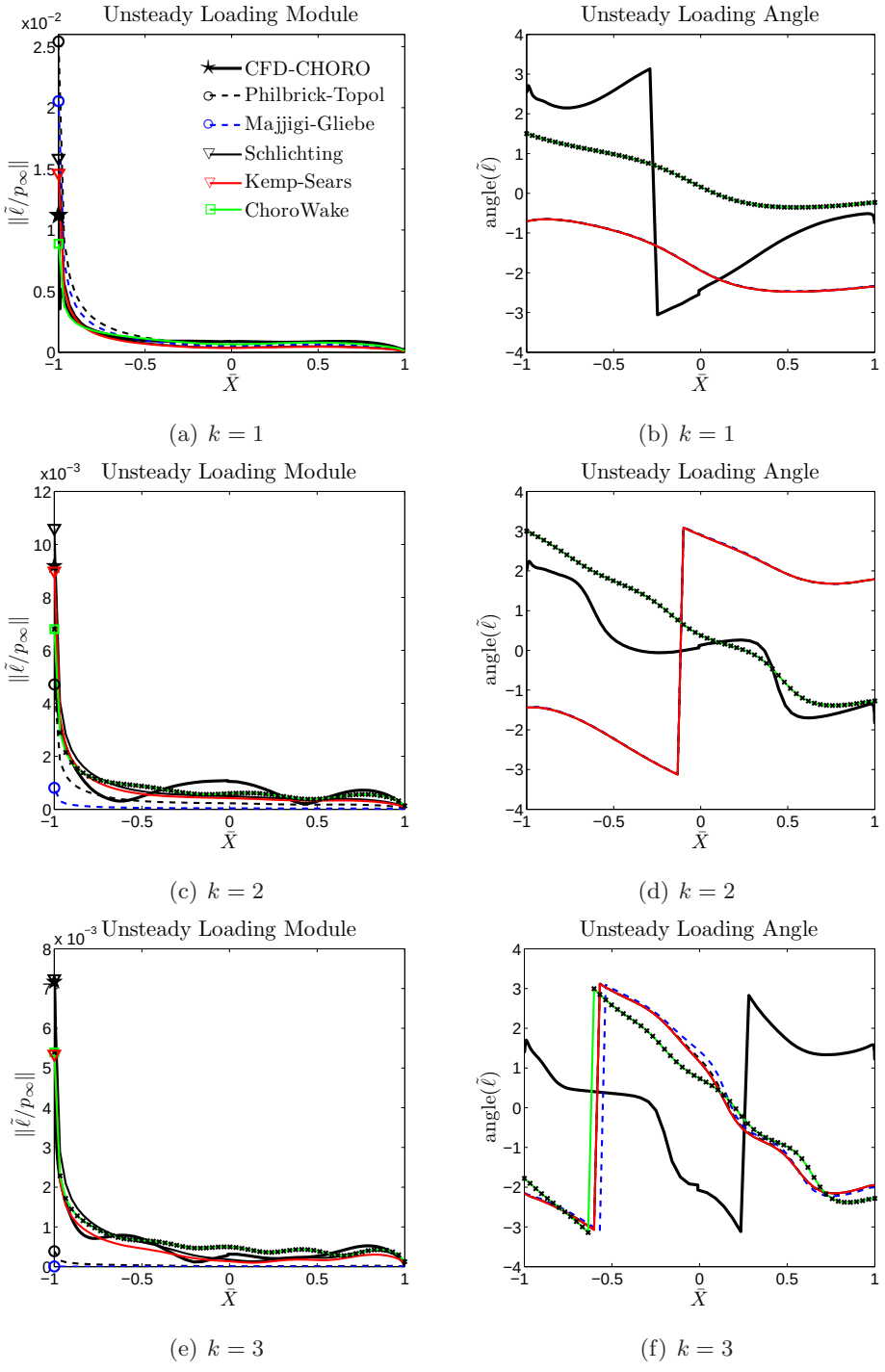

(a) $k = 1$ (b) $k = 1$

(c) $k = 2$ (d) $k = 2$

(e) $k = 3$ (f) $k = 3$

Figure 5.14: *Unsteady loading sensitivity to wake model.* $r/r_T = 0.55$.

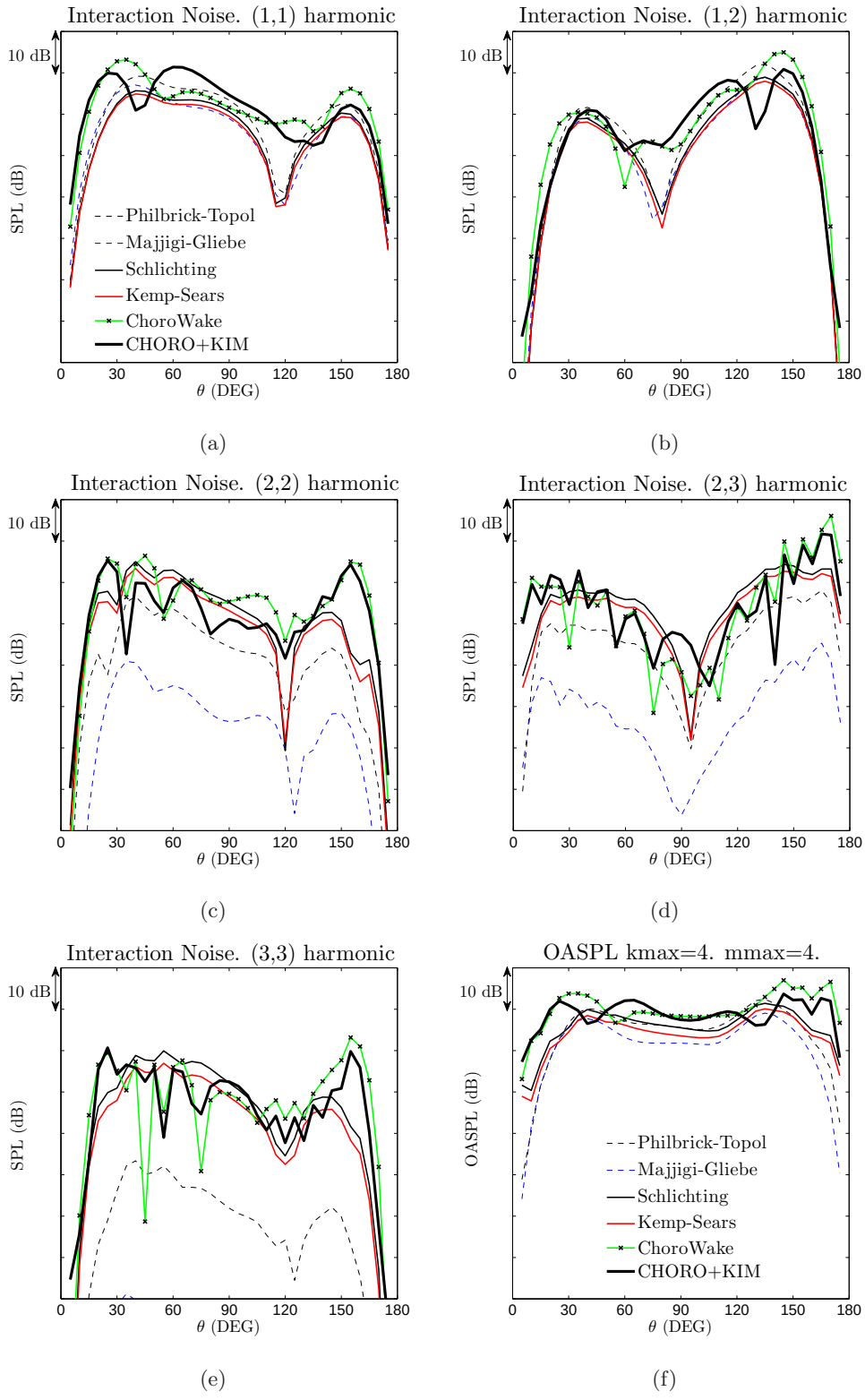

Figure 5.15: *Noise Sensitivity to wake model.*

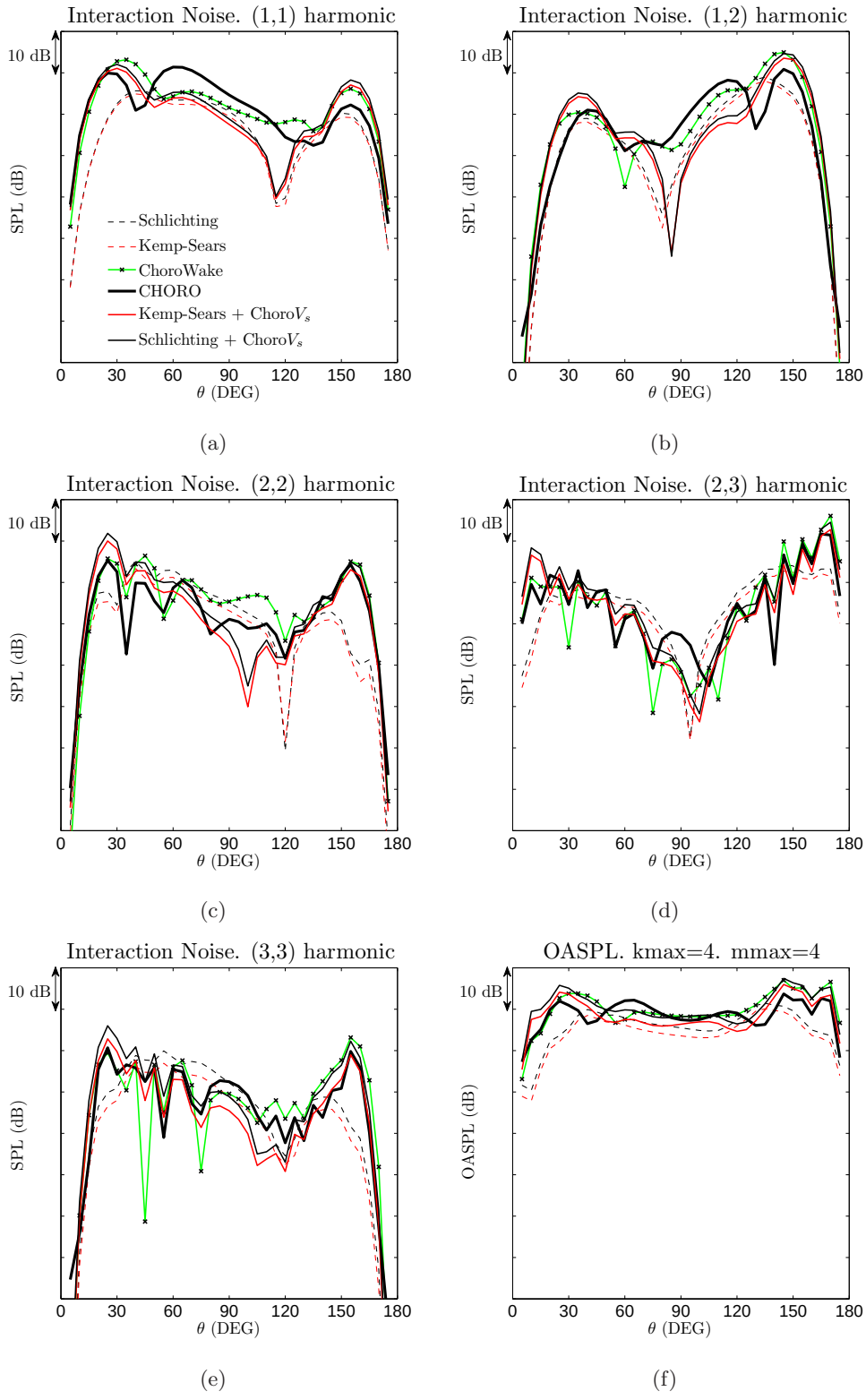

Figure 5.16: *Noise sensitivity to upwash inclination.*

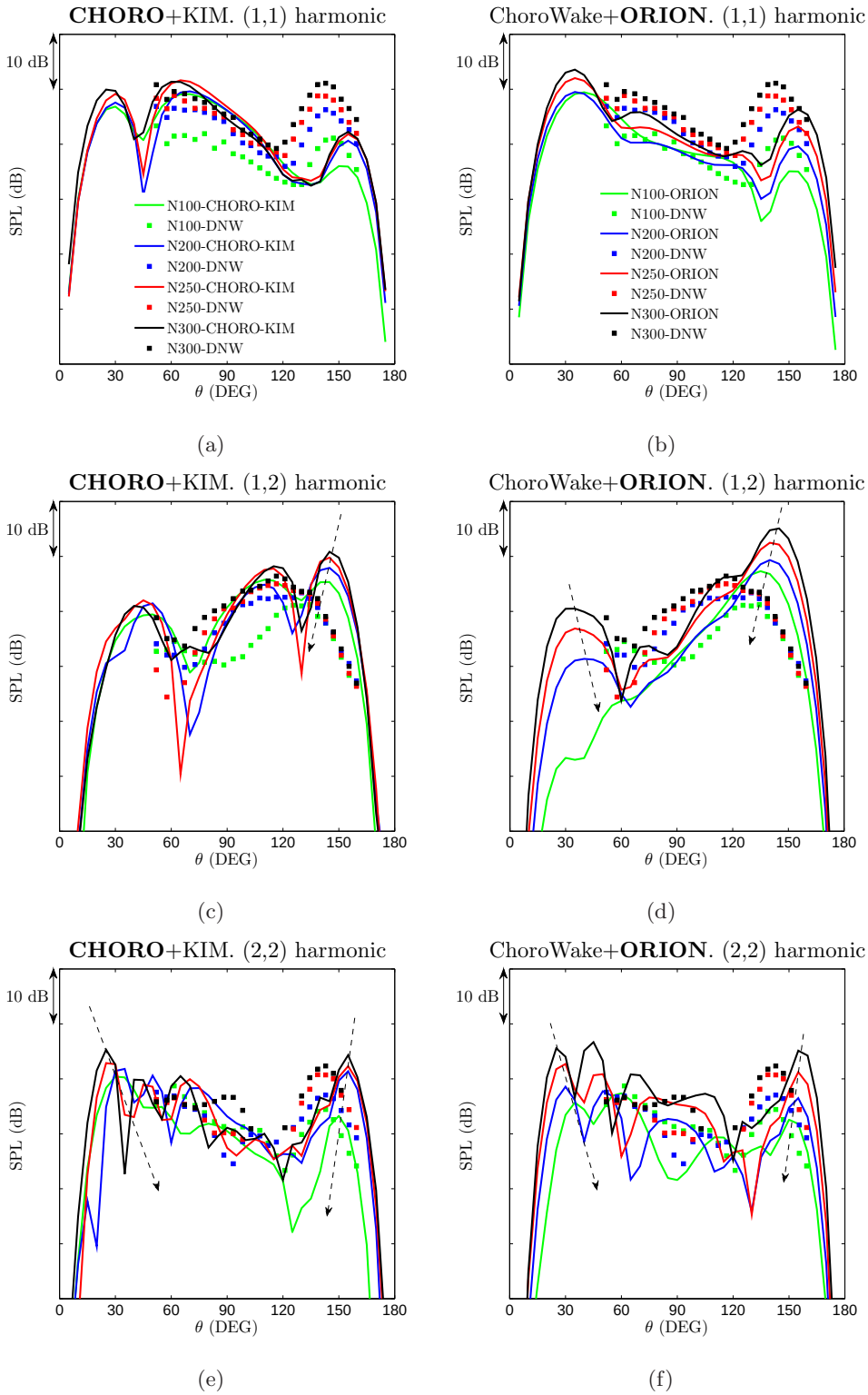

Figure 5.17: *Noise Sensitivity to engine RPM. Green: N100, blue: N200, red: N250, black: N300. Dots: DNW WTT.*

Chapter 6

Way Forward

This final chapter deals with future extensions of the proposed CROR-noise prediction scheme. The methodology has been presented and evaluated for the particular case of an isolated CROR engine embedded in a uniform axial flow. Only noise sources located on the rear-rotor have been modeled. However, since ORION is intended to be used in an industrial framework, there is a need to overcome these initial limitations. Specifically, noise radiation from the front rotor and CROR response to non-axisymmetric excitations must be included.

Some axes of code development are exposed below. First, the representation of the upwash oncoming on rear-rotor blades is addressed. Remarks on the present strategy and perspectives of development are presented. Secondly, the use of ORION for modeling installation effects is outlined. Also, noise radiation from the the front rotor due to interaction with rear-rotor potential flows is discussed. Finally, additional developments not identified as potentially critical are listed for completeness.

6.1 Upwash Modeling

6.1.1 Present Hypotheses

The aerodynamic inputs required by the blade response model can be obtained either from CFD data post-processing or from analytical modeling, using powerplant geometry and flight conditions, as explained in Sec. 1.4. Here are recalled the main hypotheses of both procedures.

Concerning the analytical wake model:

1. The wake of a front-rotor wake is assumed to follow the chordwise direction at each radial value.

2. Each blade wake is modeled independently, using isolated-body wake correlations.

3. The oncoming excitation is assumed to have small variations over the distance covering the rear-rotor chord.

The first item of this list has probably the dominant effect on noise radiation, according to the results presented in Fig. 5.16. Isolated-body wake models are shown to be good candidates for providing ORION inputs. The main disagreements on noise are found to be linked to a wrong representation of wake inclination and not to the prediction of the tangential wake profiles. This limitation should be avoided by including realistic wake center-sheet deviation parameters, such as rotor inflow and swirl. Nevertheless, the lack of rotor-wake correlations applicable to CRORs makes worthy the development of CFD strategies to provide the required inputs. The last item on the list above is also an assumption of the blade response model. It seems consistent with the fact that the rear rotor is located in the front-rotor far-wake region, where wake evolutions are slow. However, if needed, wake evolution in the rear-rotor chordwise direction could be modeled using complex aerodynamic wavenumbers, the imaginary part accounting for exponential wake decrease. Ignoring this effect in the present study is not considered critical because the induced lift concentrates in the leading-edge over a short region.

Concerning the CFD post-processing technique presented in this report, the main assumption is the independence of incident upwash to rear-rotor aerodynamic responses. The numerical data contains already the desired blade response, which has to be excluded from the inputs. The present strategy consists in computing a time-averaged flow in the front-rotor frame, in order to smear out all the excitations which are not rotor-locked. Mean values are subsequently subtracted but, since flow equations are non-linear, the resulting upwash still contains an influence of rear-blade responses. However, this problem will not be encountered in the final version of the methodology. Indeed, a chorochronic CFD upwash has been used for code validation but such refined and expensive computations cannot be prescribed to provide the fast-tool inputs. Faster CFD techniques will be used, in which rear-rotor response to incident upwash is not computed.

6.1.2 Perspectives

The perspectives concerning the analytical wake model could be listed as follows:

1. Include swirl and propeller-induced velocities as deviation parameters of the wake center-sheet. The circulation in the rotor wake can be deduced from the blade circulation due to lift [66]. This information could be imported from available lifting-line tools.
2. Evaluate the effect of tip-vortex circulation on wake inclination.
3. Include hub-vortex in the aerodynamic perturbations.
4. Model the wake decrease with a complex wavenumber in the rear-rotor chordwise direction.

Concerning CFD inputs, an important perspective is the use of fast mixing-plane computations as a part of the present noise prediction scheme. This technique consists in a RANS computation on one blade channel. The coupling between the computational regions of both propellers is ensured by a surface on which the flow is averaged in the tangential direction. In that manner, mean aerodynamic influences of the rear rotor are included in front-rotor wakes whereas its response to front-rotor excitations is properly excluded. The front-rotor wakes are transported up to the mixing plane which must be located as close as possible to the rear rotor. Available mixing-plane tools allow the definition of distorted mixing-plane surfaces featuring the rear-rotor sweep, such as the interpolation surface if Fig. 2.10(a), which increases the interest on this technique.

A preliminary study of the inputs obtained with the mixing-plane technique has been made for the same CROR geometry evaluated in Chapter 5. The mixing-plane is located at half the axial distance between both rotors. The front-rotor wake has been computed for the same meshing as in the chorochronic computation and interpolated near the mixing plane. The corresponding upwash is compared to the chorochronic result interpolated on the surface in Fig. 2.10(a). The comparisons, presented in Fig. 6.1, show the ability of this fast computation technique to provide the needed inputs. Given the shorter axial distance between front rotor and mixing plane, wakes appear more concentrated and less diffused than on the curved interpolation surface. It is also noticed that the chorochronic wakes are more tilted and have a higher hub excitation. This highlights the importance of locating a curved "mixing-plane" surface as close as possible to the rear rotor. A deeper analysis, implementation and assessment of the complete

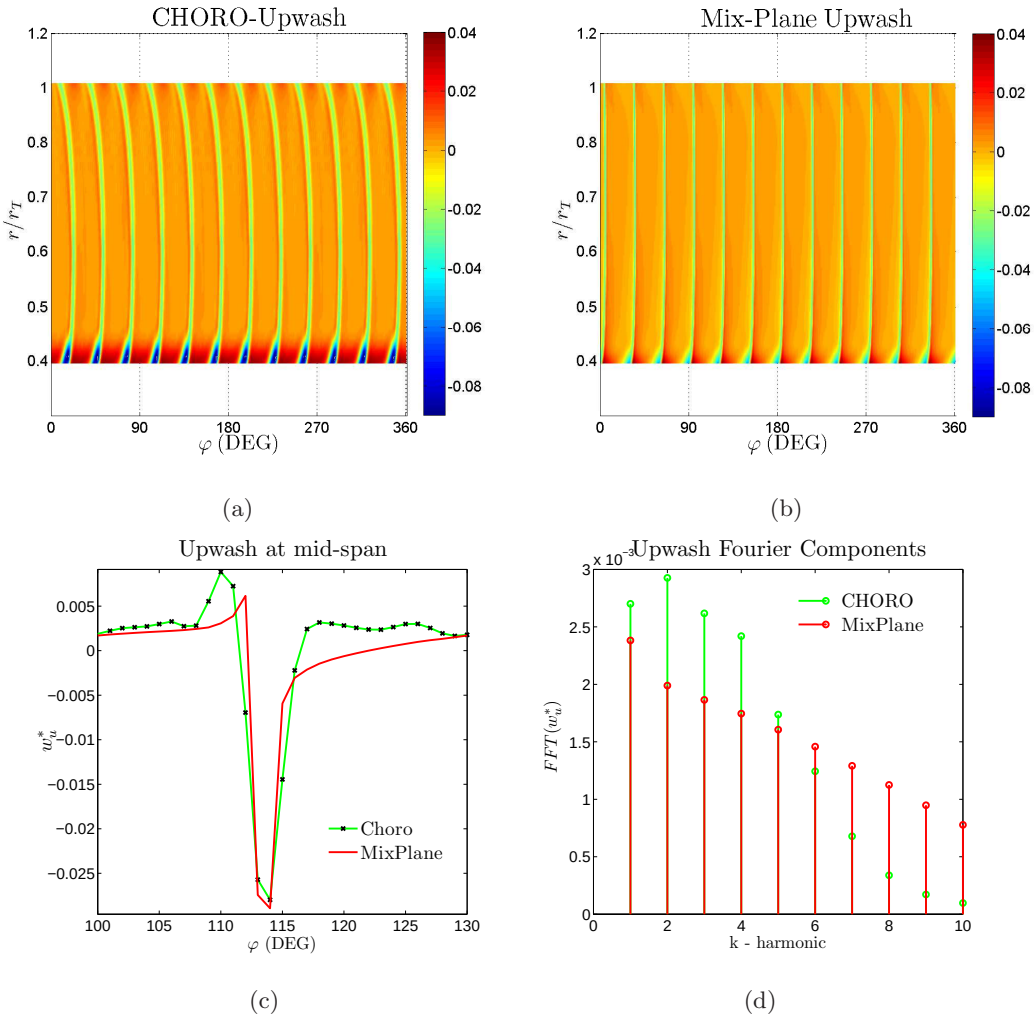

Figure 6.1: *Chorochronic upwash vs. Mixing Plane upwash. (a) and (b): Comparison of upwash inclination. (c) Tangential profiles at mid-span. (d) Fourier Components.*

technique is required for providing the final version of ORION. It should be the first step in further researches.

6.2 Installation Effects Modeling

Structure components used for engine-aircraft integration will probably distort the flow ingested by CRORs, thereby modifying the noise sources on their blades. This is typically the case of the CROR-pusher pylon, the viscous wake of which will impinge on both propellers, considerably increasing the radiated noise. Recent WTT results presented by Ricouard *et al.* show that pylon effects on noise are large on front-rotor BPFs, less pronounced for rear-rotor BPFs and almost imperceptible for the interaction tones [30]. Besides, as shown by Omaïs, the pylon wake modifies in a complex way the axisymetric directivities typical of isolated-rig configurations due to a non-homogeneous convective amplification [113].

In addition to pylon wake, the potential flow from the fuselage and propeller incidence represent non-homogeneous flows to which CROR response is noise. Besides modifying the noise source, the presence of the aircraft body also alters sound propagation. The resulting *acoustic installation effects* cannot be modeled with ORION.

The current state of ORION allows a simple assessment of CROR-pusher pylon effects by computing independently the effect of the pylon on each propeller and then making a linear addition with the already presented rotor-rotor noise results. The pylon can be modeled in the code as a propeller of one blade at zero RPM, its wake being imported from CFD or modeled analytically. Given the expected pylon effects on noise, this simple simulation should be accurate enough. However, using a quasi-stationary approach, a finer modeling of pylon-CROR interaction could be made. The effect of pylon wake on front rotor is depicted in Fig. 6.2(a). As the front-rotor blade gets into the pylon wake, the blade angle of attack is raised. This is typically accompanied by an increase on lift and drag coefficients, for which the front-rotor wake becomes less intense and more diffused, according to the empirical correlations presented in Sec. 2.2. Such lift fluctuations are also accompanied by a higher vortical dynamics in the wake, imposed by the Kutta condition. This could have an effect on the broadband noise produced by the rear-rotor due to turbulence ingestion.

The variety and complexity of installation effects encourage the post-processing of steady CFD computations to obtain the upwash excitations. Flow decomposition in sinusoidal gusts can be performed with the existing ORION routines. Front-rotor excitations must be expressed in the global frame, whereas those impinging on the rear-rotor must be expressed in the front-rotor frame. An example of the excitation seen by a rear-rotor blade is depicted in Fig. 6.2(b)

for the particular case $\Omega_1 = -\Omega_2$. A pylon wake is represented, but the analysis holds for any non-axisymmetric perturbation fixed in the aircraft frame. Since the excitations are presented in the front-rotor frame, front-rotor wakes appear fixed in space while the pylon wake moves in the angular direction at half the velocity of the rear-rotor blade. A first pylon-CROR interaction occurs at $t = t_0$. At $t = t_1$ the rear-rotor blade makes an entire revolution of front-rotor wakes, whereas the pylon wake undergoes only half of the path. Finally, the same interaction as for $t = t_0$ occurs at $t = t_2$ where the blade has covered 4π radians, which becomes the angular period of the excitation. This aerodynamic input can be used to compute the noise source with the present version of ORION. When the two rotation speeds are not equal, there is a different periodicity of the excitations.

Notice that a different upwash is seen by each rear-rotor blade, due to a different combination of pylon and front-rotor wakes. Hanson's simplification in Eq.(4.43) no longer applies. Therefore noise must be computed using Eq.(4.41) for the tonal source described in Eq.(4.42), independently for each rear-rotor blade.

6.3 Potential Interaction Modeling

This section deals with front-rotor radiation at rotor-rotor interaction frequencies. Aerodynamic distortions around the rear-rotor blades and impinging in the front-rotor trailing-edge region are responsible for these interaction noise sources. The objective here is to assess their relative importance with respect to rear-rotor sources at the same frequencies, and ultimately the worthiness of developing a code routine to model the corresponding front-rotor radiation.

In what follows isolated CROR engines are addressed. The contribution of each propeller to total CROR noise can be evaluated using the solid FW-H formulation for the sources located on each propeller, and then comparing these results to linear addition of both acoustic fields. For this test, we use the chorochronic CFD results presented in Chapter 5. Results of such noise decomposition show that front-rotor radiation has a non-negligible influence for noise harmonics verifying $k > m$. Note that the aerodynamic perturbations responsible for front-rotor radiation at rotor-rotor interaction frequencies are compulsory originated on the rear-rotor blades. The interaction mechanism could be linked to rear-rotor potential flows, reflexions of rear-rotor acoustic field or other phenomena. Now, the CFD field contains all these interaction mechanisms, but we are unable to properly separate them from each other. Potential flows retain

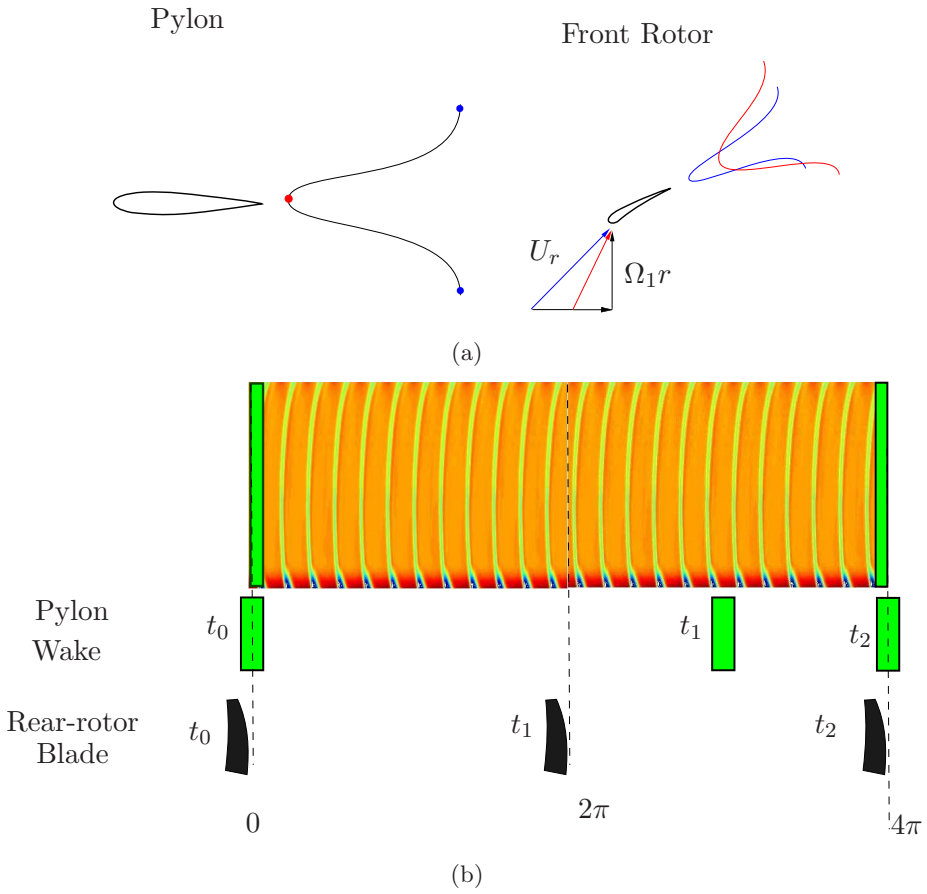

Figure 6.2: *Installation effect preliminary analysis. (a) Impact of Pylon wake on rear-rotor. Colored arrows represent the relative velocity to front-rotor blade. (b) Aerodynamic inputs seen by the rear rotor. Green rectangles represent pylon wake. The analysis holds for any non-axisymetric excitation fixed in the aircraft frame, whenever* $\Omega_1 = -\Omega_2$.

our attention since, to predict their interactions, new upwash and blade response models are required. To assess the contribution of potential flows to the total aerodynamic perturbation, a second modeling of the same problem is performed with the lifting-line code LPC2, the main hypotheses of which are exposed in App. A6.1. In these computations, the aerodynamic perturbations interacting with the front-rotor are only of potential nature. The acoustic radiation from the obtained sources is provided by KIM. In Figs. 6.3 and 6.4 is shown a comparison between the noise obtained for chorochronic and LPC2 sources. The objective here is not the assessment of trends and levels, but that of the relative importance of front-rotor radiation with

respect to that of the rear-rotor. A rough agreement of front-rotor noise between LPC2 and chorochronic computations could suggest that the related sources are produced by potential flows. LPC2 predicts that the front rotor has an important contribution to the total CROR noise at frequencies $\omega_{k1} = kB_1\Omega_1 + B_2\Omega_2$ and that its radiation is negligible for the remaining noise harmonics. The fair agreement in front-rotor noise directivity at frequencies ω_{k1}, for chorochronic and LPC2 sources, suggests that the rear-rotor flow is of potential nature only for these harmonics. This comparison does not represent a rigorous proof of this hypothesis, but encourages further investigations.

An analytical model of the front-rotor response to rear-rotor potential flows could be included in ORION. Parry derived such a model, using the Wiener-Hopf technique [43]. Rear-rotor blades are represented by point vortices, the strength of which is found from the Kutta-Joukowsky lift theorem. An analytical upwash is derived for both incompressible and compressible flows for 2D radial strips. Another approach for modeling potential interaction on rotating blades has been casted by Roger *et. al*, based on the Schwarzschild's theorem [114]. The airfoil response is deduced using the same technique used by Amiet [115], or Roger & Moreau [87], for modeling trailing-edge noise. Potential excitations are computed assuming incompressible fields whereas the blade response accounts for flow compressibility. Recently, the same approach has been used by Conte *et. al* for modeling potential interactions of Brake Cooling Fans (BCF) with structural downstream struts [116]. The application to CRORs is straightforward, but the circulation due to blade lift has to be included. For this reason Parry's model of potential inputs is preferred. However, the latter blade response model is prescribed for its larger documentation and for consistency with the theory exposed in this report. Besides, the elegance and simplicity of Schwarzshild's theorem allows for simple extensions to account, for example, for gust obliqueness with respect to the front-rotor trailing-edge.

An assessment of the response models mentioned above could be made using CFD data. The same strategy of Sec. 2.4 could be implemented, now in the vicinity of front-rotor trailing-edge, the time average being performed in the rear-rotor frame.

A preliminary analysis of unsteady loadings on front-rotor blades can be achieved using ORION routines. In Fig. 6.5(a) is shown a time snapshot of the obtained wall pressure. The source evolution over the blade surface shows the importance of implementing a source-phasing model, maybe based on sweep velocity of potential flows on the front-rotor trailing-edge. Also, by comparing this results with Fig. 5.7, it is noticed that front-rotor loading fluctuations are one

order of magnitude less than those on rear-rotor blades. A FFT of the time data at one point located near mid-chord and mid-span is shown in Fig. 6.5(b). The abscissa corresponds to the value $m = f/B_2(\Omega_1 + \Omega_2)$, which represents the harmonic index of an excitation rotating with the rear-rotor and impinging on the front-rotor blades. A high harmonic content is observed. Following the same analysis as for the loadings on rear-rotor blades, the surface distribution of the first loading harmonic ($m = 1$) is depicted in Fig. 6.5(c). For completeness, a 2D plot of the amplitude of this mode at mid-span is presented in Fig. 6.5(d). A high unsteady lift concentration is seen in the aft part of the blade with a drop to zero at the trailing-edge. From these observations one concludes that the harmonic loading on the front-rotor blades is linked to a field rotating with the rear-rotor and that its chordwise distribution seems to be consistent with trailing-edge interaction theories.

Further research could be conducted to model this interaction mechanism but, in terms of global strategy, this development should come after the modeling of installation effects in the noise scheme.

6.4 Additional Code Developments

In this section are listed further extensions for the models of blade response and acoustic radiation. Before exposing possible ways of improvement, the main hypotheses and approximations of both models are reminded.

6.4.1 Blade-Response Model Hypothesis

The blade response model developed in this thesis is based on the thin-wing theory. Its range of application is therefore restrained to thin blades, lightly loaded and of slight camber. Also, for application to rotating machines, the model resorts to a strip-theory approach. Locally the interaction is formulated in equivalent Cartesian coordinates and uniform flow properties are assumed for each extended strip. The main hypotheses of the present blade-response model could be listed as follows:

1. Mean loading, camber and angle of attack have no influence on unsteady lift. Therefore, blade segments can be approximated by flat segments at zero incidence, for unsteady lift

computation.

2. The unsteady loading produced by fluctuating velocities coplanar with the segment is negligible in comparison to that produced by perpendicular velocities.

3. The present theory accounts only for high-frequency interactions, verifying $\kappa > 0.4$ according to the initial range of application defined by Amiet. Recent research, including the present work, suggests a broader definition range encompassing interactions of lower frequencies.

4. The proposed theory extension accounts only for trapezoids verifying $\sin(\bar{\varphi}_T)\bar{y}_2/2 \ll 1$, in the notations of Sec. 3.2.

6.4.2 Blade-Response Model Perspectives

The comparison between analytical and CFD loadings is rather satisfactory. However, differences could be reduced if the following model refinements are provided:

1. Include a model of unsteady leading-edge vortex.

2. Include a model of rear-rotor tip-vortex.

3. Derive a response function for gusts with a complex wavenumber in the chordwise direction.

4. Include the reflection effect of the hub on the response.

Note that the thin-wing theory might not apply for highly loaded blades, typical of take-off conditions. Flow gradients in the leading-edge vicinity, mainly due to mean loading and actual airfoil shape, could modify the oncoming excitation. To include these coupling effects in the blade response, one could use the Rapid Distortion Theory (RDT) developed by Goldstein and Atassi [117]. The model is based on a linearization of Euler equations around the mean subsonic flow. The theory applies for high-frequency interactions for which the aerodynamic wavelength is small in comparison to the segment chord but large with respect to the displacement of the stagnation point on the airfoil. As shown by Myers and Kerschen [118], flow gradients induced by mean blade loading could have noticeable effects on noise. Since linearity is assumed, the authors

have decomposed the mean loading into two parts, produced by blade angle of attack and by blade camber, respectively. The former component is shown to have larger effects on noise [119]. Mish and Devenport presented a hybrid strategy to include mean loading effects on the incident gust, the unsteady lift being computed with gust-segment interaction Amiet's theory [120]. Fitting the airfoil leading-edge with a circular cylinder in terms of radius and stagnation point, the flow gradients in the leading-edge vicinity are approximated by an equivalent 2D potential flow. These gradients are used to distort the oncoming upwash. The produced loadings are deduced from Amiet's theory. Such a technique represents a good compromise if mean-loading effects are to be included in the present blade response model.

6.4.3 Hypotheses of the Radiation Model

Noise is computed analytically for a rotating dipole source the strength of which is equal to the pressure jump on the blades. The force orientation is assumed to be perpendicular to the local MCS lattice. Also, uniform flows (not necessarily axial) are included in the formula to account for flight effects. The main hypotheses of the present radiation routine could be listed as:

1. Free-field radiation is computed for geometric far-field.
2. A homogeneous mean flow surrounds source and observer.
3. Only dipole sources are modeled.

6.4.4 Perspectives for radiation model

The radiation routine is suited for low-speed flight cases, for which community noise is a major concern. For this reason, a far-field approximation has been made. Including the neglected near-field terms should be cumbersome but straightforward. This extension could provide a general fast-tool for propeller radiation prediction, including propeller excitation on the fuselage.

APPENDIX

A6.1 LPC2 Main Hypotheses

LPC2 is based on the lifting-line theory, initially developed for single propeller performance predictions. The code is suited for computing steady loading sources. However, unsteady loading due to non-homogeneous inflows can be reconstructed using a quasi-steady approach, in which the relative position between both rotors is computed at different time values. At each propeller relative position, the mutual velocity induction is deduced using the Biot-Savart's law, assuming steady flow properties. The code is structured as an iterative strategy in which the mutual induced velocities are taken as input at each iteration. New blade incidence, lift, blade circulation and induced velocities are computed in the new iteration, from which the inputs for the next loop are provided. The main hypotheses of the approach can be summarized as follows:

1. The fluid is inviscid and incompressible for the computation of circulation, induced velocities and incidence angle to the blade. However, the database of profile lift and drag coefficients, stored as a function of the incidence angle, are provided by viscous computations.
2. A 2D problem is solved at each blade strip.
3. The source distribution is acoustically compact in the chordwise direction. However, distribution functions of unitary integral area are used to simulate source non-compactness.
4. The vortex lattices of both propellers extent to infinity.

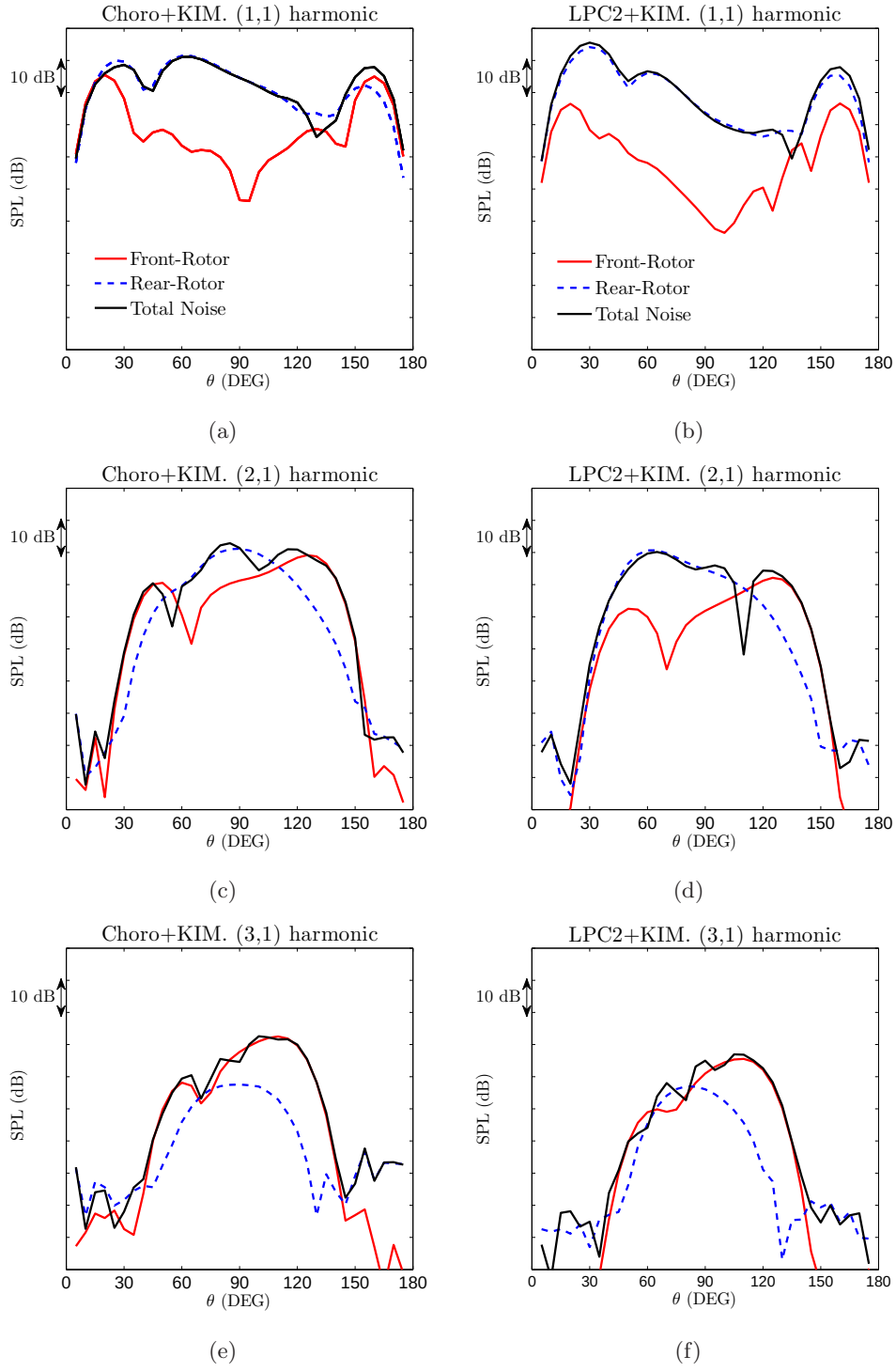

Figure 6.3: *Preliminary Assessment of Potential radiation from the front-rotor.*

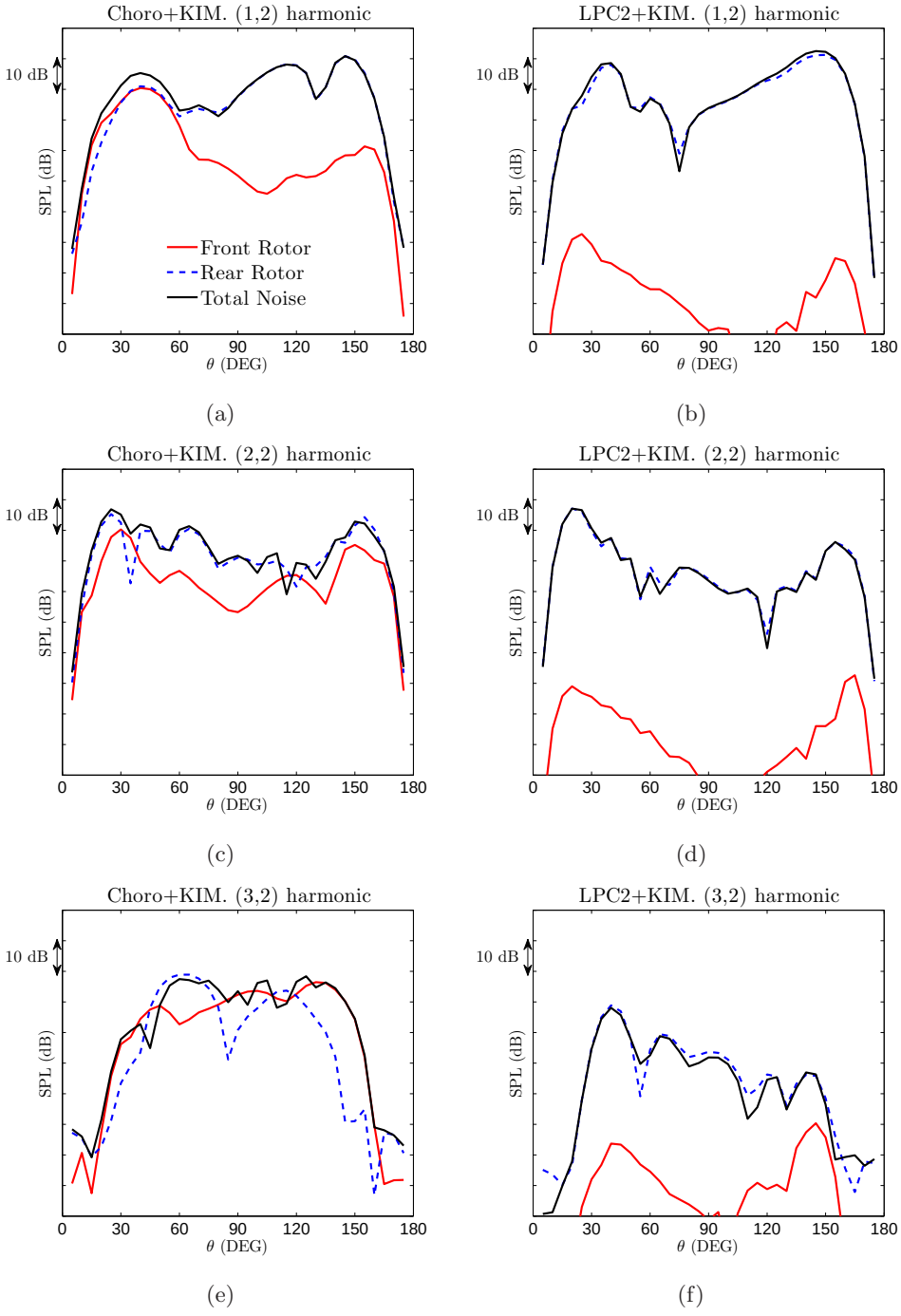

Figure 6.4: *Preliminary Assessment of Potential radiation from the front-rotor.*

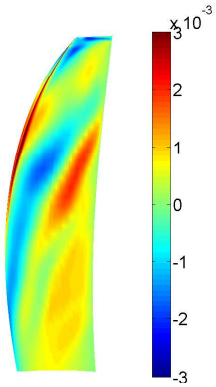

(a) Time snapshot.

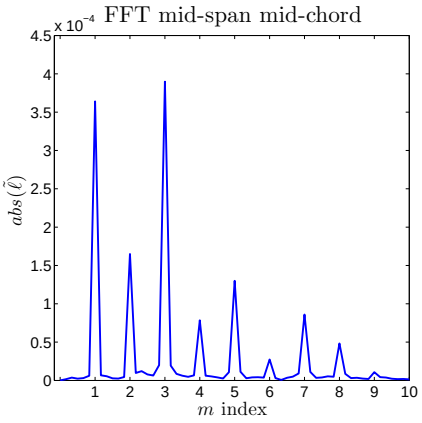

(b) FFT mid-chord mid-span.

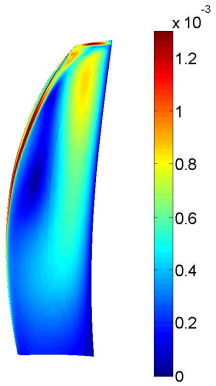

(c) Amplitude Distribution. m=1

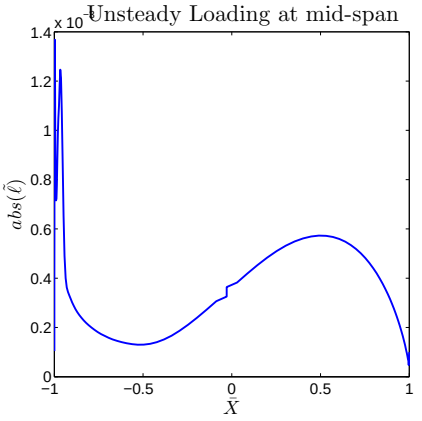

(d) Amplitude at mid-span. m=1

Figure 6.5: *Unsteady loading on the front-rotor blades. (a) Time snapshot of front-rotor unsteady lift $\tilde{\ell}/p_\infty$. (b) Fourier transform of time data near blade mid-chord at mid-span. (c) Amplitude distribution of the first loading harmonic (m=1). (d) Loading amplitude for m=1, at mid-span.*

Conclusion

A semi-analytical methodology for the prediction of CROR tonal interaction noise has been developed, in the frame of a PhD research partnership between Airbus Operations SAS and École Centrale de Lyon. The researches led to the Airbus in-house tool ORION, implemented in Matlab environment. The present thesis presents the models used in the code.

Analytical models have been developed for each physical mechanism involved in CROR noise production. First, a wake model for defining sinusoidal gusts including wake variations in the radial direction has been presented. Secondly, a blade-response model has been proposed, in which 3D geometrical blade features have been included. Finally, an extended acoustic formulation for the CROR case has been presented in detail.

The code assessment provided good results. Noise source predictions are in good agreement with the CFD reference. This trend holds for far-field noise predictions. Better results are found using CFD wakes as input data, in comparison to full analytical predictions. However, analytical wakes provide good levels and trends which could valuable for fast blade pre-design. The methodology is competitive in an industrial framework, although extensions are required for including front-rotor sources due to potential interactions and sources due to aerodynamic installation effects. A detailed conclusion is provided in each chapter. The research highlights are listed below.

Main Outcomes

Concerning aerodynamic inputs

- The proposed analytical wake model is probably a good candidate for providing ORION inputs, if isolated-wake correlations are used. However, a model refinement is needed

to provide a realistic wake inclination with respect to the rear-rotor leading-edge. Noise seems to be very sensitive to this aspect.

- CFD wakes are prescribed as reliable inputs for the present prediction scheme. Mixing-plane computations are foreseen as a part of the present methodology.

Concerning blade response model

- An extension of classic Amiet's gust-airfoil interaction theory has been presented, in order to include gust obliqueness and non-parallel segment edges in the blade response. The source phasing over the blade is deduced from sweep-velocity considerations at the leading-edge. A linear interpolation is made on the segment boundary for ensuring source continuity.
- The model seems to be robust to blade radial segmentation and chordwise discretization.
- Unsteady loadings obtained with the present model are in good agreement with numerical results, for the same wake input.
- The extended blade response provides some enhancements in noise predictions. Larger effects could be expected on blades featuring more sweep.

Concerning the acoustic formulation

- An extended CROR tonal noise formula has been derived during the present study. The radial force component is included and sources can be located on the blade MCS. Forward-flight effects are taken into account.
- Results provided by the present acoustic formulation are in excellent agreement with KIM results.

Bibliography

[1] A. L. Weisbrich, J. Godston, and E. S. Bradley. Technology and benefits of high-speed aircraft counterrotation propellers. Contractor Report NASA CR-168258, NASA, 1982.

[2] G. E. Hoff. Experimental performance and acoustic investigation of modern, counterrotating blade concepts. Contractor Report NASA CR-185158, GE Aircfrat Engines, 1990.

[3] M. D. Guynn, J. J. Berton, E. S. Hendricks, W. J. Tong, M. T. Haller, and D. R. Thurman. Initial assessment of open rotor propulsion applied to an advanced single-aisle aircraft. In *11th AIAA Aviation Technology, Integration and Operation (ATIO) Conference*, number AIAA-2011-7058, 2011.

[4] R. W. Harris. Udf/727 flight test program. In *23rd AIAA/SAE/ASME/ASEE Joint Propulsion Conference*, San Diego, CA, Juin 1987.

[5] R. E. Froude. *Trans. Inst. Naval Architects*, 30:390, 1889.

[6] W. J. M. Rankine. *Trans. Inst. Naval Architects*, 6(13), 1865.

[7] S. Drzewiecki. *Bulletin de l'Association Technique Maritime, Paris*, 1892.

[8] Q. R. Wald. The wright brothers propeller theory and design. In *37th AIAA/ASME/SAE/ASEE Joint Propulsion Conference and Exhibit*, Salt Lake City, Utah, July 2001.

[9] E. P. Lesley. Experiments with a counter-propeller. Technical Note NACA-TN-453, NACA, March 1933.

[10] D. Biermann and E. P. Hartman. Full-scale tests of 4- and 6-blade, single- and dual-rotating propellers. Special Report SR-157, NACA, 1941.

[11] U. De Caria. Counter-propeller. Technical Memorandum NACA-TM-587, NACA, October 1930.

[12] F. Weinig. Counter-rotating propellers for aircraft. *Jahrbuch der deutschen Luftfahrtforschung*, 1937.

[13] D. B. Hanson. Noise of counter-rotation propellers. *Journal of Aircraft*, 22(7):609–617, 1985.

[14] A. B. Parry and D. G. Crighton. Prediction of counter-rotation propeller noise. In *12th AIAA Aeroacoustics Conference*, San Antonio, TX, USA, 1989.

[15] J. E. Turnberg and P. C. Brown. Effect of angular inflow on the vibratory response of a counter-rotating propeller. Contractor Report NASA-CR-174819, NASA, January 1985.

[16] J. F. Groeneweg and L. J. Bober. Advanced propeller research. Technical Note ID:19920013294, NASA, 1989.

[17] ACARE2020. European Aeronautics: A Vision for 2020. 2001 (accessed January 17, 2011). http://www.acare4europe.org.

[18] U.N. Kyoto protocol to the united nations framework convention on climate change. http://unfccc.int/essential_background/kyoto_protocol/items/1678.php.

[19] A. Stuermer. Unsteady CFD simulations of contra- rotating propeller propulsion systems. In *44th AIAA/ASME/SAE/ASEE Joint Propulsion Conference*, number AIAA-2008-5218, Hartford, CT, 2008.

[20] A. Stuermer and J. Yin. Low-Speed Aerodynamics and Aeroacoustics of CROR Propulsion Systems. In *15th AIAA/CEAS Aeroacoustics Conference*, Miami, FL, USA, 2009.

[21] A. Stuermer and J. Yin. Low-Speed Aerodynamics and Aeroacoustics of CROR Propulsion Systems. In *28th AIAA Applied Aerodynamics Conference*, Chicago, IL, USA, 2010.

[22] Y. Colin, A. Carazo, B. Caruelle, T. Node-Langlois, and M. Omais. Computational strategy for predicting CROR noise at low speed. Part I: review of numerical methods. In *18th AIAA/CEAS Coference*, Colorado Springs, CO, 2012.

[23] E. Envia. NASA Open Rotor Noise Research. In *14th CEAS-ASC Workshop on Aeroacoustics of high-speed aircraft propellers and open-rotors*, Warsaw, Poland, 2010.

[24] B. Marinus, M. Roger, R. Van den Braembussche, and W. Bosschaerts. Multidisciplinary optimization of propeller blades: focus on the aeroacoustic results. In *17th AIAA/CEAS Conference*, Portland, Oregon, June 2011.

[25] S. Bechet, C. Negulescu, V. Chapin, and F. Simon. Integration of CFD tools in aerodynamic design of contra-rotating propeller blades. In *3rd CEAS- Air & Space Conference*, 2011.

[26] W. C. Strack, G. Knip, A. L. Weisbrich, J. Godston, and E. Bradley. Technology and benefits of aircraft counter rotation propellers. Technical Memorandum NASA TM-82983, NASA, 1981.

[27] D. C. Mikkelson and G. A. Mitchell. Summary of recent NASApropeller research. Technical Memorandum TM-83733, NASA, 1984.

[28] G. Ferraris, Maisonneuve V., and Lalanne M. Prediction of the dynamic behavior of non-symmetric coaxial co- or counter-rotating rotors. *Jornal of Sound and Vibration*, 195(4):649–666, 1996.

[29] B. N. Shivashankara, D. P. Johnson, and R. D. Cuthberston. Installation effects on counter-rotation propeller noise. In *AlAA 13th Aeroacoustics Conference*, number AIAA 90-4023-CP, Tallahassee, FL, October 1990.

[30] J. Ricouard, E. Julliard, M. Omaïs, V.Regnier, A. B. Parry and S. Baralon. Installation effects on contra-rotating open rotor noise. In *16th AIAA/CEAS Aeroacoustics Conference*, Stockholm, Sweden, 2010.

[31] B. Magliozzi. Noise characteristics of a rotating prop-fan. In *AIAA 11th Aeroacoustics Conference*, number AIAA-87-2656, Sunnyvale, CA, October 1987.

[32] F. B. Metzger and P. C. Brown. Results of acoustic tests of a prop-fan model. *Journal of Aircraft*, 25(7):653–658, 1988.

[33] V. P. Blandeau. *Aerodynamic Broadband Noise from Contra-Rotating Open Rotors*. PhD thesis, Institute of Sound and Vibration Research, University of Southampton, 2011.

[34] V. P. Blandeau and P. F. Joseph. Broadband noise due to rotor-wake/rotor interaction in contra-rotating open rotors. *AIAA Journal*, 48(11):2674–2686, 2010.

[35] A. B. Parry, M. J. Kingan, and B. J. Tester. Relative importance of open rotor tone and broadband sources. In *17th AIAA/CEAS Conference*, number AIAA-2011-2763, Portland, Oregon, 2011.

[36] J. E. Ffowcs Williams and D. L. Hawkings. Sound generation by turbulence and surfaces in arbitrary motion. *Philosophical Transactions of the Royal Society of London A (Mathematical and Physical Sciences)*, 264(1151):321–342, 1969.

[37] D. B. Hanson and M. R. Fink. The importance of quadrupole sources in prediction of transonic tip speed propeller. *Journal of Sound and Vibration*, 62(1):19–38, 1979.

[38] R. Boissard, G. Delattre, and F. Falissard. Assessment of aerodynamic and aero-acoustic tools for open-rotor. In *14th CEAS-ASC Workshop and 5th Scientific Workshop of X3*, Warsaw, Poland, October 2010.

[39] R. K. Majjigi and P. R. Gliebe. Development of a rotor wake/vortex model. Contractor Report NASA-CR-174849, NASA, June 1984.

[40] M. J. Kingan and R. H. Self. Counter-Rotation Propeller Tip Vortex Interaction Noise. In *15th AIAA/CEAS Aeroacoustics Conference*, Miami, FL, USA, 2009.

[41] R. K. Amiet. High frequency thin-airfoil theory for subsonic flow. *AIAA Journal*, 14(8):1076–1082, 1976.

[42] M. Roger and C. Schram. Analytical modeling of the tonal noise from open rotor due to tip-vortices. In *14th International Symposium of Transport Phenomena and Dynamics of Rotating Machinery, ISROMAC-14*, Honolulu, HI, February 2012.

[43] A. B. Parry. *Theoretical Prediction of Counter-rotating Propeller Noise*. PhD thesis, University of Leeds, 1988.

[44] J. H. Dittmar, E. B. Gordon, and R. J. Jeracki. The effect of front-to-rear propeller spacing on the interaction noise at cruise conditions of a model counterrotation propeller having a reduced diameter aft propeller. Technical Memorandum NASA TM-101329, NASA, 1988.

[45] J. H. Dittmar and D. B. Stang. Noise reduction for model counterrotation propeller at cruise by reducing aft-propeller diameter. Technical Memorandum NASA TM-88936, NASA, 1987.

[46] R. P. Woodward and C. E. Hughes. Noise of a model counterrotation propeller with simulated fuselage and support pylon at takeoff/approach conditions. Technical Memorandum NASA TM-101996, NASA, 1989.

[47] A. McAlpin and M. J. Kingan. Far-field sound radiation due to an installed open rotor: rotating point source model. In *14th CEAS-ASC Workshop and 5th Scientific Workshop of X3-Noise*, 2010.

[48] M. J. Kingan, C. Powles, and R. H. Self. Effect of centerbody scattering on advanced open-rotor noise. *AIAA Journal*, 48(5):975–980, 2010.

[49] M. J. Kingan and R. H. Self. Open rotor tone scattering. In *17th AIAA/CEAS Conference*, Portland, Oregon, June 2011.

[50] A. Silverstein, S. Katzoff, and W. K. Bullivant. Downwash and wake behind plain and flapped airfoils. Technical Report No. 651, N.A.C.A., June 1938.

[51] R. Raj and B. Lakshminarayana. Three-dimensional characteristics of turbulent wakes behind rotors of axial flow turbomachinery. *Journal of Engineering for Power*, 98:218–228, 1976.

[52] A. Betz. A method for the direct determination of wing section drag. Tecnical Memorandum No. 337, N.A.C.A., November 1925.

[53] Reid; E. G. Wake studies of eight model propellers. Technical Note No. 1040, N.A.C.A., 1946.

[54] J. C. Roberts and P. F. Yaggy. A survey of the flow at the plane of the propeller of a twin-engne airplane. Technical Note No. 2192, N.A.C.A., 1950.

[55] N. H. Kemp and W. R. Sears. The unsteady forces due to viscous wakes in turbomachines. *Journal of Aeronautical Sciences*, 22:478–483, 1955.

[56] H. Schlichting. *Boundary Layer Theory*. Mc Graw-Hill, 1960.

[57] B. Lakshminarayana and J. H. Horlock. Leakage and secondary flows in compressor cascades. Technical Report 26 821, ARC, 1967.

[58] J. H. Horlock, J. F. Louis, P. M. E. Percival, and B. Lakshminarayana. Wall stall in compressor cascades. *American Society of Mechanical Engineers*, 64-WA/FE-29, 1964.

[59] T. E. Fessler and M. J. Hartmann. Preliminary survey of compressor rotor-blade wakes and other flow phenomena with a hot-wire anemometer. Technical Report NACA-RM-E56A13, N.A.C.A., 1956.

[60] C. E. Whitfield, J. C. Kelly, and Barry B. A three-dimensional analysis of rotor wakes. *The Aeronautical Quarterly*, pages 285–300, 1972.

[61] R. Raj and B. Lakshminarayana. Characteristics of the wake behind a cascade of airfoils. *Journal of Fluid Mechanics*, 61:707–730, 1973.

[62] B. Reynolds and B. Lakshminarayana. Characteristics of lightly loaded fan rotor blade wakes. Contractor Report NASA-CR-3188, NASA, November 1979.

[63] B. Reynolds, B. Lakshminarayana, and A. Ravindranath. Characteristics of the near wake of a compressor of a fan rotor blade. *AIAA Journal*, 17(9):959–967, 1979.

[64] D. A. Philbrick and D. A. Topol. Development of a fan noise design system. part i : System design and source modeling. In *15th AIAA Aeroacoustic Conference*, Long Beach, CA, October 1993.

[65] A. J. Cooper and N. Peake. Upstream-radiated rotor-stator intercation noise in mean swirling flow. *Journal of Fluid Mechanics*, 523:219–250, 2005.

[66] Q. R. Wald. The aerodynamics of propellers. *Progress in Aerospace Sciences*, 42:85–128, 2006.

[67] Neal Douglas R. *The effects of rotation on the flow field over a controlled-diffusion airfoil*. PhD thesis, Michigan State University, 2010.

[68] E. W. M. Roosenboom and A. Schröder. Image based measurement techniques of increased complexity for industrial propeller flow investigations. In *27th AIAA Aerodynamic Measurement Technology and Ground Testing Conference*, Chicago, Ill, July 2010.

[69] A. Ravinadranath and B. Lakshminarayana. Three dimensional mean flow and turbulence characteristics of the near wake of a compressor rotor blade. Contractor Report NASA-CR 159518, NASA, 1982.

[70] M. Roger. Sur l'utilisation d'un modèle de sillages pour le calcul du bruit d'interaction rotor-stator. *ACUSTICA*, 80:238–246, 1994.

[71] M.M. Logue and H. M. Atassi. Sound generation and scattering from a rotor in a nonuniform flow. In *16th AIAA/CEAS Conference*, number 2010-3743, Stockholm, Sweeden, June 2010.

[72] M. Nallasamy and E. Envia. Computation of rotor wake turbulence noise. *Journal of Sound and Vibration*, 282(3-5):649–678, 2005.

[73] D. B. Hanson. Theory for broadband noise of rotor and stator cascades with inhomogeneous inflow turbulence including effects of lean and sweep. Technical Report 210762, NASA, 2001.

[74] R. P. Woodward, D. M. Elliot, C. E. Hughes, and J. J. Berton. Benefits of swept and leaned stators for fan noise reduction. In *37th Aerospace Sciences Meeting and Exhibit*, number AIAA-99-0479, Reno, Nevada, January 1999.

[75] E. Envia and M. Nallasamy. Design selection and analysis of a swept and leaned stator concept. *Journal of Sound and Vibration*, 4(jsvi.1999.2441):793–836, 1999.

[76] T. von Karman and W. R. Sears. Airfoil Theory in Non-Uniform Motion. *Journal of Aeronautical Sciences*, 5(10):379–390, 1938.

[77] C. Possio. L'azione aerodinamica sul profilo oscillante in un fluido compressible a velocitá iposonora. *L'Aerotecnica*, 14(4):441–458, 1938.

[78] R. K. Amiet. Compressibility effects in unsteady thin-airfoil theory. *AIAA Journal*, 12(2):252–255, 1974.

[79] R. W. Paterson and R. K. Amiet. Noise of a model helicopter rotor due to ingestion of turbulence. Technical Report 3213, NASA, 1979.

[80] L. T. Filotas. Response of an Infinite Wing to an Oblique Sinusoidal Gust: A Generalization of Sears' Problem. *NASA Special Publication*, 207:231, 1969.

[81] J. M. R. Graham. Similarity rules for thin aerofoils in non-stationary subsonic flows. *Journal of Fluid Mechanics*, 43:753–66, 1970.

[82] J. J. Adamczyk. The passage of an infinite swept airfoil through an oblique gust. Contractor Report 2395, NASA, 1974.

[83] S. Moreau and M. Roger. Competing broadband noise mechanisms in low-speed axial fans. *AIAA Journal*, 45(1):48–57, 2007.

[84] K. Schwarzschild. Die beugung und polarisation des lichts durch einen spalt. i. *Mathematische Annalen*, 55(2):177–247, 1901.

[85] B. T. Chu and L. S. G. Kováznay. Interactions in a viscous heat-conducting compressible gas. *Journal of Fluid Mechanics*, 3:494–514, 1958.

[86] M. E. Goldstein. *Aeroacoustics*. McGraw-Hill, 1976.

[87] M. Roger and S. Moreau. Back-scattering correction and further extensions of amiet's trailing-edge noise model. part 1: theory. *Journal of Sound and Vibration*, 286(3):477–506, 2005.

[88] W. J. Sears. Some aspects of non-stationary airfoil theory and its practical applications. *Journal of Aeronautical Sciences*, 8(3):104–108, 1941.

[89] S. Moreau, M. Roger, and V. Jurdic. Effect of angle of attack and airfoil shape on turbulence-interaction noise. In *11th AIAA/CEAS Aeroacoustic Conference Meeting and Exhibit*, number AIAA 2005-2973, Monterrey, CA, May 2005.

[90] M. Roger. On broadband jet-ring interaction noise and aerofoil turbulence-interaction noise predictions. *Jounal of Fluid Mechanics*, 653:337–364, 2010.

[91] M. Abramowitz and I. A. Stegun. *Handbook of Mathematical Functions with Formulas, Graphs, and Mathematical Table*. Courier Dover Publications, 1965.

[92] R. K. Amiet. Acoustic radiation from an airfoil in a turbulent stream. *Journal of Sound and Vibration*, 41(4):407–420, 1975.

[93] H. M. Atassi, M. Dusey, and C. M. Davis. Acoustic radiation from a thin airfoil in nonuniform subsonic flows, AIAA Journal. *AIAA Journal*, 31(1):12–19, 1993.

[94] D.P. Lockard and P.J. Morris. A parallel implementation of a computational aeroacoustic algorithm for airfoil noise. *Journal of Computational Acoustics*, 5(4):337–353, 1997.

[95] M. S. Howe. *Theory of Vortex Sound*. Cambridge Texts on Applied Mathematics. Cambridge Univ Press.

[96] F. Farassat. Linear acoustic formulas for calculation of rotating blade noise. *AIAA Journal*, 19:1122–1130, 1980.

[97] M. Roger. On broadband jet-ring interaction noise and aerofoil turbulence-interaction noise predictions. *Journal of Fluid Mechanics*, 653:337–364, 2010.

[98] D. B. Hanson. Influence of propeller design parameters on far-field harmonic noise in forward flight. *AIAA Journal*, 18(11):1313–1319, 1980.

[99] M. Roger and A. Carazo. Blade-geometry considerations in analytical gust-airfoil interaction noise models. Stockholm, June 2010.

[100] D. B. Hanson. Helicoidal surface theory for harmonic noise of propellers in the far field. *AIAA Journal*, 18(10):1213–1220, 1980.

[101] D. B. Hanson and D.J. Parzych. Theory for noise of propeller in angular inflow with parametric studies and experimental verification. Contractor Report 4499, NASA, 1993.

[102] D.B. Hanson. Propeller noise caused by blade tip radial forces. In *AIAA 10th Aeroacoustics Coference*, Seatle, Washington, July 1986.

[103] P.J.W. Block. Experimental studies of the effects of installation on single and counter-rotation propeller noise. Technical Report 2541, NASA, 1986.

[104] R. Mani. The radiation of sound from a propeller at angle of attack. Contractor Report 4264, NASA, 1990.

[105] E. Kresja. Prediction of the noise from a propeller at angle of attack. Technical Report 103627, NASA, 1990.

[106] D.B. Hanson. Sound from a propeller at angle of attack: A new theoretical viewpoint. *Proc. R. Soc. Lond.*, 449:315–328, 1995.

[107] F. Blanc. Patch assembly: An automated overlapping gris strategy. *Journal of Aircraft*, 47(1), 2010.

[108] J. I. Erdos, E. Alzner, and W. Mc Nally. Numerical solution of periodic transonic flow through a fan stage. *AIAA Journal*, 15(11), 1977.

[109] J. Prieur and G. Rahier. Aeroacoustic integral methods, formulation and efficient numerical implementation. *Aerospace Science and Technology*, 5:457–468, 2001.

[110] R. K. Amiet. Refraction of sound by a shear layer. *Journal of Sound and Vibration*, 58(4):467–482, 1978.

[111] R. H. Schlinker and R. K. Amiet. Experimental assessment of theory for refraction of sound by a shear layer. Contractor Report 145359, NASA, 1978.

[112] A. B. Parry. Modular prediction scheme for blade row interaction noise. *Journal of Propulsion and Power*, 13(3):334–341, 1997.

[113] Omaïs, M. Experimental and numerical analysis of the pylon-rotor interaction noise radiated by a Contra Rotating Open Rotor. In *14th CEAS-ASC Workshop on Aeroacoustics of high-speed aircraft propellers and open-rotors*, Warsaw, Poland, 2010.

[114] M. Roger, S. Moreau, and A. Guedel. Vortex-shedding noise and potential-interaction noise modeling by a reversed sears' problem. In *12th AIAA/CEAS*, Cambridge MA, June 2006.

[115] R. K. Amiet. Noise due to turbulent flow past a trailing edge. *Journal of Sound and Vibration*, 47(3):387–393, 1976.

[116] F. Conte, M. Roger, S. Moreau, M. Sanjose, and P. Caule. Modelling of installation effects on the noise from subsonic axial fans. In *17th AIAA/CEAS*, Portland, Oregon, June 2011.

[117] M. E. Goldstein and H. M. Atassi. A complete second order theory for the unsteady flow about an airfoil due to a periodic gust. *Journal of Fluid Mechanics*, 74:741–765, 1976.

[118] M. R. Myers and E. J. Kerschen. Influence of incidence angle on sound generation by airfoils interacting with high-frequency gusts. *Journal of Fluid Mechanics*, 292:271–304, 1995.

[119] M. R. Myers and E. J. Kerschen. Effect of airfoil camber on convected gust interaction noise. In *AIAA 10th Aeroacoustics Conference*, Seattle, Washington, July 1986.

[120] P. F. Mish and W. J. Devenport. An experimental investigation of unsteady surface pressure on an airfoil in turbulence – part 2. sources and prediction of mean loading effects. *Journal of Sound and Vibration*, 296(3):447–460, 2006.

dernière page de la thèse

AUTORISATION DE SOUTENANCE

Vu les dispositions de l'arrêté du 7 août 2006,

Vu la demande du Directeur de Thèse

Monsieur M. ROGER

et les rapports de

Monsieur S. MOREAU
Professeur - GAUS - Université de Sherbrooke - 2500 bd de l'Université - Sherbrooke (Québec) Canada J1K 2R1

Et de

Monsieur X. ZHANG
Professor of Aircraft Engineering - Director of Airbus Noise Technology Center of University of Southampton - School of Engineering Sciences - University Road - Southampton SO17 1BJ Royaume-Uni

Monsieur CARAZO Arnulfo

est autorisé à soutenir une thèse pour l'obtention du grade de **DOCTEUR**

Ecole doctorale MECANIQUE, ENERGETIQUE, GENIE CIVIL ET ACOUSTIQUE

Fait à Ecully, le 5 juin 2012

P/Le directeur de l'E.C.L.
La directrice des Etudes

ECOLE CENTRALE DE LYON
SCOLARITE
3ème Cycle

M-A. GALLAND

Abstract

Counter-rotating open rotors are seen as a possible alternative to turbofan engines for future subsonic aircraft propulsion, essentially for their higher fuel-efficiency. This technology leads to fuel savings and to reduced green-house gas emissions. However, these benefits are balanced by some inherent drawbacks, as the increased noise radiation. Particularly, the tonal noise produced by the impingement of the wakes issuing from the front rotor onto the rear-rotor blades is recognized as a major contributor to the emitted noise. The research presented in this thesis led to a semi-analytical methodology to predict the rotor-rotor interaction tonal noise, including three-dimensional features of both rear-rotor blades and front-rotor wakes. The space is cut into annular regions, subsequently unwrapped for formulating the problem in equivalent Cartesian coordinates. Also, the obtained blade segments are assimilated as a set of flat trapezoids with arbitrary orientation, accounting for blade sweep and chord variations in the spanwise direction. A double strategy is proposed for the description of front-rotor wakes. First, an analytical model is proposed in which wake direction and diffusion are deduced from the blade stagger angle and axial distance between the rotors. Secondly, a strategy for post-processing numerical wakes is presented. In both cases, the oncoming excitation is expanded in a series of sinusoidal gusts with two aerodynamic wavenumber components. Using this information the unsteady loading on the rear-rotor blades is obtained, in the frequency domain, from an extension of Amiet's theory for gust-airfoil interaction to account for airfoil sweep and chord variations, flow compressibility and source non-compactness. The obtained noise source is back-projected on the blade mean-camber surface. An extended far-field formulation is then used to predict the noise. This theory is derived in detail from Ffowcs Williams & Hawkings' formalism adapted for acoustic dipoles rotating in a uniformly moving atmosphere. The proposed methodology has been implemented in the tool ORION and assessed by comparing its results with numerical simulations and wind-tunnel measurements.

Résumé

Les constructeurs aéronautiques envisagent les systèmes de propulsion à hélices contra-rotatives comme une alternative aux turboréacteurs, afin de réduire la consommation de carburant et les émissions des gaz à effet de serre. En raison de l'absence de carénage, la réduction du bruit engendrée par de tels systèmes représente un enjeu majeur pour les industriels. En particulier, le bruit de raies dû à l'impact des sillages de l'hélice amont sur l'hélice aval constitue une part significative de l'émission acoustique. Le travail présenté dans cette thèse a abouti à une méthode semi-analytique de prédiction de ce bruit d'interaction, intégrant de façon relativement réaliste les effets tridimensionnels des sillages de l'hélice amont et de la géométrie des pales de l'hélice aval. L'espace balayé par une pale est décomposé en tranches annulaires, déroulées pour décrire localement l'interaction en coordonnées cartésiennes. Le segment de pale obtenu est approché par un trapèze plat de forme et d'orientation quelconques. Une double stratégie est proposée pour la description du sillage. Premièrement, il peut être décrit par un modèle analytique tenant compte du vrillage et de l'expansion avec la distance au bord de fuite. Deuxièmement, il peut être post-traité à partir des calculs numériques. Ensuite, dans chaque tranche le déficit de vitesse ressenti par le segment de pale fait l'objet d'une décomposition de Fourier à deux nombres d'onde. Le calcul de la réponse aérodynamique instationnaire du segment est fait dans le domaine fréquentiel. Il étend des solutions analytiques existantes valables pour un segment rectangulaire, et prend en compte la compressibilité du fluide et la non-compacité des pales. On restitue ainsi les effets de la flèche, du vrillage et de la variation de la corde en envergure. Les fluctuations de portance induites sur les différents segments, obtenues par le calcul, sont utilisées pour construire une répartition de sources acoustiques équivalentes sur la surface réelle des pales, au sens de l'analogie acoustique. Le bruit en champ lointain est alors calculé en utilisant le formalisme de Ffowcs Williams & Hawkings, adapté au cas d'un dipôle tournant dans un écoulement uniforme. La méthodologie proposée a été implémentée dans l'outil ORION et évaluée avec des résultats numériques et des mesures en soufflerie.

Key Words : Open rotor, analytical methods, viscous wake, unsteady aerodynamics, acoustic radiation, rotating sources

Mots Clés : Hélice contra-rotative, méthodes analytiques, sillage visqueux, aérodynamique instationnaire, rayonnement acoustique, sources tournantes